

Electronic Thesis and Dissertation Repository

1-23-2024 10:00 AM

Design of Active Pharmaceutical Ingredients Solid States in Crystallization Processes

Weizhong Gong, *The University of Western Ontario*

Supervisor: Rohani, Sohrab, *The University of Western Ontario*

A thesis submitted in partial fulfillment of the requirements for the Doctor of Philosophy degree in Chemical and Biochemical Engineering

© Weizhong Gong 2024

Follow this and additional works at: <https://ir.lib.uwo.ca/etd>

 Part of the [Other Chemical Engineering Commons](#), and the [Process Control and Systems Commons](#)

Recommended Citation

Gong, Weizhong, "Design of Active Pharmaceutical Ingredients Solid States in Crystallization Processes" (2024). *Electronic Thesis and Dissertation Repository*. 9914.
<https://ir.lib.uwo.ca/etd/9914>

This Dissertation/Thesis is brought to you for free and open access by Scholarship@Western. It has been accepted for inclusion in Electronic Thesis and Dissertation Repository by an authorized administrator of Scholarship@Western. For more information, please contact wlsadmin@uwo.ca.

Abstract

Crystallization is an important technique to obtain solid-state drugs from solutions. Physicochemical properties of the active pharmaceutical ingredients (APIs) are determined by crystallization. More than half of the active pharmaceutical ingredients exhibit polymorphism, the phenomenon of chemical species showing more than one unit-cell structure in the solid state. Controlling polymorphism is one of the most important goals during pharmaceutical manufacturing. Nevertheless, the control of polymorphism is sometimes not enough to realize the targeted physicochemical properties. Suitable additives (coformers/salt formers) are explored to generate new multi-component solid phases of poorly soluble/bioavailable active pharmaceutical ingredients (APIs). The design of pharmaceutical cocrystals and salts has thus become significantly important in recent years. With the introduction of suitable coformers or salt formers, the targeted physicochemical property can be well improved.

This work aims to provide insights into the design, characterization, optimization and control of API solid states in crystallization processes. The characterization of crystal packing structures, melting points, and tuned solubilities is carried out for all cases studied in the thesis. First, the solvent screening for an API, which is the basis of solution crystallization, is researched based on the solubility prediction using Hansen solubility parameters. Next, the optimal working conditions for harvesting the desired polymorph in continuous crystallization are investigated both experimentally and numerically. Numerical models of single-stage and two-stage mixed-suspension mixed-product removal (MSMPR) crystallizers are developed to test different working environments. The production of kinetically unfavorable polymorph of L-glutamic acid is realized by experiment. Subsequently, for APIs of low solubility (biopharmaceutics classification system (BCS) class II or IV), a screening method using hydrogen-bond propensity and hydrogen-bond coordination calculations is developed to improve the drug solubility and dissolution. Lastly, regardless of single-component or multicomponent API solid phases, poor morphology such as needle-like or plate-like would impede the downstream processes. A new spherical crystallization method depending on the liquid-liquid phase separation is developed with the help of an in-situ Pixact Crystallization

Monitoring (PCM) system. Spherical crystals are successfully produced to avoid the original plate-like morphology of vanillin crystals.

Keywords

Crystallization processes, API solid state, Polymorphism, MSMPR crystallization, Cocrystal screening, Spherical Crystallization, Hydrogen-bond propensity, Hydrogen-bond coordination, Liquid-liquid phase separation

Summary for Lay Audience

The production of fine chemicals and pharmaceuticals always uses crystallization process as the final purification step. The shape, purity, and other physicochemical properties of the crystalline products are directly determined by the crystallization process. Hence, the design and the control of the final solid states is the core issue in the pharmaceutical and fine chemical industries.

Polymorphism describes the phenomenon of chemical species showing more than one unit-cell structure in the solid state and has an influence on the product stability, solubility, and processability of the active pharmaceutical ingredient (API). In batch crystallization, seeding is often used as a means of controlling product polymorphism. Nevertheless, initial seeds would be washed out during continuous production. An investigation on seeding strategy in continuous crystallization process was conducted based on the kinetic modelling.

Although polymorph control can improve the targeted physicochemical product property, the effect is still restricted by the API itself. To improve the targeted property significantly, suitable additives (coformers/salt formers) are often needed to generate new multi-component solid phases. Screening and selection of the potential multi-component solid states (pharmaceutical cocrystals and salts) of an API is one of the most critical early stages of drug development.

After the design and control of the crystal unit cell, the crystalline product may exhibit poor morphology that would affect the flowability and bulk density of the product. Spherical crystals have smaller contact areas compared with needle, and other poor-shaped crystals. Therefore, spherical crystallization technology is developed in this thesis as it directly combines the downstream granulation processes with crystallization and thus significantly reduces the total equipment and energy cost. With the optimized crystal solid state, the product value is significantly increased, and the efficiency of the crystallization process design is improved.

Co-Authorship Statement

Chapter 1: The introduction was prepared by Weizhong Gong and reviewed by Dr. Sohrab Rohani.

Chapter 2: The experimental work, data curation, and data analysis were performed by Weizhong Gong. The manuscript was prepared by Weizhong Gong and reviewed by Dr. Sohrab Rohani. Pan Li aided this work in conducting the experiments.

A version of this chapter has been published in *Journal of Molecular Liquids*:

Gong, W., Li, P., & Rohani, S. (2022). Taurine in several aqueous binary solvents: Solubility prediction, measurement, modeling, solvent effect, and thermodynamics. *Journal of Molecular Liquids*, 367, 120522.

Chapter 3: The experimental work, data curation, and data analysis were performed by Weizhong Gong. The manuscript was prepared by Weizhong Gong and reviewed by Dr. Sohrab Rohani. Yuanyi Wu and Mengxing Lin aided this work in conducting the experiments and numerical models.

A version of this chapter has been published in *Chemical Engineering Research and Design*:

Gong, W., Wu, Y., Lin, M., & Rohani, S. (2021). Polymorphism control of l-Glutamic acid in a single-stage and a two-stage MSMR crystallizer by different seeding strategies. *Chemical Engineering Research and Design*, 170, 23-33.

Chapter 4: The experimental work and visualization were performed by Weizhong Gong. The data curation and formal analysis were performed by Weizhong Gong and Pradip Kumar Mondal together. Pradip Kumar Mondal was also in charge of the conceptualization and methodology. The manuscript was prepared by Weizhong Gong and reviewed by Pradip Kumar Mondal, Soroush Ahmadi, and Dr. Sohrab Rohani. Yuanyi Wu aided this work in the software.

A version of this chapter has been published in *International Journal of Pharmaceutics*:

Gong, W., Mondal, P. K., Ahmadi, S., Wu, Y., & Rohani, S. (2021). Cocrystals, salts, and salt-solvates of olanzapine; selection of coformers and improved solubility. *International Journal of Pharmaceutics*, 608, 121063.

Chapter 5: The experimental work, data curation, and data analysis were performed by Weizhong Gong. The manuscript was prepared by Weizhong Gong and reviewed by Dr. Sohrab Rohani. Pan Li aided this work in conducting the experiments.

A version of this chapter has been accepted by *Journal of Pharmaceutical Sciences*.

Chapter 6: The conclusion was prepared by Weizhong Gong and reviewed by Dr. Sohrab Rohani.

Acknowledgments

Time is a brisk wind. I would like to express my thanks and appreciation to those who supported me to realize this work. I would like to express my sincerest gratitude to my supervisor, Prof. Sohrab Rohani, for his warm support and guidance during my Ph.D life. It is his encouragement and patience that inspired me to achieve the best.

I would not be able to realize this work without the support from Wanhua Chemical Group Co., Ltd. Many thanks to the coordinator, Dr. Tian Nan, for his coordination as well as the assistance. I appreciate the affirmation from Mr. Xiaofei Qiao, Mr. Zhan hu, Dr. Peng Liu and Mr. Pan Li, who provided me a chance to be the first joint Ph.D candidate of the company. I would like to appreciate people from UWO who helped me on this joint program as well.

My deep appreciation to my lab members: Yuanyi Wu, Mengxing Lin, Soroush Ahmadi Nasrabadi, Pradip Mondal, and Zhenguao Gao, who taught me, led me, and showed me how a qualified Ph.D. should be. Many thanks to Chuanxin Wu, Xing Wei, Yijie Wei, Guie Xu, Hanzhuo Ding, Yuchen Zhou, Youming Ding and other friends who always stayed with me and encouraged me when I was in trouble. Thanks to Boyang Qian, Luning Chen, Haoyu Fang, Xingfu Zhang, Zheng Jiang, Alex Grenier, Zimin Zhao, Ziyi Fan, Lu Bai, Yiyi Xu, and other friends I met in Western. Without you guys, my life in Canda would have been colorless.

My endless love and gratitude to my dear family. They contributed their best to support my study. This work is also accomplished by their efforts. I would like to dedicate this work to my late grandfather, the most respected person in my life.

I'm glad to share this moment with everyone who blinks and shines my life road. Each communication with you made me who I currently am.

Table of Contents

| | |
|--|-------|
| Abstract..... | ii |
| Summary for Lay Audience..... | iv |
| Co-Authorship Statement..... | v |
| Acknowledgments..... | vii |
| Table of Contents..... | viii |
| List of Tables (where applicable)..... | xiii |
| List of Figures (where applicable)..... | xv |
| List of Appendices..... | xviii |
| Nomenclature..... | xix |
| Chapter 1..... | 1 |
| 1. Introduction..... | 2 |
| 1.1 Background..... | 2 |
| 1.1.1 Crystallization..... | 2 |
| 1.1.2 Solubility Measurement..... | 4 |
| 1.1.3 Crystallization Process Modelling..... | 5 |
| 1.1.4 Polymorphism..... | 8 |
| 1.1.5 Cocrystals and Salts..... | 10 |
| 1.1.6 Spherical Crystals..... | 15 |
| 1.2 Research Objectives and Approach..... | 17 |
| 1.3 Thesis Organization..... | 19 |
| 1.4 References..... | 20 |
| Chapter 2..... | 24 |
| 2. Taurine in several aqueous binary solvents: Solubility prediction, measurement, modeling, solvent effect, and thermodynamics..... | 25 |
| Abstract..... | 25 |

| | | |
|-------|---|----|
| 2.1 | Introduction..... | 26 |
| 2.2 | Experimental Section..... | 28 |
| 2.2.1 | Materials | 28 |
| 2.2.2 | Powder X-ray Diffraction | 28 |
| 2.2.3 | Differential Scanning Calorimetry..... | 28 |
| 2.2.4 | Isothermal Solubility Test (Myerson et al., 2019) | 29 |
| 2.3 | Theoretical Section | 30 |
| 2.3.1 | Hansen Solubility Parameter..... | 30 |
| 2.3.2 | KAT-LSER Model..... | 32 |
| 2.3.3 | Solubility Modelling | 32 |
| 2.3.4 | Model accuracy | 36 |
| 2.3.5 | Thermodynamic properties of dissolution | 37 |
| 2.4 | Results and Discussion | 38 |
| 2.4.1 | Powder X-ray Diffraction Results | 38 |
| 2.4.2 | Thermal Analysis..... | 39 |
| 2.4.3 | Hansen Solubility Parameter (HSP) Analysis..... | 40 |
| 2.4.4 | Solubility Data | 41 |
| 2.4.5 | Solvent Effect Analysis of Taurine..... | 53 |
| 2.4.6 | Thermodynamic Properties of Solutions | 54 |
| 2.5 | Conclusions..... | 57 |
| 2.6 | References..... | 58 |
| | Chapter 3..... | 63 |
| 3. | Polymorphism Control of L-Glutamic Acid in a Single-Stage and a Two-Stage MSMPR Crystallizer by Different Seeding Strategies..... | 64 |
| | Abstract | 64 |
| 3.1 | Introduction..... | 65 |

| | | |
|-------|--|-----|
| 3.2 | Materials and Methods..... | 68 |
| 3.2.1 | Materials | 68 |
| 3.2.2 | Seeds Preparation..... | 68 |
| 3.2.3 | Polymorph Characterization | 69 |
| 3.2.4 | Experimental Setup..... | 69 |
| 3.3 | Dynamic Simulation | 74 |
| 3.4 | Result and Discussion..... | 79 |
| 3.4.1 | Single-Stage MSMPR Crystallization | 79 |
| 3.4.2 | Two-stage MSMPR crystallization..... | 83 |
| 3.4.3 | Single-stage MSMPR with intermittent seeding..... | 86 |
| 3.5 | Conclusions..... | 89 |
| 3.6 | References..... | 90 |
| | Chapter 4..... | 93 |
| 4. | Cocrystals, Salts, and Salt-Solvates of Olanzapine; Selection of Coformers and Improved Solubility | 94 |
| | Abstract | 94 |
| 4.1 | Introduction..... | 95 |
| 4.2 | Experimental Section | 97 |
| 4.2.1 | Preparation of olanzapine cocrystals/salts and corresponding solvates.... | 97 |
| 4.2.2 | Single Crystal X-ray Diffraction..... | 100 |
| 4.2.3 | Powder X-ray Diffraction | 101 |
| 4.2.4 | Differential Scanning Calorimetry..... | 101 |
| 4.2.5 | Preparation of Buffer Solution..... | 101 |
| 4.2.6 | Equilibrium Solubility and Powder Dissolution Measurement | 101 |
| 4.3 | Results and Discussion | 103 |
| 4.3.1 | Selection of Candidate Molecules for OLN Multi-component Crystals | 103 |

| | | |
|-----------|--|-----|
| 4.3.2 | Thermal Analysis | 112 |
| 4.3.3 | Comparison of the PXRD Patterns | 114 |
| 4.3.4 | Solubility and Dissolution Test..... | 117 |
| 4.4 | Conclusion | 121 |
| 4.5 | References..... | 122 |
| Chapter 5 | | 127 |
| 5. | Spherical Crystallization Based on Liquid-Liquid Phase Separation In A Reverse Antisolvent Crystallization Process | 128 |
| | Abstract | 128 |
| 5.1 | Introduction..... | 129 |
| 5.2 | Materials and Methods..... | 131 |
| 5.2.1 | Materials | 131 |
| 5.2.2 | Powder X-ray Diffraction | 131 |
| 5.2.3 | Thermogravimetric analysis..... | 132 |
| 5.2.4 | Ternary Phase Diagram..... | 132 |
| 5.2.5 | Hansen Solubility Parameter (Gong et al., 2022; Hansen, 2007) | 133 |
| 5.2.6 | Reverse antisolvent spherical crystallization of vanillin | 134 |
| 5.3 | Results and Discussion | 135 |
| 5.3.1 | Ternary Phase Diagram of water:1-propanol:vanillin System..... | 135 |
| 5.3.2 | Hansen Solubility Parameter..... | 137 |
| 5.3.3 | Formation Processes and Mechanisms for Vanillin Spherical Agglomerates | 138 |
| 5.3.4 | Effect of Process Parameters on Properties of Spherical Agglomerates. | 139 |
| 5.3.5 | Properties Assessment of Vanillin Spherical Crystals..... | 144 |
| 5.4 | Conclusions..... | 146 |
| 5.5 | References..... | 146 |
| Chapter 6 | | 150 |

| | |
|--|-----|
| 6. Main Contributions and Conclusions of the Thesis, Recommendations for Future Work | 151 |
| 6.1 Conclusions..... | 151 |
| 6.1.1 Solubility Study | 151 |
| 6.1.2 Polymorph Control in Continuous Crystallization | 152 |
| 6.1.3 Cocrystal/Salt Screening..... | 153 |
| 6.1.4 Spherical Crystallization Based on LLPS..... | 154 |
| 6.2 Significance of the Research..... | 155 |
| 6.3 Recommendations..... | 156 |
| Appendices..... | 158 |
| Curriculum Vitae | 207 |

List of Tables (where applicable)

| | |
|---|-----|
| Table 2-1a. Hansen Solubility Parameters of taurine. | 40 |
| Table 2-1b. Three partial (δ , δp , δh), the total (δt), and the joint (δv) solubility parameters of five solvents and taurine | 40 |
| Table 2-2. Experimental mole fraction solubility (x_1) of taurine in three binary solvents at temperature from 298.15K to 318.15K..... | 44 |
| Table 2-3. Parameters and deviations of the modified Apelblat model..... | 46 |
| Table 2-4. Parameters and deviations of the NRTL, UNIQUAC, and Wilson model..... | 47 |
| Table 2-5. Parameters and deviations of the λh Model. | 49 |
| Table 2-6. Thermodynamic properties for taurine dissolution in binary solvents ^c | 55 |
| Table 3-1. Operating conditions of the multiple MSMPR experiments | 72 |
| Table 3-2. Crystal Properties and Kinetic Parameters used in the Simulation | 76 |
| Table 3-3. Simulation and experimental results in the single-stage MSMPR | 82 |
| Table 3-4. Simulation and experimental results in two-stage MSMPR..... | 84 |
| Table 3-5. Simulation and experimental results for intermittent seeding | 88 |
| Table 4-1a. Predicted hydrogen-bond propensities for OLN with phenol and benzoic acid | 106 |
| Table 4-1b. Predicted hydrogen-bond coordination numbers for OLN with phenol and benzoic acid..... | 127 |
| Table 4-2. List of intermolecular interactions of OLN multicomponent crystals..... | 109 |
| Table 4-3. Solubility of OLN cocrystals/salts/solvates..... | 120 |
| Table 5-1. Operating conditions of reverse antisolvent crystallization experiments | 134 |

| | |
|---|-----|
| Table 5-2. Three partial (δd , δp , δh), the total (δt) solubility parameters of three solvents and vanillin ^a | 137 |
| Table A-1. UNIQUAC parameters for taurine and related solvents | 158 |
| Table A-2. Calculated mole fraction solubilities of taurine using the modified Apelblat model, NRTL, UNIQUAC, Wilson, and λh models..... | 159 |
| Table A-3. Kamlet-Taft parameters π^* (dipolarity-polarizability), α (hydrogen bond donor parameter) and β (hydrogen bond donor parameter) and Hildebrand solubility parameter, δ_h , of aqueous solution of PG, ACN, EG, and acetone at 298.15 K | 166 |
| Table A-4. MLRA results of the KAT-LSER model on solubility of taurine in water (1) + PG (2) mixture at 298.15 K..... | 167 |
| Table A-5. MLRA results of the KAT-LSER model on solubility of taurine in water (1) + ACN (2) mixture at 298.15 K..... | 167 |
| Table A-6. MLRA results of the KAT-LSER model on solubility of taurine in water (1) + EG (2) mixture at 298.15 K..... | 168 |
| Table A-7. MLRA results of the KAT-LSER model on solubility of taurine in water (1) + acetone (2) mixture at 298.15 K | 169 |
| Table B-1. Crystal data and structure refinement of OLN-Phol, OLN-Res, OLN-SA, OLN-AA, OLN-TA, and OLN-3HBA..... | 170 |
| Table B-2. DSC data of OLN and its multicomponent crystals | 174 |
| Table C-1. Mass Fraction Solubility of Vanillin (g/g solution) and Liquid–Liquid Phase Separation Data (mass fraction, g/g solution) at Atmospheric Pressure (P = 0.1 MPa)..... | 180 |

List of Figures (where applicable)

| | |
|---|----|
| Figure 1-1. Scheme of the metastable zone (Lewis et al., 2015) | 4 |
| Figure 1-2 The temperature dependence of the enthalpy and free energy for enantiotropic (left) and monotropic (right) polymorphism (Brittain, 2018) | 10 |
| Figure 1-3. Schematic of API solid forms classification (Rodrigues et al., 2018) | 11 |
| Figure 1-4. Supramolecular homosynthons (a) carboxylic acid homosynthon exist as dimer (b) amide homosynthon exist as dimer; supramolecular heterosynthons (c) carboxylic acid–amide heterosynthon (d) carboxylic acid–pyridine heterosynthon. (Duggirala et al., 2016) | 13 |
| Figure 1-5. Spherical Crystallization Methods (a) Spherical Agglomeration (b) Quasi-Emulsion Solvent Diffusion (c) Spherulitic Growth (Cui et al., 2022; Gyulai et al., 2017; Zhang et al., 2021) | 17 |
| Figure 2-1. PXRD patterns of taurine and residue taurine after solubility tests | 38 |
| Figure 2-2. Thermographs of taurine and residue taurine after solubility tests | 39 |
| Figure 2-3. Solubility data for taurine in water (w1)-ACN with various mole fractions at different temperatures | 51 |
| Figure 2-4. Solubility data for taurine in water (w1)-EG with various mole fractions at different temperatures | 52 |
| Figure 2-5. Solubility data for taurine in water (w1)-PG with various mole fractions at different temperatures | 52 |
| Figure 2-6. ΔG_0 values versus water mole fraction (w1) | 57 |
| Figure 3-1 Solubility curves of LGA metastable form and stable form | 67 |
| Figure 3-2. Powder X-ray diffraction Patterns of the LGA metastable α -form (a) and the LGA stable β -form (b) | 69 |

| | |
|---|-----|
| Figure 3-3. Schematics of a single-stage MSMPR (a) and laboratory scale two-stage MSMPR (b)..... | 74 |
| Figure 3-4. Single-stage MSMPR dynamic simulation results at T=25°C, Ci= 0.04 kg/kg (a), T=25°C, 0.02 kg/kg (b), T= 45°C, Ci= 0.04 kg/kg (c) and T=50°C, Ci= 0.04 kg/kg (d) | 82 |
| Figure 3-5. Growth rate (left) and Birth rate (right) variations in the second stage MSMPR at different working temperature (RT = 60 min/stage)..... | 86 |
| Figure 3-6. Evolution of the mass fraction of β -form LGA with different seeding frequencies (a), working temperatures (b), feed concentrations (c), seed weight (d) | 88 |
| Figure 3-7. Simulation results of a single-stage MSMPR at 30°C with intermittent seeding | 89 |
| Figure 4-1. Crystal packing diagrams of (a) OLN-Phol-H ₂ O, (b) OLN-SA, (c) OLN-AA, (d) OLN-3HBA, and (e) OLN-TA-H ₂ O | 111 |
| Figure 4-2. Thermographs of fresh OLN multicomponent crystals | 113 |
| Figure 4-3. PXRD patterns of OLN and OLN multicomponent crystals | 116 |
| Figure 4-4. Dissolution measurement of OLN cocrystals/salts/solvates | 121 |
| Figure 5-1. The schematic diagram for the reverse antisolvent crystallization | 135 |
| Figure 5-2. Ternary phase diagrams of water:1-propanol:vanillin system under atmospheric pressure (P = 0.1 MPa) at 30 °C; Region 1: solid–liquid phase 1; Region 2: liquid–liquid phase; Region 3: solid–liquid–liquid phase; Region 4: solid–liquid phase 2; Region 5: Liquid phase. *S: Solid, L: Liquid..... | 136 |
| Figure 5-3. The formation mechanism of vanillin spherical agglomerates monitored by PCM | 139 |
| Figure 5-4. SEM images of vanillin products under different working conditions: (a) Trial 1, (b) Trial 2, (c) Trial 3, (d) Trial 4, (e) Trial 5, (f) Trial 6, (g) Trial 7 | 142 |
| Figure 5-5. Microscopic photos of vanillin agglomerates (Trial 8)..... | 143 |

| | |
|--|-----|
| Figure 5-6. The PSDs of the vanillin products obtained under different stirring rates..... | 143 |
| Figure 5-7. PXRD patterns of vanillin raw material and produced spherical agglomerates | 145 |
| Figure 5-8. TGA thermograms and their derivatives for vanillin raw material and the spherical agglomerate (Trial 6) | 145 |
| Figure B-1. The ORTEP diagrams of (a) OLN-Phol-H ₂ O, (b) OLN-SA, (c) OLN-AA, (d) OLN-3HBA, and (e) OLN-TA-H ₂ O | 175 |
| Figure B-2. Simulated PXRD patterns from sc-XRD..... | 176 |
| Figure B-3. PXRD curves of OLN-TA-H ₂ O, OLN-TA, OLN-2ATPA, OLN-3HBA-ACN, OLN-3HBA, and OLN dihydrate; buf refers to potential contamination with the buffer solution | 176 |
| Figure B-4. PXRD patterns of OLN, 3HBA, their cocrystal and cocrystal solvate | 177 |
| Figure B-5. DSC curves of OLN-3HBA before and after washing, and OLN-2ATPA, after solubility test; buf refers to potential contamination with the buffer solution..... | 177 |
| Figure B-6. HPLC diagram of OLN and its multicomponent solid phases | 178 |

List of Appendices

| | |
|--|-----|
| Appendix A: Chapter 3 appendix | 158 |
| Appendix B: Chapter 4 appendix..... | 170 |
| Appendix C: Chapter 5 appendix..... | 179 |
| Appendix D: Copyright permission | 182 |
| Appendix E: Research in Wanhua Chemical Group Co.,Ltd. | 183 |
| Appendix F: Matlab codes for crystallization process and solubility regression | 186 |

Nomenclature

Chapter 1

| | | |
|-------|---|------------|
| B^0 | Crystal nucleation rate | #/s/kg sol |
| C^* | Solubility | kg/kg sol |
| v_e | Velocity on external spatial coordinate | m/s |
| v_i | Velocity on internal spatial coordinate | m/s |
| API | Active pharmaceutical ingredient | |
| EAFUS | Everything Added to Foods in the United States | |
| FDA | Food and Drug Administration | |
| GRAS | Generally recognized as safe | |
| HBC | Hydrogen bond coordination | |
| HBP | Hydrogen bond propensity | |
| HSP | Hansen solubility parameter | |
| LLPS | Liquid-liquid phase separation | |
| PAFA | Priority-based Assessment of Food Additives | |
| PBE | Population Balance Equation | |
| PCM | Pixact crystal monitoring system | |
| t | Time | s |
| B | Birth density function | #/m/kg sol |
| C | Concentration | kg/kg sol |
| D | Death density function | #/m/kg sol |
| G | Growth rate | m/s |
| L | Crystal size | m |

| | | |
|-------|--|-------------------------------|
| Q | Volumetric flow rate | m^3/s |
| R | Phase space | m^3 |
| S | Supersaturation | - |
| V | Working volume | m^3 |
| V | Working volume | m^3 |
| j | Order of moments | |
| n | Population density | $\#/\text{m}^3/\text{kg sol}$ |
| v | Velocity | m/s |
| x | Set of internal and external coordinates comprising the phase space R, | m |
| μ | Moment of the crystal size distribution | |

Chapter 2

| | | |
|------------|---|--|
| A_{vw} | Standard segment surface | $\text{cm}^2 \cdot \text{mol}^{-1}$ |
| C_p | Heat capacity | $\text{J}/(\text{kg} \cdot \text{K})$ |
| E_{hi} | Contribution of the hydrogen bond energy for function group i | J/mol |
| F_{di} | Contribution of the dispersion force for function group i | $(\text{J} \cdot \text{m}^3)^{1/2}/\text{mol}$ |
| F_{pi} | Contribution of the polar force energy for function group i | $(\text{J} \cdot \text{m}^3)^{1/2}/\text{mol}$ |
| \bar{M} | Average molar mass of the co-solvent | g/mol |
| M_{dish} | Weight of the petri dish | g |
| M_{dry} | Measured weight after drying | g |
| M_{wet} | Total weight of the petri dish plus the filtered liquor | g |
| R_a | Solubility factor | - |

| | | |
|------------|--|--|
| T_m | Melting point of the solute | K |
| V_S | Molar volume of the solute | $\text{cm}^3 \cdot \text{mol}^{-1}$ |
| V_{vw} | Standard segment volume | $\text{cm}^3 \cdot \text{mol}^{-1}$ |
| x_1 | Mole fraction of taurine in the solution | - |
| γ_1 | Activity coefficient of the solute | - |
| δ_h | Hydrogen-bonded HSP r | $\text{MPa}^{0.5}$ |
| δ_d | Dispersion HSP | $\text{MPa}^{0.5}$ |
| δ_p | Polar HSP | $\text{MPa}^{0.5}$ |
| δ_v | Volume-dependent HSP | $\text{MPa}^{0.5}$ |
| ξ_H | Relative contributions of enthalpy | - |
| ξ_{TS} | Relative contributions of entropy | - |
| π^* | Dipolarity–polarizability parameter | |
| ACN | Acetonitrile | |
| EG | Ethylene glycol | |
| HSP | Hansen solubility parameter | |
| KAT – LSER | Kamlet and Taft linear solvation energy relationship | |
| PG | 1,2-propanediol | |
| R | Molar gas constant | $\text{J}/(\text{mol} \cdot \text{K})$ |
| S | Solubility | $\text{g}/\text{g sol}$ |
| T | Absolute temperature | K |
| α | Hydrogen bond donation ability of the solvent | |
| β | Hydrogen bond acceptance ability of the solvent | |

Chapter 3

| | | |
|-----------------|--|-----------------------------|
| g_{α} | Growth rate order of α form | - |
| $g_{\beta 1}$ | Growth rate order of β form | - |
| $g_{\beta 2}$ | Growth rate order of β form | - |
| $k_{b\alpha}$ | Secondary nucleation constant | m^3/s |
| $k_{b\beta 1}$ | Secondary nucleation constant | m^3/s |
| $k_{b\beta 2}$ | Secondary nucleation constant | m^3/s |
| $k_{d\alpha}$ | Dissolution constant | m/s |
| $k_{g\alpha 0}$ | Growth rate constant of α form | m/s |
| $k_{g\beta 0}$ | Growth rate constant of β form | m/s |
| k_v | Crystal volumetric shape factor | - |
| LGA | L-glutamic acid | |
| MSMPR | Mixed suspension and mixed product removal | |
| RT, τ | Residence time | s |
| SMPT | Solution-mediated polymorphic transformation | |
| Y | Yield | % |
| B | Crystal nucleation rate | $\#/\text{s}/\text{kg sol}$ |
| C | Solubility | $\text{kg}/\text{kg sol}$ |
| D | Dissolution rate | m/s |
| E | Active energy | J |
| G | Growth rate | m/s |
| L | Crystal size | m |
| n | Population density | $\#/\text{m}/\text{kg sol}$ |
| Q | Volumetric flow rate | m^3/s |

| | | |
|----------|---|-------------------|
| <i>S</i> | Supersaturation | - |
| <i>V</i> | Working volume | m ³ |
| <i>i</i> | Polymorph | |
| <i>j</i> | Order of moments | |
| <i>t</i> | Time | s |
| ρ | Crystal density | kg/m ³ |
| μ | Moment of the crystal size distribution | |

Chapter 4

| | |
|-------|---|
| 2ATPA | 2-aminoterephthalic acid |
| 3HBA | 3-Hydroxy benzoic acid |
| Phol | Phenol |
| Res | Resorcinol |
| AA | Anthranilic acid |
| API | Active pharmaceutical ingredient |
| BCS | Biopharmaceutical Classification System |
| CCDC | Cambridge Crystallographic Data Centre |
| HBC | Hydrogen-bond coordination |
| HBP | Hydrogen-bond propensity |
| LAG | Liquid-assisted grinding |
| OLN | Olanzapine |
| SA | Salicylic acid |
| SDG | Solvent drop grinding |

Chapter 5

| | | |
|------------|-----------------------|--------------------|
| δ_h | Hydrogen-bonded HSP r | MPa ^{0.5} |
|------------|-----------------------|--------------------|

| | | |
|-------------|--------------------------------|--------------------|
| δ_h | Hydrogen-bonded HSP r | MPa ^{0.5} |
| δ_d | Dispersion HSP | MPa ^{0.5} |
| δ_p | Polar HSP | MPa ^{0.5} |
| <i>LLPS</i> | Liquid-liquid phase separation | |
| <i>SDS</i> | Sodium dodecyl sulfate | |

Chapter 6

| | | |
|----------|--|--|
| API | Active pharmaceutical ingredient | |
| ACN | Acetonitrile | |
| BCS | Biopharmaceutics classification system | |
| EG | Ethylene glycol | |
| HBC | Hydrogen bond coordination | |
| HBP | Hydrogen bond propensity | |
| HSP | Hansen solubility parameter | |
| KAT-LSER | Kamlet and Taft linear solvation energy relationship | |
| LGA | L-glutamic acid | |
| LLPS | Liquid-liquid phase separation | |
| MSMPR | Mixed suspension mixed product removal | |
| PCM | Pixact crystal monitoring system | |
| PG | 1,2-propanediol | |

Chapter 1

Introduction

1. Introduction

1.1 Background

1.1.1 Crystallization

Crystallization is one of the oldest and most important separation and purification unit operations to produce high value-added chemicals and pharmaceuticals (Lewis et al., 2015). Solute molecules would get organized into a crystalline form during crystallization. Physicochemical properties of solid-state products are determined and controlled by the final crystallization step (Alvarez & Myerson, 2010). The solution crystallization process is driven by the supersaturation: the ratio between the solution concentration and the solubility at a given temperature (Eq. 1-1). The crystallization process can be classified into four categories: cooling crystallization, evaporative crystallization, anti-solvent crystallization, and reactive crystallization; depending on how the supersaturation is generated.

$$S = \frac{C}{C^*} \quad (1 - 1)$$

Crystallization can be separated into two main steps: crystal nucleation (birth of new crystals), and crystal growth; in addition to possible agglomeration and breakage. When the supersaturation is high, solute molecules dissolved in solution would start to form clusters leading to nucleation. A new solid phase with small nuclei would be formed during the aggregation of molecules. Based on different nucleation conditions, it could be divided into primary nucleation and secondary nucleation. Whether seed crystals are introduced to drive nucleation to happen is the difference. The primary nucleation could be further separated as homogeneous primary nucleation and heterogeneous primary nucleation. The former only exists in a very clean solution without the presence of dust particles. Although the existence of the stirrer and dust particles would reduce the barrier

energy for primary nucleation, the required supersaturation is still too high. Excess small particles would be generated at the same time, resulting in crystal agglomeration. The maximum supersaturation below which nucleation would not happen for a long time is called metastability limit, and the zone between the solubility line and the metastability limits is known as the metastable zone ([Figure 1-1](#)). Secondary nucleation is normally introduced to operate moderately in the metastable zone. For secondary nucleation, the fragments of the existing crystals act as the seeds. There are four main types of secondary nucleation: initial breeding, in which new nuclei are small fragments of the dry seeds; dendritic breeding, in which the corners and edges of the seeds first face the supersaturation and become dendrites; contact nucleation, in which the seeds contact with each other and vessel walls and get broken; fluid shear breeding, in which turbulent shear forces are exerted on the seeds to form nuclei. In many cases, crystal nucleation may not happen, instead, an intermediate state would be first generated. For example, during the cooling or antisolvent crystallization process, two coexisting liquid phases would be observed instead of crystals in some cases. This is known as liquid-liquid phase separation (LLPS) or oiling out (Xu et al., 2021). LLPS is driven by the enthalpy to generate a system including two liquid phases with different compositions and densities.

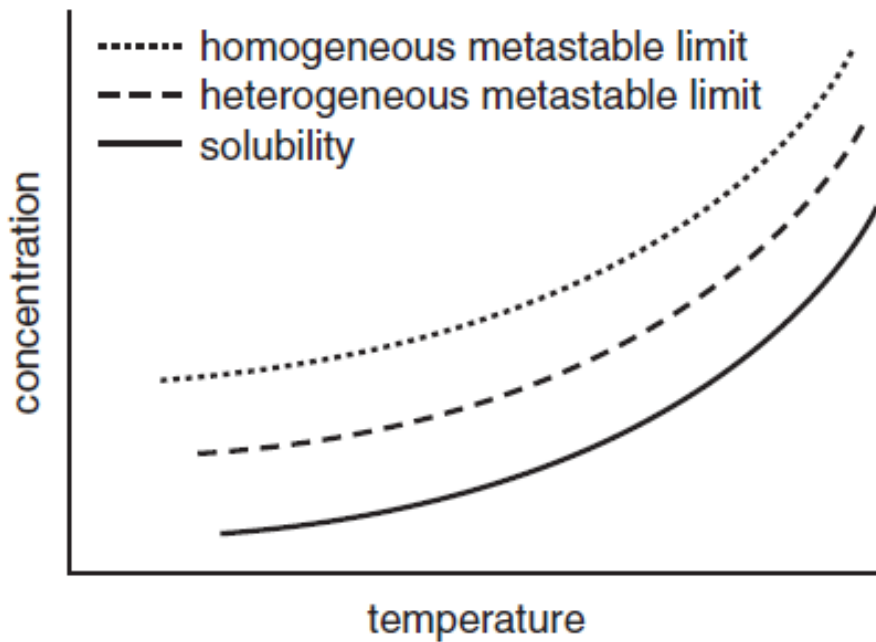


Figure 1-1. Scheme of the metastable zone (Lewis et al., 2015)

1.1.2 Solubility Measurement

Solubility measurement offers thermodynamic information of the selected crystallization system and is the most fundamental knowledge for a crystallization process design. There are two major types of solubility measurements: isothermal solubility measurement and non-isothermal solubility measurement.

1.1.2.1 Isothermal Solubility Measurement

Solubility data are always collected under a constant and pre-settled temperature while employing agitation or shaking in this method. Excess crystal solids will be added into a pre-weighed solvent under a certain temperature, the solution will be well-mixed through agitation for a long time that is enough to reach the thermodynamic equilibrium. The solution is then kept still until the solid phase settles. The clear solution at top is sampled by filtration to analyze the concentration. High-performance liquid chromatography

(HPLC) or ultraviolet/visible spectrophotometer can be applied for concentration measurement. The filtrated solution may also get dried to measure the mass difference to compute the dissolved static solubility. The achieved result is more accurate than the non-isothermal method at the cost of time. This method is not suitable for the measurement of unstable polymorphs or unstable APIs.

1.1.2.2 Non-isothermal Solubility Measurement

Non-isothermal solubility measurements take less time than isothermal measurements as the sampling and concentration analysis process are eliminated. Excess solute is mixed with a pre-weighted solvent, and the mixed solution is continuously stirred and slowly heated until all crystals dissolve. The temperature when the last crystal dissolves is considered to be the solubility temperature at the determined concentration of solution. Due to the existence of a metastable zone, the measurement is irreversible. It should be noticed that dissolution is not an instantaneous process. Therefore, the measured temperature would be above the real saturated temperature. The size of the difference is determined by the heating rate. This method offers a tool to measure the solubility of perishable samples with acceptable accuracy.

1.1.3 Crystallization Process Modelling

1.1.3.1 Population Balance Equation (PBE)

Population balance equation is a mathematical model used to describe the change of crystal size distribution with respect to time and space. The format of PBE is similar to a mass balance or an energy balance. It was firstly proposed in 1962 (Randolph & Larson, 1962) and provided a mathematical description of particulate processes including crystallization. To solve the population balance crystallization kinetics, namely

nucleation and growth kinetics are needed. A general population balance is built from the particle-number continuity equation that is:

$$\text{Accumulation} = \text{Input} - \text{Output} + \text{Net generation} \quad (1 - 2)$$

In a specific subregion R_1 , the equation can be expressed as

$$\frac{d}{dt} \int_{R_1} n dR = \int_{R_1} (B - D) dR \quad (1 - 3)$$

$$\frac{d}{dt} \int_{R_1} n dR = \int_{R_1} \frac{\partial n}{\partial t} dR + \left(n \frac{dx}{dt} \right) |_{R_1} = \int_{R_1} \left[\frac{\partial n}{\partial t} + \nabla \cdot \left(\frac{dx}{dt} n \right) \right] dR \quad (1 - 4)$$

$$\frac{dx}{dt} = v = v_e + v_i \quad (1 - 5)$$

Thus, for the arbitrary Lagrangian region R_1 :

$$\int_{R_1} \left[\frac{\partial n}{\partial t} + \nabla \cdot (v_e n) + \nabla \cdot (v_i n) + D - B \right] dR = 0 \quad (1 - 6)$$

$$\frac{\partial n}{\partial t} + \nabla \cdot (vn) - B + D = 0 \quad (1 - 7)$$

where x is the set of internal and external coordinates comprising the phase space R , v is the velocity, B and D are the birth and death density functions in the phase space. Here $(B - D)dR$ indicates the net appearance of particles. ∇ is the divergence operator, v_e is the velocity on external spatial coordinate and v_i is the velocity on internal phase space coordinate. For the population balance over a macroscopic external coordinate region (in practice), the system can be described only with the distribution of particles in the internal phase space. Averaging in the external space results in a more useful equation for backmixed systems. A suitable volume $V(t)$ of external phase space having an arbitrary number of inputs and outputs with flow rate Q_k and population density n , is chosen and multiplied by dV and integrated over $V(t)$

$$\int \left[\frac{\partial n}{\partial t} + \nabla \cdot (vn) + D - B \right] dV = 0 \quad (1 - 8)$$

This can be finally derived to a well-mixed macroscopic population balance as

$$\frac{\partial n}{\partial t} + \nabla \cdot (vn) + \frac{nd(\log V)}{dt} = B - D - \sum_k \frac{Q_k n_k}{V} \quad (1-9)$$

The particle velocity is normally assumed to be the same as the liquid velocity. Hence, the one-dimensional (the crystal characteristic length, L) PBE in a well-mixed, constant-volume, transient crystallizer could be written as

$$\frac{\partial n}{\partial t} + \frac{\partial(Gn)}{\partial L} = B - D - \sum_k \frac{Q_k n_k}{V} \quad (1-10)$$

with a boundary condition:

$$n^0 = n(L=0) = \frac{B_0}{G(L=0)} \quad (1-11)$$

Where $G = \frac{dL}{dt}$ is the growth rate, and B_0 is the nucleation rate of the crystal and an initial condition, representing the number distribution of crystals at time zero.

1.1.3.2 Method of Moments

The method of moments converts the PBE into a set of ordinary differential equations (ODEs) in terms of the moments that can be integrated numerically. Moments are defined as:

$$\mu_j = \int_0^{\infty} L^j n(t, L) dL \quad (1-12)$$

Where μ_j is the j th moment of crystal population. If we assume the agglomeration and breakage are negligible and substitute Eq. (1-12) into Eq. (1-10) results in

$$\frac{d\mu_0}{dt} = -\frac{1}{\tau} \mu_0 + B_0 \quad (1-13)$$

$$\frac{d\mu_j}{dt} = -\frac{1}{\tau}\mu_j + jG\mu_{j-1} \quad (1 - 14)$$

Where τ is the residence time. The zeroth to third moments correspond to the total number, length, area and volume of all particles in the system. The main advantage of this method is the simple and fast computational process, but it cannot generate the crystal size distribution and it does not work in non-linear or size-dependent kinetic rate systems.

1.1.4 Polymorphism

Polymorphism describes the phenomenon of chemical species showing more than one unit-cell structure in the solid state. Different crystal structures result in different physical properties, including packing, thermodynamic, spectroscopic, kinetic, surface, and mechanical properties (Brittain, 2018). Selection of the proper polymorph of an API facilitates downstream processes such as filtration, granulation, and tableting; in addition to affecting crystal properties such as solubility and stability.

There are two different routes that can form various polymorphic crystal forms. If the polymorphism is caused due to the packing of different motifs, it is referred to as packing polymorphism. If, however, the molecule is not rigid and results in distinct conformational states of the molecule leading to the formation of a different characteristic structure, it is called conformational polymorphism.

Based on the relative stability of two polymorphs, polymorphic systems can be divided into enantiotropy and monotropy. Enantiotropy describes the polymorphic systems in which a transition temperature (below the melting point) of two polymorphs exists (where the Gibbs free energies of two polymorphs are the same) over a given temperature range. Monotropy refers to the condition in which one polymorph has lower solubility and Gibbs free energy at all temperatures below the melting point. [Figure 1-2](#) shows the temperature

dependence of the enthalpy and free energy for enantiotropic and monotropic systems (Brittain, 2018).

Polymorphism transition in the manufacturing or transportation and storage process can cause an economic loss with serious legal and health issues. The unstable polymorph of Ritonavir, an antiviral medicine that prevents HIV from multiplying, is therapeutically effective. It came into the market in 1996 and was withdrawn in 1998 as the produced ritonavir of unstable polymorph transformed to the stable form and lost the effect. Hence, all pharmaceutical companies are required to perform thorough polymorphic studies/screening before submitting a New Drug Application by Food and Drug Administration (FDA) and other agencies that monitor the production and distribution of the drug.

Control of polymorphism is crucial for a robust crystallization production (Achermann et al., 2023). In a batch crystallization process, the stable polymorph can always be obtained through the solvent-mediated phase transformation (Beckmann, 2000). Doki et al. (Doki et al., 2004) found that different seed loadings of the metastable form of glycine crystals resulted in different polymorphic outcomes. High seed loadings of metastable form led to pure metastable form and low seed loadings would result in a mixture of both stable and metastable forms. In continuous crystallization, On the other hand, only few papers have studied polymorphic outcomes in the continuous crystallization systems (Lai et al., 2014, 2015; Lin et al., 2020; Nicoud et al., 2019). Seeding at initial is no longer applicable as seeds will be washed out after several residence times (Gong et al., 2021). Lai et al. (Lai et al., 2015) successfully used a two-stage MSMR to produce α -form p-aminobenzoic acid, where the first stage worked at a high temperature to produce the α -form seeds of the p-aminobenzoic acid and the second stage operated at a β -form favored low temperature. Lin et al. (Lin et al., 2020) found that the interplay of nucleation and growth rates determines the product polymorph in MSMR crystallization.

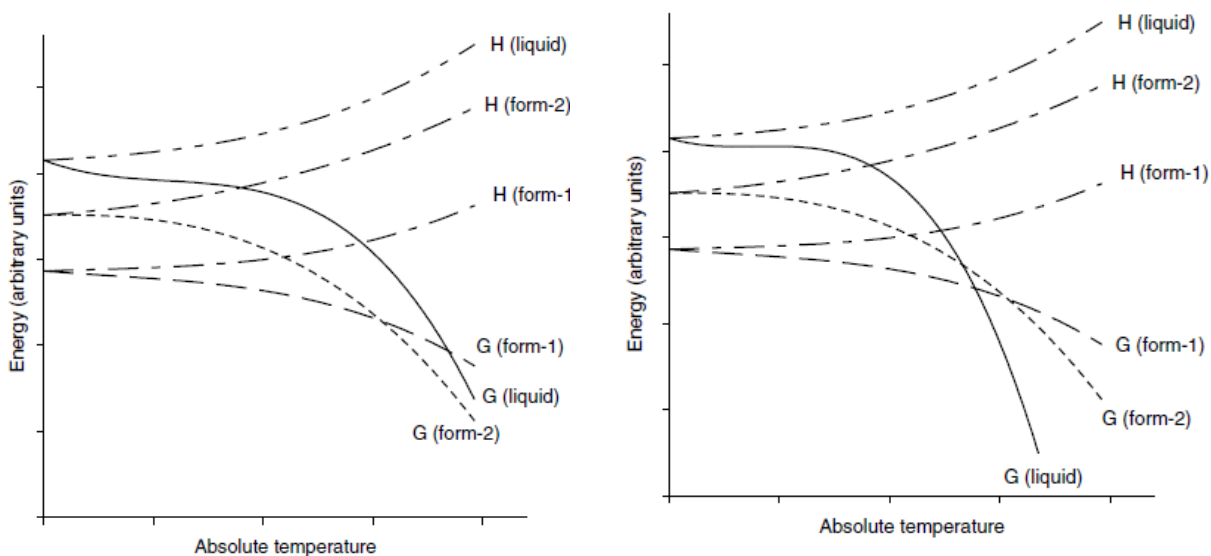


Figure 1-2 The temperature dependence of the enthalpy and free energy for enantiotropic (left) and monotropic (right) polymorphism (Brittain, 2018)

1.1.5 Cocrystals and Salts

Apart from single-component crystalline (polymorph), API solids may also form multi-component crystalline (molecular adduct and salt), including cocrystals, salts, and solvates/hydrates (Figure 1-3). Screening and selection of the potential multi-component solid states of an API is one of the most critical early stages of drug development. The stability, solubility, dissolution rate, and bioavailability of an API might improve upon cocrystallization or salt formation (Almarsson & Zaworotko, 2004; Blagden et al., 2007).

Multi-component crystals refer to the crystals in which the unit cell includes more than one type of molecule. Multi-component crystals can be further classified as salts, cocrystals, and stoichiometric solvates. A pharmaceutical salt is an ionized molecular API linked to a counterion where a hydrogen proton is exchanged to form the ionic bond. If the API is linked to a neutral molecule through the hydrogen bond, it is named as cocrystal. When the crystallization solvent is captured in the crystalline compound, it forms a solvate. Compared to other solid-state forms, pharmaceutical cocrystals have

advantages of well-defined stoichiometry, higher thermal stability, and stability to humidity and can be designed with a large number of cofomers (Duggirala et al., 2016; Huang et al., 2019; Reddy et al., 2009). Therefore, the pharmaceutical industry has an increasing interest in screening and selection of cocrystals with a concurrent patent activity rise (Clarke et al., 2012). However, in the current drug market, only a few API cocrystal formulations are approved. The salt preparation is still the first priority among all crystalline solid-state formulations (Nechipadappu et al., 2019; Sarmah et al., 2018), mainly due to the improvement in solubility and dissolution of APIs in polar solvents. But the latter is only applicable to ionizable pharmaceuticals. Crystal engineering in the field of multicomponent crystals contains various structural possibilities, providing a rich landscape for the exploration and design of novel solid states with targeted properties.

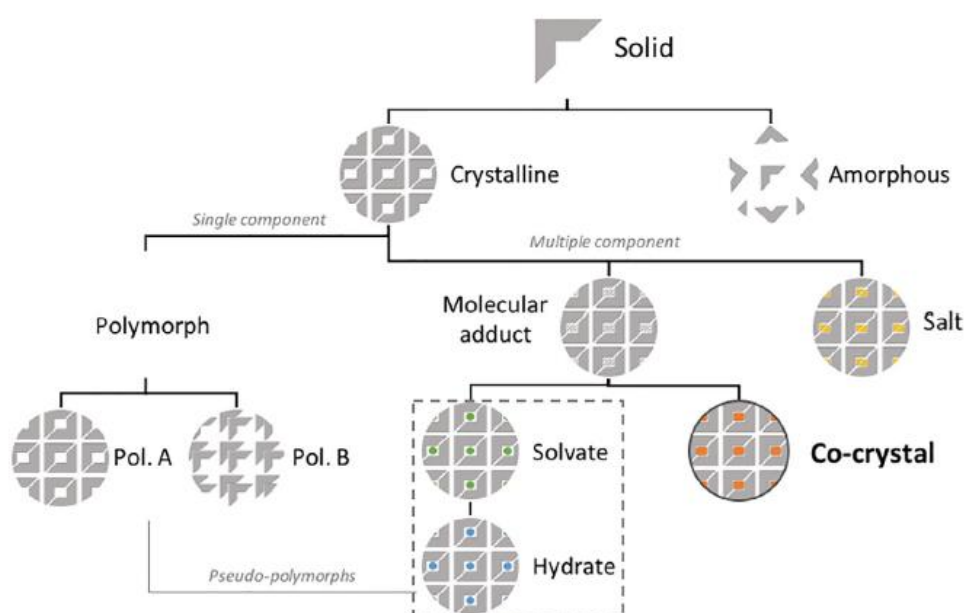


Figure 1-3. Schematic of API solid forms classification (Rodrigues et al., 2018)

1.1.5.1 Design of Pharmaceutical Cocrystals and Salts

Selection of potential coformers for a designated API is critical. Supramolecular synthons, which are special arrangements of intermolecular interactions, are applied in the design of pharmaceutical crystals. Supramolecular synthons include two main types: supramolecular homosynthons between the same complementary functional groups, and supramolecular heterosynthons between different but complementary functional groups, as shown in [Figure 1-4](#). The acid group of a carboxylic acid, the amide group, the amine group, and the alcohol group are the most common functional groups in supramolecular synthons by hydrogen bonding (Rodrigues et al., 2018). The selected coformer must ensure the safety of the drug cocrystals. Based on the Priority-based Assessment of Food Additives (PAFA) database, there are around 2000 compounds that are generally recognized as safe to be selected and there are around 40-50 potential coformers that may successfully form cocrystals or salts with a given API. The difference between cocrystals and salts is whether a proton transfer happens or not. Normally, the “ ΔpK_a rule of 3” (Lemmerer et al., 2015) is followed to determine the possible formation of cocrystals and salts: cocrystals will form if $\Delta pK_a = pK_a$ (protonated base) – pK_a (acid) is less than 0. On the other hand, molecular salts will form for differences greater than 3.

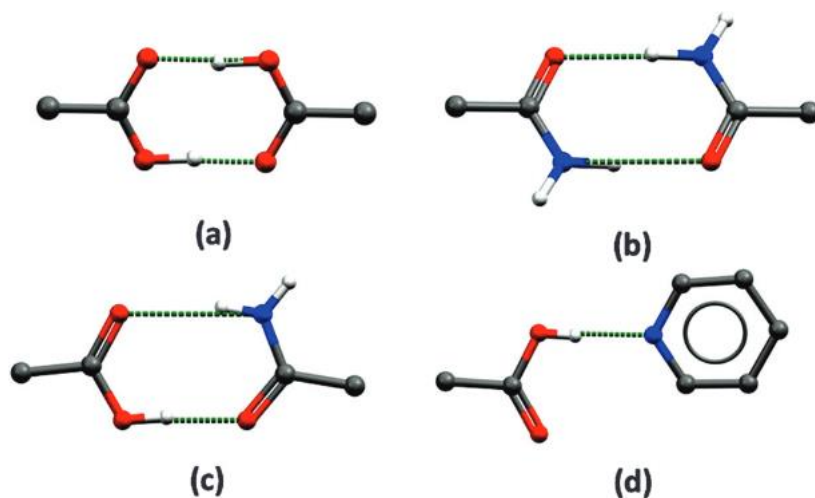


Figure 1-4. Supramolecular homosynthons (a) carboxylic acid homosynthon exist as dimer (b) amide homosynthon exist as dimer; supramolecular heterosynthons (c) carboxylic acid–amide heterosynthon (d) carboxylic acid–pyridine heterosynthon.

(Duggirala et al., 2016)

1.1.5.2 Pharmaceutical Cocrystal and Salt Screening

The approved number of potential additives from the Generally Recognized as Safe (GRAS) and Everything Added to Foods in the United States (EAFUS) is vast. Predictive tools are needed to shorten the time and resource demands of experimental “trial and error” approaches on cocrystal and salt screening.

1.1.5.2.1 Hydrogen Bond Propensity (HBP)

Hydrogen bond propensity is a tool that identifies all the possible hydrogen bonds and their networks in Mercury. With the reported crystal structures in Cambridge Structural Database (CSD), HBP analysis can compute a propensity value for each potential donor-acceptor pair (Sandhu et al., 2018). Assessment in propensity values between donors and acceptors from the API and coformers can then be held to find out the possibility of

cocrystal formation by subtracting the propensity of the most likely interaction between API:API or coformer:coformer from that of the API:coformer.

Hydrogen bond coordination (HBC) is another tool that provides the relative probability of observing coordination number between a hydrogen bond donor and an acceptor. The coordination number refers to the number of interatomic hydrogen bonds formed between a donor and an acceptor. HBP analysis can be applied with the HBC calculation to further shorten the research cycle.

Previously, the molecular complementary module in Mercury was always applied for cocrystal screening. The module was designed based on the molecular shape and polarity. Three shape factors: the length of the short axis, the short/long, and medium/long axis ratios, and two polarity factors: the fraction of nitrogen and oxygen atoms, and the dipole moment are selected as five molecular features to predict the screening result. Nevertheless, the prediction result using five descriptors lacks accuracy. The collocation of HBP and HBC calculations offers a faster and more accurate predictive tool.

1.1.5.2.2 Hansen Solubility Parameters (HSP)

The idea of Hansen Solubility Parameter (HSP) was proposed by Charles Hansen in the 1960s (Hansen, 2007). HSPs are applicable to substances interacting with dispersion forces, hydrogen bonds and considerable polar forces. Based on the theory of "similarity and inter-miscibility", for two materials, the more similar their HSPs are, the higher possibility of their miscibility would be. The HSP consists of three major parts: atomic dispersion forces (dispersion HSP shown by δ_d), molecular permanent dipole forces (polar HSP, δ_p), and hydrogen-bonding energy (hydrogen-bonded HSP, δ_h). Group contribution method is always applied to calculate these three parameters for a given API. Some scholars consider cocrystal as the "miscibility" of the API and the coformer. Hence, HSP can also be used for cocrystal screening.

1.1.6 Spherical Crystals

Spherical crystallization is a particle design technology that generates compacted spherical crystals without tableting. Applying spherical crystallization can avoid needle-like or plate-like products that suffer from poor flowability and low packing density. The spherical crystallization technology was first invented by Kawashima et al. who used a bridging liquid to promote the agglomeration of crystals in the 1980s (Kawashima et al., 1982). Spherical crystallization directly combines the downstream granulation processes with crystallization and thus significantly reduces the total investment cost (Ma et al., 2021). Spherical crystallization technology involves several advantages majorly on improvements of flow property, drug compressibility, stability, solubility, and tastes. Three main approaches of spherical crystallization have been developed so far: spherical agglomeration (SA) (Kawashima, 1984; Kawashima et al., 1982); quasi-emulsion solvent diffusion (QESD) (Chen et al., 2020), and spherulitic growth (Cui et al., 2022; Guo, 2022).

1.1.6.1 Spherical Agglomeration

This method is developed based on the formation of fine crystals and their agglomeration (Liu et al., 2022). The SA method is always realized through the antisolvent crystallization, through which the system can easily reach a large supersaturation, resulting in the production of fine crystals. Bridging liquid is then added with the agitation to wet the surface crystals preferentially to cause binding, forming primary agglomerates. Primary agglomerates would further aggregate to secondary agglomerates and the shape of these agglomerates would become spherical due to the attrition by agitation. The main disadvantage of spherical agglomeration is that the bridging liquid is always toxic. Zhang et al. (Zhang et al., 2021) successfully improved the flowability, and anticaking ability of KBH_4 by making different size spherical agglomerates.

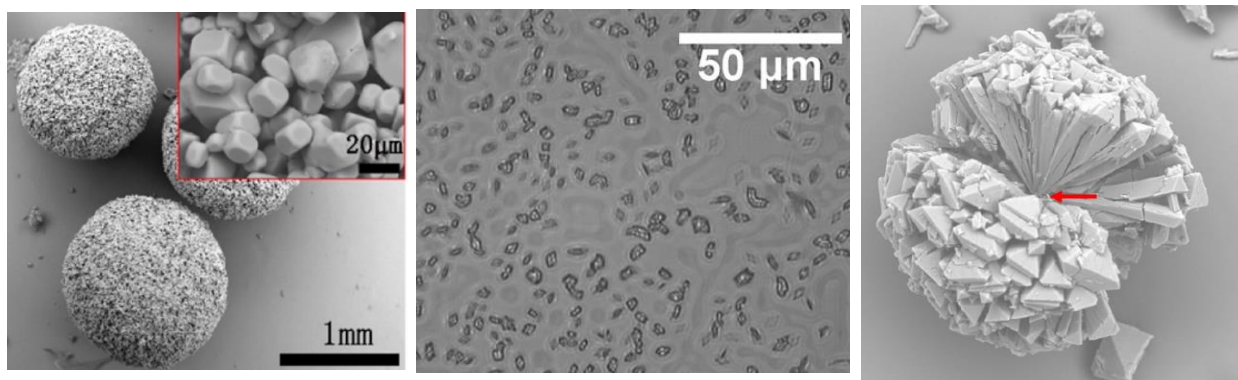
1.1.6.2 Quasi-Emulsion Solvent Diffusion

Quasi-emulsion solvent diffusion method can be carried out using a mixed system of two or three partially miscible solvents including the emulsifier (Chen et al., 2020). Solution of concentrated drug is poured into the poor solvent (dispersion medium) under agitation to generate quasi emulsion droplets. The solvent then diffuses out of the droplets into the antisolvent, and the anti-solvent diffuses into the droplets, resulting in the production of fine crystals. Fine crystals will get agglomerated since remained residual solvent in the droplets will perform as an agglomerating agent. How to keep the system emulsified and to ensure appropriate diffusion of the solvents are the main difficulties of this method. Chen et al. (Chen et al., 2020) applied this strategy to reduce the punch-sticking propensity of celecoxib with substantially improved tabletability and flowability.

1.1.6.3 Spherulitic Growth

Unlike the other two methods developed based on the agglomeration of fine crystals, spherulitic growth is a method based on crystal growth. Radial noncrystallographic branching of sub-individual crystals along the growth front is caused by additives. Mechanisms revealing spherulitic growth remain unclear and the trigger for spherulitic growth of an API is realized by trial and error. Cui et al. found that spherulites of amoxicillin sodium would be obtained by keeping agitation after seeding during the aging period of the reactive-antisolvent coupled crystallization, while no agitation would result in rod-like crystals (Cui et al., 2022).

Figure 1-5. Spherical Crystallization Methods (a) Spherical Agglomeration (b) Quasi-



Emulsion Solvent Diffusion (c) Spherulitic Growth (Cui et al., 2022; Gyulai et al., 2017; Zhang et al., 2021)

1.2 Research Objectives and Approach

The overall objective of this thesis is to improve the yield and the physicochemical properties of crystal product based on the design and control of the final crystal product solid state. The objectives of the thesis include:

- To develop a solvent screening method based on the solubility prediction of a given API in various solvents.
- To develop the methodologies to predict and to harvest the desired polymorph of a given API in continuous crystallization production.
- To develop a systematic cofomers and salt formers screening method that can improve the targeted properties of a given API.
- To develop a new spherical crystallization process based on the oiling out phenomenon using an image-based process analytical technology (PAT) instrument.

For the study of solvent screening based on solubility prediction, the proposed prediction method was based on the Hansen Solubility Parameters (HSPs). Based on the calculated HSPs, the qualitative trend of solubility in different solvents was obtained. Solubility

experiments were then conducted for the prediction validation. During the solubility tests, no phase transformation was identified by Powder X-ray diffraction (PXRD). Thermal properties like melting point and enthalpy were measured by differential scanning calorimeter (DSC) analysis. The achieved solubility data were regressed by various thermodynamic models to analyze the thermodynamic properties. The Kamlet and Taft linear solvation energy relationship (KAT-LSER) model was applied to determine the impact of molecular interactions on the solubility.

The study of polymorphism control in continuous crystallization was implemented both numerically and experimentally. The simulation of the continuous crystallization process was conducted with MATLAB. The population balance equation was solved by the method of moments. Continuous crystallization of L-glutamic acid was conducted experimentally using an intermittent withdrawal policy. Different polymorphic outcomes of L-glutamic acid were characterized by PXRD.

For cocrystal/salt screening, hydrogen bond propensity (HBP) calculation was first applied to seek potential hydrogen bond donors and acceptors, hydrogen bond coordination (HBC) analysis was held then to predict possible synthons. Solvent droplet liquid-assisted grinding (LAG) and ball milling were used to produce bulk cocrystals/salts. PXRD and DSC were used to characterize the formation of new solid phase. Single crystal X-ray diffraction (ScXRD) data were collected to analyze the crystal structure. HPLC coupled with UV–Vis detector was used in the solubility and dissolution test instead of UV–vis spectroscopy, to avoid the peak overlap between olanzapine and co-formers/salt-formers.

The spherical crystallization optimization was realized through a reverse antisolvent crystallization process. The spherical crystallization mechanism was revealed by the Pixact Crystallization Monitoring (PCM) system. Based on the revealed mechanism, a two-step mechanical stirring policy during the addition and aging steps was proposed.

Significant contributions have been made on shorten the time wasted by solvent screening, pharmaceutical cocrystal and salt screening, polymorphism tuning, and morphology transfiguration.

1.3 Thesis Organization

This thesis is in the integrated-article format.

Chapter 1 introduces the research background on crystallization process and crystal products as well as research objectives, approaches, and the organization of the thesis.

Chapter 2, the first part of this thesis, focuses on the basic of solution crystallization, namely the concept of solubility. As supersaturation is the driving force of crystallization and it highly depends on the selected solvent, efforts were put into the prediction of solubility and the molecular analysis of the solubility trend. Once the solvent is fixed, the next work is to determine the crystal product solid state.

Chapter 3 and Chapter 4 discuss the design and control of the inherent crystal product solid state. Chapter 3 focuses on the control of the single-component polymorphic outcome in MSMR crystallizers through different seeding strategies. Different seeding strategies were simulated with MATLAB to explore the optimal operation parameters. Continuous seeding was applied to secure the production of the targeted polymorph. An intermittent seeding strategy was proposed and optimized for a single-stage MSMR crystallization. Chapter 4 extends the work to the design of multicomponent solid forms. A combination of HBP and HBC analysis offered great cocrystal/salt screening result. The designed multicomponent cocrystals/salts improved the targeted physicochemical property of the product.

Chapter 5 deals with the improvement of the external poor morphology problem of the crystal product using spherical crystallization. The implementation of PAT clearly reveals

the spherical crystallization mechanism. A reverse antisolvent crystallization system with variable mechanical stirring speed during different crystallization stages is developed to optimize the size and the sphericity of the spherical particle.

Chapter 6 summarizes the current research work, the main contributions and gives suggestions for future work.

1.4 References

- (1) Achermann, R., Košir, A., Bodák, B., Bosetti, L., & Mazzotti, M. (2023). Process Performance and Operational Challenges in Continuous Crystallization: A Study of the Polymorphs of L -Glutamic Acid. *Crystal Growth & Design*, 23(4), 2485–2503. <https://doi.org/10.1021/acs.cgd.2c01424>
- (2) Almarsson, Örn, & Zaworotko, M. J. (2004). Crystal engineering of the composition of pharmaceutical phases. Do pharmaceutical co-crystals represent a new path to improved medicines? *Chemical Communications*, 17, 1889. <https://doi.org/10.1039/b402150a>
- (3) Alvarez, A. J., & Myerson, A. S. (2010). Continuous Plug Flow Crystallization of Pharmaceutical Compounds. *Crystal Growth & Design*, 10(5), 2219–2228. <https://doi.org/10.1021/cg901496s>
- (4) Beckmann, W. (2000). Seeding the Desired Polymorph: Background, Possibilities, Limitations, and Case Studies. *Organic Process Research & Development*, 4(5), 372–383. <https://doi.org/10.1021/op0000778>
- (5) Blagden, N., de Matas, M., Gavan, P. T., & York, P. (2007). Crystal engineering of active pharmaceutical ingredients to improve solubility and dissolution rates. *Advanced Drug Delivery Reviews*, 59(7), 617–630. <https://doi.org/10.1016/j.addr.2007.05.011>
- (6) Brittain, H. G. (2018). *Polymorphism in Pharmaceutical Solids*. CRC Press.
- (7) Chen, H., Paul, S., Xu, H., Wang, K., Mahanthappa, M. K., & Sun, C. C. (2020). Reduction of Punch-Sticking Propensity of Celecoxib by Spherical Crystallization via Polymer Assisted Quasi-Emulsion Solvent Diffusion. *Molecular Pharmaceutics*, 17(4), 1387–1396. <https://doi.org/10.1021/acs.molpharmaceut.0c00086>
- (8) Clarke, H. D., Hickey, M. B., Moulton, B., Perman, J. A., Peterson, M. L., Wojtas, Ł., Almarsson, Ö., & Zaworotko, M. J. (2012). *Crystal Engineering of Isostructural*

Quaternary Multicomponent Crystal Forms of Olanzapine. *Crystal Growth & Design*, 12(8), 4194–4201. <https://doi.org/10.1021/cg3007052>

- (9) Cui, P., Yang, W., Jia, L., Zhou, L., Zhang, M., Bao, Y., Xie, C., Hou, B., & Yin, Q. (2022). Spherulitic Growth Strategy for Agitation-Induced Formation of Spherical Amoxicillin Sodium Products. *Industrial & Engineering Chemistry Research*, 61(27), 9821–9832. <https://doi.org/10.1021/acs.iecr.2c01179>
- (10) Doki, N., Seki, H., Takano, K., Asatani, H., Yokota, M., & Kubota, N. (2004). Process Control of Seeded Batch Cooling Crystallization of the Metastable α -Form Glycine Using an In-Situ ATR-FTIR Spectrometer and an In-Situ FBRM Particle Counter. *Crystal Growth & Design*, 4(5), 949–953. <https://doi.org/10.1021/cg030070s>
- (11) Duggirala, N. K., Perry, M. L., Almarsson, Ö., & Zaworotko, M. J. (2016). Pharmaceutical cocrystals: Along the path to improved medicines. *Chemical Communications*, 52(4), 640–655. <https://doi.org/10.1039/C5CC08216A>
- (12) Gong, W., Wu, Y., Lin, M., & Rohani, S. (2021). Polymorphism control of l-Glutamic acid in a single-stage and a two-stage MSMPR crystallizer by different seeding strategies. *Chemical Engineering Research and Design*, 170, 23–33. <https://doi.org/10.1016/j.cherd.2021.03.032>
- (13) Guo, W. (2022). Improving powder performances of natural extracted lutein with spherulitic growth control. *Powder Technology*.
- (14) Gyulai, O., Szabó-Révész, P., & Aigner, Z. (2017). Comparison Study of Different Spherical Crystallization Methods of Ambroxol Hydrochloride. *Crystal Growth & Design*, 17(10), 5233–5241. <https://doi.org/10.1021/acs.cgd.7b00764>
- (15) Hansen, C. M. (2007). *Hansen solubility parameters: A user's handbook* (2nd ed). CRC Press.
- (16) Huang, Y., Kuminek, G., Roy, L., Cavanagh, K. L., Yin, Q., & Rodríguez-Hornedo, N. (2019). Cocrystal Solubility Advantage Diagrams as a Means to Control Dissolution, Supersaturation, and Precipitation. *Molecular Pharmaceutics*, 16(9), 3887–3895. <https://doi.org/10.1021/acs.molpharmaceut.9b00501>
- (17) Kawashima, Y. (1984). Development of spherical crystallization technique and its application to pharmaceutical systems. *Archives of Pharmacal Research*, 7(2), 145–151. <https://doi.org/10.1007/BF02856629>
- (18) Kawashima, Y., Okumura, M., & Takenaka, H. (1982). Spherical Crystallization: Direct Spherical Agglomeration of Salicylic Acid Crystals During Crystallization. *Science*, 216(4550), 1127–1128. <https://doi.org/10.1126/science.216.4550.1127>

- (19) Lai, T.-T. C., Cornevin, J., Ferguson, S., Li, N., Trout, B. L., & Myerson, A. S. (2015). Control of Polymorphism in Continuous Crystallization via Mixed Suspension Mixed Product Removal Systems Cascade Design. *Crystal Growth & Design*, 15(7), 3374–3382. <https://doi.org/10.1021/acs.cgd.5b00466>
- (20) Lai, T.-T. C., Ferguson, S., Palmer, L., Trout, B. L., & Myerson, A. S. (2014). Continuous Crystallization and Polymorph Dynamics in the l -Glutamic Acid System. *Organic Process Research & Development*, 18(11), 1382–1390. <https://doi.org/10.1021/op500171n>
- (21) Lemmerer, A., Govindraj, S., Johnston, M., Motloug, X., & Savig, K. L. (2015). Co-crystals and molecular salts of carboxylic acid/pyridine complexes: Can calculated p K a 's predict proton transfer? A case study of nine complexes. *CrystEngComm*, 17(19), 3591–3595. <https://doi.org/10.1039/C5CE00102A>
- (22) Lewis, A., Seckler, M., Kramer, H. J. M., & Rosmalen, G. van. (2015). *Industrial crystallization: Fundamentals and applications*. Cambridge University Press.
- (23) Lin, M., Wu, Y., & Rohani, S. (2020). Identifying the Polymorphic Outcome of Hypothetical Polymorphs in Batch and Continuous Crystallizers by Numerical Simulation. *Crystal Growth & Design*, 20(11), 7312–7319. <https://doi.org/10.1021/acs.cgd.0c00986>
- (24) Liu, Y., Ma, Y., Yu, C., Gao, Y., Li, K., Tong, L., Chen, M., & Gong, J. (2022). Spherical agglomeration of high melting point drugs in water at low temperature by developing a two-step oiling-out mechanism and the design strategy. *Green Chemistry*.
- (25) Ma, Y., Sun, M., Liu, Y., Chen, M., Wu, S., Wang, M., Wang, L., Gao, Z., Han, D., Liu, L., Wang, J., & Gong, J. (2021). Design of Spherical Crystallization of Active Pharmaceutical Ingredients via a Highly Efficient Strategy: From Screening to Preparation. *ACS Sustainable Chemistry & Engineering*, 9(27), 9018–9032. <https://doi.org/10.1021/acssuschemeng.1c01973>
- (26) Nechipadappu, S. K., Reddy, I. R., Tarafder, K., & Trivedi, D. R. (2019). Salt/Cocrystal of Anti-Fibrinolytic Hemostatic Drug Tranexamic acid: Structural, DFT, and Stability Study of Salt/Cocrystal with GRAS Molecules. *Crystal Growth & Design*, 19(1), 347–361. <https://doi.org/10.1021/acs.cgd.8b01451>
- (27) Nicoud, L., Licordari, F., & Myerson, A. S. (2019). Polymorph control in batch seeded crystallizers. A case study with paracetamol. *CrystEngComm*, 21(13), 2105–2118. <https://doi.org/10.1039/C8CE01428K>
- (28) Randolph, A. D., & Larson, M. A. (1962). Transient and steady state size

- distributions in continuous mixed suspension crystallizers. *AIChE Journal*, 8(5), 639–645. <https://doi.org/10.1002/aic.690080515>
- (29) Reddy, L. S., Bethune, S. J., Kampf, J. W., & Rodríguez-Hornedo, N. (2009). Cocrystals and Salts of Gabapentin: pH Dependent Cocrystal Stability and Solubility. *Crystal Growth & Design*, 9(1), 378–385. <https://doi.org/10.1021/cg800587y>
- (30) Rodrigues, M., Baptista, B., Lopes, J. A., & Sarraguça, M. C. (2018). Pharmaceutical cocrystallization techniques. Advances and challenges. *International Journal of Pharmaceutics*, 547(1–2), 404–420. <https://doi.org/10.1016/j.ijpharm.2018.06.024>
- (31) Sandhu, B., McLean, A., Sinha, A. S., Desper, J., Sarjeant, A. A., Vyas, S., Reutzel-Edens, S. M., & Aakeröy, C. B. (2018). Evaluating Competing Intermolecular Interactions through Molecular Electrostatic Potentials and Hydrogen-Bond Propensities. *Crystal Growth & Design*, 18(1), 466–478. <https://doi.org/10.1021/acs.cgd.7b01458>
- (32) Sarmah, K. K., Sarma, P., Rao, D. R., Gupta, P., Nath, N. K., Arhangel'skis, M., & Thakuria, R. (2018). Mechanochemical Synthesis of Olanzapine Salts and Their Hydration Stability Study Using Powder X-ray Diffraction. *Crystal Growth & Design*, 18(4), 2138–2150. <https://doi.org/10.1021/acs.cgd.7b01593>
- (33) Xu, S., Zhang, H., Qiao, B., & Wang, Y. (2021). Review of Liquid–Liquid Phase Separation in Crystallization: From Fundamentals to Application. *Crystal Growth & Design*, 21(12), 7306–7325. <https://doi.org/10.1021/acs.cgd.0c01376>
- (34) Zhang, Z., Wang, L., Zhao, P., Xiao, Y., Hao, H., & Bao, Y. (2021). Comparison Study of KBH 4 Spherical Agglomerates Prepared in Different Antisolvents: Mechanisms and Properties. *Industrial & Engineering Chemistry Research*, 60(15), 5600–5611. <https://doi.org/10.1021/acs.iecr.1c00270>

Chapter 2

Taurine in several aqueous binary solvents: Solubility prediction, measurement, modeling, solvent effect, and thermodynamics

A version of this chapter has been published in *Journal of Molecular Liquids*:

Gong, W., Li, P., & Rohani, S. (2022). Taurine in several aqueous binary solvents: Solubility prediction, measurement, modeling, solvent effect, and thermodynamics. *Journal of Molecular Liquids*, 367, 120522.

2. Taurine in several aqueous binary solvents: Solubility prediction, measurement, modeling, solvent effect, and thermodynamics

Abstract

The crystallization of taurine in pure water results in a low yield. Introducing anti-solvents during the cooling crystallization process increases the yield. Therefore, measuring and evaluating the solubility of taurine in different binary aqueous solvents is necessary. In this work, the qualitative trend of the solubility of taurine in the binary solvent systems of 1,2-propanediol-water, acetonitrile-water, and ethylene glycol-water was first predicted using Hansen Solubility Parameters (HSPs), and then experimentally determined using isothermal gravimetric method. The experimentally obtained solubility is correlated with the modified Apelblat model as a linear model, and NRTL, UNIQUAC, Wilson, and λh model as nonlinear models. The solubility of taurine in binary solvents is further analyzed using the KAT-LSER model to investigate the solvent effect on solubility. For all researched systems, the standard molar enthalpy and the standard molar Gibbs energy changes are computed and found to be positive, indicating the dissolution of taurine is an endothermic process.

Keywords: Taurine, Solubility, Hansen Solubility Parameters, KAT-LSER, NRTL, UNIQUAC, Wilson, Thermodynamics

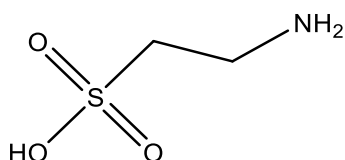
2.1 Introduction

Taurine, 2-aminoethanesulfonic acid (CAS Registry No. 107-35-7, scheme 2-1), a sulfur-containing amino acid, is isolated from bovine bile (Lourenço & Camilo, 2002) and is widely distributed in mammalian cells in human neutrophils (Green et al., 1991; Karpowicz, 2022). It plays an important role in metabolic and physiological processes (Tao et al., 2022), mainly in detoxification, energy metabolism (Kim & Cha, 2014), anti-inflammatory regulation (Kim & Cha, 2014), antitumor activity (El Agouza et al., 2011), and antioxidant activity (Green et al., 1991; Schaffer et al., 2009). Due to the low level of cysteine sulfinic acid decarboxylase (enzyme for biosynthesis of taurine) in the human body, taurine is mainly ingested through exogenous sources such as seafood, meat, and taurine-containing health drinks (Schuller-Levis & Park, 2003). Thus, the addition of taurine is encouraged in infant formula and parenteral solutions, which attracts the industry to expand its production (Lin et al., 2013).

The industrial methods for producing taurine involve chemical synthesis (Bondareva et al., 2008). Thus, the isolation of taurine from abundant raw materials is important and is most frequently realized through a cooling crystallization (Yang et al., 2010). Due to the good solubility of taurine in the aqueous solution, water is always used as the solvent for its crystallization. However, taurine product crystallized from water suffers from poor morphology and low yield (Lin et al., 2013; Yang et al., 2010). It is found that the crystallized taurine product has tetragonal-needle morphology, which results in caking and low flowability. Therefore, to avoid caking and to improve the shape of taurine crystals, effects of various crystallization conditions have been studied by several researchers (Chengxiong, 2010; Lin et al., 2013; Shishimaru et al., 1995; Wu et al., 2017). Wu et al. (Wu et al., 2017) added acetone to the water as an anti-solvent during the aqueous cooling crystallization process to increase the yield as well as to avoid caking. Lin et al. (Lin et al., 2013) investigated the effects of different operating conditions on

taurine crystals' size and morphology. It has been confirmed that the shape of crystals would not be affected by tuning process parameters. Therefore, introducing anti-solvents such as ethanol (Shishimaru et al., 1995) or other alkanol (Chengxiong, 2010) during the cooling crystallization process has been applied in industry. The solubility data of taurine in different binary aqueous solvents are thus required for further research.

Both Wu et al. (Wu et al., 2017) and Yang et al. (Yang et al., 2010) published taurine's solubility in different binary solvent systems. However, the correlation of solubility data with different thermodynamic models and the further analysis of the data have not been reported. Therefore, in this paper, first, the qualitative trend of taurine's solubility in different binary solvents (1,2-propanediol (PG) - water, acetonitrile (ACN) - water, and ethylene glycol (EG) - water) were estimated using Hansen Solubility Parameters (Hansen, 2007). Then, experiments have been held to determine the solubility. The obtained data with data published in Wu's (Wu et al., 2017) paper were correlated with linear and non-linear thermodynamic models, namely, modified Apelblat model, NRTL, UNIQUAC, Wilson, and λh model. Moreover, to estimate solubilities in various systems and determine the impact of molecular interactions on solubilities, the Kamlet and Taft linear solvation energy relationship (KAT-LSER)(Kamlet et al., 1983) model were used. Herein, the aim of this work is to: (1) estimate the solubilities by HSPs, (2) measure the solubility of taurine in different binary systems, (3) analyze the impact of molecular interactions on the solubility of taurine in aqueous mixtures by the KAT-LSER model, (3) correlate the solubility data with thermodynamic models, (4) analyze the thermodynamics properties of taurine in different binary systems.



Scheme 2-1. Molecular structure of Taurine.

2.2 Experimental Section

2.2.1 Materials

The model compound taurine was purchased from Shanghai Aladdin, with a purity of more than 99%; ethylene glycol (EG) (AR, >99.5%, China) was purchased from Sinopharm Chemical Reagent Co., Ltd; acetonitrile (ACN) (AR, >99%, China) was purchased from Kermel; 1,2-propanediol (PG) (ACS, >99.5%, China) was purchased from Thermos Scientific; and pure water was produced from Milli-Q® Direct Water Purification System. All solvents were characterized by gas chromatography and taurine was characterized by powder X-ray diffraction to ensure crystal purity.

2.2.2 Powder X-ray Diffraction

The purchased taurine and all samples after solubility tests were run on the powder X-ray diffraction (PANalytical) with the Cu-K α source (λ for K α = 1.540598 Å). Bulk powder of each sample was placed on a sample holder and its diffraction pattern measured using a continuous scan between 5° and 80° in 2 θ at 40 kV voltage and 40mA current. The scan step size was 0.013°.

2.2.3 Differential Scanning Calorimetry

Analysis of the thermal properties of taurine and all solid samples after solubility tests were conducted using a differential scanning calorimetry (DSC, Mettler Toledo) under a nitrogen gas atmosphere. Samples of precisely weighed taurine (5 mg to 10 mg) were placed in a non-hermetically sealed aluminum pan in a vacuum. Samples were scanned at a rate of 10 °C/min in the range of 25–350 °C under a dry nitrogen atmosphere at a flow rate of 100mL/min.

2.2.4 Isothermal Solubility Test (Myerson et al., 2019)

Equilibrium solubility data of taurine were generated isothermally with a gravimetric method. An excess amount of taurine powder was added into different vials with different binary solvents. The vials were then sealed and heated in a shaking water bath (SW22, Julabo). The measured temperature was adjusted from 298.15 K to 318.65 K (with a 5 K interval) and the shaking frequency was 180rpm. Vials were shaken for 24 h and were then stilled for 12 h to let the solid phase settle down. The supernatant liquor was taken and filtered through a filter membrane (0.22 μm) on petri dishes quickly for the mass measurement with an electronic analytical balance (± 0.0001 g, Mettler Toledo). Petri dishes with filtered supernatant liquor were then dried in a vacuum oven under 393.15 K, 9 kPa for 24 h. After drying, the weight of samples was measured, and the lost weight was considered as the weight of solvent. Then the solubility could be calculated from Eq. (2-1):

$$S \text{ (g/100g solvent)} = \frac{M_{dry} - M_{dish}}{M_{wet} - M_{dry}} \times 100 \quad (2 - 1)$$

Where M_{dry} is the measured weight after drying, M_{wet} is the total weight of the petri dish plus the filtered liquor, M_{dish} is the weight of the petri dish.

The computed solubility was further converted to a mole fraction of taurine in the system using Eq. (2-2):

$$x_1 = \frac{\frac{S}{125.15}}{\frac{S}{125.15} + \frac{100}{\bar{M}}} \quad (2 - 2)$$

Where x_1 is the mole fraction of taurine in the solution, \bar{M} is the average molar mass of the co-solvent.

To ensure the accuracy of the obtained data, the solubility of taurine in pure water was also measured using the gravimetric method and compared with the literature value (Wu et al., 2017; Yang et al., 2010) (discussed below).

2.3 Theoretical Section

2.3.1 Hansen Solubility Parameter

The idea of Hansen Solubility Parameter (HSP) was proposed by Charles Hansen (Hansen, 2007). It is based on the theory of “similarity and inter-miscibility”, in other words, “like dissolves like”. For two materials, the more similar their HSPs are, the higher possibility of their miscibility would be. The HSP consists of three major parts: atomic dispersion forces (dispersion HSP shown by δ_d), molecular permanent dipole forces (polar HSP, δ_p), and hydrogen-bonding energy (hydrogen-bonded HSP, δ_h). Based on these three contributions, the total HSP is defined as:

$$\delta_t = \sqrt{\delta_d^2 + \delta_p^2 + \delta_h^2} \quad (2 - 3)$$

Then, for co-solvent mixtures, the HSP of the co-solvent is the weighted average of the two solvents:

$$\delta_j = a\delta_j^1 + (1 - a)\delta_j^2 \quad (2 - 4)$$

Where j represents d, p , and h for dispersion dipole and hydrogen bond, captions 1 and 2 indicate solvent 1 and 2, a is the volume fraction of solvent 1 in the binary solvent mixture.

For the materials whose partial solubility parameters are not available, the group contribution method is widely applied (Cong et al., 2022b):

$$\delta_d = \frac{\sum F_{di}}{V} \quad (2-5)$$

$$\delta_p = \frac{\sqrt{\sum F_{pi}^2}}{V} \quad (2-6)$$

$$\delta_h = \frac{\sqrt{\sum E_{hi}}}{V} \quad (2-7)$$

where F_{di} , F_{pi} and E_{hi} are the contributions of the dispersion force, polar force, and the hydrogen-bonding energy for functional group i of the molecule.

Van Krevelen and Hoftyzer quantified the difference in HSP using the parameter $\Delta\bar{\delta}$, (H. He et al., 2020; Q. He & Zhao, 2021) which is defined by the following equation:

$$\Delta\bar{\delta} = \sqrt{(\delta_{d2} - \delta_{d1})^2 + (\delta_{p2} - \delta_{p1})^2 + (\delta_{h2} - \delta_{h1})^2} \quad (2-8)$$

If the value of $\Delta\bar{\delta}$ is smaller than $5.0 \text{ MPa}^{1/2}$, good miscibility would be attained (Alanazi et al., 2020). Furthermore, Bagley (Bagley et al., 1971) has found the thermodynamic similarity between δ_d and δ_p , and proposed a volume-dependent solubility parameter, δ_v , as Eq. (2-9):

$$\delta_v = \sqrt{(\delta_d^2 + \delta_p^2)} \quad (2-9)$$

Then, a solubility factor R_a is used to define the miscibility of two substances, which is expressed as:

$$R_a = \sqrt{(4(\delta_{v2} - \delta_{v1})^2 + (\delta_{h2} - \delta_{h1})^2)} \quad (2-10)$$

If $R_a < 5.6 \text{ MPa}^{1/2}$, good miscibility between two materials is predicted. Lower R_a value results in better miscibility.

2.3.2 KAT-LSER Model

The KAT-LSER model, which analyzes the effects of solvent-solvent, and solute-solvent interaction on solubility, was proposed by Kamlet and Taft in 1983 (Kamlet et al., 1983). Multiple linear regression analysis was applied to define the relevance between the solubility and the hydrogen bond donation (HBD) ability of the solvent (α), the hydrogen bond acceptance (HBA) ability of the solvent (β), the dipolarity–polarizability parameter (π^*), and the Hildebrand solubility parameter (δ_H). The proposed expression is shown in Eq. (2-11):

$$\ln x_1 = c_0 + c_1\alpha + c_2\beta + c_3\pi^* + c_4\left(\frac{V_S\delta_H}{100RT}\right) \quad (2 - 11)$$

where x_1 is the mole fraction solubility of the solute, V_S is the molar volume of the solute which can be estimated as the quotient of the molar mass (M) divided by the density of the solute (ρ), R is the molar gas constant and T is the absolute temperature. Coefficients c_i ($i = 0$ to 4) are computed through multiple linear regression analysis (MLRA) using solubility data at a certain temperature, c_0 indicates the effect of the crystal lattice, c_1 and c_2 refer to the sensitivity of solute-solvent and solvent-solvent nonspecific electrostatic interactions, and c_3 and c_4 quantify the sensitivity of the specific hydrogen-bonding of solute-solvent interactions, respectively (Liu et al., 2021; Zheng et al., 2018).

2.3.3 Solubility Modelling

The measured solubility data were correlated with linear and nonlinear thermodynamic models. The solubility of taurine in binary solvent mixtures of (1,2-propanediol - water, acetonitrile - water, and ethylene glycol - water) at different temperatures was correlated with the modified Apelblat model, the λh model, the NRTL model, the UNIQUAC model, and the Wilson model.

2.3.3.1 Modified Apelblat Model

The modified Apelblat model has been widely applied to the non-ideal solutions for solubility correlation and prediction. It reveals the effect of temperature on the solubility of solutes by the following equation: (Huang et al., 2021; Wang et al., 2021)

$$\ln x_1 = A + \frac{B}{T} + C \ln T \quad (2 - 12)$$

where x_1 is the mole fraction solubility of the solute, T is the absolute temperature (K), A , B , and C are model parameters. The values of A and B refer to the variation in the solution activity coefficients, and C reflects the effect of temperature on the enthalpy of fusion.

2.3.3.2 λh Model

The λh equation is also known as the Buchowski–Ksiazczak equation, was proposed by Buchowski (Buchowski et al., 1980). Solid-liquid systems can be well fitted by this equation with only two parameters as shown below:

$$\ln \left[1 + \frac{\lambda(1 - x_1)}{x_1} \right] = \lambda h \left(\frac{1}{T} - \frac{1}{T_m} \right) \quad (2 - 13)$$

where λ and h are the tuning parameters, T_m (K) is the melting point of the solute.

2.3.3.3 Activity coefficient models for solid-liquid equilibrium

(SLE)

Activity-based models relate the solubility data to temperature with the help of the activity coefficients: (Behboudi et al., 2022)

$$\ln x_1 = -\ln \gamma_1 + \frac{\Delta_{fus}H}{R} \left(\frac{1}{T_m} - \frac{1}{T} \right) - \frac{\Delta C_p}{R} \left[\ln \left(\frac{T_m}{T} \right) - \left(\frac{T_m}{T} \right) + 1 \right] \quad (2 - 14)$$

where γ_1 is the activity coefficient of the solute, R is the molar gas constant. ΔC_p is the heat capacity difference of the solute in solid and liquid phases at temperature T and is assumed to be zero to simplify the model to the following equation:

$$\ln x_1 = -\ln \gamma_1 + \frac{\Delta_{fus}H}{R} \left(\frac{1}{T_m} - \frac{1}{T} \right) \quad (2-15)$$

2.3.3.3.1 Wilson model

The Wilson model was proposed by Wilson (Wilson, 1964) and has been widely modified in multi-component SLE data modeling. The excess Gibbs free energy (g^E) is expressed as:

$$\frac{g^E}{RT} = - \sum_{i=1}^m x_i \cdot \ln \left(\sum_{j=1}^m x_j \Lambda_{ij} \right) \quad (2-16)$$

with

$$\Lambda_{ij} = \frac{v_j}{v_i} \exp \left(- \frac{\Delta \lambda_{ij}}{RT} \right) \quad (2-17)$$

$$\Lambda_{ji} = \frac{v_i}{v_j} \exp \left(- \frac{\Delta \lambda_{ji}}{RT} \right) \quad (2-18)$$

Where m is the total number of components, v_j and v_i are the molar volume of component i and j . The molar volume of taurine is calculated through the group contribution method as shown in Table 2-1a. $\Delta \lambda_{ij}$ and $\Delta \lambda_{ji}$ are the characteristic energy difference. Λ_{ij} denotes to the binary interaction parameter.

The activity coefficient of component i is expressed as

$$\ln \gamma_i = 1 - \sum_{j=1}^m \frac{x_i \Lambda_{ji}}{\sum_{k=1}^m x_k \Lambda_{ik}} - \ln \left(\sum_{j=1}^m x_j \Lambda_{ij} \right) \quad (2-19)$$

2.3.3.3.2 Non-Random Two-Liquid (NRTL) Model

The NRTL model has combined the concept of two-liquid solution theory and the local composition concept. It has been used to determine the activity coefficient of the solution in both partially and fully miscible systems according to Eq. (2-20):

$$\ln\gamma_i = \frac{\sum_{j=1}^m \tau_{ji} x_j G_{ji}}{\sum_{k=1}^m x_k G_{ki}} + \sum_{j=1}^m \frac{x_j G_{ij}}{\sum_{k=1}^m x_k G_{kj}} \left(\tau_{ij} - \frac{\sum_{l=1}^m \tau_{li} x_l G_{lj}}{\sum_{k=1}^m x_k G_{ki}} \right) \quad (2-20)$$

with

$$\tau_{ji} = \frac{\Delta g_{ji}}{RT} \quad (2-21)$$

$$\tau_{ij} = \frac{\Delta g_{ij}}{RT} \quad (2-22)$$

G_{ji} and G_{ij} could be obtained through the following equations:

$$G_{ij} = \exp(-\alpha_{ij} \cdot \tau_{ij}) \quad (2-23)$$

$$G_{ji} = \exp(-\alpha_{ji} \cdot \tau_{ji}) \quad (2-24)$$

where $\alpha_{ij} = \alpha_{ji} = \alpha$, $\tau_{ii} = \tau_{jj} = 0$. Δg_{ij} and Δg_{ji} are the differences of energy parameter characteristics. α is the non-random factor value (varies from 0.1 to 0.47) and is set to be 0.1 for taurine in different binary solvents due to its good fitting result.

2.3.3.3.3 The UNIQUAC model

The Universal Quasi-Chemical theory (UNIQUAC) was proposed by Abrams and Prausnitz (Abrams & Prausnitz, 1975). The UNIQUAC model includes two parts of the activity coefficient: residual $\ln\gamma_i^R$ and combinatorial $\ln\gamma_i^C$, which refer to the enthalpy of mixing by intermolecular forces and the entropic contribution: (Behboudi et al., 2022)

$$\ln\gamma_i = \ln\gamma_i^R + \ln\gamma_i^C \quad (2-25)$$

$$\ln\gamma_i^R = q_i \left(1 + \sum_{j=1}^m \theta_j \tau_{ji} \right) - \sum_{j=1}^m \frac{\theta_j \tau_{ji}}{\sum_{k=1}^m \theta_k \tau_{kj}} \quad (2-26)$$

$$\ln\gamma_i^C = \ln\left(\frac{\Phi_i}{x_i}\right) + \frac{z}{2} q_i \ln\left(\frac{\theta_i}{\Phi_i}\right) + l_i - \frac{\Phi_i}{x_i} \left(\sum_{j=1}^m x_j l_j \right) \quad (2-27)$$

with

$$l_i = \frac{z}{2} (r_i - q_i) - (r_i - 1) \quad (2-28)$$

$$\tau_{ij} = \exp\left(-\frac{\Delta u_{ij}}{RT}\right) = \exp\left(-\frac{\alpha_{ij}}{T}\right) \quad (2-29)$$

$$\Phi_i = \frac{x_i r_i}{\sum_{j=1}^m x_j r_j}, \theta_i = \frac{x_i q_i}{\sum_{j=1}^m x_j q_j} \quad (2-30)$$

where r_i and q_i of the solute and the solvents could be calculated through the group contribution method, based on the following equation:

$$r = \frac{\sum R_i}{V_{vw}}, q = \frac{\sum Q_i}{A_{vw}} \quad (2-31)$$

V_{vw} and A_{vw} are the standard segment volume ($15.17\text{cm}^3\cdot\text{mol}^{-1}$) and the standard segment surface ($2.5109\text{cm}^2\cdot\text{mol}^{-1}$), R_i and Q_i values are listed in [Table A-1](#) in Appendix A.

2.3.4 Model accuracy

The average relative deviation (ARD) and the root mean square deviation (RMSD) are used to evaluate the accuracy of the solubility models. The expressions are listed below:

$$ARD = \frac{1}{n} \sum_{i=1}^n \left| \frac{(x_1^{exp})_i - (x_1^{cal})_i}{(x_1^{exp})_i} \right| \quad (2-32)$$

$$RMSD = \sqrt{\frac{\sum_{i=1}^n [(x_1^{cal})_i - (x_1^{exp})_i]^2}{n}} \quad (2 - 33)$$

2.3.5 Thermodynamic properties of dissolution

Van't Hoff and Gibbs equations at the mean harmonic temperature (T_{hm}) are used to compute the thermodynamic properties of dissolution. The T_{hm} is calculated by Eq. (2-34) and its value is 308K for taurine's solubility data in EG-water, ACN-water, and PG-water. For taurine's solubility in acetone-water, the T_{hm} is 300K. Molar enthalpy of dissolution (ΔH^0) at T_{hm} is then calculated:

$$T_{hm} = \frac{n}{\sum_{i=1}^n \left(\frac{1}{T}\right)} \quad (2 - 34)$$

$$\Delta H^0 = -R \left(\frac{\partial \ln x_1}{\partial \left(\frac{1}{T} - \frac{1}{T_{hm}}\right)} \right)_p \quad (2 - 35)$$

Thus, ΔH^0 is calculated by plotting $\ln x_1$ versus $\left(\frac{1}{T} - \frac{1}{T_{hm}}\right)$, and the molar Gibbs free energy (ΔG^0) is computed by multiplying the intercept by $-RT_{hm}$, as shown in Eq. (2-36):

$$\Delta G^0 = -RT_{hm} \times \text{intercept} \quad (2 - 36)$$

With ΔG^0 and ΔH^0 , the value of the molar entropy ΔS^0 is determined by Eq. (2-37):

$$\Delta S^0 = \frac{\Delta H^0 - \Delta G^0}{T_{hm}} \quad (2 - 37)$$

Then, to calculate the relative contributions of entropy (ξ_{TS}) and enthalpy (ξ_H) to ΔG^0 of taurine dissolution behavior in the mixed solvents, the following equations are used (Perlovich et al., 2004):

$$\xi_{TS} = \frac{|TS^0|}{|\Delta H^0| + |T\Delta S^0|} \quad (2 - 38)$$

$$\xi_H = \frac{|\Delta H^0|}{|\Delta H^0| + |T\Delta S^0|} \quad (2 - 39)$$

2.4 Results and Discussion

2.4.1 Powder X-ray Diffraction Results

All residue taurine samples after the solubility tests were collected and compared to the pure taurine powder as shown in [Figure 2-1](#). No solvation or polymorphic transformation were observed as there was no change in the characteristic peaks of all tested samples. This deduction is also confirmed through the DSC results in the following part.

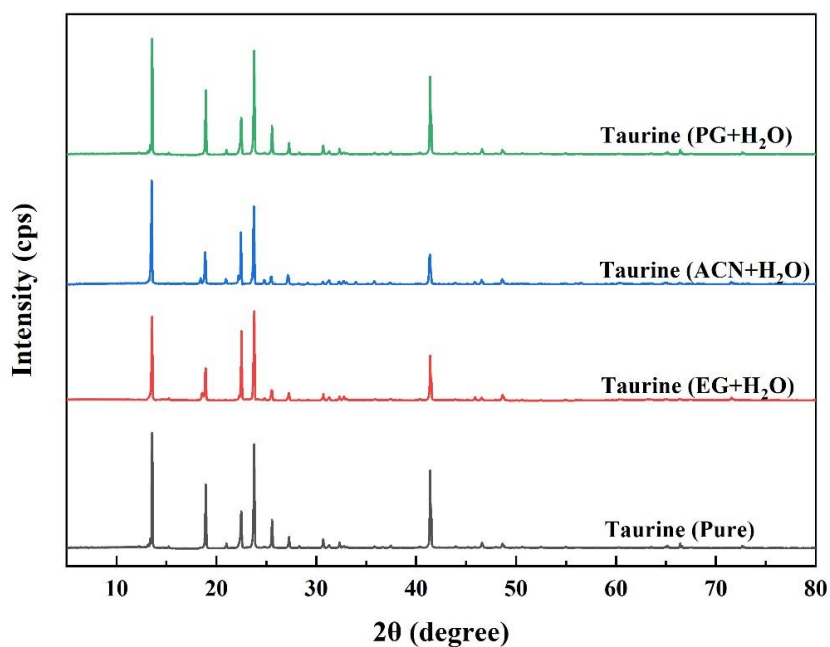


Figure 2-1. PXRD patterns of taurine and residue taurine after solubility tests

2.4.2 Thermal Analysis

The DSC curves of the pure taurine samples and solid samples obtained after solubility experiments are shown in [Figure 2-2](#). It is obvious that all samples display the same onset value of the melting peak at 330K, followed by a broad decomposition peak. No other endothermic peaks were observed, indicating that no solvation or polymorphic transformation happened during the solubility tests, which confirms the result of PXRD analysis.

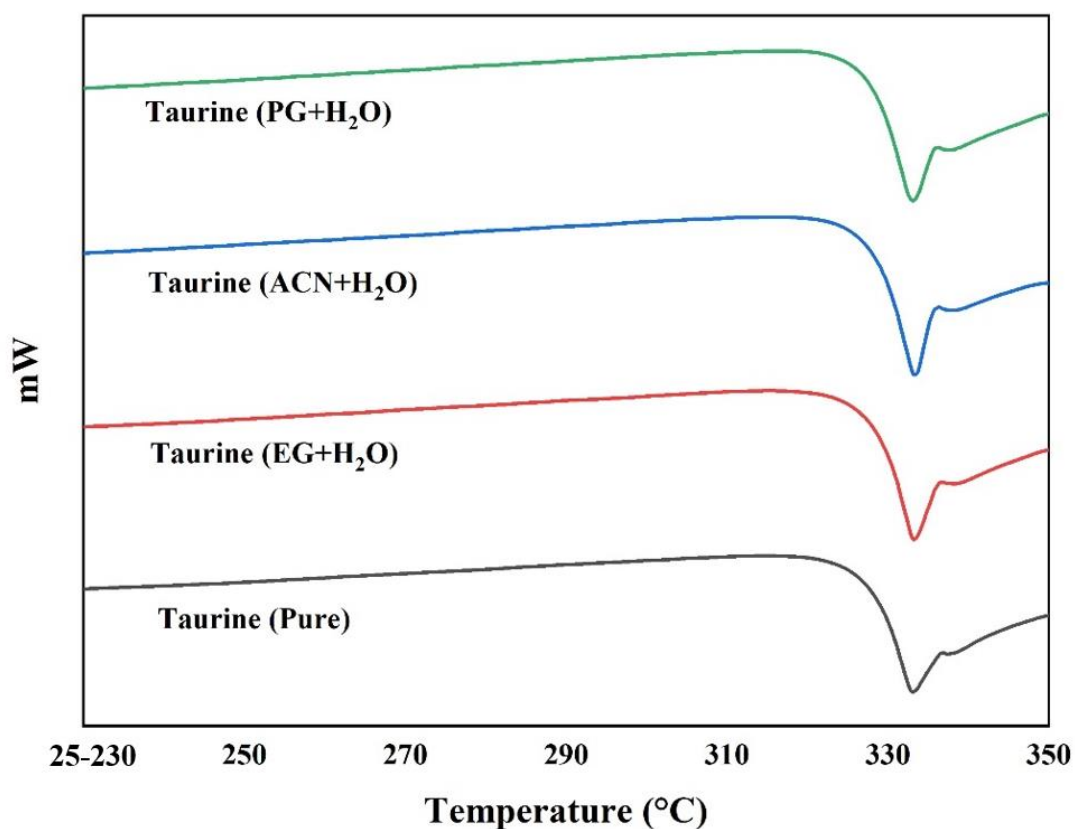


Figure 2-2. Thermographs of taurine and residue taurine after solubility tests

2.4.3 Hansen Solubility Parameter (HSP) Analysis

The HSP is used to predict taurine's solubility in different binary solvents. $\delta_d, \delta_p, \delta_h$ values of taurine are calculated through the group contribution method as shown in [Table 2-1a](#) and [Table 2-1b](#) that list three partial ($\delta_d, \delta_p, \delta_h$), a total (δ_t) and the joint (δ_v) solubility parameters of five solvents and taurine itself. As δ_h of water is too large, the analysis using $\Delta\delta$ and $\Delta\delta_t$ is not suitable as taurine shows good solubility in water but the $\Delta\delta$ and $\Delta\delta_t$ values are large ($16.89MPa^{0.5}$, $23.23MPa^{0.5}$). This also indicates that hydrogen bonding doesn't contribute significantly to the dissolution of taurine. Similarly, R_a is also excluded for the prediction as it considers δ_h . Yang's group has successfully applied the δ_v to describe the solubility behavior of actarit, to eliminate the deviation introduced by δ_h . (Cong et al., 2022b) Hence, the volume-dependent solubility parameter, δ_v , which targets the polarity and dispersion forces, is used for the solvent screening. The $\Delta\delta_v$ values (compared to taurine) of acetonitrile, ethylene glycol, 1,2-propanediol and acetone are $0.37MPa^{0.5}$, $3.75MPa^{0.5}$, $4.75MPa^{0.5}$ and $5.33MPa^{0.5}$ respectively. Therefore, the predicted solubility of taurine is largest in ACN-water, followed by EG-water, and then PG-water. The solubility of taurine in acetone-water system is the lowest.

Table 2-1a. Hansen Solubility Parameters of taurine

| | | F_d | F_p | E_h | V_i |
|--------------------|--------|--------------------|--------------------|---------|-----------------------|
| | Number | $(Jm^3)^{1/2}/mol$ | $(Jm^3)^{1/2}/mol$ | J/mol | $cm^3 \cdot mol^{-1}$ |
| -NH ₂ | 1 | 300 | 440 | 8600 | 17.5 |
| -CH ₂ - | 2 | 270 | 0 | 0 | 16.1 |
| -SO ₂ - | 1 | 1129 | 1358 | 11670 | 51 |
| -OH | 1 | 210 | 520 | 22000 | 10 |

$$\delta_d = \frac{\sum F_{di}}{\sum V_i} = 19.68 \text{ MPa}^{0.5} \quad \delta_p = \frac{\sqrt{\sum F_{pi}^2}}{\sum V_i} = 13.72 \text{ MPa}^{0.5} \quad \delta_h = \frac{\sqrt{\sum E_{hi}}}{\sum V_i} = 19.54 \text{ MPa}^{0.5}$$

$$V = \sum V_i = 110.7 \text{ cm}^3 \cdot \text{mol}^{-1}$$

Table 2-1b. Three partial (δ_d , δ_p , δ_h), the total (δ_t), and the joint (δ_v) solubility parameters of five solvents and taurine

| Solvents | $\delta_d(\text{MPa}^{0.5})$ | $\delta_p(\text{MPa}^{0.5})$ | $\delta_h(\text{MPa}^{0.5})$ | $\delta_t(\text{MPa}^{0.5})$ | $\delta_v(\text{MPa}^{0.5})$ | $\Delta\delta(\text{MPa}^{0.5})$ |
|------------------|------------------------------|------------------------------|------------------------------|------------------------------|------------------------------|----------------------------------|
| Acetonitrile | 15.3 | 18 | 6.1 | 24.4 | 23.62 | 14.77 |
| Ethylene Glycol | 17 | 11 | 26 | 32.95 | 20.25 | 7.51 |
| 1,2-propanediol | 16.8 | 9.4 | 23.3 | 30.22 | 19.25 | 6.41 |
| acetone | 15.5 | 10.4 | 7 | 19.94 | 18.67 | 13.63 |
| H ₂ O | 15.6 | 16 | 42.3 | 47.84 | 22.35 | 23.23 |
| Taurine | 19.68 | 13.72 | 19.54 | 30.95 | 24 | / |

^a the values of F_{di} , F_{pi} , E_{hi} and V_i are taken from references 32 and 33 (Breitkreutz, 1998; Krevelen & Nijenhuis, 2009)

2.4.4 Solubility Data

The mole fraction solubility data of taurine in three binary solvents including 1,2-propanediol – water, acetonitrile – water, and ethylene glycol – water in the temperature ranging from 298.15K to 318.15K are listed in [Table 2-2](#). Taurine’s solubility in pure water was also measured using the gravimetric isothermal saturation method and the results are compared to literature values reported by Wu et al. (Wu et al., 2017) to ensure

accuracy. The average relative deviation in the mole fraction solubility between our work and Wu's result is 1.4%.

As shown in [Table 2-2](#), the solubility of taurine always increases with the water mole fraction as well as the temperature of the solution. Furthermore, when the water content is low ($w_1 = 0.6, 0.5$), the solubility of taurine increases slowly. When the water content is high, the solubility of taurine increases rapidly. The experimental solubility data are correlated with some linear and non-linear models including the modified Apelblat, NRTL, UNIQUAC, Wilson, and λh models. The computed model coefficients and ARD, RMSD values are listed in [Table 2-3](#) to [2-5](#). Furthermore, the relationship between taurine's solubility in different binary solvents and experimental temperature are shown in [Figure 2-3](#) to [2-5](#). From [Table 2-3](#) to [2-5](#), it is shown that the modified Apelblat model, NRTL model and UNIQUAC model offer good regression results with low ARD and RMSD in all four binary solvents (all ARD values are lower than 6%, all RMSD values are lower than 0.08%). NRTL and UNIQUAC models belong to the class of local composition models and can be applied in mixtures with polar components. The reason the modified Apelblat model gives good fitting is that it offers different fitting parameters for different water-fraction solvents. Then, the ARD values of the Wilson model are low in water-EG and water-PG (ARD = 2.08% and 4.76%) but are high in water-ACN and water-acetone (ARD = 9.81% and 10.39%). The Wilson model is majorly applied in the polar-nonpolar miscible system; thus, its fitting result is worse than the NRTL and UNIQUAC models. The λh model offers poor fitting results, mainly because there are only two parameters in the model, which are not enough to accurately describe the system. The calculated mole fraction solubilities of taurine are listed in [Table A-2](#) in Appendix A.

As shown in [Table 2-2](#), when w_1 is larger than 0.8, under all measured temperatures, the solubility of taurine in four binary solvents always followed the order:

$$ACN - water > EG - water > PG - water > Acetone - water$$

which exactly matches the prediction results using δ_v . The result confirms that when the water content is high, the polarity and dispersion force between taurine and binary solvents determines the solubility. Nevertheless, when w_1 is less than 0.8, taurine's solubility in EG-water exceeds its solubility in ACN-water. The deduced reason for this phenomenon is that when the amount of water in the system decreases, other molecular interactions like hydrogen-bonding, self-cohesiveness, and steric hindrance affect the solubility significantly. Furthermore, the $\Delta\delta_v$ values (compared to water) of acetonitrile, ethylene glycol, 1,2-propanediol, acetone, and taurine are $1.28MPa^{0.5}$, $2.10MPa^{0.5}$, $3.10MPa^{0.5}$, $3.68MPa^{0.5}$ and $1.65MPa^{0.5}$ respectively. It could be found that the $\Delta\delta_v$ value of ACN is smaller than the $\Delta\delta_v$ value of taurine, which indicates that within the increasing amount of ACN molecules in the system, the interactions between ACN molecules and water molecules (solvent-solvent interactions) might affect the solvent-solute interactions.

It is noticed the $\Delta\delta_v$ value between water and taurine ($1.65MPa^{0.5}$) is larger than the $\Delta\delta_v$ value between acetonitrile and taurine ($0.37MPa^{0.5}$). However, taurine owns larger solubility in water. This is because taurine as an organic acid, can break into the lattice structure of water, overcome electrostatic interaction with positive and negative ions, and our prediction focuses on the general rule "like dissolves like". Factors like self-cohesiveness, steric hindrance, and the specialty of water analyzed above which are not considered might also affect the solubility. Nevertheless, as water is the co-solvent in all predicted system, the polarity and the dispersion force of the second solvent would directly determine the solubility of taurine in the binary solvent. For the pure polar solvent (ACN, EG, PG, Acetone, Water), molecules interact with each other through strong hydrogen bonds. Taurine molecule needs to break the bonds and form similar interactions to dissolve. (Tan et al., 2016) In the taurine solution, the carboxyl group of taurine form

hydrogen bonds with ACN, EG, PG, and acetone molecules, but the strength would be weakened when water molecules exist in the system and form hydrogen bonds with ACN, EG, PG, and acetone molecule. In addition, within the increase of the second polar solvent (the first solvent is water), the dielectric constant of the binary solvent decreases significantly ($\epsilon_{r,water} = 78.36$, (Gandhi & Murthy, 2012) $\epsilon_{r,ACN} = 36.55$, (Orhan et al., 2020) $\epsilon_{r,EG} = 41.12$ (Sengwa & Sankhla, 2007) $\epsilon_{r,PG} = 30.2$ (Castro et al., 2022) $\epsilon_{r,acetone} = 21.01$ (Fernandes et al., 2022)). The low dielectric constant binary solvent would prevent the taurine molecule to overcome the electrostatic interaction. Therefore, the solubility of taurine decreased significantly when the amount of the second solvent has increased in the system as shown in [Figure 2-3](#) to [2-5](#). Besides the monotone relationship between the solubility and the mole fraction of the second solvent (ACN, EG, PG, Acetone), the solubility also positively increases with the system temperature, indicating that the dissolution of taurine should be endothermic, indicating that the energy required to break the interactions between taurine molecules is higher than the energy released by new bonds forming between taurine and solvent molecules.

To further investigate how factors that affect solubility in-depth, the KAT-LSER model was used and discussed in section 4.5.

Table 2-2. Experimental mole fraction solubility (x_1) of taurine in three binary solvents at temperature from 298.15K to 318.15K^b

| T/K | x_1^{exp} | | | | | |
|----------------------------------|-------------|-------------|-------------|-------------|-------------|-------------|
| | $w_1 = 1$ | $w_1 = 0.9$ | $w_1 = 0.8$ | $w_1 = 0.7$ | $w_1 = 0.6$ | $w_1 = 0.5$ |
| water (w_1) - PG ($1-w_1$) | | | | | | |
| 298.15 | 0.0143 | 0.0055 | 0.0030 | 0.0017 | 0.0013 | 0.0007 |

| | | | | | | |
|--------|--------|--------|--------|--------|--------|--------|
| 303.15 | 0.0168 | 0.0068 | 0.0035 | 0.0019 | 0.0013 | 0.0009 |
| 308.15 | 0.0199 | 0.0082 | 0.0044 | 0.0026 | 0.0016 | 0.0010 |
| 313.15 | 0.0231 | 0.0092 | 0.0053 | 0.0031 | 0.0019 | 0.0011 |
| 318.15 | 0.0269 | 0.0114 | 0.0064 | 0.0040 | 0.0026 | 0.0016 |

water (w_1) - ACN ($1-w_1$)

| | | | | | | |
|--------|--------|--------|--------|--------|--------|--------|
| 298.15 | 0.0143 | 0.0098 | 0.0063 | 0.0037 | 0.0021 | 0.0011 |
| 303.15 | 0.0168 | 0.0117 | 0.0072 | 0.0044 | 0.0024 | 0.0011 |
| 308.15 | 0.0199 | 0.0139 | 0.0082 | 0.0047 | 0.0026 | 0.0012 |
| 313.15 | 0.0231 | 0.0165 | 0.0103 | 0.0053 | 0.0029 | 0.0013 |
| 318.15 | 0.0269 | 0.0196 | 0.0124 | 0.0066 | 0.0033 | 0.0017 |

water (w_1) - EG ($1-w_1$)

| | | | | | | |
|--------|--------|--------|--------|--------|--------|--------|
| 298.15 | 0.0143 | 0.0082 | 0.0059 | 0.0042 | 0.0033 | 0.0027 |
| 303.15 | 0.0168 | 0.0102 | 0.0072 | 0.0055 | 0.0039 | 0.0033 |
| 308.15 | 0.0199 | 0.0123 | 0.0082 | 0.0060 | 0.0047 | 0.0038 |
| 313.15 | 0.0231 | 0.0145 | 0.0096 | 0.0069 | 0.0058 | 0.0049 |
| 318.15 | 0.0269 | 0.0171 | 0.0110 | 0.0077 | 0.0065 | 0.0052 |

water (w_1) - acetone ($1-w_1$)(*Wu et al., 2017*)

| | | | | | | |
|--------|--------|--------|--------|--------|--------|--------|
| 298.15 | 0.0143 | 0.0059 | 0.0027 | 0.0014 | 0.0006 | 0.0003 |
|--------|--------|--------|--------|--------|--------|--------|

| | | | | | | |
|--------|--------|--------|--------|--------|--------|--------|
| 303.15 | 0.0168 | 0.0072 | 0.0032 | 0.0016 | 0.0007 | 0.0003 |
| 308.15 | 0.0199 | 0.0087 | 0.0040 | 0.0019 | 0.0009 | 0.0004 |
| 313.15 | 0.0231 | 0.0105 | 0.0048 | 0.0022 | 0.0011 | 0.0004 |
| 318.15 | 0.0269 | 0.0124 | 0.0053 | 0.0026 | 0.0012 | 0.0005 |

^b The standard uncertainty for temperature is $u(T) = 0.1$ K, the relative standard uncertainty for solubilities is $u_r(x) = 0.015$, w_1 represents the mole fraction of water in three binary solvents in the absence of taurine. All tests were held in the atmosphere.

Table 2-3. Parameters and deviations of the modified Apelblat model

Modified Apelblat Model

| water (w_1) - PG ($1-w_1$) | | | | | |
|-----------------------------------|----------------------|------------------------|--------------------|-------|--------|
| w_1 | A | B | C | ARD | RMSD |
| 0.9 | -6.38(± 4.28) | 269.59(± 196.04) | 0.96(± 0.64) | 2.10% | 0.020% |
| 0.8 | -5.53(± 0.44) | 239.19(± 19.94) | 0.83(± 0.06) | 0.42% | 0.002% |
| 0.7 | -5.71(1.44) | 251.95(± 65.75) | 0.85(± 0.21) | 2.43% | 0.007% |
| 0.6 | -5.44(± 0.93) | 243.42(± 42.37) | 0.81(± 0.14) | 2.29% | 0.043% |
| 0.5 | -2.44(± 1.40) | 108.22(± 64.21) | 0.36(± 0.21) | 5.70% | 0.007% |
| water (w_1) - ACN ($1-w_1$) | | | | | |
| w_1 | A | B | C | ARD | RMSD |
| 0.9 | -12.26(± 1.14) | 522.45(± 52.20) | 1.85(± 0.17) | 0.34% | 0.005% |
| 0.8 | -13.68(± 1.83) | 601.61(± 83.66) | 2.05(± 0.27) | 0.83% | 0.009% |
| 0.7 | -5.71(± 3.15) | 250.45(± 144.33) | 0.85(± 0.47) | 2.65% | 0.015% |

| | | | | | |
|---------------------------------------|---------------------|------------------------|---------------------|-------|--------|
| 0.6 | -1.69(± 0.61) | 73.08(± 27.80) | 0.25(± 0.09) | 0.98% | 0.003% |
| 0.5 | -2.92(± 1.17) | 131.09(± 53.71) | 0.44(± 0.17) | 3.87% | 0.005% |
| water (w_1) - EG ($1-w_1$) | | | | | |
| w_1 | A | B | C | ARD | RMSD |
| 0.9 | -6.39(± 1.06) | 257.52(± 48.27) | 0.97(± 0.16) | 0.31% | 0.005% |
| 0.8 | -3.09(± 1.75) | 121.05(± 80.02) | 0.47(± 0.26) | 0.86% | 0.008% |
| 0.7 | 1.37(± 3.23) | -75.94(± 147.62) | -0.19(± 0.48) | 2.32% | 0.015% |
| 0.6 | -2.93(± 2.23) | 120.83(± 102.07) | 0.44(± 0.33) | 1.82% | 0.010% |
| 0.5 | -0.56(± 3.49) | 15.40(± 15.95) | 0.09(± 0.52) | 3.25% | 0.016% |
| water (w_1) - acetone ($1-w_1$) | | | | | |
| w_1 | A | B | C | ARD | RMSD |
| 0.9 | -4.55(± 0.65) | 184.60(± 29.08) | 0.69(± 0.10) | 2.91% | 0.026% |
| 0.8 | -2.16(± 0.18) | 88.16(± 8.05) | 0.33(± 0.03) | 2.57% | 0.072% |
| 0.7 | -0.91(± 0.04) | 36.81(± 1.95) | 0.14(± 0.01) | 1.17% | 0.017% |
| 0.6 | -0.46(± 0.06) | 18.99(± 2.60) | 0.07(± 0.01) | 2.12% | 0.023% |
| 0.5 | -0.12(± 0.03) | 4.58(± 1.22) | 0.02(± 0.00) | 2.69% | 0.011% |

Table 2-4. Parameters and deviations of the NRTL, UNIQUAC, and Wilson model

| Solvents | Water-PG | water-ACN | Water-EG | Water-acetone |
|-------------------|----------------------------|--------------------------|---------------------------|-------------------------|
| NRTL Model | | | | |
| Δg_{12} | -1465.82(± 17468.95) | 376.26(± 75049.00) | -190.31(± 27106.95) | -60.48(± 4050.12) |

| | | | | |
|-----------------|------------------------------|----------------------------|-----------------------------|-----------------------------|
| Δg_{13} | 2195.09(± 20056.94) | 39504.80(± 5570.22) | 6731.95(± 7083.49) | 3589.98(± 5591.11) |
| Δg_{23} | 27909.86 (± 63355.53) | 31652.26(± 5142.21) | 16067.72(± 101158.24) | 28422.99(± 15249.56) |
| Δg_{21} | 719.04 (± 19515.32) | -1246.40(± 72670.94) | -634.54(± 27445.49) | -636.51(± 4058.72) |
| Δg_{31} | 11303.96 (± 16299.93) | 36868.30(± 46003.07) | -559.80(± 4098.82) | 31064.27(± 9265.68) |
| Δg_{32} | -27617.80 (± 50791.18) | 27992.99(± 49581.11) | -15094.65(± 81334.59) | -27253.31(± 12915.20) |
| ARD | 4.90% | 3.93% | 2.81% | 5.05% |
| RMSD | 0.040% | 0.052% | 0.043% | 0.079% |

UNIQUAC Model

| | | | | |
|---------------|---------------------------|-------------------------|-----------------------------|------------------------|
| α_{12} | -1075.68(± 578.66) | 168.09(± 30.54) | -210.75(± 205.03) | -741.23(± 35.23) |
| α_{13} | 1634.48(± 1716.34) | 3123.67(± 153.50) | 3450.09(± 7457095.50) | 347.31(± 117.47) |
| α_{23} | 1681.74(± 1517.54) | 4353.41(± 153.50) | 4027.01(± 7457245.40) | 469.51(± 122.32) |
| α_{21} | -27.75(± 399.60) | -306.60(± 63.67) | 43.13(± 71.17) | 11.95(± 26.23) |
| α_{31} | -206.53(± 404.77) | -254.75(± 40.84) | 165.54(± 39.99) | -168.89(± 33.13) |
| α_{32} | 2341.18(± 15863.54) | -492.70(± 48.10) | 307.09(± 114.97) | 910.31(± 165.60) |
| ARD | 4.53% | 3.46% | 3.29% | 3.52% |
| RMSD | 0.022% | 0.038% | 0.042% | 0.046% |

Wilson Model

| | | | | |
|-----------------------|----------------------------|--------------------------|----------------------------|------------------------------|
| $\Delta \lambda_{12}$ | 2083.73(± 1480.24) | 7539.29(± 3823.35) | -1186.38(± 840.91) | 4432.13(± 893.57) |
| $\Delta \lambda_{13}$ | 13691.04(± 16461.69) | 46142.14(± 85.16) | 11299.51(± 31363.94) | 26942.34(± 3279483.19) |
| $\Delta \lambda_{23}$ | 799.22(± 26983.12) | 6346.98(± 1842.41) | 698.08(± 308.00) | 2388.54(± 516.60) |
| $\Delta \lambda_{21}$ | 1270.14(± 283.17) | -1009.97(± 70.95) | 2128.89(± 300.25) | 829.95(± 96.69) |

| | | | | |
|----------------------|---------------------------|----------------------------|--------------------------|------------------------------|
| $\Delta\lambda_{31}$ | 1365.36(\pm 2154.30) | 14088.54(\pm 127582.38) | -979.69(\pm 2015.77) | -9636.32(\pm 3146578.47) |
| $\Delta\lambda_{32}$ | -843.52(\pm 113080.88) | 5528.67(\pm 384480.95) | -5099.60(\pm 2027.55) | -35210.62(\pm 3145943.48) |
| ARD | 4.76% | 9.81% | 2.08% | 10.39% |
| RMSD | 0.046% | 0.230% | 0.021% | 0.190% |

Table 2-5. Parameters and deviations of the λh Model

λh Model

water (w_1) - PG ($1-w_1$)

| W1 | λ | h | ARD | RMSD |
|-----|-------------------|-------------------------|--------|--------|
| 0.9 | 1.68(\pm 0.52) | 2002.44(\pm 499.35) | 1.92% | 0.019% |
| 0.8 | 9.08(\pm 8.86) | 532.50(\pm 450.15) | 7.21% | 0.032% |
| 0.7 | 2.67(\pm 1.41) | 1642.49(\pm 740.71) | 4.26% | 0.011% |
| 0.6 | 3.73(\pm 5.01) | 1302.50(\pm 1516.55) | 9.80% | 0.018% |
| 0.5 | 5.08(\pm 7.41) | 1062.49(\pm 1363.66) | 10.45% | 0.011% |

water (w_1) - ACN ($1-w_1$)

| W1 | λ | h | ARD | RMSD |
|-----|--------------------|-------------------------|--------|--------|
| 0.9 | 2.98(\pm 0.23) | 1132.38(\pm 70.83) | 0.58% | 0.008% |
| 0.8 | 1.93(\pm 0.70) | 1762.43(\pm 520.09) | 2.47% | 0.024% |
| 0.7 | 8.99(\pm 18.24) | 532.50(\pm 934.87) | 14.33% | 0.072% |
| 0.6 | 2.31(\pm 5.01) | 1862.49(\pm 3431.97) | 14.62% | 0.042% |
| 0.5 | 4.96(\pm 14.32) | 1062.48(\pm 2687.61) | 19.21% | 0.026% |

water (w_1) - EG ($1-w_1$)

| W1 | λ | h | ARD | RMSD |
|-----|---------------------|-------------------------|--------|--------|
| 0.9 | 2.78(± 0.45) | 1227.50(± 162.26) | 1.18% | 0.015% |
| 0.8 | 0.83(± 0.13) | 3498.75(± 432.05) | 1.22% | 0.010% |
| 0.7 | 8.70(± 16.88) | 532.49(± 889.08) | 13.08% | 0.085% |
| 0.6 | 8.99(± 12.70) | 532.50(± 650.44) | 9.60% | 0.050% |
| 0.5 | 9.28(± 16.92) | 532.51(± 843.25) | 12.32% | 0.052% |

water (w_1) - acetone ($1-w_1$)

| W1 | λ | h | ARD | RMSD |
|-----|---------------------|--------------------------|--------|--------|
| 0.9 | 1.60(± 0.34) | 2064.09(± 358.81) | 3.80% | 0.035% |
| 0.8 | 8.60(± 9.05) | 571.27(± 519.77) | 24.59% | 0.065% |
| 0.7 | 2.88(± 2.73) | 1620.78(± 1320.13) | 21.73% | 0.030% |
| 0.6 | 7.44(± 13.22) | 780.80(± 1228.00) | 34.69% | 0.022% |
| 0.5 | 5.94(± 16.21) | 1020.78(± 2477.03) | 40.63% | 0.018% |

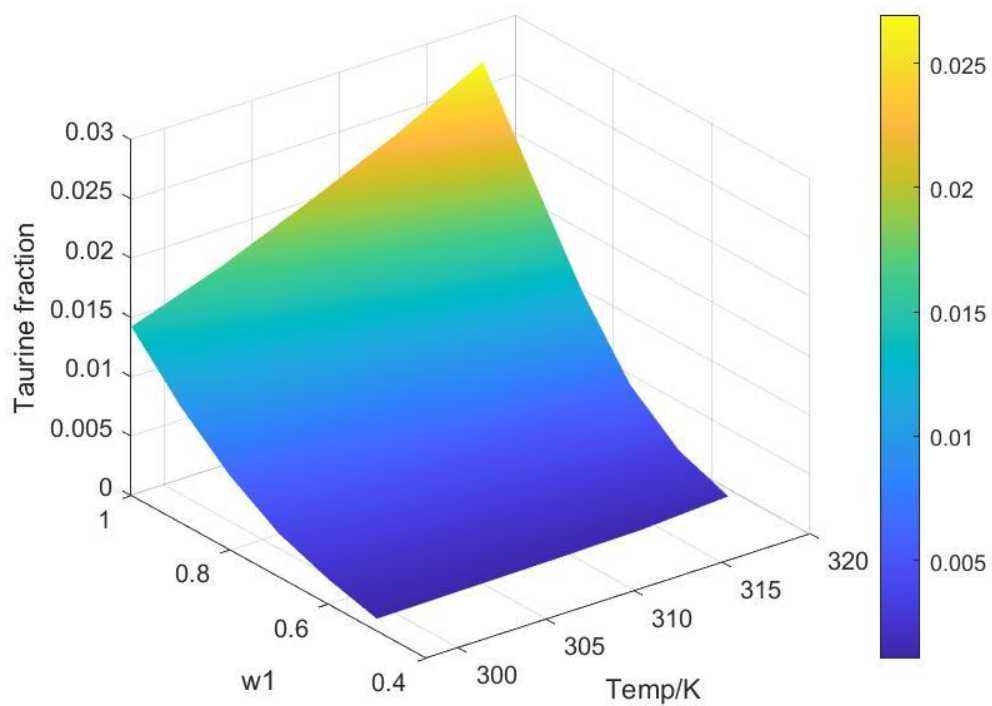


Figure 2-3. Solubility data for taurine in water (w1)-ACN with various mole fractions at different temperatures

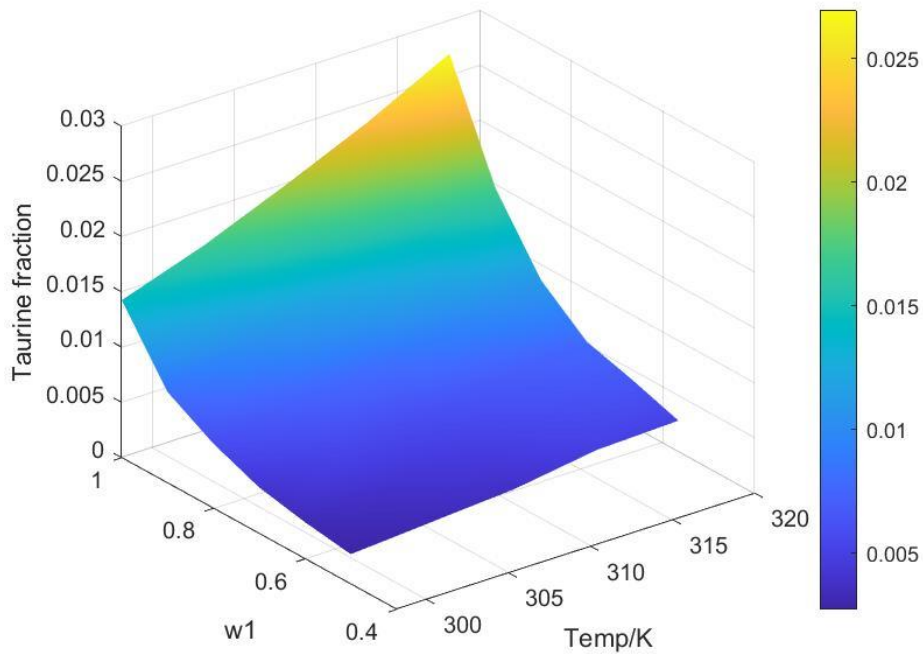


Figure 2-4. Solubility data for taurine in water (w1)-EG with various mole fractions at different temperatures

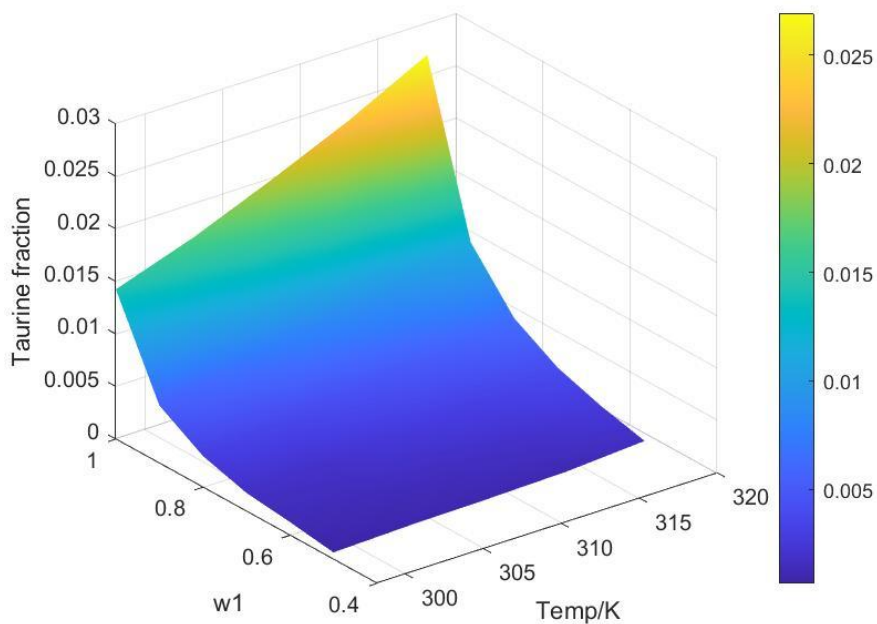


Figure 2-5. Solubility data for taurine in water (w1)-PG with various mole fractions at different temperatures

2.4.5 Solvent Effect Analysis of Taurine

The KAT-LSER model is applied to further investigate the relationship between the solubility of taurine and intermolecular interactions. Solubility data at 298.15K is used to perform the multiple linear regression analysis (MLRA). Values of the parameters α , β , and π^* are derived from reported literatures (Cong et al., 2022a; Li et al., 2020; Liu et al., 2021; Xu et al., 2018) using linear interpolation and are listed in [Table A-3](#) in Appendix A. The V_s value ($110.7 \text{ cm}^3 \cdot \text{mol}^{-1}$), which is calculated using the group contribution method in the HSP calculation, is still used. To explore the best regression model for the analysis, 15 types of regression of one system were held as four independent variables can constitute 15 different subsets. The solute-solvent interactions improve the dissolution of taurine and solvent-solvent interactions shall prevent its dissolution. Thus, a suitable KAT-LSER model shall have positive values for c_1 , c_2 and c_3 , and negative for c_4 . Thus, the best model should ensure $c_{i=1-3} > 0$ and $c_4 < 0$, as well as having the highest F-statistic with acceptable squared correlation coefficient (R^2) and standard error. The regression results are listed in [Table A-4](#) to [Table A-7](#) in Appendix A. The best model for each system is described in Eqs.(2-40) to (2-43) for PG-water, ACN-water, EG-water, and acetone-water binary solvents (shown in bold in [Table A-4](#) to [Table A-7](#)). Numbers in the brackets represent the standard error of parameters.

$$\begin{aligned} \ln(x_1) &= -19.181(1.883) + 6.214(1.450)\alpha + 6.972(2.768)\pi^* \\ n &= 6, R^2 = 0.96, F = 67.10 \end{aligned} \quad (2-40)$$

$$\begin{aligned} \ln(x_1) &= -17.785(2.841) + 3.553(3.001)\beta + 10.842(1.596)\pi^* \\ n &= 6, R^2 = 0.91, F = 27.49 \end{aligned} \quad (2-41)$$

$$\begin{aligned} \ln(x_1) &= -15.531(0.174) + 3.812(0.060)\alpha + 6.251(0.152)\pi^* \\ n &= 6, R^2 = 1.00, F = 2918.30 \end{aligned} \quad (2-42)$$

$$\ln(x_1) = -41.246(5.470) + 32.651(5.215)\pi^*$$

$$n = 6, R^2 = 0.88, F = 39.21 \quad (2 - 43)$$

From the above equations, it could be found that a two-parametric KAT-LSER model can be applied to describe the systems using PG-water, ACN-water, EG-water, and a single-parametric KAT-LSER model to describe the system of acetone-water. As shown in [Table A-4](#) to [Table A-7](#), there are other models which offer better R^2 . However, the standard error of these parameters is so high that makes them unacceptable. Then, for taurine's solubility in acetone-water, the single-parametric KAT-LSER model using α offers a better fitting result. However, considering the HSP analysis, a single-parametric KAT-LSER model using π^* is considered instead. For all four binary solvents, the correlation coefficient R^2 , is larger than 0.88, which indicates that π^* is the dominant factor that affects taurine's solubility in PG-water, ACN-water, EG-water, and acetone-water. Based on Table S3, when the water content decreases in the binary solvent, the π^* of ACN-water decreases much faster than that of EG-water. This explains why the solubility of taurine in EG-water exceeds that of ACN-water when the water content is low.

2.4.6 Thermodynamic Properties of Solutions

The related thermodynamic properties of dissolution including enthalpy, entropy, and Gibbs free energy change for taurine dissolved in four binary solvents are summarized in [Table 2-6](#). As it is clearly shown in [Table 2-6](#), all standard molar enthalpy values are positive ($27.79 - 34.02 \text{ kJ} \cdot \text{mol}^{-1}$ for water-PG, $16.43 - 27.21 \text{ kJ} \cdot \text{mol}^{-1}$ for water-ACN, $22.94 - 28.65 \text{ kJ} \cdot \text{mol}^{-1}$ for water-EG, and $23.4 - 28.36 \text{ kJ} \cdot \text{mol}^{-1}$ for water-acetone), confirming the dissolution of taurine in all four binary solvents is an endothermic process. It is found that the values of ξ_H of all fractions in four binary solvents are always larger than the values of ξ_{TS} , which means enthalpy contributes more

to the ΔG^0 than entropy. The relationship between ΔG^0 and the water mole fraction has been plotted in [Figure 2-6](#). It is shown that with the increase of the water content in the system, the ΔG^0 continuously decreases, indicating that the dissolution of taurine is more favorable. When the mole fraction of water is lower than 0.8, the ΔG^0 of ACN-water becomes larger than the ΔG^0 of EG-water, suggesting a larger solubility of taurine in EG-water than its solubility in ACN-water when the water content is low.

Table 2-6. Thermodynamic properties for taurine dissolution in binary solvents^c

water (w_1) - PG ($1-w_1$)

| w_1 | $\Delta H^0/\text{kJ} \cdot \text{mol}^{-1}$ | $\Delta G^0/\text{kJ} \cdot \text{mol}^{-1}$ | $T_{\text{hm}}\Delta S^0/\text{kJ} \cdot \text{mol}^{-1}$ | ξ_{H} | ξ_{TS} |
|-------|--|--|---|------------------|-------------------|
| 1 | 25.12(±0.13) | 10.06(±0.00) | 15.07(±0.13) | 0.625 | 0.375 |
| 0.9 | 27.79(±1.38) | 12.38(±0.03) | 15.41(±1.38) | 0.643 | 0.357 |
| 0.8 | 30.84(±0.85) | 13.93(±0.02) | 16.91(±0.85) | 0.646 | 0.354 |
| 0.7 | 34.02(±3.30) | 15.30(±0.08) | 18.72(±3.30) | 0.645 | 0.355 |
| 0.6 | 28.76(±4.73) | 16.36(±0.11) | 12.40(±4.73) | 0.699 | 0.301 |
| 0.5 | 32.46(±4.05) | 17.68(±0.09) | 14.79(±4.05) | 0.687 | 0.313 |

water (w_1) - ACN ($1-w_1$)

| w_1 | $\Delta H^0/\text{kJ} \cdot \text{mol}^{-1}$ | $\Delta G^0/\text{kJ} \cdot \text{mol}^{-1}$ | $T_{\text{hm}}\Delta S^0/\text{kJ} \cdot \text{mol}^{-1}$ | ξ_{H} | ξ_{TS} |
|-------|--|--|---|------------------|-------------------|
| 0.9 | 27.21(±0.27) | 10.95(±0.00) | 16.26(±0.27) | 0.626 | 0.374 |
| 0.8 | 26.90(±1.95) | 12.18(±0.01) | 14.72(±1.95) | 0.646 | 0.354 |
| 0.7 | 21.34(±2.15) | 13.65(±0.05) | 7.69(±2.15) | 0.735 | 0.265 |
| 0.6 | 16.43(±0.99) | 15.20(±0.02) | 1.22(±0.99) | 0.931 | 0.069 |
| 0.5 | 17.68(±4.43) | 17.08(±0.10) | 0.60(±4.43) | 0.967 | 0.033 |

| water (w_1) - EG ($1-w_1$) | | | | | |
|---------------------------------------|--------------|--------------|--------------|-------|-------|
| w_1 | | | | | |
| 0.9 | 28.65(±0.70) | 11.31(±0.02) | 17.34(±0.70) | 0.623 | 0.377 |
| 0.8 | 24.55(±0.88) | 12.31(±0.02) | 12.24(±0.88) | 0.667 | 0.333 |
| 0.7 | 22.94(±2.63) | 13.13(±0.06) | 9.81(±2.63) | 0.700 | 0.300 |
| 0.6 | 27.65(±1.27) | 13.72(±0.03) | 13.93(±1.27) | 0.665 | 0.335 |
| 0.5 | 26.77(±2.41) | 14.24(±0.06) | 12.53(±2.41) | 0.681 | 0.319 |
| water (w_1) - acetone ($1-w_1$) | | | | | |
| w_1 | | | | | |
| 0.9 | 28.36(±0.69) | 12.66(±0.03) | 15.70(±0.69) | 0.644 | 0.356 |
| 0.8 | 27.00(±0.41) | 14.54(±0.02) | 12.47(±0.41) | 0.684 | 0.316 |
| 0.7 | 26.68(±0.38) | 16.34(±0.02) | 10.34(±0.38) | 0.721 | 0.279 |
| 0.6 | 26.00(±0.55) | 18.29(±0.03) | 7.71(±0.55) | 0.771 | 0.229 |
| 0.5 | 23.40(±0.60) | 20.39(±0.03) | 3.00(±0.60) | 0.886 | 0.114 |

^c $T_{hm} = 308K$ for water-PG, water-ACN, water-EG; $T_{hm} = 300K$ for water-acetone

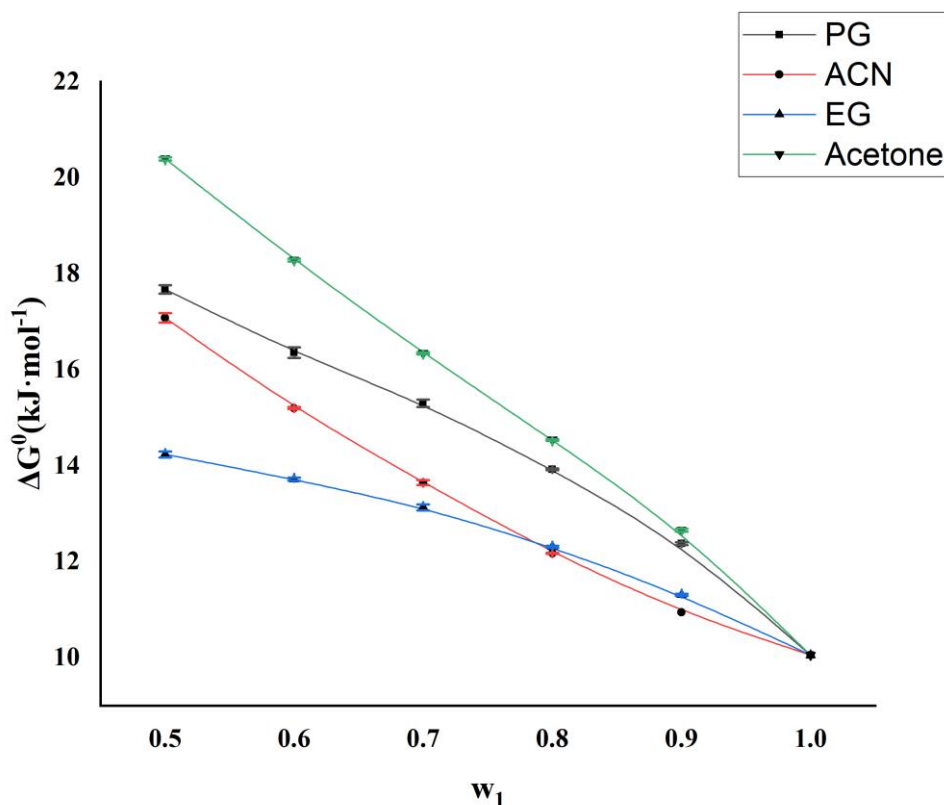


Figure 2-6. ΔG^0 values versus water mole fraction (w_1)

2.5 Conclusions

The solubility of taurine in different binary solvents was measured and modeled in this research. Unreported taurine's solubility in three binary solvents (1,2-propanediol- water, acetonitrile-water, and ethylene glycol-water) was experimentally determined. Then, the obtained data with data published in Wu's (Wu et al., 2017) paper were compared and correlated with the prediction by the modified Apelblat model, NRTL, UNIQUAC, Wilson, and λh model. It is found that the modified Apelblat model, NRTL, and UNIQUAC model offer better fitting results than Wilson, and λh model. Due to the huge error caused by δ_h , the volume-dependent solubility parameter, δ_v , is used to predict the qualitative trend of taurine's solubility in different solvents. When the water content is

high, the solubility of taurine in four binary solvents perfectly matches the prediction result. Within the increase of the second polar solvent, the dielectric constant of the binary solvent decreases significantly, which make it difficult for the taurine molecule to overcome the electrostatic interaction in water molecules. Thus, the solubility of taurine decreased significantly. Water molecules in the system form strong hydrogen bonds with ACN, EG, PG, and acetone molecules, which further prevent the dissolution of taurine. Based on the KAT-LSER analysis, the dipolarity–polarizability parameter (π^*) is found to be the factor that dominates the solubility of taurine. When the water content decreases, π^* of ACN-water decreases fast, resulting the solubility of taurine in EG-water exceed the solubility in ACN-water. The dissolution thermodynamics also confirm this phenomenon, the standard Gibbs free energy of EG-water system becomes lower than the ACN-water system when the water mole fraction in the binary solvents is lower than 0.8.

2.6 References

- (1) Lourenço, R.; Camilo, M. E. Taurine: A Conditionally Essential Amino Acid in Humans? An Overview in Health and Disease. *Nutr. Hosp.* 2002, 17 (6), 262–270.
- (2) Green, T. R.; Fellman, J. H.; Eicher, A. L.; Pratt, K. L. Antioxidant Role and Subcellular Location of Hypotaurine and Taurine in Human Neutrophils. *Biochim. Biophys. Acta BBA - Gen. Subj.* 1991, 1073 (1), 91–97. [https://doi.org/10.1016/0304-4165\(91\)90187-L](https://doi.org/10.1016/0304-4165(91)90187-L).
- (3) Karpowicz, S. J. Kinetics of Taurine Biosynthesis Metabolites with Reactive Oxygen Species: Implications for Antioxidant-Based Production of Taurine. *Biochim. Biophys. Acta BBA - Gen. Subj.* 2022, 1866 (6), 130131. <https://doi.org/10.1016/j.bbagen.2022.130131>.
- (4) Tao, X.; Zhang, Z.; Yang, Z.; Rao, B. The Effects of Taurine Supplementation on Diabetes Mellitus in Humans: A Systematic Review and Meta-Analysis. *Food Chem. Mol. Sci.* 2022, 4, 100106. <https://doi.org/10.1016/j.fochms.2022.100106>.
- (5) Kim, C.; Cha, Y.-N. Taurine Chloramine Produced from Taurine under Inflammation Provides Anti-Inflammatory and Cytoprotective Effects. *Amino Acids* 2014, 46 (1), 89–100. <https://doi.org/10.1007/s00726-013-1545-6>.

- (6) El Agouza, I. M.; Eissa, S. S.; El Houseini, M. M.; El-Nashar, D. E.; Abd El Hameed, O. M. Taurine: A Novel Tumor Marker for Enhanced Detection of Breast Cancer among Female Patients. *Angiogenesis* 2011, 14 (3), 321–330. <https://doi.org/10.1007/s10456-011-9215-3>.
- (7) Schaffer, S. W.; Azuma, J.; Mozaffari, M. Role of Antioxidant Activity of Taurine in Diabetes. *Can. J. Physiol. Pharmacol.* 2009, 87 (2), 91–99. <https://doi.org/10.1139/Y08-110>.
- (8) Schuller-Levis, G. B.; Park, E. Taurine: New Implications for an Old Amino Acid. *FEMS Microbiol. Lett.* 2003, 226 (2), 195–202. [https://doi.org/10.1016/S0378-1097\(03\)00611-6](https://doi.org/10.1016/S0378-1097(03)00611-6).
- (9) Lin, R.; Woo, M. W.; Selomulya, C.; Lu, J.; Chen, X. D. Controlling the Size of Taurine Crystals in the Cooling Crystallization Process. *Ind. Eng. Chem. Res.* 2013, 52 (37), 13449–13458. <https://doi.org/10.1021/ie4000807>.
- (10) Bondareva, O. M.; Lopatik, D. V.; Kuvaeva, Z. I.; Vinokurova, L. G.; Markovich, M. M.; Prokopovich, I. P. Synthesis of Taurine. *Pharm. Chem. J.* 2008, 42 (3), 142–144. <https://doi.org/10.1007/s11094-008-0072-3>.
- (11) Yang, J.; Zhou, C.-R.; Shi, X.-H. Determination and Correlation of the Solubility for Taurine in Water and Organic Solvent Systems. *J. Chem. Eng. Data* 2010, 55 (7), 2620–2623. <https://doi.org/10.1021/je9009877>.
- (12) Wu, D.; Song, L.; Zhu, C.; Zhang, X.; Guo, H.; Yang, C. Solubility of Taurine and Its Application for the Crystallization Process Improvement. *J. Mol. Liq.* 2017, 241, 326–333. <https://doi.org/10.1016/j.molliq.2017.06.043>.
- (13) Chengxiong, Y. Process for Refining 2-Aminoethanesulfonic Acid from Crude 2-Aminoethane-Sulfonic Acid, 2-Aminoethanesulfonic Acid Obtained There from and Use Thereof. CN101857558 (A), October 13, 2010. https://worldwide.espacenet.com/publicationDetails/biblio?FT=D&date=20101013&DB=&locale=en_EP&CC=CN&NR=101857558A&KC=A&ND=1 (accessed 2022-06-10).
- (14) Shishimaru, S.; Ura, D.; Fukuhara, N. Method for Recovering Alcohol Used for Taurine Purification. JPH07145140 (A), June 6, 1995. <https://worldwide.espacenet.com/publicationDetails/biblio?FT=D&date=19950606&DB=&locale=&CC=JP&NR=H07145140A&KC=A&ND=1> (accessed 2022-06-10).
- (15) Hansen, C. M. Hansen Solubility Parameters: A User's Handbook, 2nd ed.; CRC Press: Boca Raton, 2007.

- (16) Kamlet, M. J.; Abboud, J. L. M.; Abraham, M. H.; Taft, R. W. Linear Solvation Energy Relationships. 23. A Comprehensive Collection of the Solvatochromic Parameters, π^* , α , and β , and Some Methods for Simplifying the Generalized Solvatochromic Equation. *J. Org. Chem.* 1983, 48 (17), 2877–2887. <https://doi.org/10.1021/jo00165a018>.
- (17) Handbook of Industrial Crystallization, 3rd ed.; Myerson, A. S., Erdemir, D., Lee, A. Y., Eds.; Cambridge University Press, 2019. <https://doi.org/10.1017/9781139026949>.
- (18) Cong, Y.; Du, C.; Xing, K.; Bian, Y.; Li, X.; Wang, M. Research on Solubility Modelling of Actarit in Different Solvents: Solvent Effect, Hansen Solubility Parameter, Molecular Interactions and Solution Thermodynamics. *J. Mol. Liq.* 2022, 347, 117965. <https://doi.org/10.1016/j.molliq.2021.117965>.
- (19) He, H.; Sun, R.; Wan, Y.; Jiang, G.; Sha, J.; Li, Y.; Li, T.; Ren, B. Solubility Measurement, Model Evaluation and Hansen Solubility Parameter of Piperonylnitrile in Four Binary Solvents. *J. Chem. Thermodyn.* 2020, 151, 106249. <https://doi.org/10.1016/j.jct.2020.106249>.
- (20) He, Q.; Zhao, H. Imidacloprid (I) in Several Aqueous Co-Solvent Mixtures: Solubility, Solvent Effect, Solvation Thermodynamics and Enthalpy–Entropy Compensation. *J. Mol. Liq.* 2021, 338, 116781. <https://doi.org/10.1016/j.molliq.2021.116781>.
- (21) Alanazi, A.; Alshehri, S.; Altamimi, M.; Shakeel, F. Solubility Determination and Three Dimensional Hansen Solubility Parameters of Gefitinib in Different Organic Solvents: Experimental and Computational Approaches. *J. Mol. Liq.* 2020, 299, 112211. <https://doi.org/10.1016/j.molliq.2019.112211>.
- (22) Bagley, E. B.; Nelson, T. P.; Scigliano, J. M. Three-Dimensional Solubility Parameters and Their Relationship to Internal Pressure Measurements in Polar and Hydrogen Bonding Solvents. *J. Paint. Technol.* 1971.
- (23) Zheng, M.; Farajtabar, A.; Zhao, H. Solute-Solvent and Solvent-Solvent Interactions and Preferential Solvation of Hesperidin in Aqueous Cosolvent Mixtures of Ethanol, Isopropanol, Propylene Glycol and n-Propanol. *J. Mol. Liq.* 2018, 264, 285–291. <https://doi.org/10.1016/j.molliq.2018.05.057>.
- (24) Liu, Q.; Yan, Y.; Wu, Y.; Zhang, X.; Zhou, X. Systematic Thermodynamic Study of Clorsulon Dissolved in Ten Organic Solvents: Mechanism Evaluation by Modeling and Molecular Dynamic Simulation. *J. Mol. Liq.* 2021, 341, 117217. <https://doi.org/10.1016/j.molliq.2021.117217>.
- (25) Huang, W.; Wang, H.; Li, C.; Wen, T.; Xu, J.; Ouyang, J.; Zhang, C. Measurement

and Correlation of Solubility, Hansen Solubility Parameters and Thermodynamic Behavior of Clozapine in Eleven Mono-Solvents. *J. Mol. Liq.* 2021, 333, 115894. <https://doi.org/10.1016/j.molliq.2021.115894>.

- (26) Wang, R.; Chen, C.; Yang, W.; Zhou, P.; Zhu, F.; Xu, H.; Hu, G.; Sun, W.; Shen, W.; Hu, Y. Solubility Determination and Thermodynamic Characterization of Orotic Acid in Twelve Pure Solvents and Four Binary Mixed Solvents. *J. Mol. Liq.* 2021, 341, 117335. <https://doi.org/10.1016/j.molliq.2021.117335>.
- (27) Buchowski, H.; Ksiazczak, A.; Pietrzyk, S. Solvent Activity along a Saturation Line and Solubility of Hydrogen-Bonding Solids. *J. Phys. Chem.* 1980, 84 (9), 975–979. <https://doi.org/10.1021/j100446a008>.
- (28) Behboudi, E.; Soleymani, J.; Martinez, F.; Jouyban, A. Solubility of Amlodipine Besylate in Binary Mixtures of Polyethylene Glycol 400 + Water at Various Temperatures: Measurement and Modelling. *J. Mol. Liq.* 2022, 347, 118394. <https://doi.org/10.1016/j.molliq.2021.118394>.
- (29) Wilson, G. M. Vapor-Liquid Equilibrium. XI. A New Expression for the Excess Free Energy of Mixing. *J. Am. Chem. Soc.* 1964, 86 (2), 127–130. <https://doi.org/10.1021/ja01056a002>.
- (30) Abrams, D. S.; Prausnitz, J. M. Statistical Thermodynamics of Liquid Mixtures: A New Expression for the Excess Gibbs Energy of Partly or Completely Miscible Systems. *AIChE J.* 1975, 21 (1), 116–128. <https://doi.org/10.1002/aic.690210115>.
- (31) Perlovich, G. L.; Kurkov, S. V.; Kinchin, A. N.; Bauer-Brandl, A. Thermodynamics of Solutions III: Comparison of the Solvation of (+)-Naproxen with Other NSAIDs. *Eur. J. Pharm. Biopharm.* 2004, 57 (2), 411–420. <https://doi.org/10.1016/j.ejpb.2003.10.021>.
- (32) Krevelen, D. W. van; Nijenhuis, K. te. *Properties of Polymers: Their Correlation with Chemical Structure: Their Numerical Estimation and Prediction from Additive Group Contributions*, 4th, completely rev. ed ed.; Elsevier: Amsterdam, 2009.
- (33) Breitzkreutz, J. Prediction of Intestinal Drug Absorption Properties by Three-Dimensional Solubility Parameters. *Pharm. Res.* 1998, 15 (9), 1370–1375. <https://doi.org/10.1023/A:1011941319327>.
- (34) Tan, Q.; Leng, Y.; Wang, J.; Huang, C.; Yuan, Y. Correlation and Prediction of the Solubility of the Racemic Tartaric Acid–Ethanol–Water System with the NRTL Model. *J. Mol. Liq.* 2016, 216, 476–483. <https://doi.org/10.1016/j.molliq.2016.01.080>.

- (35) Gandhi, P. J.; Murthy, Z. V. P. Measurement of Solubility of Mitomycin C in Ethanol–Water Solutions at Different Temperatures. *Thermochim. Acta* 2012, 545, 163–173. <https://doi.org/10.1016/j.tca.2012.07.014>.
- (36) Orhan, M.; Kinaci, A.; Cagin, T. Dielectric Properties of Acetonitrile Confined in Carbon Nanotubes. *Chem. Phys.* 2020, 530, 110598. <https://doi.org/10.1016/j.chemphys.2019.110598>.
- (37) Sengwa, R. J.; Sankhla, S. Characterization of Heterogeneous Interaction in Binary Mixtures of Ethylene Glycol Oligomer with Water, Ethyl Alcohol and Dioxane by Dielectric Analysis. *J. Mol. Liq.* 2007, 130 (1–3), 119–131. <https://doi.org/10.1016/j.molliq.2006.05.011>.
- (38) Castro, G. T.; Loyola, J. M.; Gasull, E. I.; Almandoz, M. C. Solubility of Meloxicam in Ethylene Glycol-Water and Propylene Glycol-Ethanol Mixtures: Experimental Determination and Thermodynamic Analysis. *J. Mol. Liq.* 2022, 354, 118863. <https://doi.org/10.1016/j.molliq.2022.118863>.
- (39) Fernandes, A. J. F. C.; de Carvalho Bertozo, L.; Povinelli, A. P. R.; Zazeri, G.; de Souza, A. R.; Morgon, N. H.; Ximenes, V. F. 4-Dimethylamino-Beta-Nitrostyrene, a Fluorescent Solvatochromic Probe to Estimate the Apparent Dielectric Constant in Serum Albumin: Experimental and Molecular Dynamics Studies. *J. Photochem. Photobiol. Chem.* 2022, 433, 114197. <https://doi.org/10.1016/j.jphotochem.2022.114197>.
- (40) Cong, Y.; Du, C.; Xing, K.; Bian, Y.; Li, X.; Wang, M. Research on Dissolution of Actarit in Aqueous Mixtures: Solubility Determination and Correlation, Preferential Solvation, Solvent Effect and Thermodynamics. *J. Mol. Liq.* 2022, 358, 119141. <https://doi.org/10.1016/j.molliq.2022.119141>.
- (41) Li, X.; He, Y.; Xu, Y.; Zhang, X.; Zheng, M.; Zhao, H. 5-Nitrosalicylaldehyde in Aqueous Co-Solvent Mixtures of Methanol, Ethanol, Isopropanol and Acetonitrile: Solubility Determination, Solvent Effect and Preferential Solvation Analysis. *J. Chem. Thermodyn.* 2020, 142, 106014. <https://doi.org/10.1016/j.jct.2019.106014>.
- (42) Xu, R.; Zheng, M.; Farajtabar, A.; Zhao, H. Solubility Modelling and Preferential Solvation of Adenine in Solvent Mixtures of (N,N-Dimethylformamide, N-Methyl Pyrrolidone, Propylene Glycol and Dimethyl Sulfoxide) plus Water. *J. Chem. Thermodyn.* 2018, 125, 225–234. <https://doi.org/10.1016/j.jct.2018.05.030>.

Chapter 3

Polymorphism Control of L-Glutamic Acid in a Single-Stage and a Two-Stage MSMPR Crystallizer by Different Seeding Strategies

A version of this chapter has been published in *Chemical Engineering Research and Design*:

Gong, W., Wu, Y., Lin, M., & Rohani, S. (2021). Polymorphism control of l-Glutamic acid in a single-stage and a two-stage MSMPR crystallizer by different seeding strategies. *Chemical Engineering Research and Design*, 170, 23-33.

3. Polymorphism Control of L-Glutamic Acid in a Single-Stage and a Two-Stage MSMPR Crystallizer by Different Seeding Strategies

Abstract

Control of polymorphism in continuous crystallization processes has been investigated. Using population balance modeling, we found that the relative growth and birth kinetics of different polymorphs play a major role on the steady-state polymorph outcome in a mixed-suspension mixed-product removal (MSMPR) crystallizer. In this communication, we present the conditions to harvest the desirable polymorph of L-glutamic acid (LGA) by numerical simulation and experimental observation in a two-stage MSMPR and a single MSMPR with intermittent seeding. Different polymorphic outcomes of L-glutamic acid can be achieved at different operating temperatures of the MSMPR crystallizer. The interplay of growth and nucleation kinetic makes the stable β -form hard to secure at low operating temperatures. The design of a two-stage MSMSPR crystallizer configuration with different working temperatures realizes the continuous seeding of the stable β form from the first MSMPR to the production crystallizer. The purpose of such a design is to improve the secondary nucleation of the β form under a kinetic-unfavorable condition.

Another approach to ensure the production of the desired polymorph is the use of intermittent seeding with the desirable polymorph to a single-stage MSMPR. The feasibility of both continuous seeding and intermittent seeding strategies is demonstrated in this paper. Based on the L-glutamic acid crystallization kinetics, numerical simulation is used to figure out the best inlet concentration, working temperature, and intermittent seeding frequency for producing the desired yield and polymorph.

Keywords: Harvesting the desirable polymorph, Single stage and double stage mixed-suspension mixed-product removal (MSMPR) crystallizer, Intermittent seeding, L-glutamic acid, Numerical simulation, Experimental results

3.1 Introduction

Crystallization is widely applied as a separation and purification process in the pharmaceutical and chemical industry. It is driven by supersaturation which can be generated through solvent evaporation, cooling, addition of anti-solvent, and chemical reaction (Myerson et al., 2019). Among all, controlled batch cooling crystallization is the most used process in industry because of its ability to produce uniformly sized particles and the simplicity of process equipment (Lewis et al., 2015). Recently, there is a rising interest on transferring the batch manufacturing to the continuous process in the pharmaceutical industry. This ensures a large capacity, uniform product quality, ease of maintenance and control, and the reduced cost (Li et al., 2016). The ultimate objective is to obtain the desired yield, purity, polymorph and crystal size distribution (CSD) of active pharmaceutical ingredients (APIs). The continuous MSMPR crystallizer is widely used as an ideal process for operation and extracting the crystallization kinetics of a given API (Myerson et al., 2019). An MSMPR provides an easy route for switching from batch processes to continuous processes (Park et al., 2016).

Polymorphism describes the phenomenon of chemical species showing more than one unit-cell structure in solid state. The polymorphic variation results in different solubility, stability, and other physicochemical properties of the active pharmaceutical ingredients (Brittain, n.d.). The proper polymorphs of an API, in addition to improved bioavailability, facilitate downstream processes such as filtration, granulation and tableting. Thus, the control of polymorphism is one major target during crystallization (Lai et al., 2014). In batch crystallization, with enough batch time, the thermodynamically most stable form at the final temperature can be achieved through solution-mediated polymorphic

transformation (SMPT) (Beckmann, 2000). Seeding the desired polymorph is the most widely used method. In a batch operation, the primary nucleation of the undesired polymorphs can be avoided through a well-controlled cooling profile (Beckmann, 2000; Kee et al., 2009; Schöll et al., 2006). On the other hand, only a few papers have studied polymorphic outcomes in the continuous crystallization systems (Lai et al., 2014, 2015; Lin et al., 2020; Nicoud et al., 2019). It is well known that, unlike batch crystallization, initial seeding will not affect the final polymorphic outcome of a continuous process. The initial seeds will finally be washed out and newly born crystals in the MSMPR crystallizer will be the sites for secondary nucleation. However, using a method of continuous seeding through the design of a two-stage MSMPR under different working conditions may affect the polymorphic outcome. Lai et al. (Lai et al., 2015) successfully used a two-stage MSMPR to produce α -form p-aminobenzoic acid, where the first stage worked at a high temperature to produce the α -form seeds of the p-aminobenzoic acid and the second stage operated at a β -form favored low temperature. The purpose of such a design was to use continuous seeding of the second MSMPR to improve the secondary nucleation of a specific polymorph under a kinetic-unfavored condition.

Similar to the p-aminobenzoic acid-water system, different polymorphic outcomes of L-glutamic acid can be obtained through MSMPR operation under different working temperatures (Lai et al., 2014). L-glutamic acid is monotropic with a stable β form and a metastable α form. (Figure 3-1) Unlike in batch crystallization where the stable β form can always be achieved through the SMPT (Schöll et al., 2006), it has been proven that the interplay of nucleation and growth rates makes harvesting the stable β form hard to secure at low operating temperatures in MSMPR crystallization. Under 25 °C, The $Rk_g \cdot Rk_b^{1/3}$ value ($Rk_g = \frac{k_{gstable}}{k_{gmetastable}}$, $Rk_b = \frac{k_{bstable}}{k_{bmetastable}}$) is lower than 0.1 indicating the stable form is with slow kinetics (Lai et al., 2014; Lin et al., 2020). The pure stable form can be accessed in an MSMPR operating at 45°C and the metastable form can be obtained below 25°C. The product polymorph of L-glutamic acid in MSMPR crystallization can

be altered by the process operation variables. Therefore, applying the continuous seeding strategy is assumed to have the same effect on L-glutamic acid-water system as has been shown in the p-aminobenzoic acid-water system.

Another seeding strategy that improves the secondary nucleation of the desired polymorph is intermittent seeding. Using intermittent seeding can improve the mean crystal size and reduce the amount of necessary seeds (Qamar, 2012). In this article, the feasibility of both continuous seeding and intermittent seeding in a single MSMPR is also studied experimentally and theoretically. The effects of the process operation variables (namely, feed concentration, working temperature, residence time, and intermittent seeding frequency) are analyzed through numerical simulation and verified by experimentation. For the MSMPR crystallization experiment, an intermittent side withdraw is applied to avoid plugging. Products at steady state are collected and compared with the simulation results. The product polymorphic nature is characterized by powder X-ray diffraction (PXRD).

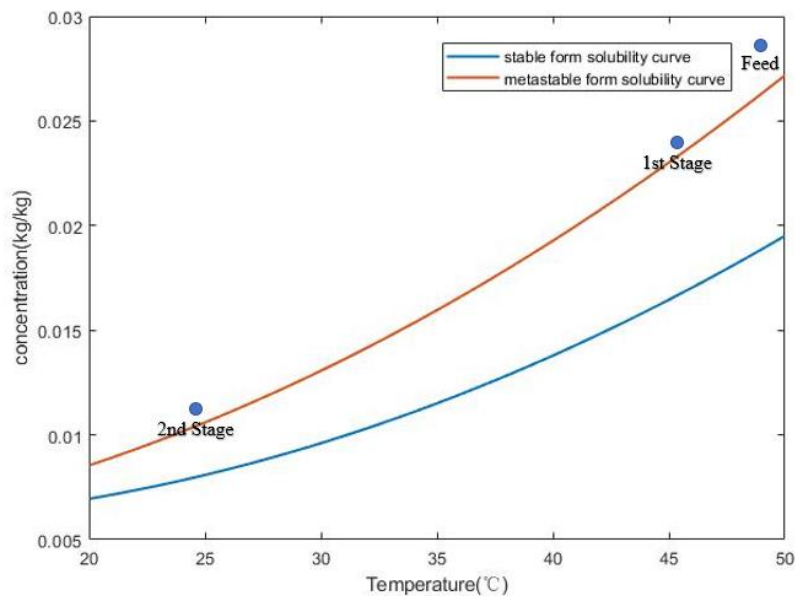


Figure 3-1 Solubility curves of LGA metastable form and stable form

3.2 Materials and Methods

3.2.1 Materials

The selected model compound is L-glutamic acid which has a metastable α polymorph and a stable β form. The commercial β form L-glutamic acid was purchased from Alfa Aesar (Ward Hill, MA, with a purity of more than 99%) and characterized by the powder X-ray diffraction to ensure purity. Deionized water was the chosen solvent in all experiments.

3.2.2 Seeds Preparation

Seeds of the α form were prepared through fast cooling of aqueous L-glutamic acid solution in batch. A clear solution of L-glutamic acid (0.04 kg/kg) at 80°C was made in a 150ml batch crystallizer with a Teflon-coated magnetic stirrer and was then cooled to room temperature rapidly by refrigerated circulator (Julabo F32). The whole batch operation time was 1.5 hours. The product slurry was filtered and dried in an oven at 50°C under vacuum for two hours. The seeds were then sieved in the range of 50 μ m to 150 μ m using Gilson Gil Sonic Auto Siever (GA-6). Particles were separated using both horizontal and vertical tapping with a maximum amplitude set at 20, and an amplitude increasing time (Time A) of 3 minutes. Then, the sieving ran under maximum amplitude for 5 minutes (Time B), and finally, the amplitude decreased to zero in 2 minutes (Time C). β form seeds in the range of 45 μ m to 90 μ m were prepared by GA-6 auto-siever following the same operating procedure. The seed amount is calculated as the percentage of the maximum theoretical yield achieved in a batch crystallizer with the same initial and final temperatures.

3.2.3 Polymorph Characterization

The commercial β form L-glutamic acid and the obtained products from experiments were checked by the powder X-ray diffraction (Rigaku, Miniflex) with the Cu-K α source (λ for K α = 1.54059 Å). Conditions of voltage (30 kV), current (15 mA), scan angle (5° to 40°), and scan speed (2°/min) were used for all samples. The PXRD patterns of both LGA metastable form and stable form are shown in [Figure 3-2](#). α -form LGA owns characteristic peaks at 15.2°, 16.1° and 18.2° and β -form LGA owns characteristic peaks at 10.2°, 13.6° and 17.8°.

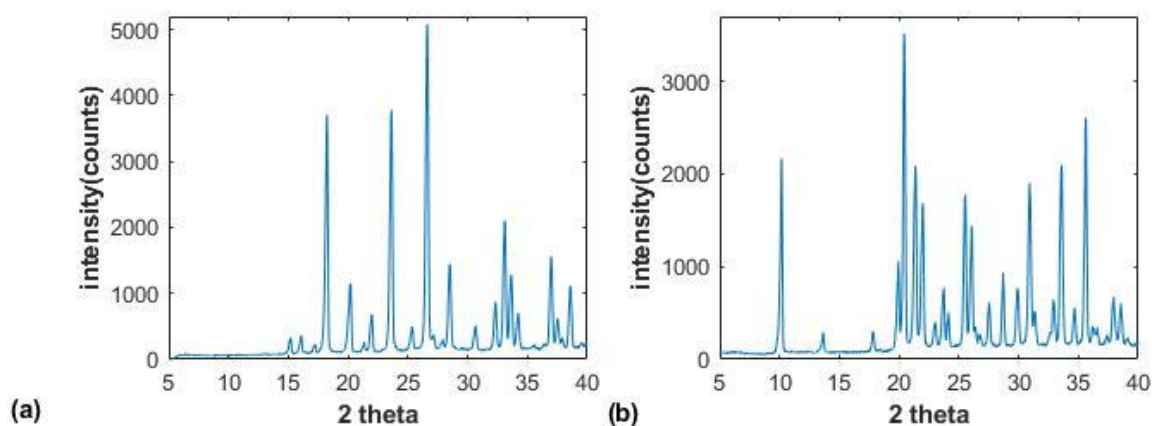


Figure 3-2. Powder X-ray diffraction Patterns of the LGA metastable α -form (a) and the LGA stable β -form (b)

3.2.4 Experimental Setup

Multiple MSMPR experiments under different conditions were conducted. Single-stage MSMPR experiments under high temperature were first carried out to see whether the stable β -form can be produced in the MSMPR. Based on the result, two-stage MSMPR experiments at different temperatures were carried out. Finally, the intermittent seeding strategy was implemented in a single stage MSMPR at low temperature.

3.2.5 Single-Stage MSMPR

The single-stage MSMPR scheme is shown in [Figure 3-3\(a\)](#). The mother liquor concentration was kept at 0.04 kg/kg in the feed tank with a mechanical stirring (5.0Hz) and was kept at 80°C using a water bath. The saturated mother liquor was sent to the MSMPR crystallizer by a peristaltic pump with thermal insulation covering the tube. The working volume in the glass-jacketed crystallizer (YPJ, China) was set to be 150ml and was controlled by the position of the outlet port. The outlet of the MSMPR was pumped intermittently through a peristaltic pump, removing 10% of the slurry at every one-tenth of the residence time, to avoid the potential blockage in the transfer tube.

Different MSMPR operating conditions are tabulated in [Table 3-1 \(Trial 1 to 5\)](#). For experiments 1, 2, 4 and 5, the initial solution in the crystallizer was saturated at 50°C or 45°C and was seeded with pure β crystals (60wt%, 45 μ m to 90 μ m). As the working volume was fixed (150ml), the residence time (30min or 60min) was determined by the feed flow rate (5ml/min or 2.5ml/min), which was controlled through a microcontroller connected to the wireless network. An S-function block in MATLAB/Simulink was used to send the control command to the microcontroller to realize the remote control. The slurry was withdrawn through a side port using an intermittent pump. Every 3 minutes or 6 minutes (one-tenth of the residence time), 15ml of the slurry in the crystallizer was pumped out (discharge time was 5.5seconds). For trial 3, a small amount of α seeds (16wt%) was introduced as a disturbance after a 4-hour MSMPR operation (steady state). Trial 0 was designed to verify the outcome under 25°C. Different feed concentrations were tested to see whether the polymorphic outcome could be affected or not. The total counts inside the crystallizer were monitored using an in-situ process analytical technology (PAT), namely, focused beam reflectance measurement (FBRM) (S400, Mettler Toledo) to demonstrate achieving the steady state. The collected products were characterized by the PXRD to determine the polymorph.

3.2.6 Two-Stage MSMPR (Continuous Seeding)

Based on the validation of the single-stage MSMPR results, continuous seeding strategy was realized through a two-stage MSMPR design. The experimental setup is shown in [Figure 3-3\(b\)](#). The first stage was designed similar to the 50°C single-stage MSMPR. The intermittent outlet of the first stage was fed to the second stage as seed supply. The working temperature of the second stage was set at a β -form unfavored condition (35°C, 30°C, 25°C). Lower working temperature resulted in higher yield and suspension density in the solution. Using the same intermittent withdrawal, flow rate from the second stage prevented the blockage. Detailed working conditions are shown in [Table 1 \(Trial 6 to 9\)](#). Low initial seed loading was found to generate α -form LGA in the second stage during start-up, so a seed loading of 60wt% was taken.

3.2.7 Intermittent Seeding in single-stage MSMPR

It is predicted that applying intermittent seeding will have the same effect as continuous seeding in promoting the secondary nucleation of the seeded form at low operating temperature. The intermittent seeding was realized manually. Every one-fifth of the residence time (12min), 0.1g of the sieved β seeds (45 μ m to 90 μ m) were added to the MSMPR crystallizer (150ml). The inlet concentration and the seeding frequency were previously determined based on the kinetic simulation results, which would be explained in the following section. The rest of the operational procedure was the same as in the single-stage MSMPR experiments, but at a lower operating temperature (30°C). The operating conditions during the intermittent seeding experiments are tabulated in [Table 3-1 \(Trial 10, 11\)](#). For trial 10, the feed concentration was decreased to 0.02 kg/kg based on our simulation results, as with a high feed concentration, pure β -form products cannot be obtained.

Table 3-1. Operating conditions of the multiple MSMPR experiments

| Variable | Trial 0 | Trial 1 | Trial 2 | Trial 3 | Trial 4 | Trial 5 |
|--------------------------------|------------------------|------------------------|------------------------|-------------------------|------------------------|------------------------|
| Inlet Concentration (kg/kg) | 0.02;0.04 | 0.04 | 0.04 | 0.04 | 0.04 | 0.04 |
| Inlet Temperature (°C) | 80 | 80 | 80 | 80 | 80 | 80 |
| MSMPR Working Temperature (°C) | 25 | 45 | 45 | 45 | 50 | 50 |
| Inlet Flow rate (ml/min) | 5 | 5 | 2.5 | 5 | 5 | 2.5 |
| Residence Time (min) | 60 | 30 | 60 | 30 | 30 | 60 |
| Seeding conditions | β seeds (60% wt) | β seeds (60% wt) | β seeds (60% wt) | β seeds (60% wt) | β seeds (60% wt) | β seeds (60% wt) |
| Disturbance after steady state | / | / | / | α seeds (16% wt) | / | / |

| Variable | Trial 6 | Trial 7 | Trial 8 | Trial 9 |
|--------------------------------|------------------------|------------------------|------------------------|------------------------|
| Inlet Concentration (kg/kg) | 0.04 | 0.04 | 0.04 | 0.04 |
| Inlet Temperature (°C) | 80 | 80 | 80 | 80 |
| 1st stage Working Temp (°C) | 50 | 50 | 50 | 50 |
| 2nd stage Working Temp | 35 | 30 | 25 | 35 |
| Stream Flow rate (ml/min) | 2.5 | 2.5 | 2.5 | 5.0 |
| 1st stage Residence Time (min) | 60 | 60 | 60 | 30 |
| 2nd stage Residence Time (min) | 60 | 60 | 60 | 30 |
| 1st stage Seeding condition | β seeds (60% wt) | β seeds (60% wt) | β seeds (60% wt) | β seeds (60% wt) |

| Variable | Trial 10 | Trial 11 |
|----------|----------|----------|
|----------|----------|----------|

| | | |
|--------------------------------|-----------------|------------------|
| Inlet Concentration (kg/kg) | 0.02 | 0.04 |
| Inlet Temperature (°C) | 80 | 60 |
| Working Temp (°C) | 30 | 30 |
| Inlet Flow rate (ml/min) | 2.5 | 2.5 |
| Residence Time (min) | 60 | 60 |
| Initial Seeding condition | β seeds (60%wt) | β seeds (60%wt) |
| Intermittent Seeding frequency | 5 Times/*RT | 5 Times/*RT |
| Intermittent Seed weight | β seeds (2%wt) | β seeds (5.6%wt) |

*RT is residence time

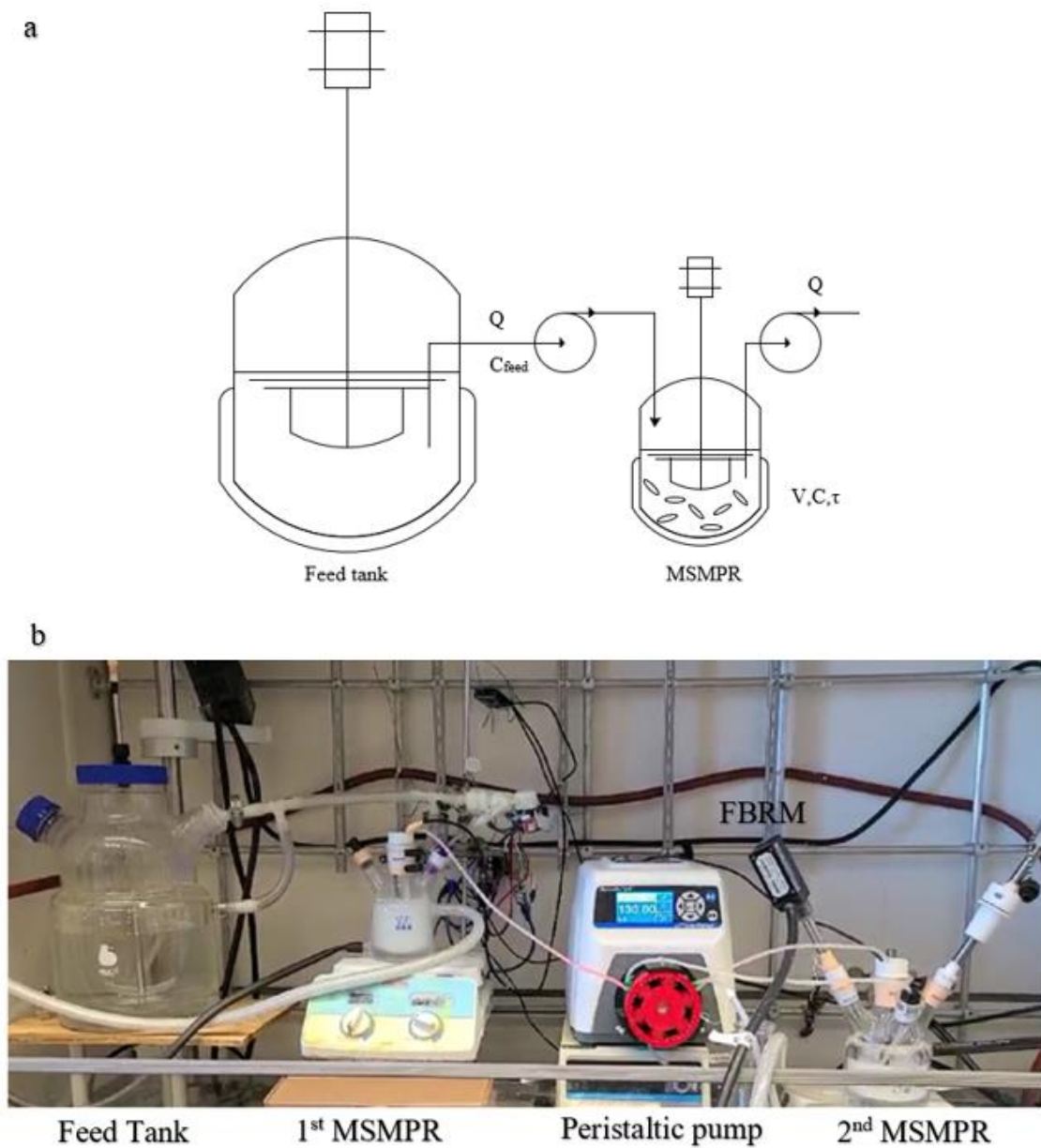


Figure 3-3. Schematics of a single-stage MSMPR (a) and laboratory scale two-stage MSMPR (b)

3.3 Dynamic Simulation

The dynamic mathematical model of L-glutamic acid polymorphic system, consisting of population balance equations (PBEs) and a material balance for the concentration of LGA

in the solution, has been well developed to describe the crystallization process in the batch and MSMPR crystallization (Cornel et al., 2009; Hermanto et al., 2009; Köllges & Vetter, 2019; Lai et al., 2014; Lin et al., 2020; Schöll et al., 2006; Sheikholeslamzadeh & Rohani, 2013). The one-dimensional population balance and material balance in a single-stage MSMPR can be written as

$$\frac{\partial n_i(t, L)}{\partial t} + \frac{\partial [G_i(t, L)n_i(t, L)]}{\partial L} = \frac{Q[(n_{i,feed}(t, L) - n_i(t, L))]}{V} \quad (3 - 1)$$

$$\frac{dC(t)}{dt} = \frac{C_{feed} - C(t)}{\tau} - 3 \sum_i \rho_{c,i} k_{v,i} \int_0^{\infty} G_i(t, L) L^2 n_i(t, L) dL \quad (3 - 2)$$

with the boundary condition

$$n_i(t, 0) = \frac{B_i(t, 0)}{G_i(t, 0)} \quad (3 - 3)$$

where $n_i(t, L)$ refers to the number density [#m/kg solvent] of polymorph i at time t [s] in the crystallizer, $n_{i,feed}(t, L)$ refers to the number density in the feed stream [#m/kg solvent], L is the crystal size [m], $\tau = V/Q$ is the residence time [s] of the MSMPR crystallizer, Q is the volumetric flow rate [m³/s], V is the working volume [m³], G_i and B_i are the nucleation rate [#s/kg solvent] and the growth rate of polymorph i [m/s], $C(t)$ is the solute concentration [kg solute/kg solvent], C_{feed} is the inlet solute concentration [kg solute/kg solvent], $\rho_{c,i}$ is the crystal density [kg/m³] of polymorph i and $k_{v,i}$ is the crystal volumetric shape factor [m³/m³].

The following empirical expressions of the nucleation, growth and dissolution rates were used to solve PBEs and the material balance (Hermanto et al., 2009).

$$G_{\alpha} = k_{g\alpha 0} \exp \left[-\frac{E_{\alpha}}{R(T + 273.15)} \right] (S_{\alpha} - 1)^{g_{\alpha}} \quad (3 - 4)$$

$$G_{\beta} = k_{g\beta 0} \exp \left[-\frac{E_{\beta}}{R(T + 273.15)} \right] (S_{\beta} - 1)^{g_{\beta 1}} \exp \left(-\frac{g_{\beta 2}}{S_{\beta} - 1} \right) \quad (3 - 5)$$

$$B_{\alpha} = k_{b\alpha}(S_{\alpha} - 1)\mu_{\alpha,3} \quad (3 - 6)$$

$$B_{\beta} = k_{b\beta 1}(S_{\beta} - 1)\mu_{\alpha,3} + k_{b\beta 2}(S_{\beta} - 1)\mu_{\beta,3} \quad (3 - 7)$$

$$D_{\alpha} = k_{d\alpha}(S_{\alpha} - 1)^{g_{\alpha}} \quad (3 - 8)$$

where T is the operating temperature ($^{\circ}\text{C}$), R is the gas constant [J/K/mol], $k_{g\alpha 0}$, $k_{g\beta 0}$ are growth rate constants [m/s], $k_{d\alpha}$ is the dissolution constant [m/s], $k_{b\alpha}$ and $k_{b\beta 2}$ are secondary nucleation constants [#s/m³ crystal] and $k_{b\beta 1}$ is the constant for the cross-nucleation of β -form [#s/m³ crystal], $g_{\beta 1}$, g_{α} are the exponents, $g_{\beta 2}$ is a dimensionless number to improve the accuracy of the equation, E_{α} and E_{β} are active energies [J] required for growth, and $\mu_{i,3}$ is the third moment of the crystal size distribution. Values of constant variables and parameters (Hermanto et al., 2009) used in the simulations are shown in the [Table 3-2](#). S_i is the supersaturation and is defined as below:

$$S_i = \frac{C(t)}{C_i^*} \quad (3 - 9)$$

where C_i^* is the solubility of polymorph i [kg solute/kg solvent]. The following solubility data of L-glutamic acid is applied in this paper (Hermanto et al., 2008).

$$C_{\alpha}^* = 8.437 \times 10^{-3}T^2 - 0.03032T + 4.564 \quad (3 - 10)$$

$$C_{\beta}^* = 7.644 \times 10^{-3}T^2 - 0.1165T + 6.622 \quad (3 - 11)$$

where T is the solution temperature ($^{\circ}\text{C}$).

Table 3-2. Crystal Properties and Kinetic Parameters used in the Simulation

| Variable | Value | unit |
|-----------------|-------|-------------------|
| Crystal Density | 1540 | kg/m ³ |

| | | |
|---------------------------------------|----------------------|-------------------|
| Solvent Density | 1000 | kg/m ³ |
| Volume-shape factor of α -form | 0.48 | - |
| Volume-shape factor of β -form | 0.031 | - |
| Activation Energy of α -form | 4.3088×10^4 | J/mol |
| Activation Energy of β -form | 1.7596×10^5 | J/mol |

| Parameter | value | unit |
|-----------------|-------------------------|-------------------|
| $k_{g\alpha 0}$ | 6.54 | m/s |
| $k_{g\beta 0}$ | 3.8387×10^{22} | m/s |
| $k_{b\alpha}$ | 3.0493×10^7 | m ³ /s |
| $k_{b\beta 1}$ | 7.2826×10^6 | m ³ /s |
| $k_{b\beta 2}$ | 4.8517×10^8 | m ³ /s |
| $k_{d\alpha}$ | 3.5006×10^{-5} | m/s |
| g_α | 1,859 | - |
| $g_{\beta 1}$ | 1.047 | - |
| $g_{\beta 2}$ | 0.778 | - |

For the two-stage MSMPR and the single-stage MSMPR with intermittent seeding, population balance equations and material balance equations are as shown below.

For the two-stage MSMPR

$$\frac{\partial n_{k,i}(t,L)}{\partial t} + \frac{\partial [G_i(t,L)n_{k,i}(t,L)]}{\partial L} = \frac{[(n_{k-1,i}(t,L) - n_{k,i}(t,L))]}{\tau_k}; k > 1 \quad (3-12)$$

where k is the stage number and is larger than 1, for k equals to 1, the equation is the same as Eq. (3-1). The material balance equation is always the same as Eq. (3-2) with different residence time τ_k in the k th stage.

For the single-stage MSMPR with intermittent seeding

$$\frac{\partial n_i(t, L)}{\partial t} + \frac{\partial [G_i(t, L)n_i(t, L)]}{\partial L} = \frac{[(n_{i,feed}(t, L) - n_i(t, L))]}{\tau} + \frac{n_{seed}}{\tau} \text{III}_{\frac{\tau}{f}}(t) \quad (3-13)$$

$$\frac{dC(t)}{dt} = \frac{C_{feed} - C(t)}{\tau} + \frac{C_{seed}}{\tau} \text{III}_{\frac{\tau}{f}}(t) - 3 \sum_i \rho_{c,i} k_{v,i} \int_0^{\infty} G_i(t, L) L^2 n_i(t, L) dL \quad (3-14)$$

$$\text{III}_T(t) \triangleq \sum_{k=-\infty}^{\infty} \delta(t - kT) \quad (3-15)$$

addition of seeds is considered to follow an impulse function in the concentration and crystal population at every $\frac{\tau}{f}$, where f is the seeding frequency [times/RT]. The impulse is indicated as a Dirac comb function, $\text{III}_{\frac{\tau}{f}}(t)$, in the balance equations.

Method of moments was applied to solve the above PBEs in this study. The j th moment of the CSD of polymorph i is defined as

$$\mu_{j,i} = \int_0^{\infty} L^j n_i(t, L) dL \quad (3-16)$$

By applying the method of moments, the PBEs can be written as:

$$\frac{d\mu_{0,i}}{dt} = -\frac{1}{\tau} \mu_{0,i} + B_i \quad (3-17)$$

$$\frac{d\mu_{j,i}}{dt} = -\frac{1}{\tau} \mu_{j,i} + j(G_i - D_i) \mu_{j-i,i} \quad (3-18)$$

Thus, all partial differential equations (PDEs) are converted to ordinary differential equations (ODEs) and are solved by Matlab ODE45.

3.4 Result and Discussion

3.4.1 Single-Stage MSMPR Crystallization

Single-stage MSMPR experiments were conducted under the conditions specified in [Table 3-1](#). The purpose of the single-stage MSMPR operation was to ascertain the temperature effect and the residence time effect on the polymorphic outcome. The crystallization in the MSMPR is a sudden change in the phase diagram, the SMPT is not going to happen. Thus, at a low working temperature, α -form LGA will always be obtained as the final product. This was confirmed from the simulation results. The residence time of the simulated MSMPR was set to be 60 minutes. As shown in [Figure 3-4\(a\)](#) and [3-4\(b\)](#), even with a 100:1 wt% ratio of the amount of initial seeds, β seeds were washed out during the startup, and α crystals were the only product at steady state at 25°C, irrespective of the feed concentration. Experiments under 25°C (Trial 0) also verified this result. Experiments at working temperatures of 45°C and 50°C with different residence times confirmed that β -form LGA was always the obtained polymorph at steady state. In the simulation, as displayed in [Figure 3-4\(c\)](#) and [3-4\(d\)](#), at 45°C or higher working temperature, with the same amount α and β seeds, β -form LGA will always be achieved at steady state. The residence time will affect the start-up process and the final yield. The simulation and experimental results in a single-stage MSMPR are depicted in [Table 3-3](#). The polymorphic outcomes from simulation and experiment matched perfectly. Nevertheless, yields, the production rate, calculated from all experiments were lower than those from simulation. Several reasons are considered to explain this observation. β -form LGA products from experiments were first filtered from the outlet slurry and were dried in the oven under vacuum. Dried crystals were then weighed to calculate the yield and the production rate.

$$Yield_i = \frac{C_{feed} - C(t)}{C_{feed} - C_i^*(T)} \times 100\% = \frac{M_{Ti}}{C_{feed} - C_i^*(T)} \times 100\% \quad (3 - 19)$$

$$Production\ rate = \frac{M_T \times V_{crystallizer} \times \rho_{solvent}}{\tau} \quad (3 - 20)$$

where M_{Ti} is the suspension density of polymorph i [kg /kg solvent]. During this process, crystals could be lost either due to pipe transportation or due to the filtration. The withdrawn sample slurry was filtrated by the buchner funnel, some small crystals on the filter paper were not able to be collected. Crystallization happened on the crystallizer wall was also an important reason for introducing error. With the level change caused by the intermittent side withdraw, some of the crystals on the wall could not be well mixed in the solution, resulting in the decrease in the suspension density in the product slurry. Furthermore, it was found that the intermittent side withdrawal didn't work very accurately. This was caused by the peristaltic pump inevitably. With operating time increased, the withdrawn volume would oscillate near the settled volume. As the calculation was based on one-tenth of the volume per withdrawn, error would be introduced. Another important reason is that our simulation relies on empirical equations developed by Hermanto (Hermanto et al., 2009). In his model, linear dependencies on supersaturation and third moments of α and β crystals in the birth rates are assumed which may not describe the MSMPR system accurately, resulting in an error between experiment and simulation exists at the beginning.

Comparing results of Trial 1,2,4,5, it was easily found that under the same working temperature, 60-minutes RT should have a higher yield (%). However, production rates with 30-minutes RT were much compared to those with 60-minutes RT (0.063 to 0.033 g/min compared to 0.050 to 0.027 g/min) as the flowrate with 30-minutes RT was doubled. Comparing the experimental results to simulation results, it was concluded that with the same feed concentration, lower temperatures and longer residence times resulted in a higher yield, which confirms the general trends expected in MSMPR crystallization. No yield analysis was held in trial 3 (45°C and 30min RT). Trial 3 was used to determine whether the production of β crystals at 45°C or higher would achieve a real steady state.

A disturbance in the form of α -form LGA (16wt%) was introduced into the crystallizer once the process reached the steady state. After two and a half hours (5RT), the second steady state was monitored through FBRM. Products were filtered and pure β -form LGA was confirmed through PXRD. Thus, it was verified that at a high operating temperature (45°C or higher), β -form was obtained at steady state.

The simulation and experimental results in single stage MSMPR were compared to previous studies on the LGA-water system (Hermanto et al., 2009; Köllges & Vetter, 2019; Lai et al., 2014). Kinetics developed by Hermanto et al. (Hermanto et al., 2009) were used to conduct the modeling study as the kinetic models they reported covered the temperature range (both are 25°C to 50°C) encountered in this research. The main difference is that the kinetics developed by Hermanto et al. was for batch crystallization, not an MSMPR crystallization. However, the reliability of applying Hermanto's kinetic model in a continuous MSMPR crystallization was proven by Vetter et al. (Köllges & Vetter, 2019). Vetter's et al. successfully applied Hermanto's kinetic model to predict the MSMPR crystallization with and without a milling process qualitatively. Both our simulation and experimental results are in agreement with these studies. Lai et al. (Lai et al., 2014) discovered that under 25°C, only α -form LGA was obtained at steady state with the 0.0224 kg/kg solution concentration for a 60-minutes residence time and only β -form LGA was obtained at steady state with the 0.0353 kg/kg solution concentration under 45°C. The polymorphic outcomes they observed agree with our simulation results and experimental results, while the solution concentrations are higher than ours. Vetter et al. (Köllges & Vetter, 2019) also used Hermanto's model to simulate their continuous MSMPR crystallization processes with and without a milling process. As milling process was not taken in this research, only the single-stage MSMPR simulation under 25°C with the feed concentration of 0.02 kg/kg was compared. It could be found that our simulation result [Figure 3-4(b)] is with the same trend as theirs and both these two simulations get steady at the solution concentration near 0.015 kg/kg with pure α -form LGA crystals.

Table 3-3. Simulation and experimental results in the single-stage MSMPR

| Variable | Trial 0 | Trial 1 | Trial 2 | Trial 3 | Trial 4 | Trial 5 |
|--------------------------------------|---------------|--------------|--------------|--------------|--------------|--------------|
| Working Temp (°C) | 25 | 45 | 45 | 45 | 50 | 50 |
| Residence Time (min) | 60 | 30 | 60 | 30 | 30 | 60 |
| Product Polymorph | pure α | pure β | pure β | pure β | pure β | pure β |
| Simulated Yield | 38.67%;77.14% | 67.02% | 75.10% | - | 67.08% | 73.99% |
| Experimental Yield | 29.39%;63.93% | 54.50% | 57.40% | - | 48.90% | 53.66% |
| Simulated Production Rate (g/min) | 0.012;0.062 | 0.078 | 0.044 | - | 0.068 | 0.037 |
| Experimental Production Rate (g/min) | 0.007;0.047 | 0.063 | 0.033 | - | 0.050 | 0.027 |

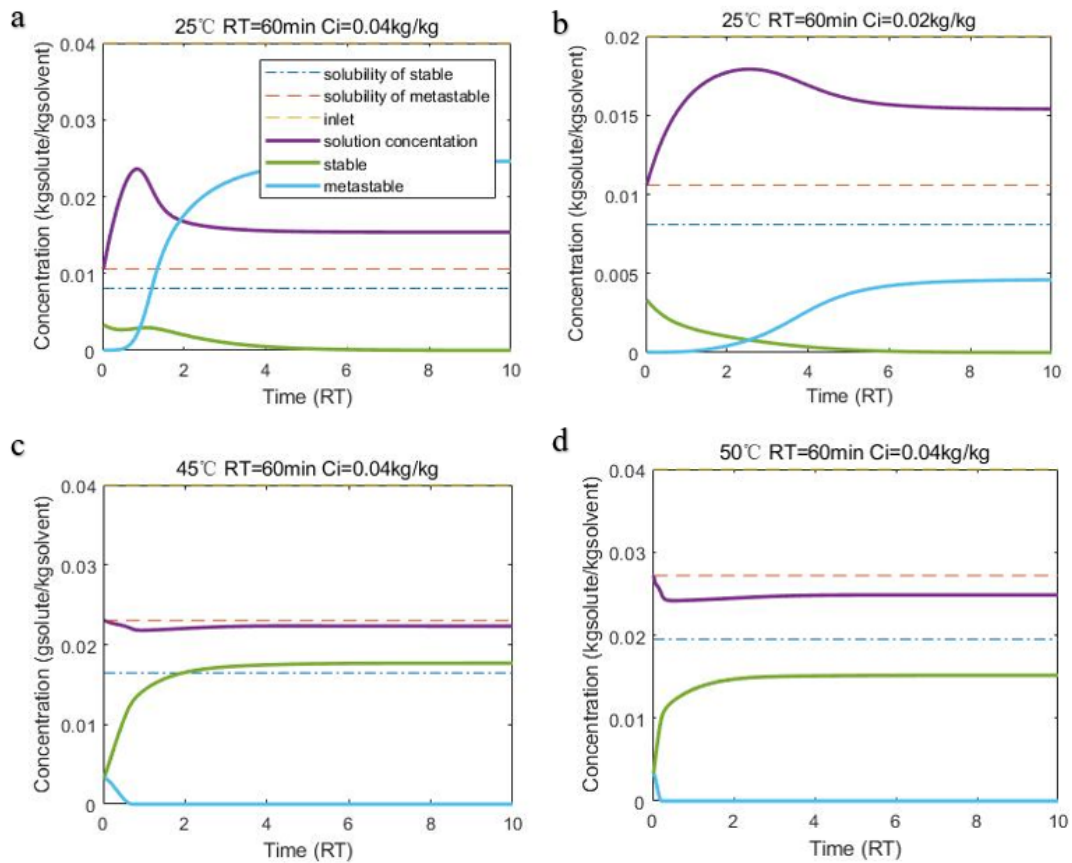


Figure 3-4. Single-stage MSMPR dynamic simulation results at T=25°C, Ci= 0.04 kg/kg (a), T=25°C, 0.02 kg/kg (b), T= 45°C, Ci= 0.04 kg/kg (c) and T=50°C, Ci= 0.04 kg/kg (d)

3.4.2 Two-stage MSMPR crystallization

With the temperature effect on the polymorphic outcome, a two-stage MSMPR was herein tried to realize the β -form production at low working temperature in the second stage and increase the yield. To ensure the purity of the produced β -form LGA, the slurry in the first stage working at 50°C, was pumped to a second MSMPR as the feed. The working temperature of the second stage varied from 35°C to 25°C and the residence time was also changed to see its impact. It was hypothesized that increasing the total surface area of the β crystals can improve the secondary nucleation rate and the mass deposition rate of the β crystals as Lai et al. (Lai et al., 2015) has also observed in the *p*-aminobenzoic acid-water system.

Simulated and experimental results of the two-stage MSMPR are summarized in [Table 3-4](#). It is confirmed by simulation and experiments that applying continuous seeding strategy could change the polymorphic outcome of LGA from the second stage working at low MSMPR temperature. Only pure β -form LGA was obtained as the product. Therefore, continuous seeding was confirmed to be an effective strategy to change the polymorphic outcome in MSMPR. Several interesting facts were also discovered. It was predicted that the startup duration for the two-stage MSMPR operation would be long. Four to six residence time was taken for the process to reach the steady state. Based on simulation, it could be found that as the working temperature in the first MSMPR crystallizer was fixed, the startup duration was predominantly determined by the second stage working temperature. Since a lower temperature in the second stage would result in a higher supersaturation, it would take a longer time for the system to reach steady state (from 4RT to 5.5RT). An unexpected result was the difference in the final stage production rate and yield. Usually, the higher the supersaturation it is, the more final crystals should be achieved. However, based on our simulation, the opposite result was obtained. Using the same residence time (60 min), the simulated production rate was

lowest at 25°C (0.052g/min), compared to 30°C (0.056g/min) and 35°C (0.056g/min). This was caused by the decrease of the β -form growth rate as shown in [Figure 3-5](#). As crystallization was determined by the competition between the nucleation and growth rates, even though the nucleation rate was higher due to the increased supersaturation at lower temperature, the decrease of the growth rate influenced the process more which resulted in the lower production rate. Our experimental result showed the opposite trend on the production rate of β -form of LGA. The experimental production rate increased from 0.040 g/min (at 35°C) to 0.044 g/min (at 25°C). Factors that might cause discrepancies between the simulation and experimental results were analyzed in the previous section. One confirmed phenomenon from both simulation and experiment was that decreasing the second stage working temperature didn't improve the production rate significantly. With the same residence time, the production rate was close in the simulation and experimental results (0.056g/min to 0.052g/min compared to 0.040g/min to 0.044g/min). During the simulation of the continuous seeding strategy, the secondary nucleation of β -form LGA jeopardizes the growth rate. It is important to note the increase of the production rate after applying the continuous seeding. Comparing the production rates from the two-stage MSMPR to the single-stage MSMPR (trial 2 & 8, trial 1 & 9), a significant improvement in the production rate was observed (0.033g/min compared to 0.044g/min, and 0.063g/min compared to 0.073g/min). Then, comparing trial 6 and trial 9, the impact of residence time was also reflected. Under the same operating temperature, increasing the residence time can increase the yield (51.60% to 56.14%).

Table 3-4. Simulation and experimental results in two-stage MSMPR

| Variable | Trial 6 | Trial 7 | Trial 8 | Trial 9 |
|--------------------------------|---------|---------|---------|---------|
| 1st stage Working Temp (°C) | 50 | 50 | 50 | 50 |
| 2nd stage Working Temp | 35 | 30 | 25 | 35 |
| 1st stage Residence Time (min) | 60 | 60 | 60 | 30 |

| | | | | |
|--------------------------------------|--------------|--------------|--------------|--------------|
| 2nd stage Residence Time (min) | 60 | 60 | 60 | 30 |
| Product Polymorph | pure β | pure β | pure β | pure β |
| Simulated Final Product yield | 79.34% | 74.01% | 64.71% | 70.82% |
| Experimental Final Product yield | 56.14% | 53.30% | 56.40% | 51.60% |
| Simulated Production Rate (g/min) | 0.056 | 0.056 | 0.052 | 0.100 |
| Experimental Production Rate (g/min) | 0.040 | 0.041 | 0.044 | 0.073 |
| Simulated Start up Duration | 4RT | 5RT | 5.5RT | 4RT |
| Experimental Start up Duration | 4RT | 4.5RT | 7RT | 5RT |

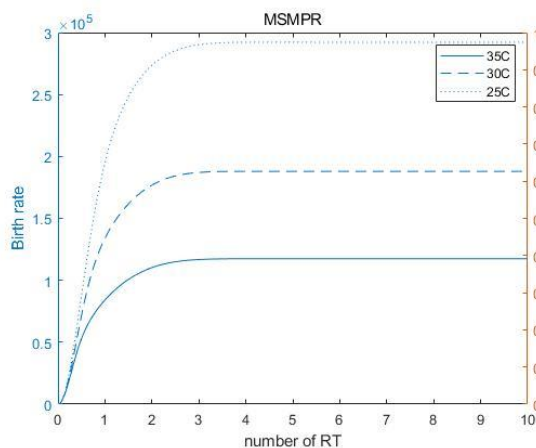
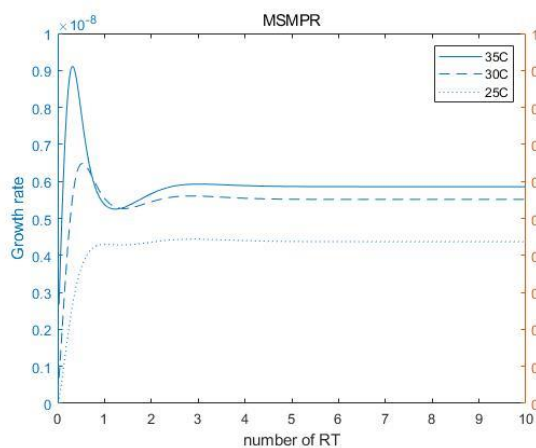


Figure 3-5. Growth rate (left) and Birth rate (right) variations in the second stage MSMMPR at different working temperature (RT = 60 min/stage)

3.4.3 Single-stage MSMMPR with intermittent seeding

It was expected that intermittent seeding of a single stage MSMMPR can also improve the secondary nucleation of β -form LGA. Seeding frequency was first researched by simulation. The feed concentration and residence time were kept at 0.04 kg/kg and 60 minutes, but the MSMMPR working temperature was decreased to 25°C (favoring the production of the α -form, and seeding mass was set as 0.5g per charge. The simulated results are depicted in [Figure 3-6\(a\)](#). It is clear that applying intermittent seeding successfully produces the β polymorph at 25°C in a single MSMMPR crystallizer. The fluctuation is caused by the introduction of seeds. Also, the β -form mass fraction in the product increases with the seeding frequency. Nevertheless, in the simulation at 25°C, even when the seeding frequency was increased to 10 times/RT, β polymorph purity did not increase beyond 90.6%. The high supersaturation was thought to be the reason behind it promoting the metastable form. As we illustrated in the previous section, the lower the working temperature, the harder it was to harvest β crystals. The supersaturation could be affected either by tuning the feed concentration or by changing the MSMMPR working temperature. Both methods were tried, and their effects are shown in [Figure 3-6\(b\)](#) and [3-6\(c\)](#). Seeding frequency was fixed at 5 times/RT, seed mass was 0.5g per charge and residence time was set at 60 minutes in both simulations. The simulation results verified that decreasing the supersaturation by either increasing the MSMMPR working temperature or decreasing the feed concentration can alter the final polymorphic outcome. The decrease of supersaturation also reduces the start-up duration of the process to reach the steady state.

In the 150ml MSMMPR, adding 0.5g of β seeds (approx. 30wt%) every time (per charge) was considered too much for the process. Our simulation was then run to find out the

minimum number of seed charges required in the single MSMPR operating at 30°C. The feed concentration was assumed to be 0.02 kg/kg and residence time was 60 minutes. The amount of seeds was decreased from 0.5g to 0.01g per charge. The simulation results are shown in [Figure 3-6\(d\)](#). When the seed weight was 0.01g per charge, the product was no longer pure β polymorph. Two experimental validations were carried out to test the accuracy of our simulation results under the working conditions shown in [Table 3-1](#). For these two trials, the intermittent seed weight was set at 0.1g per charge and the seeding frequency was 5 times/RT. Different feed concentration was adopted to see its impact on the polymorphic outcome. As depicted in [Table 3-5](#), pure β crystals were successfully obtained in a single MSMPR operating at 30°C with 0.02 kg/kg feed concentration. The production rate was close to the simulated result (0.016g/min compared to 0.019g/min). When the feed concentration increased to 0.04 kg/kg, the high supersaturation led to the birth of α crystals inevitably. This is consistent with the simulation results ([Figure 3-7](#)). The product purity was determined by PXRD using a similar method as Lai et al. (Lai et al., 2014) There was a large difference between the experimental product purity and simulated product purity (β -form weight percent: 22.1wt% versus 70%). In addition to the discussion mentioned in the previous sections regarding the discrepancies between the simulation and experimental results, it is also important to note that kinetic equations developed by Hermanto et al. (Hermanto et al., 2009) provide accurate qualitative trends for the polymorphic outcome, but are less reliable for a quantitative analysis.

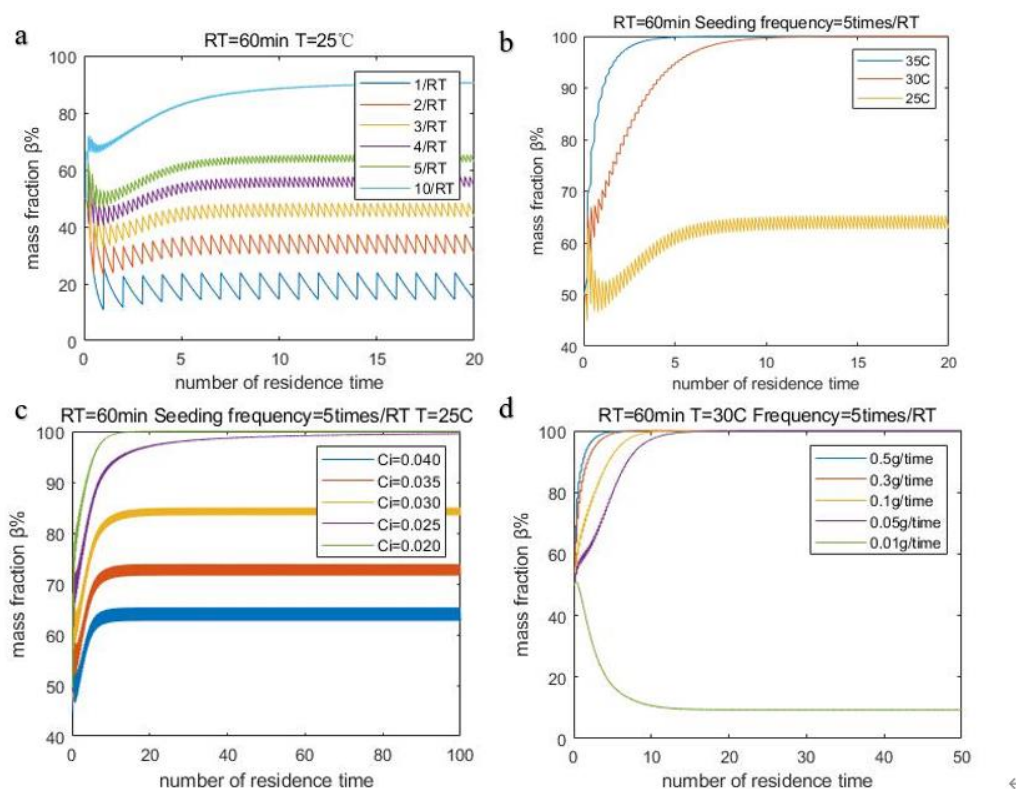


Figure 3-6. Evolution of the mass fraction of β -form LGA with different seeding frequencies (a), working temperatures (b), feed concentrations (c), seed weight (d)

Table 3-5. Simulation and experimental results for intermittent seeding

| Variable | Trial 10 | Trial 11 |
|--------------------------------------|--------------|------------------|
| Feed Concentration (kg/kg) | 0.02 | 0.04 |
| Working Temp. ($^{\circ}\text{C}$) | 30 | 30 |
| Residence Time (min) | 60 | 60 |
| Intermittent Seeding frequency | 5 Times/RT | 5 Times/RT |
| Intermittent Seed weight per charge | 0.1g | 0.1g |
| Product Polymorph | pure β | 22.1 wt% β |
| Simulated Production Rate (g/min) | 0.019 | - |
| Experimental Production rate (g/min) | 0.016 | - |

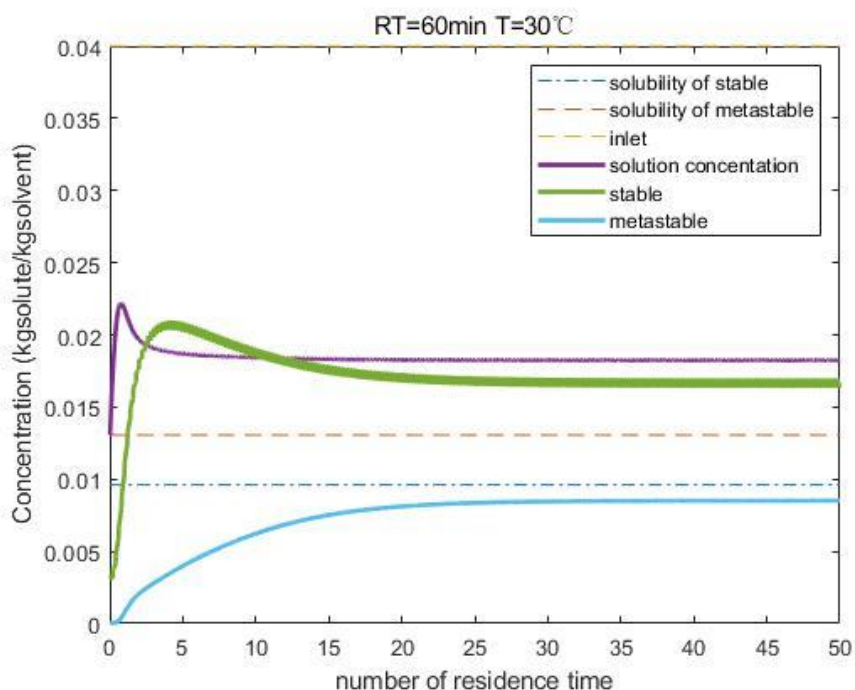


Figure 3-7. Simulation results of a single-stage MSMPR at 30°C with intermittent seeding

3.5 Conclusions

In this work, the impact of different seeding strategies on the polymorphic outcome and product yield of L-glutamic acid in MSMPR crystallization was studied. The polymorphic outcome of LGA in a two-stage MSMPR and a single stage MSMPR with intermittent seeding was first investigated. Then, the effects of both continuous and intermittent seeding strategies were studied by numerical simulation and experimental validation. A two-stage MSMPR design working at different temperatures was applied to realize the continuous seeding of the second stage with the effluent from the first stage. With the same feed concentration and residence time, switching from a single-stage MSMPR to a two-stage MSMPR, resulted in a significant improvement in the production rate (0.033g/min to 0.044g/min at 60-minutes residence time, 0.063g/min to 0.073g/min at 30-minutes residence time). Nevertheless, decreasing the second stage temperature did

not improve the yield (the experimental yields were 56.1%, 53.3%, and 56.4% under 35°C, 30°C, and 25°C). On the contrary, the production rate decreased due to a decrease of the β -form growth rate in the simulation results. The production rate was improved subtly in experiments as the working temperature decreased (0.040g/min at T=35°C to 0.044g/min at T=45°C). An increase in the residence time can improve the yield significantly as expected. The application of intermittent seeding was realized manually. It was found that supersaturation played a decisive role in harvesting the pure β -form LGA while operating at a temperature that was kinetically unfavorable. Under low operating temperature, β -form LGA owns slow kinetics which makes it hard to obtain from MSMPR. Suitable feed concentration and working temperature must be properly selected based on the crystallization kinetics. An operating temperature of 30°C in a 150ml MSMPR crystallizer, with 5times/RT seeding frequency with 0.1g per charge, and a feed concentration of 0.02 kg/kg were considered as the most suitable conditions to produce pure β -form L-glutamic acid. It is also important to notice that Hermanto's model can predict the polymorphic outcomes in MSMPR crystallization under 25°C to 50°C, but a well-tuned kinetic model is required for the prediction on the yield and crystal size. The results of the present investigation provide guidelines to harvest the desirable polymorph of an active pharmaceutical and maximize its yield and purity for the operation of a single MSMPR, a two-stage MSMPR, intermittent seeding of a single stage MSMPR. These results also extrapolate to the operation of a single MSMPR with partial solids recycling.

3.6 References

- (1) Beckmann, W. (2000). Seeding the Desired Polymorph: Background, Possibilities, Limitations, and Case Studies. *Organic Process Research & Development*, 4(5), 372–383. <https://doi.org/10.1021/op0000778>
- (2) Brittain, H. G. (n.d.). *Polymorphism in Pharmaceutical Solids*. 654.
- (3) Cornel, J., Lindenberg, C., & Mazzotti, M. (2009). Experimental Characterization and Population Balance Modeling of the Polymorph Transformation of L-Glutamic Acid. *Crystal Growth & Design*, 9(1), 243–252. <https://doi.org/10.1021/cg800387a>

- (4) Hermanto, M. W., Chiu, M.-S., & Braatz, R. D. (2009). Nonlinear model predictive control for the polymorphic transformation of L-glutamic acid crystals. *AIChE Journal*, 55(10), 2631–2645. <https://doi.org/10.1002/aic.11879>
- (5) Hermanto, M. W., Kee, N. C., Tan, R. B. H., Chiu, M.-S., & Braatz, R. D. (2008). Robust Bayesian estimation of kinetics for the polymorphic transformation of L-glutamic acid crystals. *AIChE Journal*, 54(12), 3248–3259. <https://doi.org/10.1002/aic.11623>
- (6) Kee, N. C. S., Tan, R. B. H., & Braatz, R. D. (2009). Selective Crystallization of the Metastable α -Form of L-Glutamic Acid using Concentration Feedback Control. *Crystal Growth & Design*, 9(7), 3044–3051. <https://doi.org/10.1021/cg800546u>
- (7) Köllges, T., & Vetter, T. (2019). Polymorph Selection and Process Intensification in a Continuous Crystallization–Milling Process: A Case Study on L-Glutamic Acid Crystallized from Water. *Organic Process Research & Development*, 23(3), 361–374. <https://doi.org/10.1021/acs.oprd.8b00420>
- (8) Lai, T.-T. C., Cornevin, J., Ferguson, S., Li, N., Trout, B. L., & Myerson, A. S. (2015). Control of Polymorphism in Continuous Crystallization via Mixed Suspension Mixed Product Removal Systems Cascade Design. *Crystal Growth & Design*, 15(7), 3374–3382. <https://doi.org/10.1021/acs.cgd.5b00466>
- (9) Lai, T.-T. C., Ferguson, S., Palmer, L., Trout, B. L., & Myerson, A. S. (2014). Continuous Crystallization and Polymorph Dynamics in the L-Glutamic Acid System. *Organic Process Research & Development*, 18(11), 1382–1390. <https://doi.org/10.1021/op500171n>
- (10) Lewis, A., Seckler, M., Kramer, H. J. M., & Rosmalen, G. van. (2015). *Industrial crystallization: Fundamentals and applications*. Cambridge University Press.
- (11) Li, J., Trout, B. L., & Myerson, A. S. (2016). Multistage Continuous Mixed-Suspension, Mixed-Product Removal (MSMPR) Crystallization with Solids Recycle. *Organic Process Research & Development*, 20(2), 510–516. <https://doi.org/10.1021/acs.oprd.5b00306>
- (12) Lin, M., Wu, Y., & Rohani, S. (2020). Identifying the Polymorphic Outcome of Hypothetical Polymorphs in Batch and Continuous Crystallizers by Numerical Simulation. *Crystal Growth & Design*, 20(11), 7312–7319. <https://doi.org/10.1021/acs.cgd.0c00986>
- (13) Myerson, A. S., Erdemir, D., & Lee, A. Y. (Eds.). (2019). *Handbook of Industrial Crystallization* (3rd ed.). Cambridge University Press. <https://doi.org/10.1017/9781139026949>

- (14) Nicoud, L., Licordari, F., & Myerson, A. S. (2019). Polymorph control in batch seeded crystallizers. A case study with paracetamol. *CrystEngComm*, 21(13), 2105–2118. <https://doi.org/10.1039/C8CE01428K>
- (15) Park, K., Kim, D. Y., & Yang, D. R. (2016). Operating Strategy for Continuous Multistage Mixed Suspension and Mixed Product Removal (MSMPR) Crystallization Processes Depending on Crystallization Kinetic Parameters. *Industrial & Engineering Chemistry Research*, 55(26), 7142–7153. <https://doi.org/10.1021/acs.iecr.6b01386>
- (16) Qamar, S. (2012). Seeding strategies and residence time characteristics of continuous preferential crystallization. *Chemical Engineering Science*, 13.
- (17) Schöll, J., Bonalumi, D., Vicum, L., Mazzotti, M., & Müller, M. (2006). In Situ Monitoring and Modeling of the Solvent-Mediated Polymorphic Transformation of l -Glutamic Acid. *Crystal Growth & Design*, 6(4), 881–891. <https://doi.org/10.1021/cg0503402>
- (18) Sheikholeslamzadeh, E., & Rohani, S. (2013). Modeling and Optimal Control of Solution Mediated Polymorphic Transformation of l -Glutamic Acid. *Industrial & Engineering Chemistry Research*, 52(7), 2633–2641. <https://doi.org/10.1021/ie302683u>

Chapter 4

Cocrystals, Salts, and Salt-Solvates of Olanzapine; Selection of Coformers and Improved Solubility

A version of this chapter has been published in *International Journal of Pharmaceutics*: Gong, W., Mondal, P. K., Ahmadi, S., Wu, Y., & Rohani, S. (2021). Cocrystals, salts, and salt-solvates of olanzapine; selection of coformers and improved solubility. *International Journal of Pharmaceutics*, 608, 121063.

4. Cocrystals, Salts, and Salt-Solvates of Olanzapine; Selection of Coformers and Improved Solubility

Abstract

Pharmaceutical cocrystals and salts are extensively researched in recent years due to their ability to tune the physicochemical properties of active pharmaceutical ingredients (APIs). A model API, olanzapine, an atypical antipsychotic drug classified as Biopharmaceutical Classification System class II, is used in this study. Cocrystals and salts of olanzapine are discovered using solvent drop grinding and ball milling. Appropriate coformers were selected based on a combination of hydrogen-bond propensity (HBP) and hydrogen-bond coordination (HBC) calculations. Eight new multicomponent phases of olanzapine, including one cocrystal hydrate with phenol; four anhydrous salts with salicylic acid, terephthalic acid, anthranilic acid, 3-hydroxybenzoic acid, and 2-aminoterephthalic acid; one salt dihydrate with terephthalic acid; and one salt solvate with 3-hydroxybenzoic acid and acetonitrile, have been discovered and characterized by PXRD and DSC. One reported cocrystal (olanzapine-resorcinol) has also been considered for the dissolution test. All these newly formed solid phases followed the “ ΔpK_a rule of 3”. The crystal structures of cocrystal/salts were determined by single-crystal X-ray (sc-XRD) diffraction. With the collected single-crystal data, the crystal packings were found to be primarily stabilized via strong hydrogen bonds between carboxyl, phenolic hydroxyl of co-formers/salt-formers with the piperazine and diazepine nitrogen of olanzapine, which confirmed the predicted result from the HBP and HBC calculations. HPLC coupled with UV-vis detector was used in the solubility and dissolution test instead of UV-vis spectroscopy, to avoid the peak overlap between olanzapine and co-formers/salt-formers. A threefold increase in the solubility was observed in olanzapinium 3-hydroxybenzoate and olanzapinium anthranilate, and an almost fivefold increase in solubility of olanzapinium 2-aminoterephthalate.

Keywords: Olanzapine, Salts, Cocrystals, Solvates, Crystal Engineering, Solubility Enhancement

4.1 Introduction

In recent years, the pharmaceutical industry has increasingly utilized the potential of crystal engineering to tune the performance of active pharmaceutical ingredients (APIs) (Duggirala et al., 2016). Crystal engineering can be applied to most crystalline APIs to improve their stability, solubility, dissolution, and bioavailability (Almarsson & Zaworotko, 2004; Blagden et al., 2007). Therefore, screening and selection of the potential solid states of an API is one of the most critical early stages of drug development. A suitable solid-state of an API offers convenience in formulation and therapeutic efficacy (Duggirala et al., 2016; Karimi-Jafari et al., 2018; Rodrigues et al., 2018). The various crystalline solids of APIs include polymorphs, solvates and hydrates, cocrystals, and salts. Compared to other solid-state forms, pharmaceutical cocrystals usually have well-defined stoichiometry, higher thermal and humidity stability (Dalpiaz et al., 2018; Duggirala et al., 2016; Huang et al., 2019; L. S. Reddy et al., 2009; Weyna et al., 2009), and can be designed with a large number of potential cocrystal formers (coformers). Therefore, pharmaceutical cocrystals have recently emerged as an important pharmaceutical solid form selection with a concurrent patent activity rise (Clarke et al., 2012). Nevertheless, only a few API cocrystal formulations are approved in the current market. Thus, salt preparation has still the highest potential among all crystalline solid-state formulations (Nechipadappu et al., 2019; Sarmah et al., 2016, 2018a). Salt formulation can increase the solubility and dissolution of APIs in polar solvents. A detailed study of crystalline solid states of olanzapine, as a model compound, has been researched in this paper using a large number of coformers/salt-formers to test the well-known ΔpK_a rule. As olanzapine molecule has a strong unbonded hydrogen bond acceptor in its pure crystal, acidic functional groups were considered that have potential

to form the hydrogen bond. Regarding carboxylic acid cofomers, a number of olanzapinium salts have already been reported (Sarmah et al., 2018a). Therefore, in this paper, we focused on exploring phenol and benzoic acid derivatives as hydrogen bond donors. The experimental data have been confirmed/predicted by a combination of hydrogen-bond propensity (HBP) and hydrogen-bond coordination (HBC) calculations.

2-Methyl-4-(4-methyl-1-piperazinyl)-10H-thieno[2,3-b]-[1,5]benzodiazepine, well-known as olanzapine (OLN), is an atypical antipsychotic drug widely used to treat schizophrenia and bipolar disorder (Bymaster et al., 1996; Nanubolu & Ravikumar, 2017). It represents a good crystal engineering model compound as it displays a low solubility and a high permeability (Clarke et al., 2012; Thakuria & Nangia, 2013), which belongs to the BCS (Biopharmaceutics Classification System) (Tsume et al., 2014) class II. For APIs belonging to this class, solid-state modification is expected to offer better efficacy and efficiency (Sarmah et al., 2016). Thus, previous studies have reported six anhydrous polymorphs (Clarke et al., 2012; Nanubolu & Ravikumar, 2017; Reutzel-Edens et al., 2003; Sarmah et al., 2016; Thakuria & Nangia, 2013; Tiwari et al., 2007), three polymorphic dihydrates, two polymorphic sesquihydrates, several solvates (Cavallari et al., 2013; *The Cambridge Structural Database (CSD) - The Cambridge Crystallographic Data Centre (CCDC)*, n.d.), mixed solvated forms (Wawrzycka-Gorczyca et al., 2007), cocrystals and salts (Clarke et al., 2012; Sarmah et al., 2016, 2018b; Surampudi et al., 2020; Thakuria & Nangia, 2013). Zawarotko et al. (Clarke et al., 2012) has systematically studied few quaternary solvated isostructural cocrystals of olanzapine and categorized them based on the crystal packing arrangement. Ranjit et al. (Sarmah et al., 2018b, 2020) used a mechanochemical liquid-assisted grinding (LAG) approach to prepare olanzapinium salts with dicarboxylic acids to improve the hydration stability and solubility of OLN. The elimination of side effects of OLN was realized by the design of olanzapine-nateglinide and olanzapine-pyrazinoic acid cocrystals (Sarmah

et al., 2020), and the thermal properties of OLN were improved by dihydroxybenzene cofomers (Surampudi et al., 2020).

Despite the existence of several publications on olanzapine, it continues to serve as a useful model API. Herein in this paper, a systematic study on the prediction and selection of proper salt-formers and cofomers, the synthesis of multi-component crystals of a model API, and the characterization of the targeted physicochemical property of OLN was proposed for first time. Several crystal engineering tools are studied on olanzapine: first, with synthon analysis a set of cofomers and salt-formers were selected, and their newly discovered crystals were fully characterized. The experimental screening was performed on more than 50 cocystal/salt formers, only salicylic acid, terephthalic acid, anthranilic acid, 3-hydroxybenzoic acid, 2-aminoterephthalic acid, phenol and resorcinol resulted in new phases. The formation of these new crystalline forms agreed with hydrogen bonding propensity and coordination predictions, as well as ΔpK_a rule of 3 to differentiate salts from cocystals. Lastly, the solubility and dissolution tests of the discovered OLN multicomponent crystals were performed that showed promising improvements in these physicochemical properties.

4.2 Experimental Section

4.2.1 Preparation of olanzapine cocystals/salts and corresponding solvates

Olanzapine was donated by Apotex Pharmachem Inc. 3-Hydroxy benzoic acid (3HBA) (>99%) was purchased from ACROS Organics; anthranilic acid (AA) (>98%) and phenol (Phol) were purchased from Sigma-Aldrich; terephthalic acid (TA) (98+%), salicylic acid (SA) (99+%), resorcinol (Res) (99.0-100.5%), and 2-aminoterephthalic acid (2ATPA) (99%) were all purchased from Alfa Aesar. Cofomers were used as purchased. Liquid-assisted grinding (LAG), also known as solvent drop grinding (SDG), was used by

mechanical grinding of the API and the coformer/salt-former using an agate mortar and pestle, for the preparation of cocrystals/salts. Methanol was used as the solvent for grinding. Ball milling process was used in parallel to prepare bulk powders using a Retsch Mixer Miller 200 (Haan, Germany), a mixer mill equipped with a stainless-steel jar (PTFE SmartSnap Jar -5ml), and two 5 mm Zirconia grinding balls. The mixture in the stainless-steel jar was blended for 10 min under a 12.5 Hz vibrational frequency on the Mixer Mill. A 1:1 stoichiometric ratio of the solid API and a coformer (200mg in total) was used in the initial studies for both ball milling and SDG. The product obtained from grinding was air-dried and characterized by PXRD and DSC. The product powder was then crystallized using different HPLC grade solvents (dichloromethane, chloroform, isopropanol, acetonitrile, ethanol, toluene, tetrahydrofuran, ethyl acetate and methanol) in 5.0 mL beakers and then kept for crystallization at room temperature (24 °C) or at a lower temperature (5 °C). Single crystals obtained from crystallization were then characterized structurally using sc-XRD. After the cocrystal/salt structure was obtained by sc-XRD, the observed stoichiometric ratio was used to produce the bulk cocrystals/salts (500 mg in total) through ball milling and SDG. The produced bulk cocrystals were characterized by PXRD. The PXRD patterns of these reproduced bulk samples were compared with the simulated PXRD patterns obtained from the sc-XRD data to check the consistency. The detailed procedure of the production of the OLN multicomponent crystals is described below.

OLN-SA, OLN-Res, OLN-AA , OLN-3HBA , OLN-2ATPA

A one-to-one stoichiometric ratio mixture of OLN with SA, Res, AA, 3HBA, and 2ATPA was manually ground with mortar and pestle using liquid assisted grinding conditions. Every 10 min, 8-10 drops of methanol were added, and the materials were ground for about 30 min until a dry homogenous powder was obtained. PXRD was then used to compare the X-ray pattern of the mixture with the starting compounds to ensure a new phase was formed.

OLN-TA and OLN-TA-H₂O

A mixture of 2 to 1 stoichiometric ratio of OLN and TA was manually ground in mortar and pestle using liquid assisted grinding with the same procedure discussed above, and the product was characterized by the PXRD to produce the anhydrous OLN-TA powder. Based on the single-crystal data, OLN-TA hydrate was detected in the asymmetric unit. Two drops of deionized water were introduced into half of the obtained ground bulk crystals and the mixture was then ground for another fifteen minutes to produce the hydrate phase. The products were then characterized by the PXRD. The diffraction patterns were compared to the simulated patterns from the sc-XRD analysis.

OLN-3HBA-ACN

Initially, the SDG process was used to produce the OLN-3HBA-ACN. Acetonitrile was used instead of methanol as the added solvent to produce the solvate. It was found that the obtained product was gummy and amorphous. Therefore, rotary vaporization was employed instead of SDG. Mixtures of 1:1 stoichiometric ratio of OLN and 3HBA were put in a 100 mL round-bottomed flask and were then dissolved in 50 mL HPLC grade acetonitrile with the help of ultrasound (110-120 V, 50/60 Hz, 10 min). The flask was set in a 50 °C water bath for 1 h to evaporate the excess acetonitrile. The dried bulk OLN-3HBA-ACN was collected, characterized by the PXRD, and compared to the simulated pattern from the sc-XRD.

OLN-Phol-H₂O

An SDG process similar to the production of OLN-3HBA-ACN, was adopted to produce the OLN-Phol-H₂O. A 1:1 stoichiometric ratio of OLN and Phol mixture was ground in the presence of methanol. After 30-min of grinding, a gummy mixture was formed as the product. Toluene, a non-polar solvent, was used to make the powder product. Ball milling

with the assistance of methanol and several droplets of toluene led to the formation of OLN-Phol-H₂O powder. Crystals were dried after SDG and characterized by the PXRD.

OLN-MeOH

Olanzapine methanol solvate was made to confirm the purity of the produced salts and cocrystals. Pure olanzapine was ground with several droplets of methanol for thirty minutes. The product was characterized by the PXRD and DSC.

4.2.2 Single Crystal X-ray Diffraction

The single crystal X-ray diffraction patterns of the obtained OLN multicomponent single crystals were obtained on the Bruker APEX-II CCD diffractometer using Mo K α radiation ($\lambda = 0.7107 \text{ \AA}$). APEX2 software was used for data integration and reduction with SAINT. The data were collected at 110(2) K using an Oxford Cryostream low-temperature device. Based on the obtained information from sc-XRD, crystal structures were solved by direct methods using SIR 2014 (Burla et al., 2015). Structure refinement was performed in the program package WinGX (Farrugia, 2012) and Olex2 1.3 (Dolomanov et al., 2009). All the non-hydrogen atoms were refined anisotropically by full-matrix least-squares calculations based on F2 with SHELXL-2016 (Sheldrick, 2015). All hydrogen atoms bonded to carbon were placed in the calculated positions, whereas acidic hydrogen atoms were located to confirm the salt formation. Mercury programs were utilized for structure analysis and the generation of crystal structures and packing diagrams. Linear acetonitrile introduces a strong disorder in the asymmetric unit of OLN-3HBA salt. To displace the disorder, we used Squeeze in the Olex2, and we removed the acetonitrile from the asymmetric unit. TWINABS-Version 2012/1-Bruker AXS scaling was used to identify 2 twin components of OLN-Phol-H₂O crystals (Weyna et al., 2009).

4.2.3 Powder X-ray Diffraction

The API, cofomers, and all product cocrystals/salts samples were run on the powder X-ray diffraction (Rigaku, Miniflex) with the Cu-K α source (λ for K α = 1.54059 Å). Bulk powder of each sample was placed on a quartz-glass sample holder and measured using a continuous scan between 5° and 45° in 2 θ with the 3°/min scan speed at 30 kV voltage and 15mA current.

4.2.4 Differential Scanning Calorimetry

Analysis of the thermal properties of the API, cofomers, cocrystals/salts was conducted using a differential scanning calorimetry (DSC, Mettler Toledo, Chicago, United States) under nitrogen gas atmosphere. Samples of precisely weighed cocrystals (5 mg to 10 mg) were placed in a non-hermetically sealed aluminum pan in a vacuum. Samples were scanned at a rate of 5 °C/min in the range of 25–280 °C under a dry nitrogen atmosphere at a flow rate of 100mL/min.

4.2.5 Preparation of Buffer Solution

For the solubility tests, a phosphate buffer (0.1 M, pH 7.2) solution was prepared by dissolving monobasic potassium phosphate (KH₂PO₄, 27.2 g) and potassium hydroxide (KOH, 8.8 g) in 2L distilled water at room temperature and adjusting the pH to 7.2 with 2N hydrochloric acid.

4.2.6 Equilibrium Solubility and Powder Dissolution Measurement

Excess amounts (100-150 mg) of powder samples (OLN/ cocrystals/ salts/ solvates/ hydrates) were added to 10 mL of aqueous buffer medium (at pH 7.2), and the mixture was stirred gently at 3.2 Hz for 24 h at 37 °C to measure the equilibrium solubility. After

24 h, the slurry was filtered using non-pyrogenic Filtropur S syringe filters with 0.45 μm pore size (Sarstedt AG & Co. KG, Germany) at room temperature.

It was found that the concentration of olanzapine in the solution computed from the characteristic peak (262 nm^{-1}) in UV-vis spectroscopy interferes with coformers/salt-formers. Thus, High-Performance Liquid Chromatography (HPLC) was used in this study. Reddy et al. (B. V. Reddy et al., 2007) also applied HPLC method to determine the OLN concentration in the solution. The reliability of the HPLC method was also verified by Basavaiah et al. (Basavaiah et al., 2014) After filtration, the clear solution was diluted with the aqueous buffer medium (10 times or 20 times) and was then quantified by HPLC coupled with UV-vis detector with the external standard method to determine its solubility. The peak area of OLN was traced and used for calculation.

Powder dissolution studies were performed in a similar way to the solubility test. Excess amounts (100-150 mg) of powder samples were placed in 15 mL glass vials, which were then filled with 10 mL of buffer solution and stirred at 3.2 Hz and 37 °C. After specific time intervals, 0.2 mL of the slurry of samples were syringe filtered. The resultant solution was then diluted with the aqueous buffer medium (10 or 20 times) and quantified by HPLC to determine its concentration. Chromatographic separation was achieved on an HPLC Cartridge column (ChromSep, C18, 250x4.6 mm). The mobile phase was a 50:50 (v/v) mixture of 0.01M phosphate buffer and HPLC grade acetonitrile, the flowrate was fixed at 1.2 mL/min, and UV-detection was performed at 252nm (B. V. Reddy et al., 2007). The column temperature was settled at 25 °C, and the analysis time was 15 min.

A standard calibration curve was used for solubility and dissolution calculations. The standard curve was determined with known concentrated OLN-buffer solution (OLN concentrations at 5.5, 4.4, 2.2, 1.1, and 0.55 mg/100mL). Ten microliters of the standard solution were injected automatically into the column in triplicate, and the chromatograms were recorded. Test solutions during the solubility and dissolution experiments were

injected, and their corresponding OLN peak areas were used to compute the solution concentration. For higher accuracy, OLN-2ATPA in buffer solution was diluted twenty times before the measurement, and all other samples were diluted ten times in order to maintain the peak height lower than 1 mAU.

The pH of the buffer medium was measured at the beginning and the end of both equilibrium solubility and dissolution experiments using a Beckman pH meter. The excess solids remaining after the equilibrium solubility and dissolution experiments were dried and their PXRD and DSC patterns recorded.

4.3 Results and Discussion

4.3.1 Selection of Candidate Molecules for OLN Multi-component

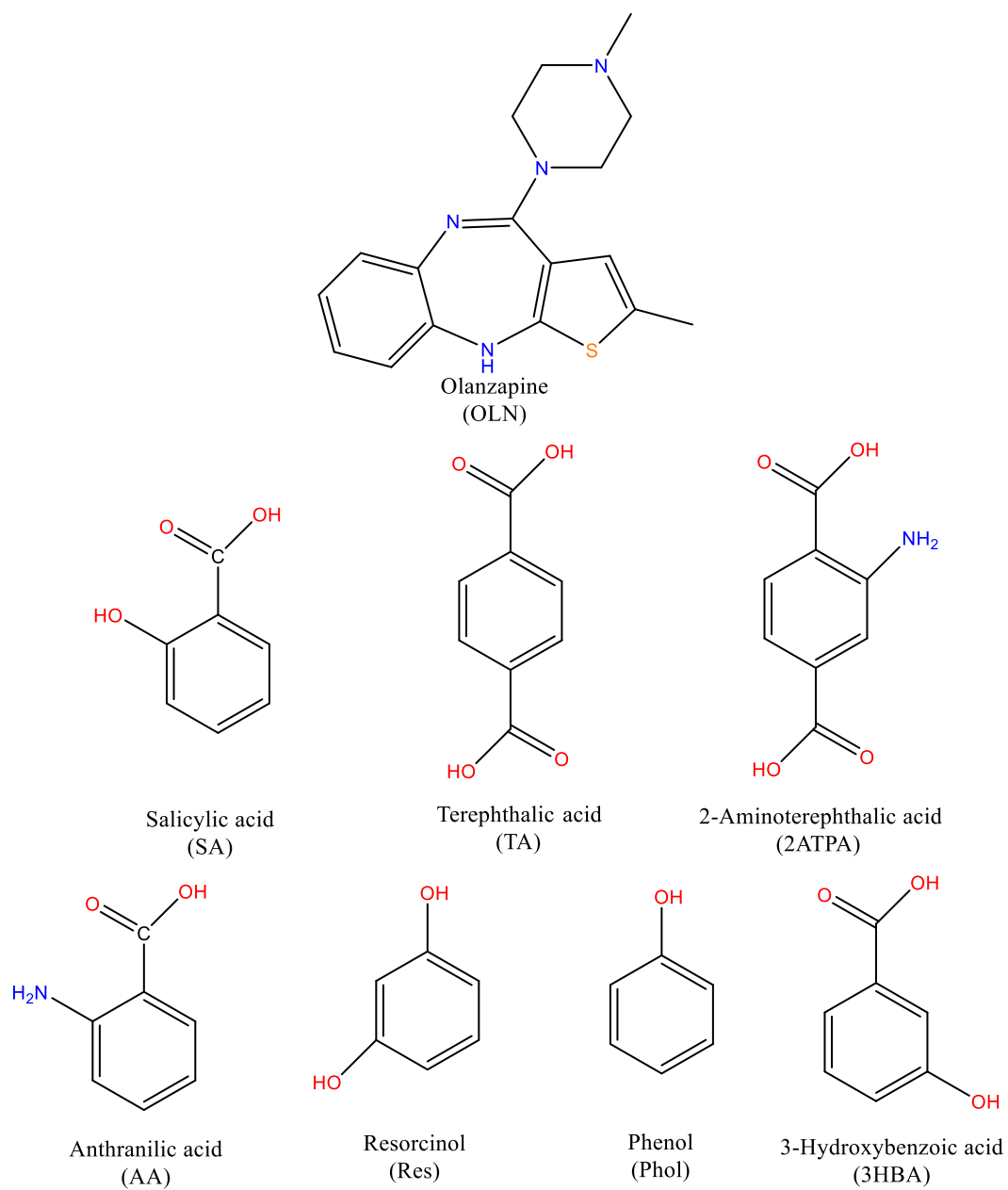
Crystals

The selection of coformers and salt-formers of OLN, in this study, was based on the hydrogen-bond propensity and hydrogen-bond coordination calculations. Typical synthons used in these calculations for OLN with phenol and benzoic acid are provided in [Table 4-1](#). (Sandhu et al., 2018) CCDC Mercury (2020.2.0) (Macrae et al., 2020) was used for the calculation. The observed interaction in OLN crystal structure showed a rather low propensity of 0.25. This is an indication that the main hydrogen bond in OLN can be replaced with API-coformer interactions with higher propensities. As shown in [Table 4-1a](#), one can see that phenol and benzoic acid derivatives bond with significantly higher propensities (approximately 0.4) to OLN, which makes them ideal candidates for multicompetent crystallization. More specifically, the aromatic hydroxy and carboxy would act as the hydrogen bond donor and the piperazine N of OLN would act as the hydrogen bond acceptor (synthon A and B). For the OLN-benzoic acid, there exists another potential hydrogen bond former between the diazepine N (donor) and the carbonyl group (C=O) (acceptor) (synthon C).

Hydrogen bond coordination analysis, shown in [Table 4-1b](#), provided further evidence on candidacy of phenol and benzoic acid derivatives for formation of salts/cocrystals with OLN. The coordination number for the primary donor atom of OLN (0.852-0.855) to form one hydrogen bond is lower than the equivalent value for phenol (0.930) and benzoic acid (0.951). On the other hand, the main OLN acceptor (0.610-0.636) has a higher coordination number than benzoic acid (0.570) and phenol (0.203) acceptors. Therefore, pairing of the cofomers donor and API acceptor is favored, making these compounds excellent candidates for salts/cocrystal formation with OLN. According to the molecular structure of OLN, there are 3 acceptors (N) and only 1 donor (NH). This imbalance of hydrogen bond moieties leads to uncoordinated sites that favors the formation of multicomponent crystals.

All selected cofomers and salt-formers followed the “ ΔpK_a rule of 3” (Lemmerer et al., 2015), which states that cocrystals will form if $\Delta pK_a = pK_a$ (protonated base) – pK_a (acid) is less than 0. On the other hand, molecular salts will form if the difference is greater than 3. The OLN molecule has two strong basic acceptors, piperazine N with a pK_a value of 7.37 and diazepine N with a pK_a value of 4.69. Based on the ΔpK_a rule, acids with pK_a value < 4.5 will form salts with OLN, and acids with pK_a value > 7 will form cocrystals.

Consequently, resorcinol ($pK_{a1} = 9.26$), phenol ($pK_a = 10.02$) as cofomers; and 3-hydroxybenzoic acid ($pK_a = 3.84$), salicylic acid ($pK_{a1} = 2.79$), anthranilic acid ($pK_a = 4.89$), 2-aminoterephthalic acid ($pK_a = 3.95$), and terephthalic acid ($pK_{a1} = 3.32$) as salt-formers (see scheme 1) have been selected for this study. The hydrogen bond donors of these cofomers and salt-formers (carboxyl, phenolic hydroxyl) participate in intermolecular hydrogen bonds with strong acceptors of OLN.



Scheme 4-1. Molecular structure of OLN and coformers/salt formers used in this study.

Table 4-1a. Predicted hydrogen-bond propensities for OLN with phenol and benzoic acid

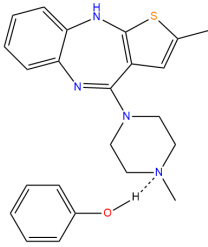
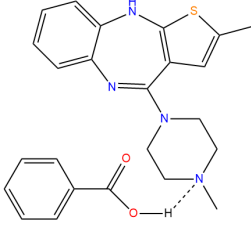
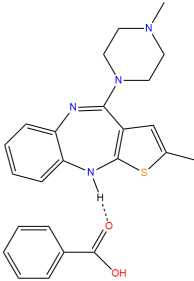
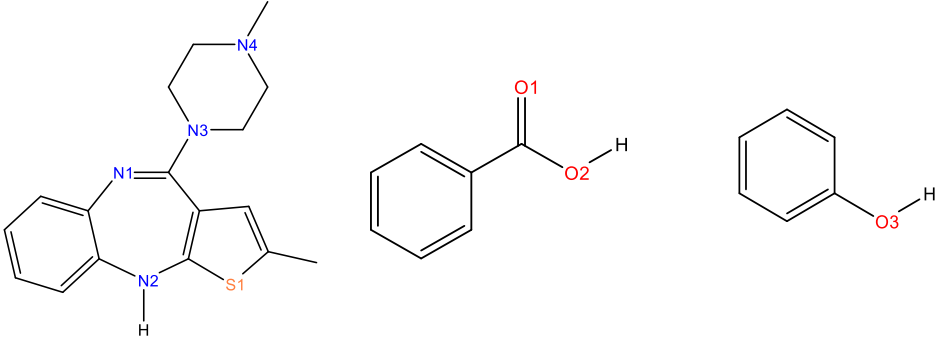
| Synthon A | Synthon B | Synthon C |
|---|---|---|
|  |  |  |
| Hydrogen-bond propensities (lower bound, upper bound) | | |
| 0.38 (0.27, 0.50) | 0.39 (0.28, 0.52) | 0.42 (0.28, 0.57) |

Table 4-1b Predicted hydrogen-bond coordination numbers for OLN with phenol and benzoic acid

| Hydrogen-bond coordination numbers | | | |
|--|-------------------------|-------------------------|-------------------------|
|  | | | |
| Donor (D)/Acceptor (A) atom | Coordination number = 0 | Coordination number = 1 | Coordination number = 2 |
| N1(A) in OLN-Phol | 0.603 | 0.392 | 0.005 |
| N1(A) in OLN-BA | 0.657 | 0.339 | 0.004 |
| N2 (D) in OLN-Phol | 0.095 | 0.852 | 0.053 |
| N2 (D) in OLN-BA | 0.090 | 0.855 | 0.055 |

| | | | |
|----------------------------|-------|-------|-------|
| N3 (A) in OLN-Phol | 0.940 | 0.060 | 0 |
| N3 (A) in OLN-BA | 0.946 | 0.054 | 0 |
| N4 (A) in OLN-Phol | 0.364 | 0.636 | 0 |
| N4 (A) in OLN-BA | 0.390 | 0.610 | 0 |
| O1 (A) in OLN-BA | 0.378 | 0.570 | 0.050 |
| O2 (D) in OLN-BA | 0.006 | 0.951 | 0.043 |
| O3 (D) in OLN-Phol | 0.020 | 0.930 | 0.050 |
| O3 (A) in OLN- Phol | 0.787 | 0.203 | 0.010 |

Structural analysis

Single-crystal X-ray diffraction data summarized in [Table B-1](#) confirm the formation of new solid phases of OLN. The single crystal structure of Olanzapinium·Salicylate Benzene (1:1:1.5) (Thakuria & Nangia, 2013), Olanzapine·Resorcinol (1:1) (Surampudi et al., 2020), and the structure of anhydrous Olanzapine·Phenol (1:1)(Andrusenko et al., 2020) obtained by 3D electron diffraction have already been reported. Single crystals of anhydrous OLN with Res [OLN-Res, cocrystal]; anhydrous OLN with SA [OLN-SA, salt]; and AA [OLN-AA, salt] were successfully isolated and characterized. Meanwhile, hydrated cocrystal of OLN-Phol (water from air); hydrated salt of OLN-TA and solvated salt OLN-3HBA were also isolated and characterized. No suitable-size single crystal of OLN-2ATPA for the sc-XRD could be isolated using various crystallization methods that were employed. The ORTEP diagrams and detailed crystal packing diagrams for each of the OLN multicomponent crystals are shown in [Figure B-1](#) and [Figure 4-1](#). As the OLN-Res structure was already reported by Surampudi et al. (Surampudi et al., 2020), its structure was not analyzed by sc-XRD. The list of primary intermolecular interactions of OLN multicomponent crystals is summarized in [Table 4-2](#). All anhydrous cocrystals and salts followed the predicted synthons (synthon A, B and C) depicted in [Table 4-1a](#).

OLN-Phol-H₂O crystallizes in toluene solvent with the $P\bar{1}$ space group with one OLN molecule, one Phol molecule, and one water molecule in the asymmetric unit. One OLN molecule interacts with one Phol molecule by an O-H...N hydrogen bond (Interaction I). The hydrogen bond donor of one water molecule, is connected to the piperazine N (hydrogen acceptor) O-H...N (Interaction II). The oxygen of the same water molecule, as a hydrogen bond acceptor, interacts with the diazepine through the N-H...O (Interaction III). Another hydrogen of the same water molecule is connected to the Phol molecule through an O-H...O hydrogen bond (Interaction IV). Two water molecules and two OLN molecules form a ring (see [Table 4-2](#) and [Figure B-1](#) and [Figure 4-1\(a\)](#)).

OLN-SA crystallizes in ethanol solvent with the $P\bar{1}$ space group, and it consists of one olanzapinium and one salicylate ion in the asymmetric unit. An acidic proton from SA is transferred to the piperazine N atom of OLN, forming a salt through the N⁺-H...O⁻ charge-assisted hydrogen bond (Interaction I). The second O of the SA carboxyl group interacts with the diazepine N of the OLN via N-H...O⁻ (Interaction II) (see [Table 4-2](#) and [Figure B-1](#) and [Figure 4-1\(b\)](#)).

OLN-AA crystallizes in dichloromethane with the $P2_1/c$ space group. It includes one olanzapinium and one anthranilate ion in the asymmetric unit. Similar to the OLN-SA, an acidic proton from AA is transferred to the piperazine N of OLN, forming the salt through the N⁺-H...O⁻ charge-assisted hydrogen bond (Interaction I). The second O of the AA carboxyl group interacts with the diazepine N of the OLN via N-H...O⁻ (Interaction II) (see [Table 4-2](#) and [Figure B-1](#) and [Figure 4-1\(c\)](#)).

OLN-3HBA crystallizes in acetonitrile with the $P\bar{1}$ space group, and it includes one olanzapinium and one 3-hydroxybenzoate ion in the asymmetric unit. The acidic proton from 3HBA carboxyl is transferred to the piperazine N of OLN, forming the salt through the N⁺-H...O⁻ charge-assisted hydrogen bond (Interaction I). The second O of the 3HBA carboxyl group is connected to the diazepine N of OLN through the N-H...O⁻ hydrogen

bond (Interaction II). The phenolic hydroxyl of 3HBA is connected to the diazepine N of another olanzapinium ion through the hydrogen bond O-H...N (Interaction III). Two 3HBA ions and two OLN ions form a ring (see [Table 4-2](#) and [Figure B-1](#) and [Figure 4-1\(d\)](#)).

OLN-TA-H₂O crystallizes in methanol with *P2₁/n* space group, and it constitutes one olanzapinium, half terephthalate ion, and two water molecules in the asymmetric unit. Two acidic protons from the two carboxyls of TA are transferred to two piperazine N of OLN, forming a 2:1 molar ratio salt through the N⁺-H...O⁻ charge-assisted hydrogen bond (Interaction I). The second O of the TA carboxyl group from both sides is connected to two diazepine N of OLN through the N-H...O⁻ hydrogen bond (Interaction II). The first O of the TA carboxyl is also connected to a hydrogen atom of a water molecule as a hydrogen bond acceptor via the O-H...O⁻ hydrogen bond (Interaction III). Another hydrogen atom from this water molecule forms a different hydrogen bond (O-H...O) (Interaction IV) with the second water molecule. The second water, which also interacts with the diazepine N of the OLN via O-H...N hydrogen bond (Interaction V) is connected to another pair of water molecules through the O-H...O hydrogen bond (Interaction VI) to form an 8-member ring as shown in the packing diagram [Figure 4-1\(e\)](#).

Table 4-2. List of intermolecular interactions of OLN multicomponent crystals

| Interaction | D-X...A | Symmetry Code | X...A (Å) | D...A (Å) | ∠D-X...A (°) |
|---------------------------------------|-------------|---------------|-----------|-----------|--------------|
| <u>OLN-Phol-H₂O</u> | | | | | |
| I | O1-H1...N1 | x, y, z | 1.87 | 2.74 | 174 |
| II | O2-H2C...N4 | 1-x, 2-y, 2-z | 1.80 | 2.83 | 162 |
| III | N2-H2...O2 | x, -1+y, z | 2.04 | 2.88 | 162 |
| IV | O2-H2B...O1 | x, y, z | 2.12 | 2.97 | 169 |

OLN-SA

| | | | | | |
|----|--|--------------|------|------|-----|
| I | N4 ⁺ -H4N···O1 ⁻ | -1-x,-y, -z | 1.64 | 2.66 | 166 |
| II | N2-H2N···O2 ⁻ | -1-x,-y, 1-z | 2.04 | 2.92 | 171 |

OLN-AA

| | | | | | |
|----|--|-------------|------|------|-----|
| I | N4 ⁺ -H4A···O1 ⁻ | x, ½-y, ½+z | 1.64 | 2.65 | 172 |
| II | N2-H2A···O2 ⁻ | -x,-y,-z | 2.12 | 2.96 | 168 |

OLN-3HBA

| | | | | | |
|-----|---------------------------------------|---------------|------|------|-----|
| I | N4 ⁺ -H4···O1 ⁻ | x, y, z | 1.47 | 2.56 | 176 |
| II | N2-H2···O2 ⁻ | x, y, -1+z | 2.07 | 2.95 | 169 |
| III | O3-H3···N1 | 2-x, 1-y, 2-z | 1.97 | 2.78 | 165 |

OLN-TA-H₂O

| | | | | | |
|-----|---------------------------------------|-------------------|------|------|-----|
| I | N4 ⁺ -H4···O1 ⁻ | 1.5-x, ½+y, 1.5-z | 1.77 | 2.68 | 165 |
| II | N2-H2···O2 ⁻ | ½+x, ½-y, ½+z | 1.95 | 2.85 | 172 |
| III | O4-H4C···O1 ⁻ | 1.5-x, ½+y, 1.5-z | 2.00 | 2.82 | 156 |
| IV | O4-H4B···O3 | 1-x, 1-y, 1-z | 1.97 | 2.80 | 159 |
| V | O3-H3A···N1 | x, y, z | 2.24 | 3.15 | 159 |
| VI | O3-H3B···O4 | x, y, z | 1.87 | 2.72 | 165 |

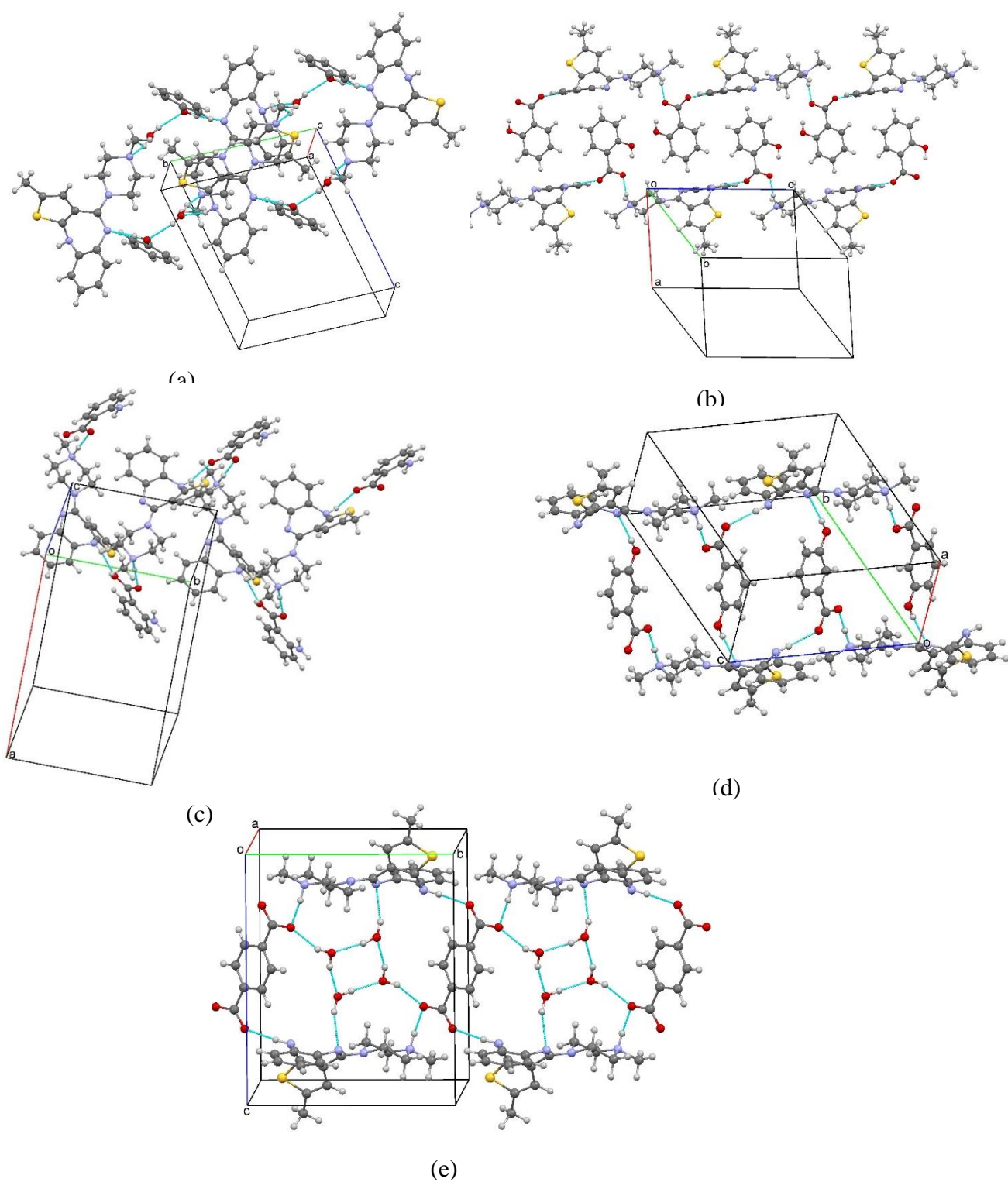


Figure 4-1. Crystal packing diagrams of (a) OLN-Phol-H₂O, (b) OLN-SA, (c) OLN-AA, (d) OLN-3HBA, and (e) OLN-TA-H₂O

4.3.2 Thermal Analysis

The DSC curves of OLN and its multicomponent crystals are shown in [Figure 4-2](#) (split into two figures to reduce crowdedness) and their endothermic peaks information reported in [Table B-2](#). It was confirmed that each of the cocrystals and salts reported in this article displays a different onset value of the melting peak, compared to the pure OLN (onset value: 195 °C) and the corresponding salt-formers/coformers. Hydrates and solvates formed (OLN-MeOH, OLN-3HBA-ACN, OLN-TA-H₂O) all show the loss of their corresponding solvents during DSC analysis. OLN-MeOH shows a broad endothermic peak ranging from 95 °C to 133 °C, suggesting the methanol evaporation, followed by another endothermic melting peak at 193 °C, close to the melting point of pure OLN. The DSC curve of OLN-3HBA acetonitrile solvate indicates a similar melting point to OLN-3HBA at 202 °C, following a broad endothermic peak starting at 100 °C due to the loss of acetonitrile. The dihydrate of OLN-TA [OLN-TA-H₂O] shows a melting point at 260 °C close to that of OLN-TA, following the broad endothermic peak at 73 °C due to the loss of water. OLN-2ATPA shows an endothermic melting point of 224 °C, different from both OLN and 2ATPA.

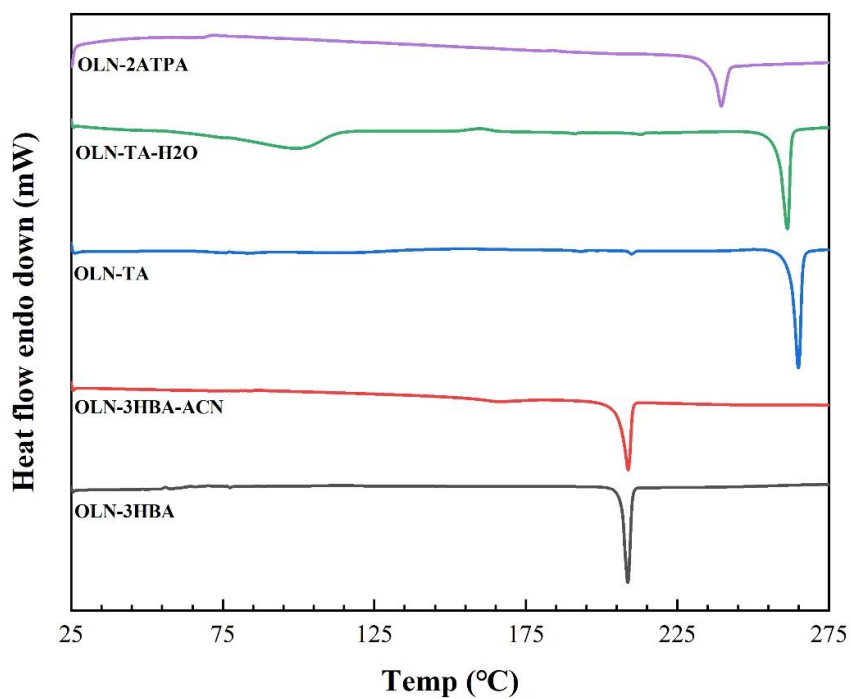
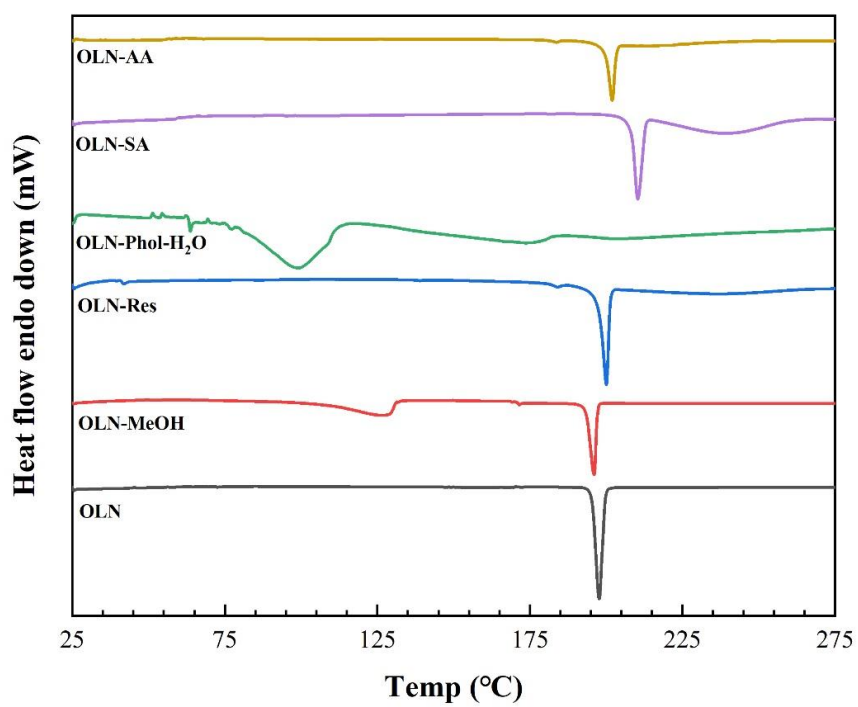


Figure 4-2. Thermographs of fresh OLN multicomponent crystals

4.3.3 Comparison of the PXRD Patterns

All ground bulk crystals exhibit unique PXRD patterns compared to OLN and their corresponding coformers/salt-formers, indicating the formation of new crystalline phases, as shown in [Figure 4-3](#) (split into three figures to reduce crowdedness). The simulated PXRD patterns from the sc-XRD are shown in [Figure B-2](#). Pure OLN and its methanol solvate were run as references. It was clearly shown that some of the main peaks at 8.6°, 17.0°, 17.8°, 18.7°, 19.8°, 21.0°, 22.2°, 23.9°, and 25.2° of pure OLN, and some of the main peaks at 16.3°, 22.9°, 24.6° of OLN methanolate disappeared in the new multicomponent crystal x-ray diffraction patterns.

The main peaks at 7.6°, 13.2°, 19.2°, are new in OLN-Phol-H₂O, compared to pure OLN. The simulated sc-XRD ([Figure B-2](#)) displays the same diffraction pattern as the PXRD of the bulk OLN-Phol-H₂O crystals.

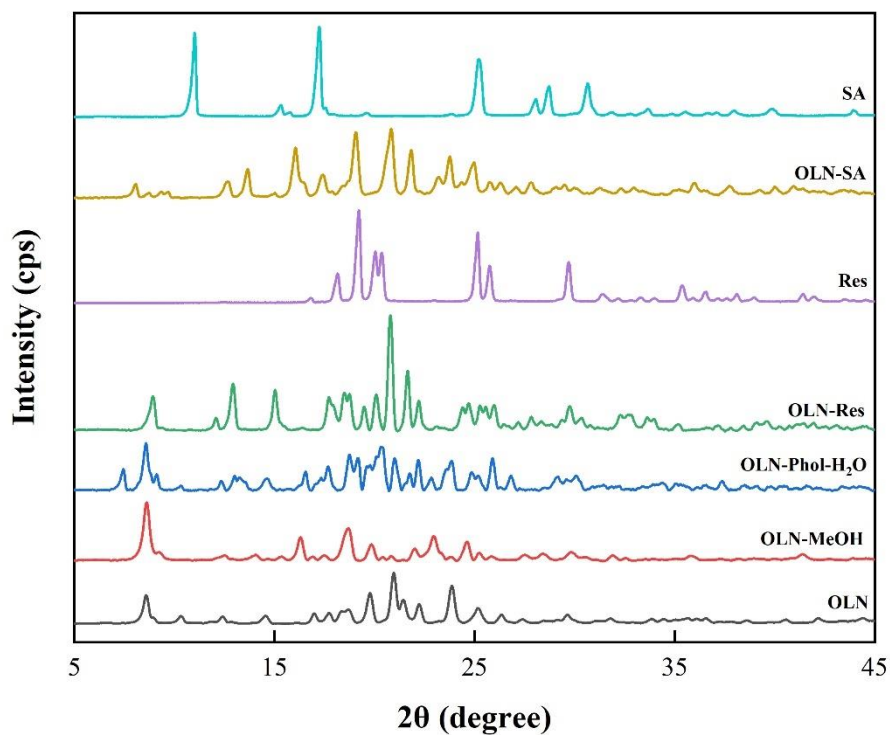
Peaks at 19.4°, 23.7°, 26.6°, 28.3° of pure 3HBA disappeared in OLN-3HBA and OLN-3HBA-ACN. Instead, peaks at 13.6°, 16.7°, 18.2°, 20.4° in OLN-3HBA; and 12.7°, 18.0°, 22.5° in OLN-3HBA-ACN were detected. The simulated PXRD patterns ([Figure B-2](#)) by sc-XRD are similar to the OLN-3HBA-ACN, confirming the reliability of our structural analysis.

Peaks at 17.4°, and 35.2° in TA disappeared, with new peaks appearing at 6.7°, 13.2°, 14.1°, 15.6°, 19.3°, 21.5° and 23.2° in OLN-TA. The PXRD pattern of OLN-TA-H₂O is similar to the OLN-TA anhydrate, with peaks at 6.7° and 23.2° disappearing and new peaks appearing at 9.8° and 20.0°. The simulated PXRD pattern ([Figure B-2](#)) by sc-XRD is the same as OLN-TA-H₂O, as we analyzed in the structural analysis previously.

Peaks at 13.8°, 16.4°, 18.6°, 20.2°, 27.6° in AA; 19.2°, 20.0° in Res; and 11.0°, 15.3° in SA disappeared, while new sharp peaks at 6.1°, 12.0°, 19.4° in OLN-AA; 13.0°, 18.5°, 21.7°, 24.4° in OLN-Res; and 8.0°, 13.7°, 19.1° in OLN-SA appeared. The simulated

PXRD patterns (Figure B-2) from sc-XRD and the characterized excess crystals after dissolution and solubility tests are the same as the PXRD patterns of anhydrides of OLN-AA, OLN-Res, OLN-SA, indicating no hydrates or solvates were formed in these multi-component crystals.

Peaks of pure 2ATPA at 15.0° and 27.1° disappeared in the PXRD patterns of OLN-2ATPA, while new peaks at 9.6° , 19.4° , 21.7° , 23.5° appeared.



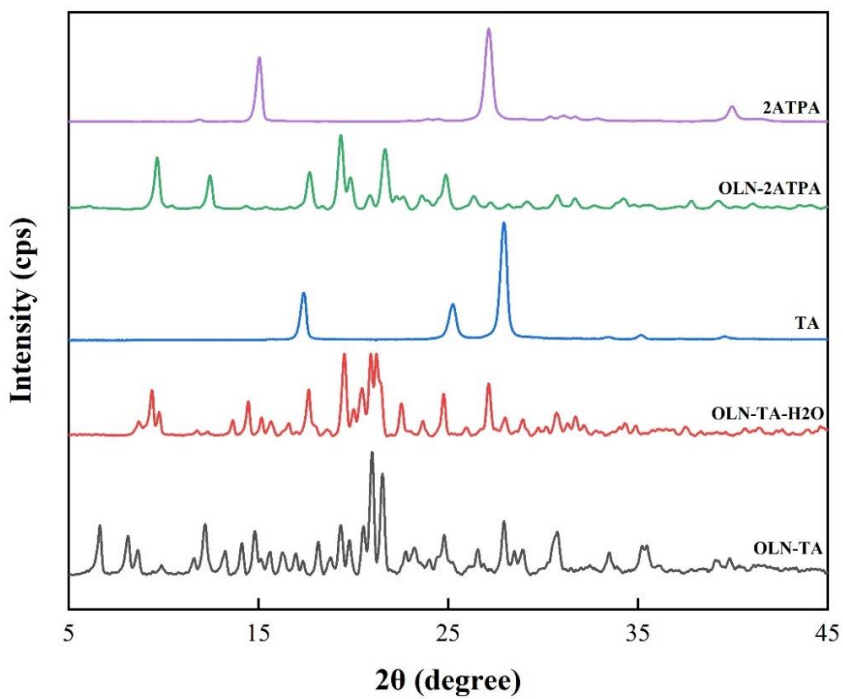
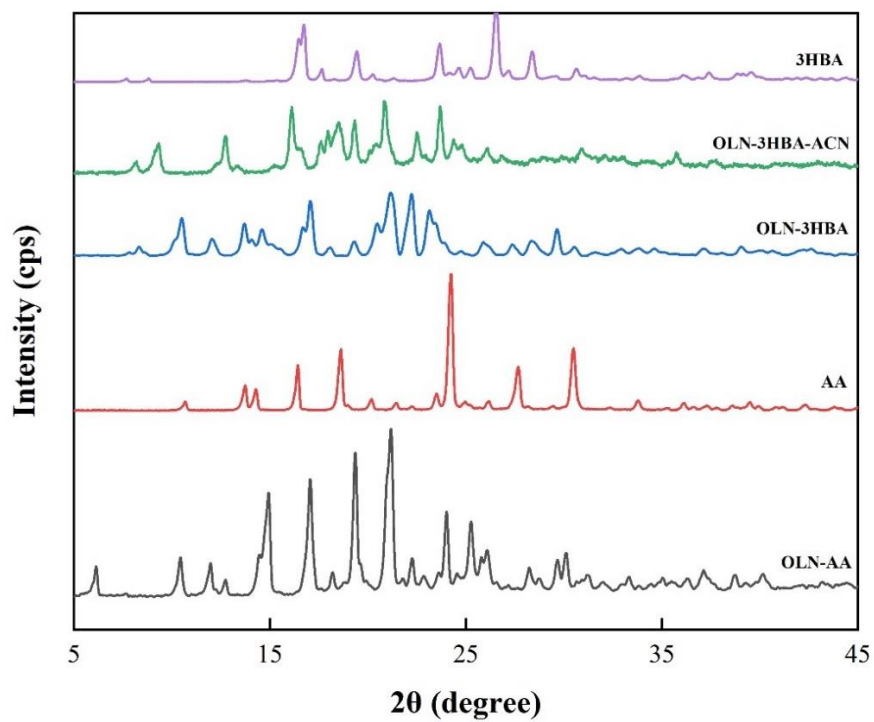


Figure 4-3. PXR D patterns of OLN and OLN multicomponent crystals

4.3.4 Solubility and Dissolution Test

In this research, we used the same solid phase of OLN-Res confirmed by sc-XRD to test its solubility and dissolution. In addition, due to phenol's toxicity, only the single crystal structure of OLN-Phol-H₂O was examined and reported in this paper. The solubility of all other new multicomponent crystals is considered in this study.

HPLC curves of each sample in the solubility test are shown in [Figure B-6](#). The retention time of OLN was around 9 min. The linear correlation between area and concentration was found with a slope of 2575600 peak area/(mg/100mL). The R-squared of this linear regression was 0.9986, indicating high degree of correlation between the peak area and the OLN concentration.

The measured equilibrium solubility data of OLN and multicomponent crystals in the pH 7.2 phosphate buffer solution are presented in [Table 4-3](#). It is clearly shown that, except OLN-Res, all the new-found OLN cocrystals/salts have improved solubility compared to pure OLN.

OLN-2ATPA displays the equilibrium solubility of $1.15 \pm (0.10)$ mg/mL, which is almost five times the original OLN solubility. OLN-3HBA, OLN-AA have double the solubility, and the solubilities of OLN-SA and OLN-TA are 1.5 times of the pure OLN.

The left-over solid phases after the solubility and dissolution tests, were checked by PXRD and DSC. No phase transformation was noted for OLN-Res, OLN-SA, and OLN-AA samples. On the contrary, a phase change occurred during the test of OLN-2ATPA, OLN-TA, OLN-3HBA, and OLN-3HB-ACN. The PXRD patterns of the excess OLN-2ATPA crystals remaining in the solution indicated that part of the crystals formed OLN dihydrate (Reutzel-Edens et al., 2003) during the solubility and dissolution tests. The PXRD pattern is an overlap of both OLN dihydrate and OLN-2ATPA ([Figure B-3](#)). The DSC pattern confirmed the formation of OLN dihydrate, as shown in [Figure B-5](#). The

DSC data shows a broad endothermic peak starting from 92 °C indicating the loss of water in the OLN dihydrate, following a small OLN melting peak and an OLN-2ATPA melting peak. Similarly, OLN dihydrate also formed during the solubility tests of OLN-3HBA and OLN-3HBA-ACN. From the PXRD analysis of the remaining solid samples after the solubility tests of OLN-3HBA and OLN-3HBA-ACN, a mixture of OLN dihydrate and OLN-3HBA was observed in both cases. The DSC curve of the remaining solid samples after the solubility tests after filtration, indicated the melting peak of OLN-3HBA. The crystals were then washed with deionized water and characterized by DSC again. The DSC data showed ([Figure B-5](#)) a broad endothermic peak starting from 93 °C indicating the loss of water in the OLN dihydrate, followed by an OLN melting point and a small OLN-3HBA melting point, confirming the presence of the OLN dihydrate.

The PXRD analysis of the remaining solid samples after the solubility tests of both OLN-TA and OLN-TA-H₂O ([Figure B-3](#)) showed the same patterns as the OLN-TA-H₂O, indicating the OLN-TA-H₂O was formed during the solubility and dissolution tests of anhydrous OLN-TA.

As shown in [Figure 4-4](#), most of the multicomponent crystals except OLN-Res improved the OLN dissolution at pH 7.2. The concentration of pure OLN and OLN-TA gradually decreased in the first two hours and remained stable at nearly $0.24 \pm (0.05)$ mg/mL and $0.38 \pm (0.05)$ mg/mL, respectively. This might be attributed to the fact that during the dissolution tests, hydrates of OLN and OLN-TA were gradually formed. Compared to the hydrates, anhydrous crystals of OLN and OLN-TA are easier to dissolve in water. Therefore, the dissolution was high initially; with the formation of the hydrate, the OLN concentration decreased and finally reached a plateau.

The major difference between the dissolution profiles of OLN-3HBA and OLN-3HBA-ACN was at t=30 min. The dissolution of OLN-3HBA-ACN peaked at 30 min before dropping back to the dissolution profile of OLN-3HBA at 1 hour. To explain this trend,

excess crystals of OLN-3HBA and OLN-3HBA-ACN after dissolution tests were washed by the buffer solution and characterized by PXRD. A new diffraction pattern, different from OLN-3HBA and OLN-3HBA-ACN, emerged in both experiments. The new observed PXRD pattern was determined to be a mixture of anhydrous OLN-3HBA and Olanzapine dihydrate ([Figure B-4](#)). Therefore, the peak in concentration in the dissolution test of OLN-3HBA-ACN at t=30 min can be associated with the loss of acetonitrile.

The OLN-2ATPA showed ([Figure 4-4](#)) a continuous decrease in the dissolution during the whole four hours, probably due to the partial dissociation of the salt and the formation of OLN hydrate. The formed OLN hydrate displays a lower solubility compared to the OLN-2ATPA salt. Thus, a decrease in the dissolution was observed during the experiment.

The pH of the buffer solution was measured before and after the equilibrium solubility tests to determine the influence of the ionizing components. As shown in [Table 4-3](#), it was observed that the pH of the buffer medium varied differently after the 24-hour equilibrium solubility tests. The pH of the buffer solution did not change during the equilibrium solubility study of pure OLN and OLN-Res at 37°C due to the similar pH value of the OLN aqueous solution. As OLN is a weak base, the salts of OLN reported here all belong to acidic salts. They all show a significant decrease in pH as the hydrolysis of olanzapinium will produce protons. As the solubility increased, more olanzapinium ions were formed in the buffer solution. Thus, the pH of the buffer medium from the OLN-2ATPA solubility test was the lowest, as OLN-2ATPA displays the highest equilibrium solubility (1.149 mg/mL).

Table 4-3. Solubility of OLN cocrystals/salts/solvates

| Name | OLN Solubility (mg/mL) | pH before/after the equilibrium solubility experiment |
|------------------------------|-----------------------------------|--|
| OLN | 0.24±(0.05) | 7.2/7.2 |
| OLN-Res | 0.19±(0.05) | 7.2/7.1 |
| OLN-SA | 0.37±(0.05) | 7.2/7.0 |
| OLN-AA | 0.61±(0.05) | 7.2/6.8 |
| OLN-3HBA-ACN | 0.69±(0.05) | 7.2/6.7 |
| OLN-TA | 0.32±(0.05) | 7.2/6.9 |
| OLN-TA-H₂O | 0.31±(0.05) | 7.2/7.0 |
| OLN-3HBA | 0.71±(0.05) | 7.2/6.9 |
| OLN-2ATPA | 1.15±(0.10) | 7.2/6.2 |

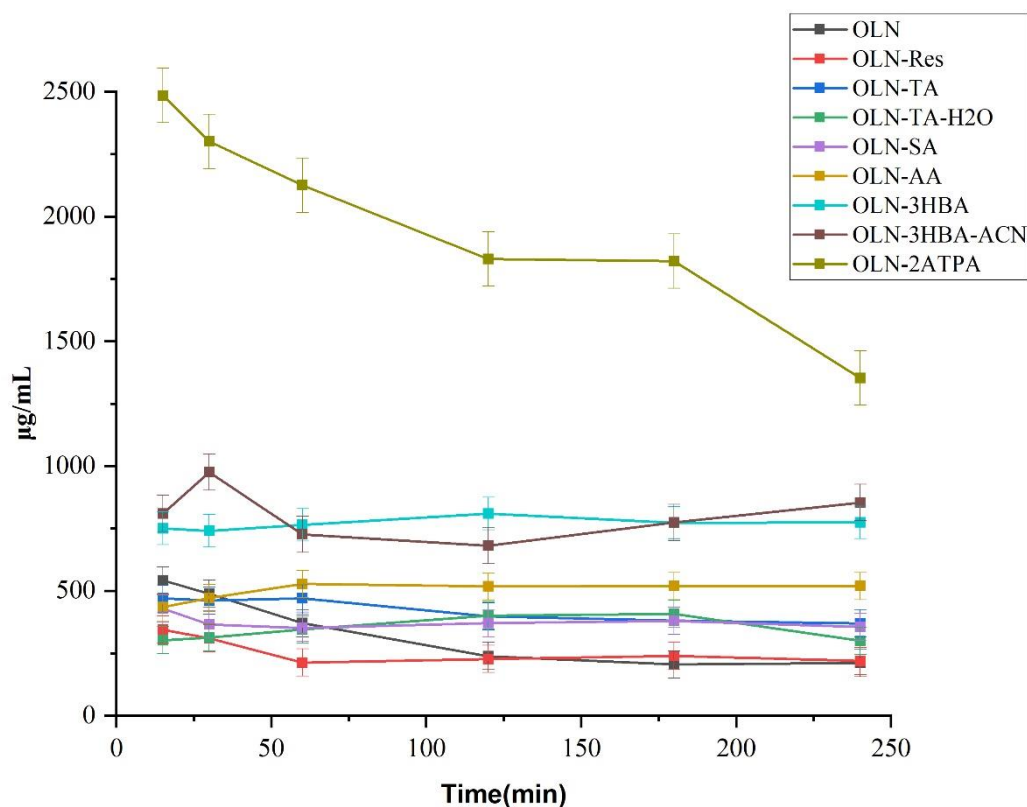


Figure 4-4. Dissolution measurement of OLN cocrystals/salts/solvates

4.4 Conclusion

Based on the prediction using hydrogen bond propensity and coordination (HBP and HBC) calculations, multicomponent crystals of OLN with cofomers (Phol, Res) and salt-formers (SA, AA, 3HBA, 2ATPA) were successfully obtained through liquid-assisted grinding and ball millings and were characterized through PXRD and DSC. All achieved cocrystals and salts followed the “ ΔpK_a rule of 3”. Except for OLN-2ATPA, single crystals of the discovered OLN multicomponent solid-phases were obtained, and the salt formations/cocrystal formations were confirmed with their crystal structure data. The crystal packing analyses were conducted to shed light on the primary intermolecular interactions. Olanzapinium salts showed similar charge-assisted bonds and hydrogen bonds in their structures. The acidic proton of carboxylic acid transferred to the piperidine

N, and the carbonyl group also interacted with the diazepine N of OLN as a hydrogen acceptor.

The solubility and dissolution tests of these new OLN multicomponent crystals were obtained by HPLC. It was found that all salts show significant improvements in the solubility; OLN-2ATPA showed almost a fivefold increase, and OLN-AA, OLN-3HBA showed a threefold increase in the solubility. This was reflected by the pH value of the solution after tests as a result of the hydrolysis of the olanzapinium ion. No significant variation in the solubility was found in the OLN-Res cocrystal.

4.5 References

- (1) Almarsson, Örn, & Zaworotko, M. J. (2004). Crystal engineering of the composition of pharmaceutical phases. Do pharmaceutical co-crystals represent a new path to improved medicines? *Chemical Communications*, 17, 1889. <https://doi.org/10.1039/b402150a>
- (2) Andrusenko, I., Potticary, J., Hall, S. R., & Gemmi, M. (2020). A new olanzapine cocrystal obtained from volatile deep eutectic solvents and determined by 3D electron diffraction. *Acta Crystallographica Section B Structural Science, Crystal Engineering and Materials*, 76(6), 1036–1044. <https://doi.org/10.1107/S2052520620012779>
- (3) Basavaiah, K., Rajendraprasad, N., & Vinay, K. B. (2014). Isocratic High-Performance Liquid Chromatographic Assay of Olanzapine: Method Development and Validation. *ISRN Analytical Chemistry*, 2014, 1–6. <https://doi.org/10.1155/2014/616941>
- (4) Blagden, N., de Matas, M., Gavan, P. T., & York, P. (2007). Crystal engineering of active pharmaceutical ingredients to improve solubility and dissolution rates. *Advanced Drug Delivery Reviews*, 59(7), 617–630. <https://doi.org/10.1016/j.addr.2007.05.011>
- (5) Burla, M. C., Caliendo, R., Carrozzini, B., Cascarano, G. L., Cuocci, C., Giacovazzo, C., Mallamo, M., Mazzone, A., & Polidori, G. (2015). Crystal structure determination and refinement via SIR2014. *Journal of Applied Crystallography*, 48(1), Article 1. <https://doi.org/10.1107/S1600576715001132>
- (6) Bymaster, F. P., Calligaro, D. O., Falcone, J. F., Marsh, R. D., Moore, N. A., Tye, N.

- C., Seeman, P., & Wong, D. T. (1996). Radioreceptor Binding Profile of the Atypical Antipsychotic Olanzapine. *Neuropsychopharmacology*, 14(2), 87–96. [https://doi.org/10.1016/0893-133X\(94\)00129-N](https://doi.org/10.1016/0893-133X(94)00129-N)
- (7) Cavallari, C., Santos, B. P.-A., & Fini, A. (2013). Olanzapine Solvates. *Journal of Pharmaceutical Sciences*, 102(11), 4046–4056. <https://doi.org/10.1002/jps.23714>
- (8) Clarke, H. D., Hickey, M. B., Moulton, B., Perman, J. A., Peterson, M. L., Wojtas, Ł., Almarsson, Ö., & Zaworotko, M. J. (2012). Crystal Engineering of Isostructural Quaternary Multicomponent Crystal Forms of Olanzapine. *Crystal Growth & Design*, 12(8), 4194–4201. <https://doi.org/10.1021/cg3007052>
- (9) Dalpiaz, A., Ferretti, V., Bertolasi, V., Pavan, B., Monari, A., & Pastore, M. (2018). From Physical Mixtures to Co-Crystals: How the Coformers Can Modify Solubility and Biological Activity of Carbamazepine. *Molecular Pharmaceutics*, 15(1), 268–278. <https://doi.org/10.1021/acs.molpharmaceut.7b00899>
- (10) Dolomanov, O. V., Bourhis, L. J., Gildea, R. J., Howard, J. A. K., & Puschmann, H. (2009). OLEX2: A complete structure solution, refinement and analysis program. *Journal of Applied Crystallography*, 42(2), 339–341. <https://doi.org/10.1107/S0021889808042726>
- (11) Duggirala, N. K., Perry, M. L., Almarsson, Ö., & Zaworotko, M. J. (2016). Pharmaceutical cocrystals: Along the path to improved medicines. *Chemical Communications*, 52(4), 640–655. <https://doi.org/10.1039/C5CC08216A>
- (12) Farrugia, L. J. (2012). WinGX and ORTEP for Windows: An update. *Journal of Applied Crystallography*, 45(4), 849–854. <https://doi.org/10.1107/S0021889812029111>
- (13) Huang, Y., Kuminek, G., Roy, L., Cavanagh, K. L., Yin, Q., & Rodríguez-Hornedo, N. (2019). Cocrystal Solubility Advantage Diagrams as a Means to Control Dissolution, Supersaturation, and Precipitation. *Molecular Pharmaceutics*, 16(9), 3887–3895. <https://doi.org/10.1021/acs.molpharmaceut.9b00501>
- (14) Karimi-Jafari, M., Padrela, L., Walker, G. M., & Croker, D. M. (2018). Creating Cocrystals: A Review of Pharmaceutical Cocrystal Preparation Routes and Applications. *Crystal Growth & Design*, 18(10), 6370–6387. <https://doi.org/10.1021/acs.cgd.8b00933>
- (15) Lemmerer, A., Govindraj, S., Johnston, M., Motloun, X., & Savig, K. L. (2015). Co-crystals and molecular salts of carboxylic acid/pyridine complexes: Can calculated pK_a's predict proton transfer? A case study of nine complexes. *CrystEngComm*, 17(19), 3591–3595. <https://doi.org/10.1039/C5CE00102A>

- (16) Macrae, C. F., Sovago, I., Cottrell, S. J., Galek, P. T. A., McCabe, P., Pidcock, E., Platings, M., Shields, G. P., Stevens, J. S., Towler, M., & Wood, P. A. (2020). Mercury 4.0: From visualization to analysis, design and prediction. *Journal of Applied Crystallography*, 53(1), 226–235. <https://doi.org/10.1107/S1600576719014092>
- (17) Nanubolu, J. B., & Ravikumar, K. (2017). Designing a new cocrystal of olanzapine drug and observation of concomitant polymorphism in a ternary cocrystal system. *CrystEngComm*, 19(2), 355–366. <https://doi.org/10.1039/C6CE02227H>
- (18) Nechipadappu, S. K., Reddy, I. R., Tarafder, K., & Trivedi, D. R. (2019). Salt/Cocrystal of Anti-Fibrinolytic Hemostatic Drug Tranexamic acid: Structural, DFT, and Stability Study of Salt/Cocrystal with GRAS Molecules. *Crystal Growth & Design*, 19(1), 347–361. <https://doi.org/10.1021/acs.cgd.8b01451>
- (19) Reddy, B. V., Reddy, K. V. N. S., Sreeramulu, J., & Kanumula, G. V. (2007). Simultaneous Determination of Olanzapine and Fluoxetine by HPLC. *Chromatographia*, 66(1–2), 111–114. <https://doi.org/10.1365/s10337-007-0257-z>
- (20) Reddy, L. S., Bethune, S. J., Kampf, J. W., & Rodríguez-Hornedo, N. (2009). Cocrystals and Salts of Gabapentin: pH Dependent Cocrystal Stability and Solubility. *Crystal Growth & Design*, 9(1), 378–385. <https://doi.org/10.1021/cg800587y>
- (21) Reutzel-Edens, S. M., Bush, J. K., Magee, P. A., Stephenson, G. A., & Byrn, S. R. (2003). Anhydrates and Hydrates of Olanzapine: Crystallization, Solid-State Characterization, and Structural Relationships. *Crystal Growth & Design*, 3(6), 897–907. <https://doi.org/10.1021/cg034055z>
- (22) Rodrigues, M., Baptista, B., Lopes, J. A., & Sarraguça, M. C. (2018). Pharmaceutical cocrystallization techniques. Advances and challenges. *International Journal of Pharmaceutics*, 547(1–2), 404–420. <https://doi.org/10.1016/j.ijpharm.2018.06.024>
- (23) Sandhu, B., McLean, A., Sinha, A. S., Desper, J., Sarjeant, A. A., Vyas, S., Reutzel-Edens, S. M., & Aakeröy, C. B. (2018). Evaluating Competing Intermolecular Interactions through Molecular Electrostatic Potentials and Hydrogen-Bond Propensities. *Crystal Growth & Design*, 18(1), 466–478. <https://doi.org/10.1021/acs.cgd.7b01458>
- (24) Sarmah, K. K., Nath, N., Rao, D. R., & Thakuria, R. (2020). Mechanochemical synthesis of drug–drug and drug–nutraceutical multicomponent solids of olanzapine. *CrystEngComm*, 22(6), 1120–1130. <https://doi.org/10.1039/C9CE01504C>
- (25) Sarmah, K. K., Sarma, A., Roy, K., Rao, D. R., & Thakuria, R. (2016). Olanzapine Salts and Diversity in Molecular Packing. *Crystal Growth & Design*, 16(2), 1047–

1055. <https://doi.org/10.1021/acs.cgd.5b01605>

- (26) Sarmah, K. K., Sarma, P., Rao, D. R., Gupta, P., Nath, N. K., Arhangel'skis, M., & Thakuria, R. (2018a). Mechanochemical Synthesis of Olanzapine Salts and Their Hydration Stability Study Using Powder X-ray Diffraction. *Crystal Growth & Design*, 18(4), 2138–2150. <https://doi.org/10.1021/acs.cgd.7b01593>
- (27) Sarmah, K. K., Sarma, P., Rao, D. R., Gupta, P., Nath, N. K., Arhangel'skis, M., & Thakuria, R. (2018b). Mechanochemical Synthesis of Olanzapine Salts and Their Hydration Stability Study Using Powder X-ray Diffraction. *Crystal Growth & Design*, 18(4), 2138–2150. <https://doi.org/10.1021/acs.cgd.7b01593>
- (28) Sheldrick, G. M. (2015). Crystal structure refinement with SHELXL. *Acta Crystallographica Section C: Structural Chemistry*, 71(1), Article 1. <https://doi.org/10.1107/S2053229614024218>
- (29) Surampudi, A. V. S. D., Rajendrakumar, S., Nanubolu, J. B., Balasubramanian, S., Surov, A. O., Voronin, A. P., & Perlovich, G. L. (2020). Influence of crystal packing on the thermal properties of cocrystals and cocrystal solvates of olanzapine: Insights from computations. *CrystEngComm*, 22(39), 6536–6558. <https://doi.org/10.1039/D0CE00914H>
- (30) Thakuria, R., & Nangia, A. (2013). Olanzapinium Salts, Isostructural Solvates, and Their Physicochemical Properties. *Crystal Growth & Design*, 13(8), 3672–3680. <https://doi.org/10.1021/cg400692x>
- (31) The Cambridge Structural Database (CSD) - The Cambridge Crystallographic Data Centre (CCDC). (n.d.). Retrieved March 5, 2021, from <https://www.ccdc.cam.ac.uk/solutions/csd-core/components/csd/>
- (32) Tiwari, M., Chawla, G., & Bansal, A. K. (2007). Quantification of olanzapine polymorphs using powder X-ray diffraction technique. *Journal of Pharmaceutical and Biomedical Analysis*, 43(3), 865–872. <https://doi.org/10.1016/j.jpba.2006.08.030>
- (33) Tsume, Y., Mudie, D. M., Langguth, P., Amidon, G. E., & Amidon, G. L. (2014). The Biopharmaceutics Classification System: Subclasses for in vivo predictive dissolution (IPD) methodology and IVIVC. *European Journal of Pharmaceutical Sciences*, 57, 152–163. <https://doi.org/10.1016/j.ejps.2014.01.009>
- (34) Wawrzycka-Gorczyca, I., Borowski, P., Osypiuk-Tomasik, J., Mazur, L., & Koziol, A. E. (2007). Crystal structure of olanzapine and its solvates. Part 3. Two and three-component solvates with water, ethanol, butan-2-ol and dichloromethane. *Journal of Molecular Structure*, 830(1–3), 188–197.

<https://doi.org/10.1016/j.molstruc.2006.07.017>

- (35) Weyna, D. R., Shattock, T., Vishweshwar, P., & Zaworotko, M. J. (2009). Synthesis and Structural Characterization of Cocrystals and Pharmaceutical Cocrystals: Mechanochemistry vs Slow Evaporation from Solution. *Crystal Growth & Design*, 9(2), 1106–1123. <https://doi.org/10.1021/cg800936d>

Chapter 5

Spherical Crystallization Based on Liquid-Liquid Phase Separation In A Reverse Antisolvent Crystallization Process

A version of this chapter has been accepted by *Journal of Pharmaceutical Sciences*.

5. Spherical Crystallization Based on Liquid-Liquid Phase Separation In A Reverse Antisolvent Crystallization Process

Abstract

Vanillin crystals undergo needle-like morphology that results in poor flowability, crystal breakage, and low packing density. The spherical crystallization technology can produce particles with improved flowability and stability. A reverse antisolvent crystallization based on liquid-liquid phase separation is proposed in this work to produce vanillin spherical agglomerates. Hansen Solubility Parameters are applied to explain the liquid-liquid phase separation (LLPS) phenomenon. The Pixact Crystallization Monitoring system is applied to in-situ monitor the whole process. A six-step spherical crystallization mechanism is revealed based on the recorded photos, including the generation of oil droplets, nucleation inside oil droplets, the coalescence and split of oil droplets, crystal growth and agglomeration, breakage of oil droplets, and attrition of agglomerates. Different working conditions are tested to explore the best operation parameters and a frequency-conversion stirring strategy is proposed to improve the production of spherical agglomerates.

Keywords: Liquid-liquid phase separation, Spherical crystallization, Hansen Solubility Parameters, Improved morphology, Vanillin

5.1 Introduction

Applying crystal engineering to tune the performance of active pharmaceutical ingredients (APIs) can improve the stability, solubility, dissolution, and bioavailability of most crystalline APIs (Almarsson & Zaworotko, 2004; Blagden et al., 2007; Duggirala et al., 2016). The outer shape and the inner structure of the crystal product, which can influence the powder quality and physicochemical properties, are controlled through the crystallization process (Zhou et al., 2019). Needle-like or plate-like crystals always cause difficulties for downstream processes due to the poor flowability, crystal breakage, and low packing density (Hatcher et al., 2020).

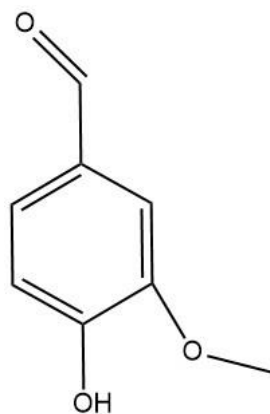
Kawashima et al. developed the spherical crystallization using a bridging liquid in the 1980s (Kawashima et al., 1982). The invention of spherical crystallization directly combines the downstream granulation processes with crystallization and thus significantly reduces the total equipment and energy cost (Ma et al., 2021). Currently, there are three main approaches to realize the spherical crystallization: spherical agglomeration (SA) (Kawashima, 1984; Kawashima et al., 1982); quasi-emulsion solvent diffusion (QESD) (Chen et al., 2020), and spherulitic growth (Cui et al., 2022; Guo, 2022). To follow the idea of green chemistry, applying SA is undesirable as a biohazardous bridging liquid such as chloroform is always needed to promote the crystals' agglomeration. Similar to the SA method, an emulsifier is required for the QESD strategy to generate the emulsion in the system, however, the emulsifier is normally less harmful compared to the bridging liquid. For the spherulitic growth strategy, a stable and effective method that controls the radial noncrystallographic branching growth remains lacking.

In the pharmaceutical industry, a clean and safe production strategy for sustainable development is desired (Wang et al., 2022). The oiling-out spherical agglomeration technology is recently developed for water-insoluble drugs (Ma et al., 2021; Sun et al.,

2019). In this technology, a thermally-induced liquid-liquid phase separation (LLPS) between the API and water is achieved during heating and is well dispersed by stirring. The emulsion is then suddenly quenched to let the API oil phase crystallize and thus produce the spherical product.

The main disadvantage of this method is that it can only be applied to low melting-point APIs otherwise an oiling-out mate must be introduced (Liu et al., 2022). Another type of LLPS consists of binary solvents in which the different concentrations of the API in two phases make the LLPS happen. Herein, we applied such LLPS to the reverse antisolvent crystallization method to produce spherical agglomerates so melting point is no longer a limitation. The number and the size of oil droplets in the system could be easily controlled by the inlet flow rate and the mechanical stirring rate and the stirrer geometry. Unlike the spherical crystals from common QESD which are small, the final spherical agglomerates in our method are large.

In this paper, vanillin (Scheme 1), which exhibits a needle-like or flaky crystal habit in industrial production, was selected as the model compound. The oiling out phenomenon of vanillin in water and 1-propanol binary solvent (Du et al., 2016; Zhang et al., 2022) was validated first. The Hansen solubility parameter (HSP) was applied to explore the oiling-out behaviour. A reverse antisolvent crystallization technology based on LLPS was then developed and different working parameters were tuned. The whole process was monitored by the Pixact Crystallization Monitoring system (PCM), and the crystallization mechanism was monitored. The achieved spherical crystals were characterized by PXRD and the thermal stability was checked.



Scheme 5-1. Molecular structure of vanillin

5.2 Materials and Methods

5.2.1 Materials

The model compound: vanillin (HPLC grade, 99%), the selected solvent: 1-propanol (HPLC grade, 99.9%), and ethanol (AR, 99.7%) were purchased from Beijing Innochem. The surfactant: sodium dodecyl sulfate (SDS)(Liu et al., 2023) was purchased from Tianjin Zhiyuan Chemical Reagent Co., Ltd. Ultrapure water (resistivity = 18.0 MΩcm) was produced from Milli-Q® Direct Water Purification System.

5.2.2 Powder X-ray Diffraction

The purchased vanillin and obtained spherical agglomerates were run on the powder X-ray diffraction (PANalytical) with the Cu-K α source (λ for K α = 1.540598 Å). Bulk powder of each sample was placed on a sample holder and measured using a continuous scan between 5° and 80° in 2 θ at 40 kV voltage and 40mA current. The scan step size is 0.013°.

5.2.3 Thermogravimetric analysis

Analysis of the thermal properties of vanillin and the obtained spherical agglomerates was conducted using a TGA/DSC 3⁺ (Mettler Toledo) under a nitrogen gas atmosphere. Samples of precisely weighed (5 mg to 10 mg) were placed in a non-hermetically sealed aluminum pan. Samples were heated at a rate of 10 °C/min in the range of 30–350 °C under a dry nitrogen atmosphere at a flow rate of 100mL/min.

5.2.4 Ternary Phase Diagram

Previous studies have confirmed that no LLPS would happen below the critical oiling out temperature, and the lowest critical temperature of water:1-propanol:vanillin system is 27.5°C regarding to all water:1-propanol ratios (Zhao et al., 2012). Thus, the phase diagram under 30°C is explored. Equilibrium solubility data under 30°C was tested by the gravimetric method. Excess vanillin powder was added into different vials with different ratios of 1-propanol and water binary solvent. These vials were then sealed and heated in a shaking water bath (SW22, Julabo). The shaking frequency was settled at 180rpm. Vials were shaken for 24 hours and were then stilled for 12 hours to let the solid phase settle down. The supernatant liquor was taken and filtered through a filter membrane (0.22µm) on Petri dishes quickly for the mass measurement with an electronic analytical balance ($\pm 0.0001\text{g}$, Mettler Toledo). Petri dishes with filtered supernatant liquor were then dried in a vacuum oven under 35°C, 1kPa for 24 hours. After drying, weight of samples was measured, and the loss weight was considered as the weight of the solvent.

LLPS curve was determined by the following method. The antisolvent solvent, water, was added into the 1-propanol+vanillin solution dropwise, with different ratios at a rate of 500µL/min with mechanical stirring until the solution changed from clear to turbid. The mass of added water was then measured to compute the composition of each compound.

5.2.5 Hansen Solubility Parameter (Gong et al., 2022; Hansen, 2007)

Hansen solubility parameter is applied to explain the oiling out phenomenon. HSP is based on the theory of "similarity and intermiscibility". If the HSP values are close for two different materials, it is more likely that they are miscible. Three major parts are included in HSPs: atomic dispersion forces (dispersion HSP, δ_d), molecular permanent dipole-permanent dipole forces (polar HSP, δ_p), and hydrogen-bonding energy (hydrogen-bonded HSP, δ_h). The total HSP is defined based on these three factors as:

$$\delta_t = \sqrt{\delta_d^2 + \delta_p^2 + \delta_h^2} \quad (5 - 1)$$

For those materials whose partial solubility parameters are not available, the group contribution method is used for estimation (Cong et al., 2022):

$$\delta_d = \frac{\sum F_{di}}{V} \quad (5 - 2)$$

$$\delta_p = \frac{\sqrt{\sum F_{pi}^2}}{V} \quad (5 - 3)$$

$$\delta_h = \frac{\sqrt{\sum E_{hi}}}{V} \quad (5 - 4)$$

where F_{di} , F_{pi} and E_{hi} are the contributions of the dispersion force, polar force, and the hydrogen-bonding energy for functional group i of the material molecule.

Van Krevelen and Hoftyzer quantified the difference in HSP using the parameter $\Delta\bar{\delta}$, (H. He et al., 2020; Q. He & Zhao, 2021) which is defined as:

$$\Delta\bar{\delta} = \sqrt{(\delta_{d2} - \delta_{d1})^2 + (\delta_{p2} - \delta_{p1})^2 + (\delta_{h2} - \delta_{h1})^2} \quad (5 - 5)$$

If the value of $\Delta\bar{\delta}$ is smaller than $5.0\text{MPa}^{1/2}$, it is observed that a good miscibility would be attained more probably (Alanazi et al., 2020).

5.2.6 Reverse antisolvent spherical crystallization of vanillin

Reverse antisolvent crystallization experiments under different conditions were conducted and the schematic diagram is shown in [Figure 5-1](#). The mother liquor with the mass ratio of (water:1-propanol:vanillin) as (40g/20g/10g) was prepared in a 200ml jacketed vessel under 50°C . The antisolvent, ultrapure water (50g), with surfactant (SDS), was prepared in a 200ml three necked crystallizer under 30°C with a two-bladed stirring impeller. The vanillin solution was added to the crystallizer by a peristaltic pump under a rate of 2.5ml/min. After the adding process, the slurry was stirred for another half an hour for aging. The whole process was monitored inline by PCM and was recorded to reveal the mechanism for the oiling-out spherical crystallization. Key operating parameters including feeding rate, stirring rate, and feed concentration were adjusted; and all tested working conditions were tabulated in [Table 5-1](#). The obtained products were characterized by PXRD and TGA. The crystal morphology was identified by scanning electron microscopy (SEM, TM3000, Hitachi). The particle size distribution (PSD) was directly analyzed by PCM. The reliability of the PCM results is validated using a standard sample purchased from Malvern Panalytical as shown in the Appendix C.

Table 5-1. Operating conditions of reverse antisolvent crystallization experiments

| Variable | Trial 1 | Trial 2 | Trial 3 | Trial 4 | Trial 5 | Trial 6 | Trial 7 | Trial 8 |
|--|---------|---------|---------|---------|---------|-----------|---------|---------|
| Working Temp ($^{\circ}\text{C}$) | 30 | 30 | 30 | 30 | 10 | 30 | 30 | 30 |
| Inlet Composition (water:1-propanol:vanillin) | 2:1:4 | 2:1:5 | 2:1:4 | 2:1:4 | 2:1:4 | 2:1:4 | 2:1:4 | 2:1:4 |
| Stirring Rate (rpm) | 110 | 110 | 200 | 110 | 110 | 110 + 200 | 110 | 50 |

| | | | | | | | | |
|------------------------|-------|-------|-------|-------|-------|-------|-------|-------|
| SDS Amount | 0.20% | 0.50% | 0.50% | 0.50% | 0.50% | 0.50% | 1.00% | 0.50% |
| Addition Rate (ml/min) | 2.5 | 2.5 | 2.5 | 2.5 | 2.5 | 2.5 | 2.5 | 2.5 |

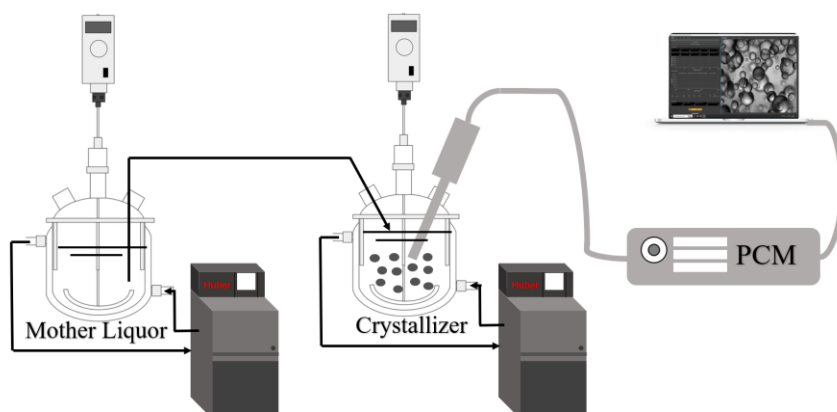


Figure 5-1. The schematic diagram for the reverse antisolvent crystallization

5.3 Results and Discussion

5.3.1 Ternary Phase Diagram of water:1-propanol:vanillin System

The ternary phase diagram of water:1-propanol:vanillin system under 30°C that provides ternary compositions of different phases is shown in [Figure 5-2](#), which validates the oiling out phenomenon of vanillin (Zhang et al., 2022). The solubility data and the liquid-liquid phase separation data at 30°C are listed in [Table C-1](#). The obtained ternary phase diagram followed the one obtained by Zhang et al (Zhang et al., 2022). It could be found that the cosolvency effect existed in this system. Vanillin has high solubility in 1-propanol and water is a poor solvent for it. However, the solubility of vanillin first increases with the water content until the water:1-propanol (mass ratio) is around 1:2. The solubility then suddenly decreases with the increase of water amount in the solution, followed by the LLPS. Five phase regions exist in this ternary system. Region 1 contains vanillin-

saturated solution (1-propanol rich) with excess vanillin solids. Similar to Region 1, Region 4 is the phase that vanillin-saturated solution (water-rich) exists with excess vanillin solids. In Region 3, vanillin solid is saturated with two liquid phases; and in Region 2, two liquid phases are in equilibrium. Region 5 is the unsaturated liquid phase. Ethanol was used to replace 1-propanol to see whether the LLPS would happen. Nevertheless, no matter how the concentration was adjusted, no LLPS was observed in the vanillin–water–ethanol system.

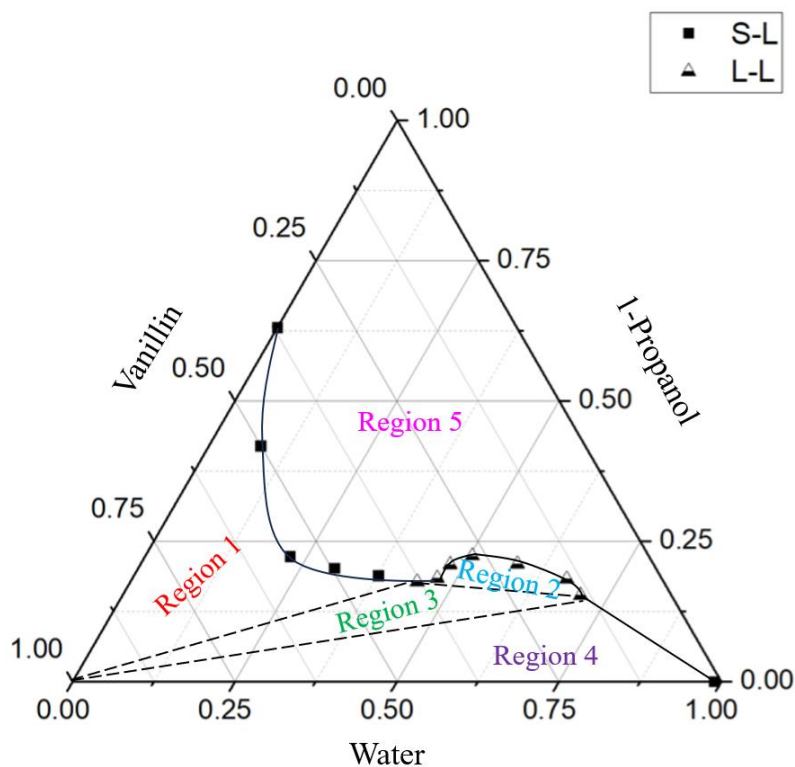


Figure 5-2. Ternary phase diagrams of water:1-propanol:vanillin system under atmospheric pressure ($P = 0.1$ MPa) at 30 °C; Region 1: solid–liquid phase 1; Region 2: liquid–liquid phase; Region 3: solid–liquid–liquid phase; Region 4: solid–liquid phase 2; Region 5: Liquid phase. *S: Solid, L: Liquid

5.3.2 Hansen Solubility Parameter

The HSP is applied to analyze the oiling out phenomenon. Related HSP values of vanillin, water, ethanol, and 1-propanol are shown in [Table 5-2](#), which include three partial (δ_d , δ_p , δ_h), a total (δ_t) and the $\Delta\bar{\delta}$ solubility parameters of three solvents and vanillin itself. The $\Delta\delta_t$ values (compared to vanillin) of ethanol, 1-propanol, and water are $2.07MPa^{0.5}$, $0.15MPa^{0.5}$, and $23.39MPa^{0.5}$, which indicate that the vanillin is more soluble in 1-propanol and ethanol and has poor miscibility in water. The $\Delta\bar{\delta}$ calculation gives the same miscibility order: 1 – propanol > ethanol \gg water ($7.68 MPa^{0.5} < 9.01 MPa^{0.5} \ll 31.94MPa^{0.5}$). The HSP analysis reveals that the solute-solvent interaction between ethanol and vanillin is weaker than that between 1-propanol and vanillin, which explains why no LLPS was observed in vanillin-water-ethanol system as the interaction between solute and the good solvent must be stronger than the interaction between two solvents.

Table 5-2. Three partial (δ_d , δ_p , δ_h), the total (δ_t) solubility parameters of three solvents and vanillin^a

| Components | $\delta_d(MPa^{0.5})$ | $\delta_p(MPa^{0.5})$ | $\delta_h(MPa^{0.5})$ | $\delta_t(MPa^{0.5})$ | $\Delta\delta_t(MPa^{0.5})$ | $\Delta\bar{\delta}(MPa^{0.5})$ |
|------------------|-----------------------|-----------------------|-----------------------|-----------------------|-----------------------------|---------------------------------|
| Ethanol | 15.8 | 8.8 | 19.4 | 26.52 | 2.07 | 9.01 |
| 1-Propanol | 16 | 6.8 | 17.4 | 24.60 | 0.15 | 7.68 |
| H ₂ O | 15.6 | 16 | 42.3 | 47.84 | 23.39 | 31.94 |
| Vanillin | 19.4 | 9.8 | 11.2 | 24.45 | / | / |

^a the values of δ_d , δ_p , δ_h are taken from references 21 and 25 (Cong et al., 2022; Kim, 2018)

5.3.3 Formation Processes and Mechanisms for Vanillin Spherical

Agglomerates

The reverse antisolvent crystallization process under 30°C was conducted based on the phase diagram and was monitored by PCM as shown in [Figure 5-3](#). The water to 1-propanol ratio of the mother liquor was selected to be 2:1 as it's close to the oil phase composition. When the mother liquor was first introduced into the water, LLPS happened as the temperature was above the critical temperature ([Figure 5-3a](#)). Upon continuous addition of vanillin solution, the supersaturation was accumulated both by cooling and the contact with antisolvent. Therefore, the nucleation of vanillin happened inside of oil droplets after a while as vanillin was enriched and supersaturated ([Figure 5-3b](#)). At the same time, the mechanical stirring let small oil droplets merge and made big oil droplets separate by the shearing force ([Figure 5-3c](#)). Vanillin crystals continuously grew and agglomerated inside the oil phase after the nucleation during the addition of mother liquor. Thus, the oil droplet got opaque (dark crystals as shown in [Figure 5-3d](#)). With the growth of the vanillin primary agglomerates, the oil droplets finally broke, and 1-propanol diffused into the water. Once the oil droplet was broken, no secondary agglomeration between the grown agglomerates was observed, indicating that agglomeration would only happen inside the oil droplet. Hence, similar to the QESD method, the crystal shape and size was majorly decided by the shape of the oil droplet. After the oil droplet got opaque, the addition of vanillin solution was stopped. The agglomerates were attrited by the impeller to become more spherical during the aging period. Based on the revealed mechanism, the formation of vanillin spherical agglomerates can be divided into 6 steps: (a) the generation of oil droplets, (b) nucleation inside oil droplets, (c) the coalescence and split of oil droplets, (d) crystal growth and agglomeration, (e) breakage of oil droplets, (f) attrition. With this revealed mechanism, it is experimentally noticed that the crystal size and morphology are predominantly determined during step (c) and step (f).

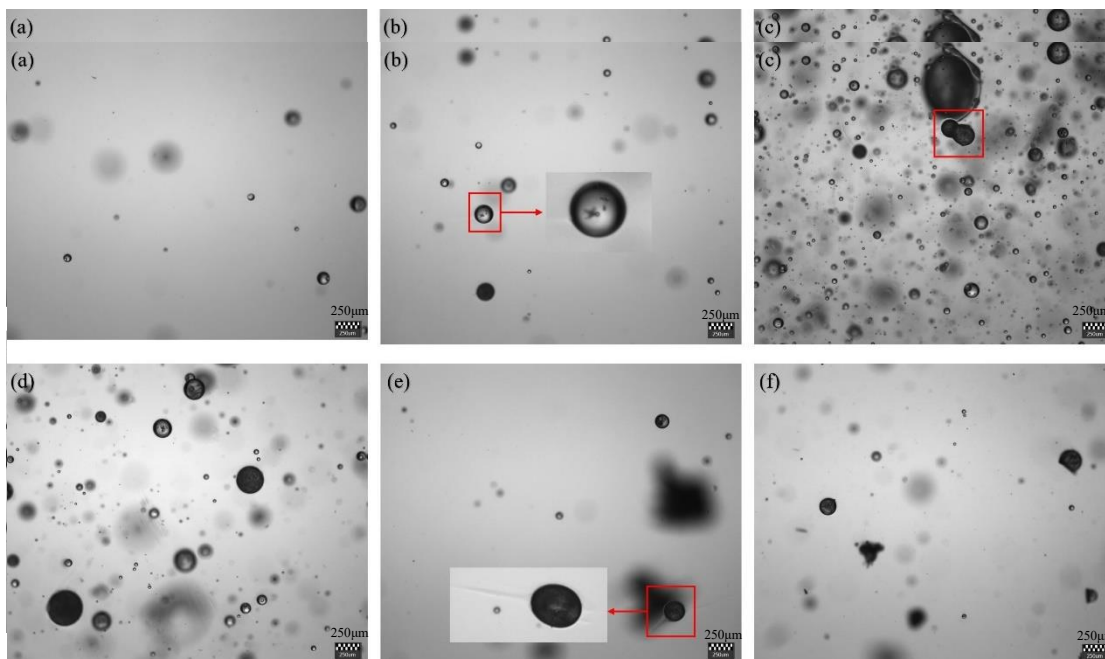


Figure 5-3. The formation mechanism of vanillin spherical **agglomerates** monitored by PCM

5.3.4 Effect of Process Parameters on Properties of Spherical Agglomerates.

The operating parameters can influence the final particle size distribution and the crystal morphology of vanillin agglomerates. Therefore, five major parameters including the working temperature, inlet concentration of vanillin, the amount of surfactant, and the stirring rate were investigated in this study.

5.3.4.1 Working Temperature. Since the mechanical stirring would affect the size of the oil droplet and it is difficult to control the coalescence of the oil droplets, it is not desired that the oil droplets would exist in the system too long. Hence, a low working temperature was selected to stimulate the primary nucleation in the oil phase. Two working temperatures were tested in this section: 30°C (Trial 4) and 10°C (Trial 5). The stirring rate was set to 110rpm and the feed composition was 2:1:4 (water:1-propanol:vanillin). The addition rate was fixed to be 2.5ml/min. As shown in [Figure 5-4e](#), when the working

temperature was below the LLPS critical temperature (10°C), LLPS would not happen during the process. Needle-like vanillin crystals would be achieved since no oil site for agglomeration existed. Spherical agglomerates ([Figure 5-4d](#)) were successfully obtained when the working temperature was increased to 30°C. Since 30°C is close to the lowest LLPS critical temperature, it was chosen to be the working temperature for the rest of experiments.

5.3.4.2 Inlet Concentration. The inlet concentration of vanillin would influence the initial supersaturation of spherical crystallization. Compared to Trial 4, the vanillin concentration in the mother liquor increased from 57.14wt% to 62.5wt% in Trial 2. Large agglomerates were obtained after filtration ([Figure 5-4b](#)). This is because, with the increased vanillin amount in the system, the number of vanillin oil droplets also increased during addition. Therefore, the possibility that two oil droplets collided and coalesced also increased, resulting in large agglomerates. The sphericity of the agglomerate was also poor as the morphology of big oil droplets would be strongly affected by the mechanical stirring. Concentration that is lower than 57.14wt% would prevent the nucleation of vanillin crystals inside the oil phase as the supersaturation is too low. Therefore, an initial ratio of 2:1:4 (water:1-propanol:vanillin) was selected to be the best inlet composition.

5.3.4.3 SDS Amount. The surfactant, sodium dodecyl sulfate, was used as the stabilizer in the system. (Liu et al., 2023) The purpose is to prevent the counter diffusion between water and 1-propanol so as to maintain the oil phase and allow the nucleation and agglomeration inside the oil droplets to proceed. However, in order to consider the principles of green chemistry and sustainability, only a few drops of SDS were used. Three different SDS loadings of the antisolvent (Trial 1, 4, 7) were tested and the obtained vanillin agglomerates were shown in [Figure 5-4a](#), [5-4d](#), and [5-4g](#). It is clearly depicted that with the increased amount of SDS in the system, the size of the vanillin agglomerates also increased. When the SDS loading was low, the interfacial tension was not high enough to

prevent the counter diffusion, which resulted in the fast breakage of oil droplets, and thus small irregular vanillin agglomerates ([Figure 5-4a](#)) were observed. On the contrary, when the SDS loading was too high, oil droplets were hard to break. Hence, the abundant oil droplets coalesced during the process and large agglomerates were obtained ([Figure 5-4g](#)). The ideal SDS loading appears to be 0.5wt%, as oil droplets would be stable enough to offer the nucleation and agglomeration, and would not be large to break once the vanillin agglomerates were formed.

5.3.4.4 The Stirring Rate. In this section, three different stirring rates (50, 110, 200 rpm) were used to carry out the reverse antisolvent crystallization experiments (Trial 3, 4, and 8). When the stirring rate was low (50 rpm), oil phase would sink to the bottom and coalescence, which resulted in large vanillin agglomerates as shown in [Figure 5-5](#). As the agglomerates get large, they are more prone to attrition by the stirrer. Therefore, small pieces of vanillin agglomerates were generated by attrition in trial 8. The SEM images of vanillin agglomerates in trial 3 are shown in [Figure 5-4c](#). It is clearly shown that the particle size was reduced when the stirring rate increased, and the irregularity also increased with increasing the stirring rate.

The particle size distributions of the products are shown in [Figure 5-6](#). At high stirring rate, a multi-modal PSD was observed, indicating that vanillin spherical agglomerates with different sizes were produced and some agglomerates were broken into small pieces by mechanical stirring. When the stirring rate was low, a broad distribution with a large particle mean size was obtained. Based on the revealed mechanism of the process, we adopted a new technique that during the nucleation and agglomeration of vanillin crystals inside the oil droplet, a slow mechanical stirring was desired to maintain the shape of oil droplets and to avoid the coalescence of oil droplets. At high stirring speed, the oil droplets break and form irregular agglomerates. Hence, a stirring rate of 110rpm at the beginning of the process (the first minute) and a 200rpm stirring during the aging process (thirty minutes) was adopted to improve the product quality. For such a stirring policy,

the product PSD was shown as the red line in [Figure 5-6](#) and the morphology of the product agglomerate was shown in [Figure 5-4f](#). It could be found that both the PSD and the morphology have substantially improved using this stirring policy. The achieved vanillin agglomerates were then characterized by PXRD and TGA to check the product purity and thermal stability.

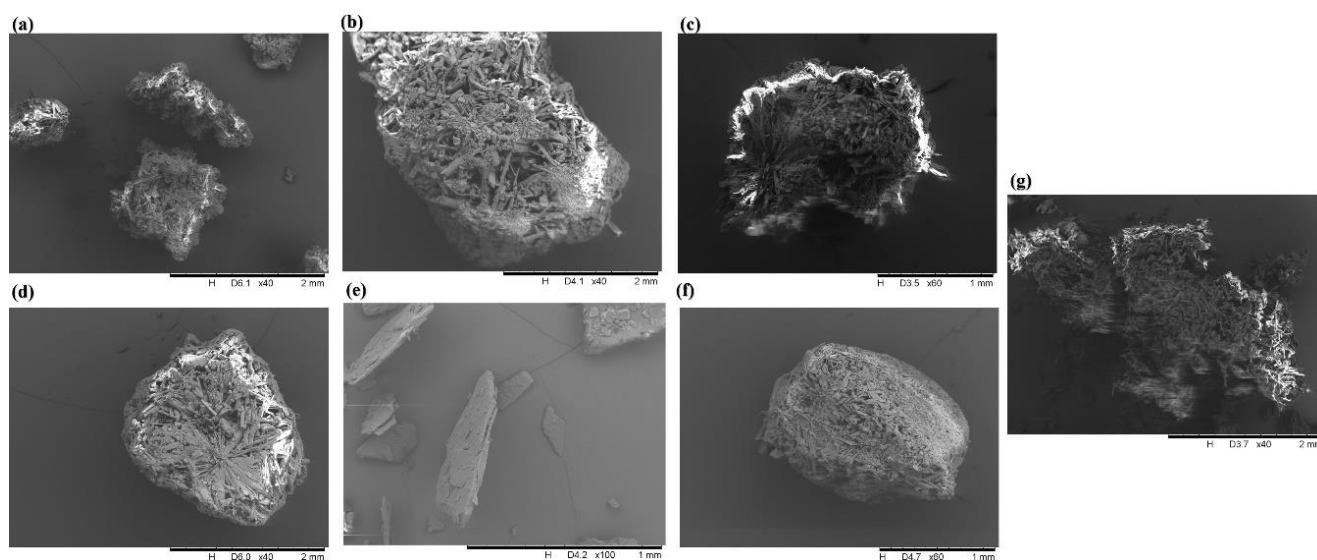


Figure 5-4. SEM images of vanillin products under different working conditions: (a) Trial 1, (b) Trial 2, (c) Trial 3, (d) Trial 4, (e) Trial 5, (f) Trial 6, (g) Trial 7

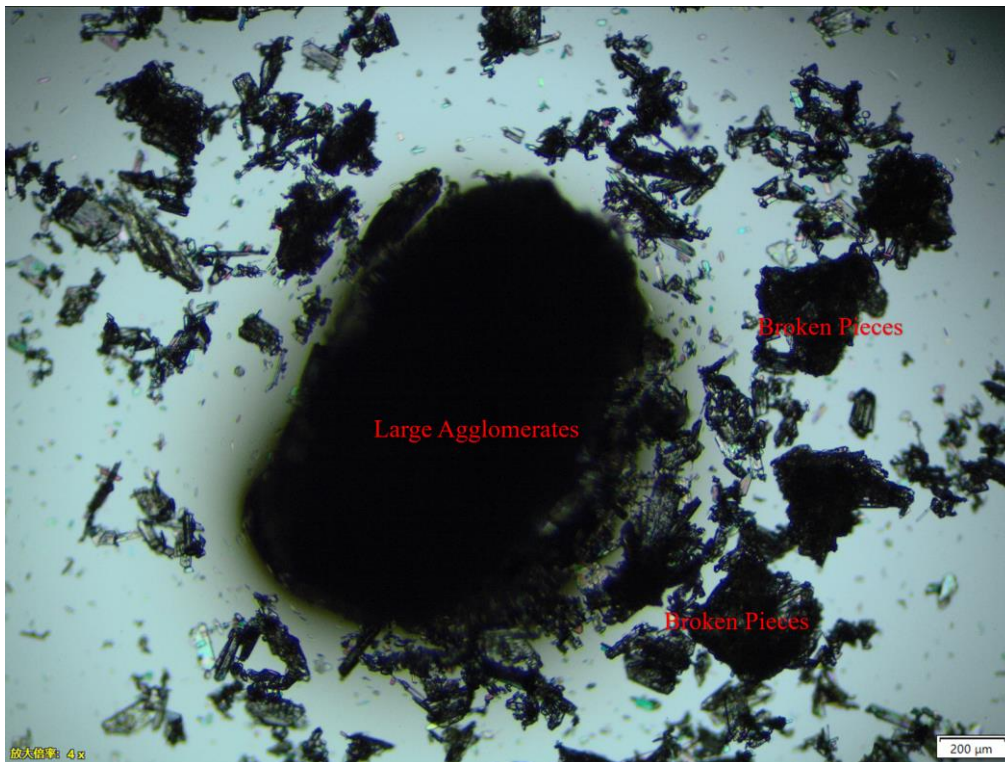


Figure 5-5. Microscopic photos of vanillin agglomerates (Trial 8)

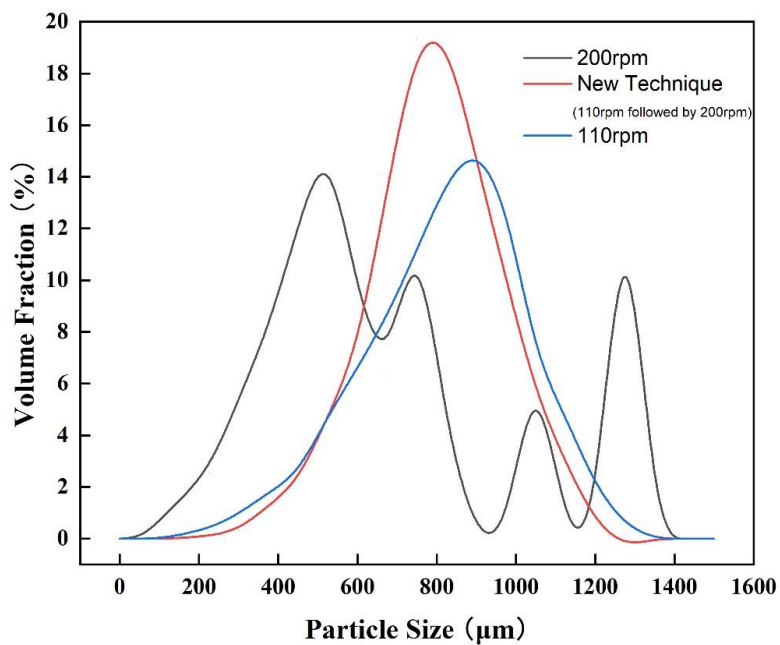


Figure 5-6. The PSDs of the vanillin products obtained under different stirring rates

5.3.5 Properties Assessment of Vanillin Spherical Agglomerates

5.3.5.1 Powder X-ray Diffraction Results The purity of all vanillin agglomerates were 99w%+ and no SDS residue was found using gas chromatography detected by Wanhua Chemical Group Co., Ltd. Vanillin agglomerates after the reverse antisolvent crystallization with different SDS loadings were also characterized by PXRD as shown in [Figure 5-7](#). All characterized peaks of vanillin were kept and no new diffraction peaks were observed in all produced agglomerates, indicating that no solvation or polymorphic transformation happened. The achieved PXRD patterns also confirmed that there was no remaining SDS in the vanillin product. Since the obtained PXRD patterns indicated that no morphology changes of the vanillin single crystal happened, it further verified that the spherical agglomerate was aggregated by block-like vanillin crystals.

5.3.5.2 Thermogravimetric analysis TGA was conducted to produce information on the volatility and thermal stability of the produced vanillin product (Trial 6). TGA thermograms are shown in [Figure 5-8](#). The thermal evaporation of vanillin raw material started at around 100°C and continued to lose weight till 214,3°C. For the produced vanillin spherical agglomerates, the thermal evaporation also started at around 100°C but the weight was totally lost at 223.5°C. The evaporation of vanillin spherical agglomerates is slower than the common plate-form crystals, indicating better thermal stability.

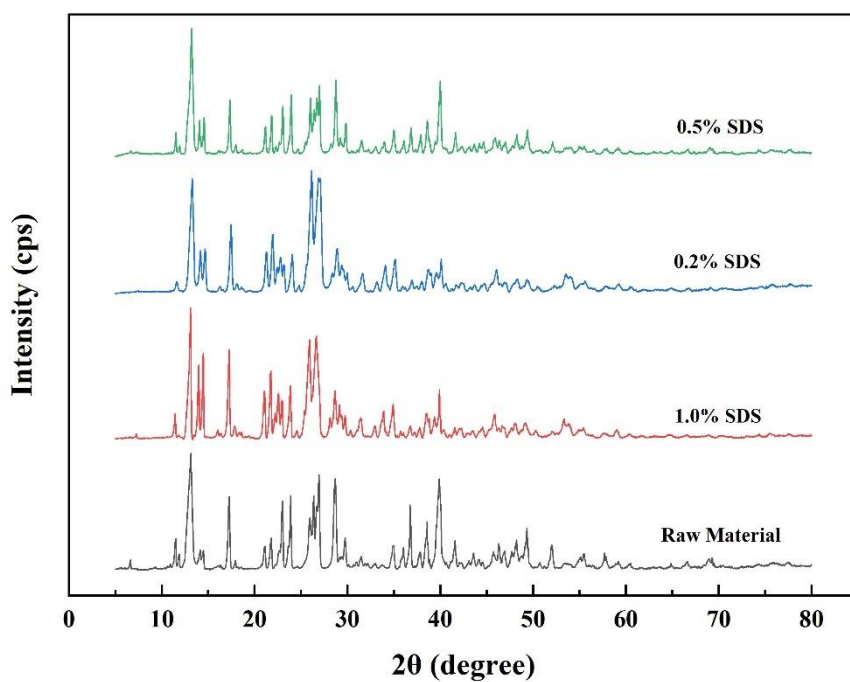


Figure 5-7. PXRD patterns of vanillin raw material and produced spherical agglomerates

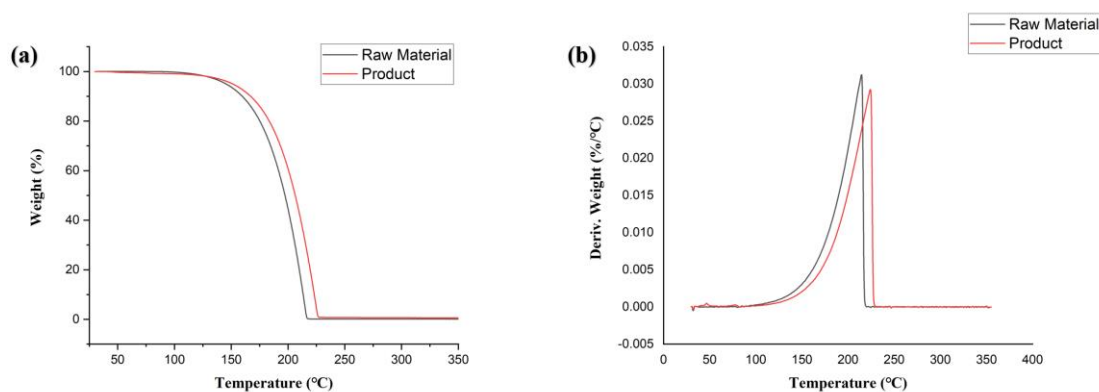


Figure 5-8. TGA thermograms and their derivatives for vanillin raw material and the spherical agglomerate (Trial 6)

5.4 Conclusions

Spherical particles of vanillin were successfully produced using a reverse antisolvent crystallization process in this work. Hansen solubility parameters explain the LLPS between vanillin, water and 1-propanol, as well as the failure in ethanol. With the help of PCM, a six-step spherical crystallization mechanism was clearly revealed and summarized as: (a) the generation of oil droplets, (b) nucleation inside oil droplets, (c) the coalescence and split of oil droplets, (d) crystal growth and agglomeration, (e) breakage of oil droplets, (f) attrition. Based on the revealed mechanism, a frequency conversion of the mechanical stirring was designed to produce better spherical agglomerates. It is found that the working temperature must be above the LLPS critical temperature to realize the spherical crystallization and the surfactant is needed to maintain the oil phase that offers the platform of vanillin nucleation and agglomeration. An inlet composition of 2:1:4 (water:1-propanol:vanillin) under 30°C with 0.5wt% SDS in the antisolvent using a 110rpm mechanical stirring during addition and a 200rpm stirring during aging is found to be the best working condition to produce narrow PSD and good morphology of the resulting vanillin spherical agglomerates, otherwise irregular agglomerates would be generated. The results of the present investigation provide a new technology to produce spherical agglomerates in an LLPS system and HSPs are considered to be able to predict the happen of LLPS.

5.5 References

- (1) Alanazi, A., Alshehri, S., Altamimi, M., & Shakeel, F. (2020). Solubility determination and three dimensional Hansen solubility parameters of gefitinib in different organic solvents: Experimental and computational approaches. *Journal of Molecular Liquids*, 299, 112211. <https://doi.org/10.1016/j.molliq.2019.112211>
- (2) Almarsson, Örn, & Zaworotko, M. J. (2004). Crystal engineering of the composition of pharmaceutical phases. Do pharmaceutical co-crystals represent a new path to improved medicines? *Chemical Communications*, 17, 1889. <https://doi.org/10.1039/b402150a>

- (3) Blagden, N., de Matas, M., Gavan, P. T., & York, P. (2007). Crystal engineering of active pharmaceutical ingredients to improve solubility and dissolution rates. *Advanced Drug Delivery Reviews*, 59(7), 617–630. <https://doi.org/10.1016/j.addr.2007.05.011>
- (4) Chen, H., Paul, S., Xu, H., Wang, K., Mahanthappa, M. K., & Sun, C. C. (2020). Reduction of Punch-Sticking Propensity of Celecoxib by Spherical Crystallization via Polymer Assisted Quasi-Emulsion Solvent Diffusion. *Molecular Pharmaceutics*, 17(4), 1387–1396. <https://doi.org/10.1021/acs.molpharmaceut.0c00086>
- (5) Cong, Y., Du, C., Xing, K., Bian, Y., Li, X., & Wang, M. (2022). Research on solubility modelling of actarit in different solvents: Solvent effect, Hansen solubility parameter, molecular interactions and solution thermodynamics. *Journal of Molecular Liquids*, 347, 117965. <https://doi.org/10.1016/j.molliq.2021.117965>
- (6) Cui, P., Yang, W., Jia, L., Zhou, L., Zhang, M., Bao, Y., Xie, C., Hou, B., & Yin, Q. (2022). Spherulitic Growth Strategy for Agitation-Induced Formation of Spherical Amoxicillin Sodium Products. *Industrial & Engineering Chemistry Research*, 61(27), 9821–9832. <https://doi.org/10.1021/acs.iecr.2c01179>
- (7) Du, Y., Wang, H., Du, S., Wang, Y., Huang, C., Qin, Y., & Gong, J. (2016). The liquid–liquid phase separation and crystallization of vanillin in 1-propanol/water solution. *Fluid Phase Equilibria*, 409, 84–91. <https://doi.org/10.1016/j.fluid.2015.09.011>
- (8) Duggirala, N. K., Perry, M. L., Almarsson, Ö., & Zaworotko, M. J. (2016). Pharmaceutical cocrystals: Along the path to improved medicines. *Chemical Communications*, 52(4), 640–655. <https://doi.org/10.1039/C5CC08216A>
- (9) Gong, W., Li, P., & Rohani, S. (2022). Taurine in several aqueous binary solvents: Solubility prediction, measurement, modeling, solvent effect, and thermodynamics. *Journal of Molecular Liquids*, 367, 120522. <https://doi.org/10.1016/j.molliq.2022.120522>
- (10) Guo, W. (2022). Improving powder performances of natural extracted lutein with spherulitic growth control. *Powder Technology*.
- (11) Hansen, C. M. (2007). *Hansen solubility parameters: A user's handbook* (2nd ed). CRC Press.
- (12) Hatcher, L. E., Li, W., Payne, P., Benyahia, B., Rielly, C. D., & Wilson, C. C. (2020). Tuning Morphology in Active Pharmaceutical Ingredients: Controlling the Crystal Habit of Lovastatin through Solvent Choice and Non-Size-Matched Polymer Additives. *Crystal Growth & Design*, 20(9), 5854–5862.

<https://doi.org/10.1021/acs.cgd.0c00470>

- (13) He, H., Sun, R., Wan, Y., Jiang, G., Sha, J., Li, Y., Li, T., & Ren, B. (2020). Solubility measurement, model evaluation and Hansen solubility parameter of piperonylnitrile in four binary solvents. *The Journal of Chemical Thermodynamics*, 151, 106249. <https://doi.org/10.1016/j.jct.2020.106249>
- (14) He, Q., & Zhao, H. (2021). Imidacloprid (I) in several aqueous co-solvent mixtures: Solubility, solvent effect, solvation thermodynamics and enthalpy–entropy compensation. *Journal of Molecular Liquids*, 338, 116781. <https://doi.org/10.1016/j.molliq.2021.116781>
- (15) Kawashima, Y. (1984). Development of spherical crystallization technique and its application to pharmaceutical systems. *Archives of Pharmacal Research*, 7(2), 145–151. <https://doi.org/10.1007/BF02856629>
- (16) Kawashima, Y., Okumura, M., & Takenaka, H. (1982). Spherical Crystallization: Direct Spherical Agglomeration of Salicylic Acid Crystals During Crystallization. *Science*, 216(4550), 1127–1128. <https://doi.org/10.1126/science.216.4550.1127>
- (17) Kim, H. (2018). Correlation between solubility parameters and recovery of phenolic compounds from fast pyrolysis bio-oil by diesel extraction.
- (18) Liu, Y., Ma, Y., Yu, C., Gao, Y., Li, K., Tong, L., Chen, M., & Gong, J. (2022). Spherical agglomeration of high melting point drugs in water at low temperature by developing a two-step oiling-out mechanism and the design strategy. *Green Chemistry*.
- (19) Liu, Y., Wang, S., Li, J., Guo, S., Yan, H., Li, K., Tong, L., Gao, Y., Li, T., Chen, M., Gao, Z., & Gong, J. (2023). Preparation of ethyl vanillin spherical particles with functions of sustained release and anti-caking by an organic solvent-free process. *Food Chemistry*, 402, 134518. <https://doi.org/10.1016/j.foodchem.2022.134518>
- (20) Ma, Y., Sun, M., Liu, Y., Chen, M., Wu, S., Wang, M., Wang, L., Gao, Z., Han, D., Liu, L., Wang, J., & Gong, J. (2021). Design of Spherical Crystallization of Active Pharmaceutical Ingredients via a Highly Efficient Strategy: From Screening to Preparation. *ACS Sustainable Chemistry & Engineering*, 9(27), 9018–9032. <https://doi.org/10.1021/acssuschemeng.1c01973>
- (21) Sun, M., Shichao, D., Tang, W., Jia, L., & Gong, J. (2019). Design of Spherical Crystallization for Drugs Based on Thermal-Induced Liquid–Liquid Phase Separation: Case Studies of Water-Insoluble Drugs. *Industrial & Engineering Chemistry Research*, 58(44), 20401–20411. <https://doi.org/10.1021/acs.iecr.9b03795>

- (22) Wang, S., Liu, Y., Guo, S., Yan, H., Li, K., Tong, L., Li, T., Chen, M., Gao, Z., & Gong, J. (2022). Design of Single and Multicomponent Drug Spherical Particles with Improved Powder Properties in Water Instead of Organic Solvents: A Case Study of Gemfibrozil. *ACS Sustainable Chemistry & Engineering*, 10(37), 12411–12422. <https://doi.org/10.1021/acssuschemeng.2c03982>
- (23) Zhang, H., Zhang, K., Yu, M., Guo, J., Xu, S., & Wang, Y. (2022). Insight into solid-liquid and liquid-liquid phase equilibrium behavior of vanillin and ethyl vanillin. *Journal of Molecular Liquids*, 365, 120059. <https://doi.org/10.1016/j.molliq.2022.120059>
- (24) Zhao, H., Xie, C., Xu, Z., Wang, Y., Bian, L., Chen, Z., & Hao, H. (2012). Solution Crystallization of Vanillin in the Presence of a Liquid–Liquid Phase Separation. *Industrial & Engineering Chemistry Research*, 51(45), 14646–14652. <https://doi.org/10.1021/ie302360u>
- (25) Zhou, Y., Wang, J., Wang, T., Wang, N., Xiao, Y., Zong, S., Huang, X., & Hao, H. (2019). Self-Assembly of Monodispersed Carnosine Spherical Crystals in a Reverse Antisolvent Crystallization Process. *Crystal Growth & Design*, 19(5), 2695–2705. <https://doi.org/10.1021/acs.cgd.8b01818>

Chapter 6

Main Contributions and Conclusions of the Thesis, Recommendations for Future Work

6. Main Contributions and Conclusions of the Thesis, Recommendations for Future Work

6.1 Conclusions

In this work, the design and control of pharmaceuticals solid state was studied numerically and experimentally. The work started from the solubility prediction of an API, which is the basis of solution crystallization. With a given solvent, a guideline of polymorph control in continuous crystallization was developed based on the corresponding seeding strategies. For an API that has undesired physicochemical properties regardless of the polymorph, a systematic screening method for coformers and salt formers was developed and applied to generate new API multicomponent solid states. Lastly, a new spherical crystallization technology was developed with the help of an in-situ image-based PAT instrument.

6.1.1 Solubility Study

The driving force of solution crystallization: supersaturation, is based on the solubility of the API in a selected solvent. The solvent screening based on solubility prediction is the basis of the crystallization research. A solubility prediction using Hansen solubility parameters and the molecular interaction analysis based on KAT-LSER was fully developed and validated by experimental observation, in Chapter 2.

With the aid of Hansen solubility parameters, taurine's solubility in four binary solvents was predicted. The solubility was highest in ACN-water, followed by EG-water, PG-water, and then acetone-water. With the decrease of the water content in the system, the dielectric constant of the binary solvent decreases significantly, which makes it difficult for the taurine molecule to overcome the electrostatic interaction in water molecules. Thus, the solubility of taurine decreased significantly. The dipolarity–polarizability

parameter (π^*) was found to be the most important factor that affects the solubility of taurine.

The findings in Chapter 2 provided a qualitative solubility prediction tool for solvent screening, future research applying machine learning with HSPs would be a useful tool for other crystallization processes.

6.1.2 Polymorph Control in Continuous Crystallization

In batch crystallization, a thermodynamically stable polymorph can be obtained through solution-mediated polymorphic transformation with enough batch time. Introducing seed crystals at the beginning is the common strategy of polymorph control in a batch operation. However, initial seeds would be washed out of the crystallizer in a continuous production. The interplay of growth and nucleation kinetics of polymorphs under different working temperatures dominates the product polymorphic outcome in a continuous crystallization. The pure stable β form of L-glutamic acid was obtained at 45°C in an MSMPR and the metastable α form can be obtained below 25°C.

A design of a two-stage MSMSPR crystallizer configuration with different working temperatures realizes the continuous seeding of the stable β form of L-glutamic acid from the first MSMPR to the second (production) crystallizer. Another design using the intermittent seeding strategy with the desirable polymorph to a single-stage MSMPR was also explored. The idea is to stimulate the secondary nucleation of the targeted polymorph in the MSMPR. Numerical simulation and crystallization experiments of these two designs were attempted and optimized in MATLAB and were discussed in detail in Chapter 3.

It has been found that with the same feed concentration and residence time, switching from a single-stage MSMPR to a two-stage MSMPR, a significant improvement in the production rate (0.033g/min to 0.044g/min at 60-minutes residence time, 0.063g/min to

0.073g/min at 30-minutes residence time) of L-glutamic acid was observed. Nevertheless, decreasing the operating temperature of the second stage MSMPR did not improve the yield (the experimental yields were 56.1%, 53.3%, and 56.4% under 35°C, 30°C, and 25°C) as β form LGA reached kinetically unfavorable temperatures. For the intermittent seeding strategy, it was found that supersaturation played a decisive role in harvesting the pure β -form LGA while operating under low temperatures. An operating temperature of 30°C in a 150-ml MSMPR crystallizer, with five times per one residence time seeding frequency with 0.1g of seeds loading per charge, and a feed concentration of 0.02 kg/kg were considered as the most suitable conditions for the production of pure β -form L-glutamic acid. The results of this research provide guidelines to harvest the desirable polymorph of an active pharmaceutical and maximize its yield and purity for the operation of a single MSMPR, a two-stage MSMPR, and the intermittent seeding of a single-stage MSMPR.

6.1.3 Cocrystal/Salt Screening

The crystalline solid states contain polymorphs, solvates and hydrates, cocrystals, and salts. Pharmaceutical cocrystals advantages include a well-defined stoichiometry, higher thermal and humidity stability. Pharmaceutical salts formulation can increase the solubility and dissolution of APIs in polar solvents. Crystalline solid state of olanzapine (OLN), a BCS class II API, was researched to improve its solubility and dissolution by cocrystal and salt formation design in Chapter 4.

With the aim of the hydrogen bond propensity and coordination calculations, multicomponent crystals of OLN with coformers (phenol, resorcinol) and salt-formers (salicylic acid, anthranilic acid, 3-hydroxy benzoic acid, 2-aminoterephthalic acid) were successfully obtained through liquid-assisted grinding and ball milling. The “ ΔpK_a rule of 3” was proven to be accurate in the distinction of cocrystals and salts formation. Olanzapinium salts showed similar charge-assisted bonds and hydrogen bonds in their

structures. The acidic proton of carboxylic acid transferred to the piperidine N, and the carbonyl group also interacted with the diazepine N of OLN as a hydrogen acceptor.

It was found that all salts showed significant improvement in solubility; OLN-2ATPA showed almost a fivefold increase, and OLN-AA, OLN-3HBA showed a threefold increase in solubility.

6.1.4 Spherical Crystallization Based on LLPS

Crystals with poor morphologies always cause difficulties for the downstream processes. Spherical crystallization technology directly combines the downstream granulation processes with crystallization and thus avoid such problems. An additive is always required to be introduced as the bridging liquid or the emulsifier in spherical crystallization. A new spherical crystallization technology based on the vanillin liquid-liquid phase separation phenomenon was developed in this thesis and discussed in detail in Chapter 5.

The ternary phase diagram was first developed experimentally and drawn to confirm the oiling out phenomenon. Based on the phase diagram, a reverse antisolvent crystallization process was proposed to produce spherical crystals. The process was monitored by an in-situ process analytical technology: PCM. Then a six-step spherical crystallization mechanism was clearly revealed by PCM and summarized as: (a) the generation of oil droplets, (b) nucleation of vanillin inside oil droplets, (c) the coalescence and splitting of oil droplets, (d) crystal growth and agglomeration, (e) breakage of oil droplets, (f) attrition. It is found that only primary agglomeration inside the oil droplet can form spherical crystals. Thus, a surfactant is needed to maintain the oil phase that offers the platform of vanillin nucleation and agglomeration. An inlet composition of 2:1:4 (water:1-propanol:vanillin) at 30°C with 0.5wt% sodium dodecyl sulfate in the antisolvent using a 110-rpm mechanical stirring during addition and a 200-rpm stirring

during aging is found to be the best working condition to produce narrow particle size distribution and good morphology of the resulting vanillin spherical agglomerates. The results of the present investigation provide a new technology to produce spherical agglomerates without introducing any additives.

6.2 Significance of the Research

This work has made significant contributions to the design and control of API solid states. Several numerical predictions offer fast and accurate results for solubility prediction, cocrystal and salt screening, and polymorphism control.

First, contributions have been made in solvent screening and prediction of solubility of a given pharmaceutical in different solvents. Efforts were made to predict the solubility, solvent effect, and molecular interactions of a given API in some aqueous co-solvent mixtures by means of experiment and mathematical correlations. The selection of proper solvent is the basis of the crystallization process design.

Another major contribution of the present work is the development of efficient numerical modeling for a single-stage and two-stage MSMPR for the harvesting of a desired pharmaceutical polymorph. Polymorphism control is a fundamental requirement for the production of pharmaceuticals and fine chemicals using crystallization. A systematic guideline for the polymorphism control in continuous crystallization is lacking. The present work offers a clear seeding strategy based on the secondary nucleation for continuous crystallization.

The work has also provided significant elucidation of the pharmaceutical cocrystals and salts screening. Although polymorphism control can improve physicochemical properties like solubility to some extent, the biggest restriction is still the API molecule itself. The formation of pharmaceutical cocrystals and salts can significantly improve the targeted property by introducing suitable cofomers or salt formers. The screening of

pharmaceutical cocrystals and salts primarily depend on experimental validations. A conjunction of hydrogen-bond propensity and hydrogen-bond coordination calculations offers an accurate screening procedure and saves great amount of time and money.

Finally, an effective approach is proposed to successfully conduct spherical crystallization of pharmaceutical products with poor morphology and hence improve their morphology. Poor crystal morphology affects the dissolution and filtration of the crystal product. The spherical crystallization based on liquid-liquid phase separation omits the the downstream granulation process without introducing hazardous solvents.

Overall, significant contributions have been made in a few highly important areas of crystal engineering and industrial crystallization of active pharmaceutical ingredients.

6.3 Recommendations

Future works on the accuracy of the screening results and the scale-up of the cocrystallization process with suitable process analytical technologies (PATs) would be valuable.

The following is a list of the most important recommendations based on the studies carried out in this thesis for future consideration:

1. Machine learning has gained attention and has been developed fast in recent years. For cocrystal/salt screening and solubility prediction, AI techniques combined with HSP or HBC, HBP calculations can not only offer a statistically accurate prediction result, but also provide scientific explanations behind it.
2. In an industrial setup, introducing seeds manually is cumbersome and the efficiency is low. Most APIs are toxic and would cause harm to operators. To realize the intermittent seeding strategy proposed in this work is therefore highly significant. The adoption of the proposed strategy in the design of pharmaceutical products using solid

recycle with wet milling would provide significant advantage. Part of the crystal products with the desired polymorph can be recycled and milled to a suitable size as seed crystals and sent back to the continuous crystallizer. Manual work is no longer required as a result. The design idea is based on the use of secondary nucleation using the recycling of the some of the crystalline product.

3. Currently, the production scale of pharmaceutical cocrystal is very small. The scale up procedure for large-scale cocrystal production is an important area that remains to be solved. Unlike the liquid assisted grinding in lab, a huge amount of a suitable solvent approved by FDA that dissolves both the API and the selected cofomer or salt former can be used during crystallization. How to realize a continuous cocrystallization process is an area open for further investigation.
4. Single crystals are not always achievable. High-throughput electron diffraction could be applied to obtain the information of crystal structures without making single crystals.
5. The spherical crystallization based on liquid-liquid separation is restricted to APIs that cause the oiling out phenomenon. The melting of the API can also cause the LLPS and research of spherical crystallization can be extended on such types of oiling out. In solution crystallization, the search for a green additive is the future target. The shape of the final spherical agglomerate is determined by the shape of oil droplets inside the crystallizer when using this technique. A process control system on the number and shape of the oil phase droplets in the system is important for industrial production.

Appendices

Appendix A: Chapter 3 appendix

Table A-1. UNIQUAC parameters for taurine and related solvents ^a

| UNIQUAC | Acetonitrile ^S (Rabhi et al., 2021) | H ₂ O ^S (Abrams & Prausnitz, 1975) | Ethylene Glycol ^S (Haghnazarloo et al., 2013) | 1,2-propanediol ^S (Chang et al., 2015) | Taurine | acetone ^S (Abrams & Prausnitz, 1975) |
|---|--|--|--|---|------------|---|
| r | 1.87 | 0.92 | 2.4088 | 3.2822 | 3.995 | 2.57 |
| q | 1.724 | 1.4 | 2.2488 | 2.7839 | 4.921 | 2.34 |
| Taurine ^S (Huang et al., 2021) | number | R_i | Q_i | $\sum R_i$ | $\sum Q_i$ | |
| C | 2 | 12.39 | 2.19 | 24.78 | 4.38 | |
| H | 7 | 4.36 | 1.09 | 30.52 | 7.63 | |
| N | 1 | 9.39 | 1.82 | 9.39 | 1.82 | |
| O | 3 | 8.51 | 1.7 | 25.53 | 5.1 | |
| S | 1 | 14.7 | 2.45 | 14.7 | 2.45 | |
| C-H | 4 | -3.17 | -0.092 | -12.68 | -0.368 | |
| N-H | 2 | -2.95 | -0.66 | -5.9 | -1.32 | |
| C-N | 1 | -3.76 | -1.07 | -3.76 | -1.07 | |
| C-S | 1 | -4.82 | -1.16 | -4.82 | -1.16 | |
| SO ₃ | 1 | -10.27 | -3.17 | -10.27 | -3.17 | |
| O-H | 1 | -2.59 | -0.83 | -2.59 | -0.83 | |
| C-C | 1 | -4.3 | -1.16 | -4.3 | -1.16 | |
| V_{vw} | 15.17 | total | R | 60.6 | r | 3.99 |
| A_{vw} | 2.5 | | Q | 12.302 | q | 4.92 |

Table A-2. Calculated mole fraction solubilities of taurine using the modified Apelblat model, NRTL, UNIQUAC, Wilson, and λ h models

| water (w_1) - PG ($1-w_1$) | | | | | |
|----------------------------------|----------|----------|----------|----------|----------|
| NRTL | | | | | |
| $w_1/T(K)$ | 298.15 | 303.15 | 308.15 | 313.15 | 318.15 |
| 1 | 0.013576 | 0.016362 | 0.020001 | 0.023806 | 0.028465 |
| 0.9 | 0.00514 | 0.006673 | 0.008241 | 0.008911 | 0.0119 |
| 0.8 | 0.002888 | 0.003378 | 0.00438 | 0.005473 | 0.00695 |
| 0.7 | 0.001696 | 0.001645 | 0.002538 | 0.003123 | 0.004472 |
| 0.6 | 0.001416 | 0.001341 | 0.001507 | 0.001884 | 0.003047 |
| 0.5 | 0.000615 | 0.000885 | 0.000902 | 0.001032 | 0.001786 |
| UNIQUAC | | | | | |
| $w_1/T(K)$ | 298.15 | 303.15 | 308.15 | 313.15 | 318.15 |
| 1 | 0.01454 | 0.016919 | 0.019975 | 0.022989 | 0.026596 |
| 0.9 | 0.005184 | 0.006658 | 0.008135 | 0.008724 | 0.011489 |
| 0.8 | 0.00289 | 0.003374 | 0.004361 | 0.00543 | 0.006864 |
| 0.7 | 0.001733 | 0.001682 | 0.002593 | 0.003189 | 0.004563 |
| 0.6 | 0.001443 | 0.001367 | 0.001537 | 0.001924 | 0.003118 |
| 0.5 | 0.000598 | 0.000862 | 0.000878 | 0.001007 | 0.00175 |
| Wilson | | | | | |
| $w_1/T(K)$ | 298.15 | 303.15 | 308.15 | 313.15 | 318.15 |
| 1 | 0.015592 | 0.017598 | 0.020166 | 0.022599 | 0.025508 |
| 0.9 | 0.005399 | 0.006726 | 0.007978 | 0.008361 | 0.01061 |
| 0.8 | 0.003009 | 0.003465 | 0.004393 | 0.00536 | 0.006615 |
| 0.7 | 0.001756 | 0.001708 | 0.002597 | 0.003164 | 0.004437 |
| 0.6 | 0.001421 | 0.001359 | 0.001533 | 0.001916 | 0.003053 |
| 0.5 | 0.000595 | 0.000863 | 0.000891 | 0.001028 | 0.001771 |

Modified Apelblat Model

| $w_1/T(K)$ | 298.15 | 303.15 | 308.15 | 313.15 | 318.15 |
|------------|----------|----------|----------|----------|----------|
| 1 | 0.014256 | 0.016818 | 0.019802 | 0.02318 | 0.026925 |
| 0.9 | 0.00557 | 0.006668 | 0.007989 | 0.009516 | 0.011237 |
| 0.8 | 0.002962 | 0.003541 | 0.004322 | 0.005294 | 0.006444 |
| 0.7 | 0.001721 | 0.001979 | 0.002458 | 0.003142 | 0.004019 |
| 0.6 | 0.001284 | 0.001305 | 0.001543 | 0.001983 | 0.002613 |
| 0.5 | 0.000703 | 0.000785 | 0.000962 | 0.001228 | 0.001576 |

 λh Model

| $w_1/T(K)$ | 298.15 | 303.15 | 308.15 | 313.15 | 318.15 |
|------------|----------|----------|----------|----------|----------|
| 1 | 0.013457 | 0.01632 | 0.019658 | 0.023527 | 0.027982 |
| 0.9 | 0.005547 | 0.00668 | 0.007995 | 0.009514 | 0.011258 |
| 0.8 | 0.002483 | 0.003243 | 0.004197 | 0.005387 | 0.006858 |
| 0.7 | 0.001581 | 0.002013 | 0.002545 | 0.003192 | 0.003975 |
| 0.6 | 0.000985 | 0.001289 | 0.001671 | 0.002149 | 0.00274 |
| 0.5 | 0.00054 | 0.000727 | 0.000971 | 0.001283 | 0.001682 |

water (w_1) - ACN ($1-w_1$)**NRTL**

| $w_1/T(K)$ | 298.15 | 303.15 | 308.15 | 313.15 | 318.15 |
|------------|----------|----------|----------|----------|----------|
| 1 | 0.015236 | 0.017532 | 0.020075 | 0.022885 | 0.025972 |
| 0.9 | 0.010537 | 0.01217 | 0.013992 | 0.016014 | 0.01825 |
| 0.8 | 0.006336 | 0.007314 | 0.008407 | 0.009625 | 0.010977 |
| 0.7 | 0.003681 | 0.004222 | 0.004824 | 0.005492 | 0.006233 |
| 0.6 | 0.002043 | 0.002318 | 0.002623 | 0.002958 | 0.003326 |
| 0.5 | 0.001017 | 0.001138 | 0.001272 | 0.001417 | 0.001577 |

UNIQUAC

| $w_1/T(K)$ | 298.15 | 303.15 | 308.15 | 313.15 | 318.15 |
|------------|----------|----------|----------|----------|----------|
| 1 | 0.013941 | 0.016686 | 0.019931 | 0.023659 | 0.027984 |
| 0.9 | 0.010007 | 0.011756 | 0.013761 | 0.016065 | 0.018712 |
| 0.8 | 0.006406 | 0.007405 | 0.008534 | 0.009827 | 0.011278 |
| 0.7 | 0.003764 | 0.004311 | 0.004923 | 0.005603 | 0.006357 |
| 0.6 | 0.002029 | 0.002309 | 0.00262 | 0.002962 | 0.00334 |
| 0.5 | 0.000988 | 0.001119 | 0.001263 | 0.001422 | 0.001594 |

Wilson

| $w_1/T(K)$ | 298.15 | 303.15 | 308.15 | 313.15 | 318.15 |
|------------|----------|----------|----------|----------|----------|
| 1 | 0.015039 | 0.016862 | 0.019195 | 0.021395 | 0.024031 |
| 0.9 | 0.010372 | 0.011969 | 0.013644 | 0.015656 | 0.018197 |
| 0.8 | 0.007138 | 0.00755 | 0.008229 | 0.010368 | 0.01233 |
| 0.7 | 0.004255 | 0.004889 | 0.004783 | 0.005059 | 0.006422 |
| 0.6 | 0.002559 | 0.002681 | 0.002598 | 0.002771 | 0.003008 |
| 0.5 | 0.001146 | 0.001098 | 0.001051 | 0.001039 | 0.001577 |

Modified Apelblat Model

| $w_1/T(K)$ | 298.15 | 303.15 | 308.15 | 313.15 | 318.15 |
|------------|----------|----------|----------|----------|----------|
| 1 | 0.014256 | 0.016818 | 0.019802 | 0.02318 | 0.026925 |
| 0.9 | 0.009852 | 0.011662 | 0.013906 | 0.016558 | 0.01959 |
| 0.8 | 0.006315 | 0.007084 | 0.008376 | 0.010157 | 0.012396 |
| 0.7 | 0.00379 | 0.004151 | 0.004729 | 0.00551 | 0.00648 |
| 0.6 | 0.002169 | 0.002358 | 0.00261 | 0.00292 | 0.003283 |
| 0.5 | 0.001092 | 0.001076 | 0.001177 | 0.001388 | 0.001701 |

 λh Model

| $w_1/T(K)$ | 298.15 | 303.15 | 308.15 | 313.15 | 318.15 |
|------------|----------|---------|----------|----------|----------|
| 1 | 0.013457 | 0.01632 | 0.019658 | 0.023527 | 0.027982 |

| | | | | | |
|-----|----------|----------|----------|----------|----------|
| 0.9 | 0.009699 | 0.011673 | 0.013961 | 0.016598 | 0.01962 |
| 0.8 | 0.005972 | 0.007206 | 0.008641 | 0.0103 | 0.012209 |
| 0.7 | 0.002677 | 0.003485 | 0.004499 | 0.005759 | 0.007312 |
| 0.6 | 0.001558 | 0.001976 | 0.002487 | 0.003108 | 0.003856 |
| 0.5 | 0.000648 | 0.000867 | 0.00115 | 0.00151 | 0.001967 |

water (w_1) - EG ($1-w_1$)

NRTL

| $w_1/T(K)$ | 298.15 | 303.15 | 308.15 | 313.15 | 318.15 |
|------------|----------|----------|----------|----------|----------|
| 1 | 0.014936 | 0.017193 | 0.019695 | 0.02246 | 0.0255 |
| 0.9 | 0.008885 | 0.010392 | 0.01209 | 0.013995 | 0.016123 |
| 0.8 | 0.005898 | 0.006964 | 0.008176 | 0.00955 | 0.011097 |
| 0.7 | 0.004277 | 0.00508 | 0.005993 | 0.007035 | 0.008215 |
| 0.6 | 0.003329 | 0.003962 | 0.00469 | 0.005524 | 0.006468 |
| 0.5 | 0.00274 | 0.003264 | 0.003867 | 0.004561 | 0.005343 |

UNIQUAC

| $w_1/T(K)$ | 298.15 | 303.15 | 308.15 | 313.15 | 318.15 |
|------------|----------|----------|----------|----------|----------|
| 1 | 0.013667 | 0.016535 | 0.019914 | 0.023863 | 0.028467 |
| 0.9 | 0.008234 | 0.009885 | 0.011813 | 0.014053 | 0.016653 |
| 0.8 | 0.005847 | 0.006945 | 0.008211 | 0.009674 | 0.01135 |
| 0.7 | 0.004432 | 0.005219 | 0.006113 | 0.007137 | 0.008302 |
| 0.6 | 0.003483 | 0.004066 | 0.00473 | 0.005486 | 0.006335 |
| 0.5 | 0.002805 | 0.003253 | 0.003758 | 0.004333 | 0.004968 |

Wilson

| $w_1/T(K)$ | 298.15 | 303.15 | 308.15 | 313.15 | 318.15 |
|------------|----------|----------|----------|----------|----------|
| 1 | 0.014073 | 0.01675 | 0.019812 | 0.023295 | 0.027225 |
| 0.9 | 0.008594 | 0.010233 | 0.012123 | 0.014287 | 0.016765 |

| | | | | | |
|-----|----------|----------|----------|----------|----------|
| 0.8 | 0.005815 | 0.006913 | 0.008164 | 0.009615 | 0.011264 |
| 0.7 | 0.004264 | 0.005076 | 0.005978 | 0.007026 | 0.008217 |
| 0.6 | 0.003343 | 0.003963 | 0.004681 | 0.005521 | 0.006456 |
| 0.5 | 0.002759 | 0.003274 | 0.003864 | 0.004566 | 0.005322 |

Modified Apelblat Model

| $w_1/T(K)$ | 298.15 | 303.15 | 308.15 | 313.15 | 318.15 |
|------------|----------|----------|----------|----------|----------|
| 1 | 0.014256 | 0.016818 | 0.019802 | 0.02318 | 0.026925 |
| 0.9 | 0.008244 | 0.010162 | 0.012278 | 0.014578 | 0.01705 |
| 0.8 | 0.005898 | 0.007045 | 0.00828 | 0.009599 | 0.010994 |
| 0.7 | 0.004279 | 0.005245 | 0.006127 | 0.006932 | 0.007662 |
| 0.6 | 0.003277 | 0.003972 | 0.004764 | 0.005646 | 0.006611 |
| 0.5 | 0.002658 | 0.003308 | 0.00396 | 0.004615 | 0.005272 |

λh Model

| $w_1/T(K)$ | 298.15 | 303.15 | 308.15 | 313.15 | 318.15 |
|------------|----------|----------|----------|----------|----------|
| 1 | 0.013457 | 0.01632 | 0.019658 | 0.023527 | 0.027982 |
| 0.9 | 0.008467 | 0.010215 | 0.012247 | 0.014594 | 0.01729 |
| 0.8 | 0.005979 | 0.007025 | 0.008211 | 0.00955 | 0.011056 |
| 0.7 | 0.003367 | 0.004346 | 0.005563 | 0.007062 | 0.008894 |
| 0.6 | 0.002668 | 0.003475 | 0.004486 | 0.005743 | 0.007292 |
| 0.5 | 0.002117 | 0.002782 | 0.003621 | 0.004674 | 0.005983 |

water (w_1) - acetone ($1-w_1$)

NRTL

| $w_1/T(K)$ | 278.15 | 283.15 | 288.15 | 293.15 | 298.15 | 303.15 | 308.15 | 313.15 | 318.15 | 323.15 |
|------------|----------|----------|----------|----------|----------|----------|----------|----------|----------|----------|
| 1 | 0.00764 | 0.008996 | 0.01053 | 0.012259 | 0.0142 | 0.016359 | 0.018761 | 0.021422 | 0.024355 | 0.027551 |
| 0.9 | 0.002926 | 0.003514 | 0.004193 | 0.004964 | 0.005837 | 0.006825 | 0.007936 | 0.009177 | 0.010562 | 0.012136 |
| 0.8 | 0.001329 | 0.001607 | 0.001931 | 0.002306 | 0.002736 | 0.003227 | 0.003785 | 0.004417 | 0.00513 | 0.005928 |

| | | | | | | | | | | |
|-----|----------|----------|----------|----------|----------|----------|----------|----------|----------|----------|
| 0.7 | 0.000638 | 0.000772 | 0.000929 | 0.001111 | 0.001321 | 0.001563 | 0.001838 | 0.002152 | 0.002508 | 0.002909 |
| 0.6 | 0.000298 | 0.000361 | 0.000434 | 0.000518 | 0.000617 | 0.00073 | 0.000859 | 0.001007 | 0.001176 | 0.001366 |
| 0.5 | 0.000126 | 0.000153 | 0.000184 | 0.00022 | 0.000261 | 0.00031 | 0.000365 | 0.000429 | 0.000502 | 0.000584 |

UNIQUAC

| $w_1/T(K)$ | 278.15 | 283.15 | 288.15 | 293.15 | 298.15 | 303.15 | 308.15 | 313.15 | 318.15 | 323.15 |
|------------|----------|----------|----------|----------|----------|----------|----------|----------|----------|----------|
| 1 | 0.006283 | 0.007744 | 0.009494 | 0.011564 | 0.014001 | 0.01688 | 0.020229 | 0.024111 | 0.028593 | 0.033805 |
| 0.9 | 0.002712 | 0.003309 | 0.004012 | 0.004841 | 0.005814 | 0.006945 | 0.008257 | 0.009774 | 0.011517 | 0.013467 |
| 0.8 | 0.001325 | 0.001614 | 0.001953 | 0.00235 | 0.00281 | 0.003345 | 0.003965 | 0.004674 | 0.005479 | 0.006405 |
| 0.7 | 0.000621 | 0.000756 | 0.000914 | 0.001098 | 0.001311 | 0.001558 | 0.001841 | 0.002164 | 0.002533 | 0.002951 |
| 0.6 | 0.000285 | 0.000346 | 0.000418 | 0.000501 | 0.000598 | 0.000709 | 0.000837 | 0.000982 | 0.001148 | 0.001333 |
| 0.5 | 0.000128 | 0.000155 | 0.000187 | 0.000225 | 0.000268 | 0.000317 | 0.000374 | 0.000438 | 0.000511 | 0.000593 |

Wilson

| $w_1/T(K)$ | 278.15 | 283.15 | 288.15 | 293.15 | 298.15 | 303.15 | 308.15 | 313.15 | 318.15 | 323.15 |
|------------|----------|----------|----------|----------|----------|----------|----------|----------|----------|----------|
| 1 | 0.005144 | 0.006729 | 0.008838 | 0.011376 | 0.014421 | 0.01839 | 0.022967 | 0.028258 | 0.034378 | 0.042002 |
| 0.9 | 0.002154 | 0.002746 | 0.003459 | 0.004395 | 0.005607 | 0.007075 | 0.00887 | 0.011073 | 0.013689 | 0.016262 |
| 0.8 | 0.001018 | 0.001284 | 0.001598 | 0.001988 | 0.002436 | 0.003003 | 0.003715 | 0.004531 | 0.005448 | 0.006615 |
| 0.7 | 0.000514 | 0.000636 | 0.000784 | 0.000961 | 0.001168 | 0.001415 | 0.001711 | 0.002047 | 0.002452 | 0.002916 |
| 0.6 | 0.00027 | 0.00033 | 0.000402 | 0.000487 | 0.000586 | 0.000703 | 0.000841 | 0.001002 | 0.001187 | 0.001386 |
| 0.5 | 0.000144 | 0.000175 | 0.000212 | 0.000256 | 0.000307 | 0.000365 | 0.000433 | 0.000511 | 0.000599 | 0.000697 |

Modified Apelblat Model

| $w_1/T(K)$ | 278.15 | 283.15 | 288.15 | 293.15 | 298.15 | 303.15 | 308.15 | 313.15 | 318.15 | 323.15 |
|------------|----------|----------|----------|----------|----------|----------|----------|----------|----------|----------|
| 1 | 0.006902 | 0.008143 | 0.009807 | 0.011864 | 0.014287 | 0.017051 | 0.020133 | 0.02351 | 0.027162 | 0.031072 |
| 0.9 | 0.002513 | 0.0031 | 0.003878 | 0.004834 | 0.005956 | 0.007231 | 0.008651 | 0.010203 | 0.011881 | 0.013674 |
| 0.8 | 0.001283 | 0.001522 | 0.001853 | 0.00227 | 0.002767 | 0.003337 | 0.003977 | 0.004681 | 0.005446 | 0.006266 |
| 0.7 | 0.000611 | 0.000744 | 0.000915 | 0.001121 | 0.001359 | 0.001629 | 0.001926 | 0.00225 | 0.002599 | 0.002971 |
| 0.6 | 0.000295 | 0.000346 | 0.000417 | 0.000507 | 0.000614 | 0.000736 | 0.000874 | 0.001025 | 0.00119 | 0.001366 |
| 0.5 | 0.000129 | 0.000158 | 0.000192 | 0.000231 | 0.000273 | 0.000318 | 0.000367 | 0.000419 | 0.000474 | 0.000532 |

λh Model

| $w_1/T(K)$ | 278.15 | 283.15 | 288.15 | 293.15 | 298.15 | 303.15 | 308.15 | 313.15 | 318.15 | 323.15 |
|------------|----------|----------|----------|----------|----------|----------|----------|----------|----------|----------|
| 1 | 0.005482 | 0.006909 | 0.008635 | 0.010707 | 0.013175 | 0.016095 | 0.019524 | 0.023523 | 0.028158 | 0.033493 |
| 0.9 | 0.002671 | 0.003293 | 0.004031 | 0.004899 | 0.005914 | 0.007096 | 0.008462 | 0.010035 | 0.011834 | 0.013884 |
| 0.8 | 0.000634 | 0.000866 | 0.00117 | 0.001565 | 0.002071 | 0.002716 | 0.003531 | 0.00455 | 0.005815 | 0.007374 |
| 0.7 | 0.000344 | 0.000463 | 0.000615 | 0.000811 | 0.001059 | 0.00137 | 0.001758 | 0.002237 | 0.002826 | 0.003543 |
| 0.6 | 9.61E-05 | 0.000139 | 0.000198 | 0.00028 | 0.00039 | 0.000538 | 0.000734 | 0.000992 | 0.001327 | 0.00176 |
| 0.5 | 4.66E-05 | 6.86E-05 | 9.94E-05 | 0.000142 | 0.000202 | 0.000282 | 0.00039 | 0.000534 | 0.000724 | 0.000973 |

Table A-3. Kamlet-Taft parameters π^* (dipolarity-polarizability), α (hydrogen bond donor parameter) and β (hydrogen bond donor parameter) and Hildebrand solubility parameter, δ_h , of aqueous solution of PG, ACN, EG, and acetone at 298.15 K ^a

| EG (w_2)-Water ($1 - w_2$) ^S (Liu et al., 2021) | | | | | ACN (w_2)-Water ($1 - w_2$) ^S (Li et al., 2020) | | | | | PG (w_2)-Water ($1 - w_2$) ^S (Zheng et al., 2018) | | | | | Acetone (w_2)-Water ($1 - w_2$) ^S (Cong et al., 2022) | | | | |
|--|---------|---------|----------|------------|--|---------|---------|----------|------------|--|---------|---------|----------|------------|--|---------|---------|----------|------------|
| w_2 | π^* | β | α | δ_h | w_2 | π^* | β | α | δ_h | w_2 | π^* | β | α | δ_h | w_2 | π^* | β | α | δ_h |
| 0 | 1.09 | 0.47 | 1.17 | 47.82 | 0 | 1.09 | 0.47 | 1.17 | 47.82 | 0 | 1.09 | 0.47 | 1.17 | 47.82 | 0 | 1.09 | 0.47 | 1.17 | 47.82 |
| 0.1 | 1.17 | 0.47 | 0.90 | 44.07 | 0.1 | 1.04 | 0.60 | 0.99 | 42.08 | 0.1 | 1.11 | 0.61 | 1.04 | 42.35 | 0.1 | 1.08 | 0.53 | 1.13 | 44.38 |
| 0.2 | 1.15 | 0.48 | 0.83 | 41.44 | 0.2 | 0.96 | 0.60 | 0.91 | 37.99 | 0.2 | 1.06 | 0.70 | 0.95 | 38.95 | 0.2 | 1.07 | 0.58 | 1.07 | 41.11 |
| 0.3 | 1.09 | 0.49 | 0.84 | 39.43 | 0.3 | 0.91 | 0.60 | 0.90 | 34.81 | 0.3 | 1.02 | 0.72 | 0.91 | 36.68 | 0.3 | 1.05 | 0.63 | 1.01 | 38.00 |
| 0.4 | 1.06 | 0.49 | 0.84 | 37.95 | 0.4 | 0.87 | 0.58 | 0.90 | 32.35 | 0.4 | 0.99 | 0.73 | 0.88 | 35.02 | 0.4 | 1.02 | 0.66 | 0.94 | 35.05 |
| 0.5 | 1.03 | 0.50 | 0.83 | 36.71 | 0.5 | 0.85 | 0.57 | 0.90 | 30.38 | 0.5 | 0.96 | 0.73 | 0.87 | 33.71 | 0.5 | 0.98 | 0.68 | 0.87 | 32.24 |

^alinear interpolation is applied to calculate the values of π^* , β , α , δ_h at exact $w_2 = 0, 0.1, 0.2, 0.3, 0.4, \text{ and } 0.5$

Table A-4. MLRA results of the KAT-LSER model on solubility of taurine in water (1)
+ PG (2) mixture at 298.15 K*

| c0 | c1 | c2 | c3 | c4 | R2 | F |
|------------------------|----------------------|------------------|----------------------|-----------------|--------------|--------------|
| 29.981 (29.244) | -47.700 (28.875) | -18.382 (15.357) | 6.517 (3.464) | 22.633 (8.839) | 0.992 | 157.52 |
| -41.338 (17.319) | 23.945 (13.855) | 16.913 (13.156) | 1.006 (5.276) | | 0.970 | 55.01 |
| -18.190 (3.025) | | 6.433 (4.358) | 2.061 (2.967) | 8.483 (2.980) | 0.985 | 112.16 |
| -4.625 (4.859) | -13.892 (6.619) | | 2.945 (1.939) | 13.136 (4.297) | 0.990 | 172.27 |
| -13.522 (26.973) | -5.395 (27.290) | 6.510 (11.744) | | 12.299 (10.434) | 0.982 | 92.01 |
| -11.829 (3.741) | | -5.721 (1.608) | 9.330 (2.775) | | 0.950 | 48.74 |
| -19.181 (1.883) | 6.214 (1.450) | | 6.972 (2.768) | | 0.964 | 67.10 |
| -14.438 (1.933) | | | 5.414 (2.253) | 4.175 (0.707) | 0.979 | 120.00 |
| -44.087 (7.895) | 26.356 (4.657) | 19.119 (5.154) | | | 0.980 | 121.54 |
| -18.817 (2.626) | | 8.750 (2.550) | | 10.263 (1.381) | 0.988 | 203.03 |
| 1.264 (3.507) | -19.989 (6.304) | | | 17.567 (3.778) | 0.986 | 179.26 |
| -23.317 (3.738) | | | 16.766 (3.603) | | 0.805 | 21.67 |
| 0.527 (1.330) | | -9.801 (1.997) | | | 0.822 | 24.09 |
| -14.882 (1.216) | 9.231 (1.248) | | | | 0.915 | 54.72 |
| -9.834 (0.289) | | | | 5.626 (0.545) | 0.955 | 106.76 |

Table A-5. MLRA results of the KAT-LSER model on solubility of taurine in water (1)
+ ACN (2) mixture at 298.15 K*

| c0 | c1 | c2 | c3 | c4 | R2 | F |
|-----------------|------------------|------------------|-----------------|----------------|-------|--------|
| -1.024 (0.140) | 1.306 (0.164) | 21.658 (0.284) | -32.418 (0.351) | 19.977 (0.130) | 1.000 | 174245 |
| -2.436 (15.091) | -14.373 (13.884) | -14.221 (17.423) | 19.867 (8.860) | | 0.916 | 19.12 |
| -0.218 (0.546) | | 19.508 (0.502) | -30.221 (1.232) | 19.329 (0.578) | 1.000 | 7206.9 |

| | | | | | | |
|------------------------|-----------------|----------------------|-----------------------|----------------|--------------|--------------|
| 4.388 (6.481) | -10.576 (2.753) | | -7.607 (7.077) | 11.783 (3.980) | 0.979 | 79.24 |
| 0.962 (9.011) | -10.602 (6.623) | -2.680 (6.942) | | 8.264 (1.985) | 0.969 | 53.76 |
| -17.785 (2.841) | | 3.553 (3.001) | 10.842 (1.596) | | 0.914 | 27.49 |
| -14.709 (1.198) | -3.206 (2.228) | | 12.974 (2.523) | | 0.925 | 31.90 |
| -18.062 (6.624) | | | 14.638 (9.618) | -2.040 (4.018) | 0.884 | 19.96 |
| -34.189 (7.986) | 16.264 (3.782) | 23.024 (8.056) | | | 0.803 | 11.17 |
| -13.297 (1.673) | | 7.957 (2.479) | | 5.168 (0.551) | 0.953 | 52.18 |
| -2.479 (1.116) | -8.155 (1.623) | | | 7.582 (0.768) | 0.978 | 112.47 |
| -14.785 (1.347) | | | 9.820 (1.407) | | 0.905 | 48.69 |
| -1.155 (5.060) | | -7.486 (8.847) | | | 0.152 | 0.716 |
| -11.91 (2.895) | 6.745(2.994) | | | | 0.449 | 5.076 |
| -8.004 (0.510) | | | | 3.995 (0.751) | 0.845 | 28.29 |

Table A-6. MLRA results of the KAT-LSER model on solubility of taurine in water (1)
+ EG (2) mixture at 298.15 K*

| c0 | c1 | c2 | c3 | c4 | R2 | F |
|------------------------|----------------------|------------------|----------------------|----------------|--------------|----------------|
| -22.249 (5.203) | 5.775 (2.274) | 9.927 (2.915) | 9.751 (3.462) | -1.667 (2.173) | 0.999 | 1877.09 |
| -18.572 (1.805) | 4.035 (0.138) | 3.876 (2.293) | 7.136 (0.537) | | 1.000 | 3150.99 |
| -9.775 (3.313) | | 1.040 (4.787) | 1.018 (0.774) | 3.839 (0.286) | 0.998 | 671.36 |
| -15.430 (4.563) | 3.756 (2.687) | | 6.167 (3.801) | 0.059 (2.664) | 0.999 | 1297.34 |
| -7.976 (2.489) | -0.586 (0.556) | -0.101 (4.869) | | 4.360 (0.800) | 0.997 | 559.80 |
| 31.236 (10.079) | | -59.091 (13.327) | -7.218 (3.690) | | 0.849 | 15.05 |
| -15.531 (0.174) | 3.812 (0.060) | | 6.251 (0.152) | | 0.999 | 2918.30 |
| -9.059 (0.246) | | | 0.863 (0.247) | 3.782 (0.084) | 0.998 | 1475.74 |
| 5.118 (2.125) | 2.360 (0.432) | -25.826 (3.919) | | | 0.969 | 77.98 |
| -5.627 (1.127) | | -4.767 (2.064) | | 3.542 (0.195) | 0.997 | 809.32 |

| | | | | | | |
|-----------------|----------------|-----------------|---------------|---------------|-------|---------|
| -8.027 (0.0874) | -0.597 (0.189) | | | 4.377 (0.162) | 0.998 | 1259.28 |
| -12.362 (5.271) | | | 6.499 (4.788) | | 0.144 | 1.842 |
| 12.753 (4.581) | | -37.238 (9.491) | | | 0.742 | 15.39 |
| -8.715 (1.134) | 3.880 (1.246) | | | | 0.635 | 9.70 |
| -8.224 (0.110) | | | | 3.931 (0.141) | 0.994 | 773.98 |

Table A-7. MLRA results of the KAT-LSER model on solubility of taurine in water (1)
+ acetone (2) mixture at 298.15 K*

| c0 | c1 | c2 | c3 | c4 | R2 | F |
|------------------------|-----------------|-----------------|-----------------------|----------------|--------------|--------------|
| -21.573 (3.435) | -4.0411 (3.249) | 4.581 (7.018) | 9.043 (5.960) | 9.091 (3.089) | 1.000 | 1804.18 |
| -12.387 (3.154) | -4.3369 (7.124) | -15.091 (4.703) | 17.909 (11.304) | | 0.997 | 497.34 |
| -20.791 (3.816) | | 7.437 (7.495) | 2.627 (3.392) | 9.210 (3.488) | 0.999 | 1884.14 |
| -19.721 (1.636) | -4.7322 (2.588) | | 11.859 (3.4723) | 7.170 (0.795) | 1.000 | 3373.42 |
| -22.741 (4.302) | 0.20935 (2.099) | 12.289 (6.222) | | 11.459 (3.425) | 0.999 | 1456.50 |
| -11.418 (2.420) | | -12.302 (0.938) | 11.141 (1.820) | | 0.998 | 943.85 |
| -9.248 (6.071) | 17.942 (3.236) | | -15.528 (8.873) | | 0.986 | 180.72 |
| -17.183 (1.155) | | | 5.750 (1.261) | 5.758 (0.252) | 0.999 | 2840.42 |
| -9.129 (2.932) | 6.7637 (1.582) | -8.223 (2.236) | | | 0.995 | 495.39 |
| -23.070 (2.261) | | 12.823 (2.600) | | 11.778 (1.007) | 0.999 | 3260.89 |
| -14.357 (0.974) | 3.7739 (1.503) | | | 4.795 (0.823) | 0.998 | 1109.73 |
| -41.246 (5.470) | | | 32.651 (5.215) | | 0.884 | 39.21 |
| 3.325 (0.771) | | -17.477 (1.293) | | | 0.973 | 182.77 |
| -19.805 (0.836) | 12.396 (0.806) | | | | 0.979 | 236.47 |
| -11.925 (0.165) | | | | 6.829 (0.221) | 0.995 | 951.43 |

*Best Model Parameters are bolded in [Table A-4](#) to [Table A-7](#)

Appendix B: Chapter 4 appendix

Table B-1. Crystal data and structure refinement of OLN-Phol, OLN-Res, OLN-SA, OLN-AA, OLN-TA, and OLN-3HBA

| Identification code | OLN-Phol-H ₂ O | OLN-SA | OLA-AA |
|-------------------------|---|---|---|
| CCDC number | 2071661 | 2071662 | 2071665 |
| Crystallization Solvent | Toluene | Ethanol | Dichloromethane |
| Empirical formula | C ₂₃ H ₂₈ N ₄ O ₂ S | C ₂₄ H ₂₆ N ₄ O ₃ S | C ₂₄ H ₂₇ N ₅ O ₂ S |
| Formula weight | 424.55 | 450.55 | 449.56 |
| Temperature | 110(2) K | 110(2) K | 110(2) K |
| Wavelength | 0.71073 Å | 0.71073 Å | 0.71073 Å |
| Crystal system | Triclinic | Triclinic | Monoclinic |
| Space group | $P\bar{1}$ | $P\bar{1}$ | $P2_1/c$ |
| Unit cell dimensions | a = 9.250(3) Å | a = 9.230(5) Å | a = 14.745(6) Å |
| | b = 10.392(3) Å | b = 10.950(5) Å | b = 10.226(4) Å |
| | c = 11.851(3) Å | c = 12.042(6) Å | c = 15.356(7) Å |
| | $\alpha = 97.118(18)^\circ$. | $\alpha = 66.291(12)^\circ$. | $\alpha = 90^\circ$. |
| | $\beta = 94.895(7)^\circ$. | $\beta = 86.603(9)^\circ$. | $\beta = 102.759(3)^\circ$. |
| | $\gamma = 104.240(10)^\circ$. | $\gamma = 83.130(19)^\circ$. | $\gamma = 90^\circ$. |
| Volume | 1087.6(5) Å ³ | 1106.3(10) Å ³ | 2258.2(16) Å ³ |
| Z | 2 | 2 | 4 |

| | | | |
|-----------------------------------|--|--|--|
| Density (calculated) | 1.296 Mg/m ³ | 1.353 Mg/m ³ | 1.322 Mg/m ³ |
| Absorption coefficient | 0.176 mm ⁻¹ | 0.181 mm ⁻¹ | 0.175 mm ⁻¹ |
| F(000) | 452 | 476 | 952 |
| Crystal size | 0.170 x 0.140 x 0.090 mm ³ | 0.340 x 0.210 x 0.050 mm ³ | 0.260 x 0.200 x 0.060 mm ³ |
| Theta range for data collection | 2.481 to 29.612°. | 2.857 to 27.508°. | 2.720 to 29.160°. |
| Index ranges | -12<=h<=12, -14<=k<=14, -16<=l<=16 | -11<=h<=11, -14<=k<=14, -15<=l<=15 | -20<=h<=20, -14<=k<=14, -21<=l<=21 |
| Reflections collected | 6115 | 41638 | 113131 |
| Completeness | 99.9 % | 99.9 % | 99.9 % |
| Data / restraints / parameters | 6115 / 0 / 299 | 5078 / 0 / 297 | 6083 / 0 / 305 |
| Goodness-of-fit on F ² | 1.096 | 1.022 | 1.017 |
| Final R indices [I>2sigma(I)] | R1 = 0.0400, wR2 = 0.1008 | R1 = 0.0452, wR2 = 0.1014 | R1 = 0.0420, wR2 = 0.1045 |
| R indices (all data) | R1 = 0.0499, wR2 = 0.1056 | R1 = 0.0779, wR2 = 0.1149 | R1 = 0.0608, wR2 = 0.1161 |
| Largest diff. peak and hole | 0.547 and -0.269 e.Å ⁻³ | 0.344 and -0.366 e.Å ⁻³ | 0.476 and -0.473 e.Å ⁻³ |

| | | |
|---------------------|----------|-------------------------|
| Identification code | OLN-3HBA | OLN-TA-H ₂ O |
|---------------------|----------|-------------------------|

| | | |
|-------------------------|--|---|
| CCDC number | 2071664 | 2071663 |
| Crystallization Solvent | Acetonitrile | Methanol |
| Empirical formula | C ₂₄ H ₂₆ N ₄ O ₃ S [+ solvent] | C ₂₁ H ₂₇ N ₄ O ₄ S |
| Formula weight | 450.55 | 431.52 |
| Temperature | 110(2) K | 110(2) K |
| Wavelength | 0.71073 Å | 0.71073 Å |
| Crystal system | Triclinic | Monoclinic |
| Space group | $P\bar{1}$ | $P2_1/n$ |
| Unit cell dimensions | a = 9.4152(18) Å | a = 12.705(4) Å |
| | b = 11.471(2) Å | b = 11.725(4) Å |
| | c = 11.828(2) Å | c = 14.211(5) Å |
| | α = 68.234(10)°. | α = 90°. |
| | β = 89.340(8)°. | β = 90.609(16)°. |
| | γ = 86.609(15)°. | γ = 90°. |
| Volume | 1184.2(4) Å ³ | 2116.7(13) Å ³ |
| Z | 2 | 4 |
| Density (calculated) | 1.551 Mg/m ³ | 1.354 Mg/m ³ |
| Absorption coefficient | 0.188 mm ⁻¹ | 0.189 mm ⁻¹ |
| F(000) | 586.479 | 916 |

| | | |
|-----------------------------------|--|--|
| Crystal size | 0.380 x 0.180 x 0.140 mm ³ | 0.390 x 0.350 x 0.220 mm ³ |
| Theta range for data collection | 2.84 to 24.99°. | 2.364 to 28.318°. |
| Index ranges | -16<=h<=16, -20<=k<=20, -21<=l<=21 | -16<=h<=16, -15<=k<=15, -18<=l<=18 |
| Reflections collected | 119303 | 67317 |
| Completeness | 99.7 % | 99.9 % |
| Data / restraints / parameters | 4153 / 0 / 298 | 5257 / 0 / 304 |
| Goodness-of-fit on F ² | 1.0611 | 1.033 |
| Final R indices [I>2sigma(I)] | R1 = 0.0307, wR2 = 0.0786 | R1 = 0.0440, wR2 = 0.1077 |
| R indices (all data) | R1 = 0.0330, wR2 = 0.0807 | R1 = 0.0692, wR2 = 0.1226 |
| Largest diff. peak and hole | 0.2578 and -0.2179 e.Å ⁻³ | 0.322 and -0.327 e.Å ⁻³ |

Table B-2. DSC data of OLN and its multicomponent crystals

| Name | Melting Point Onset Value (°C) | Solvent Evaporation Onset (°C) | Melting Point of Coformer/Salt Formers |
|---------------------------|--------------------------------|--------------------------------|--|
| OLN | 195 | - | - |
| OLN-MeOH | 193 | 107 | - |
| OLN-Phol-H ₂ O | 79* | - | 41 |
| OLN-Res | 197 | - | 110 |
| OLN-SA | 208 | - | 159 |
| OLN-AA | 199 | - | 146-148 |
| OLN-3HBA-ACN | 202 | 157 | 202 |
| OLN-3HBA | 206 | - | 202 |
| OLN-TA | 263 | - | 300 |
| OLN-TA-H ₂ O | 260 | 73 | 300 |
| OLN-2ATPA | 224 | - | 324 ¹ |

* This onset value corresponds to a phase transformation with a broad peak which could not be differentiated as two separated steps for solvent evaporation and melting.

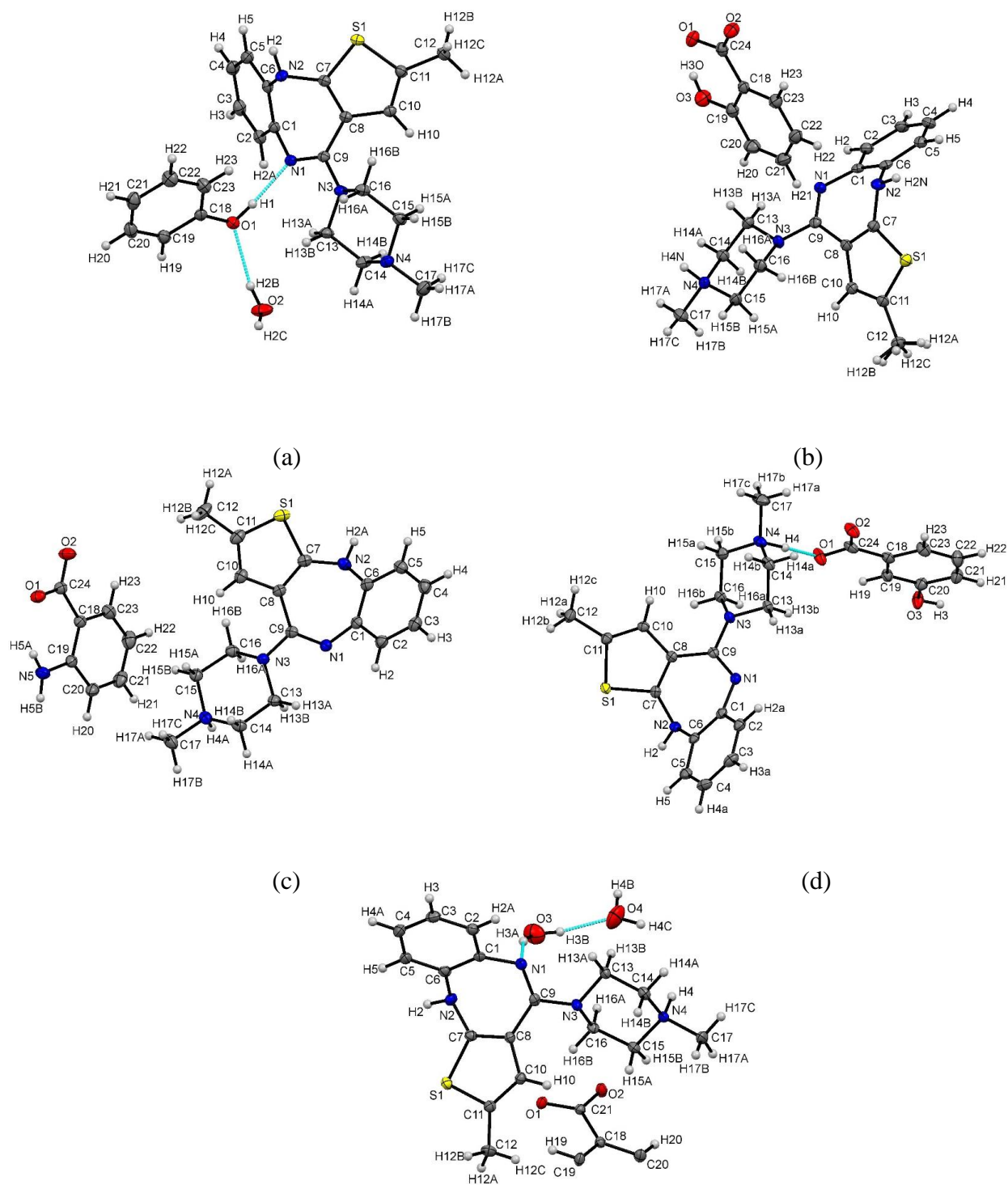


Figure B-1. The ORTEP diagrams of (a) OLN-Phol-H₂O, (b) OLN-SA, (c) OLN-AA, (d) OLN-3HBA, and (e) OLN-TA-H₂O

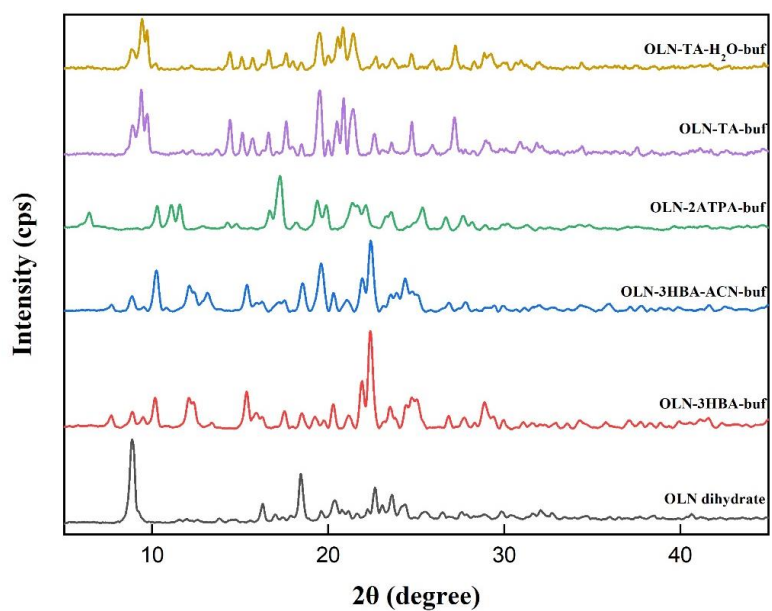
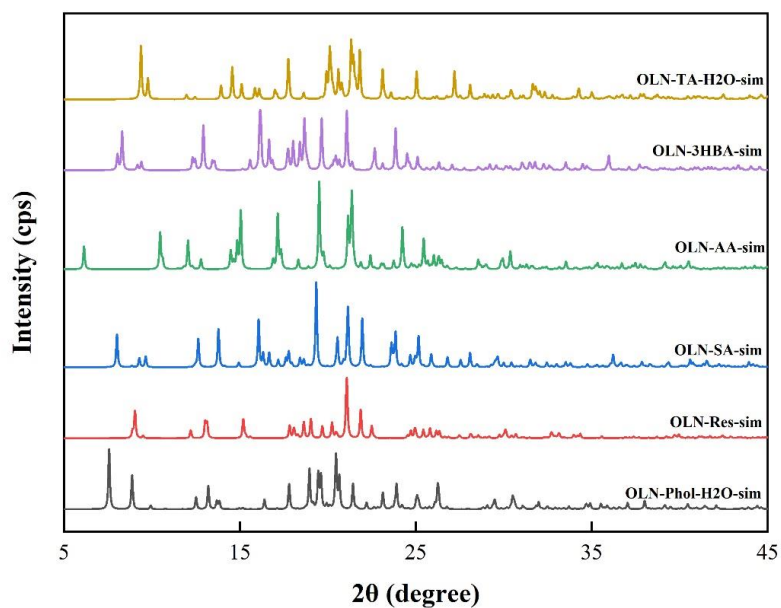
Figure B-2. Simulated PXRD patterns from sc-XRD

Figure B-3. PXRD curves of OLN-TA-H₂O, OLN-TA, OLN-2ATPA, OLN-3HBA-ACN, OLN-3HBA, and OLN dihydrate; buf refers to potential contamination with the buffer solution

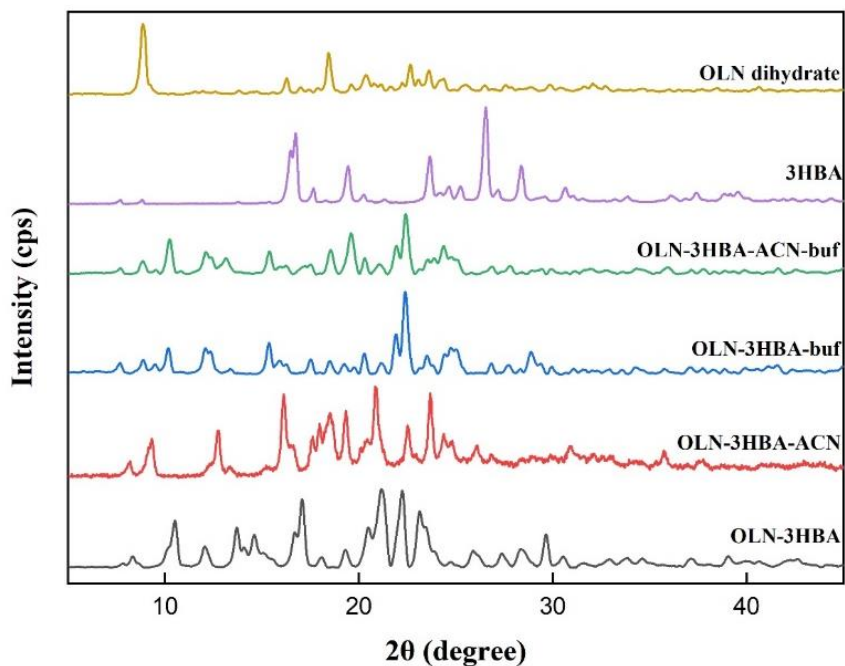


Figure B-4. PXRD patterns of OLN, 3HBA, their cocrystal and cocrystal solvate

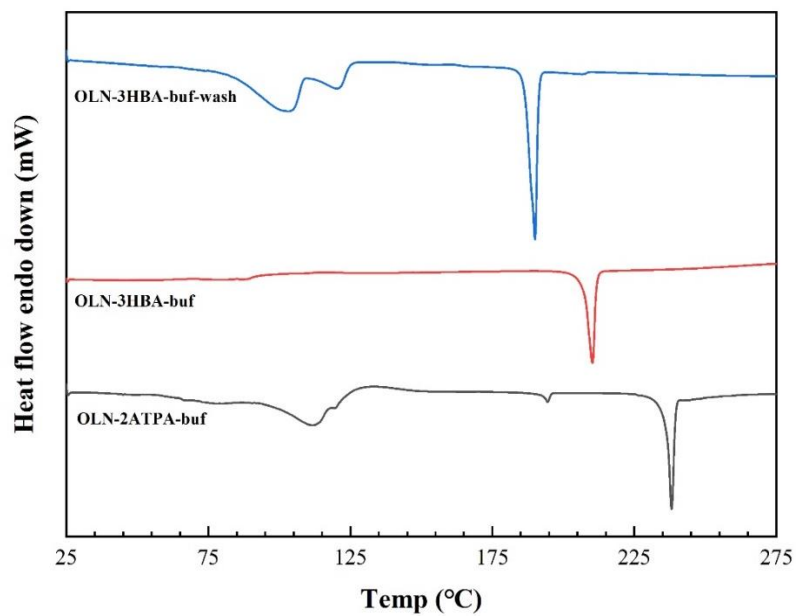


Figure B-5. DSC curves of OLN-3HBA before and after washing, and OLN-2ATPA, after solubility test; buf refers to potential contamination with the buffer solution

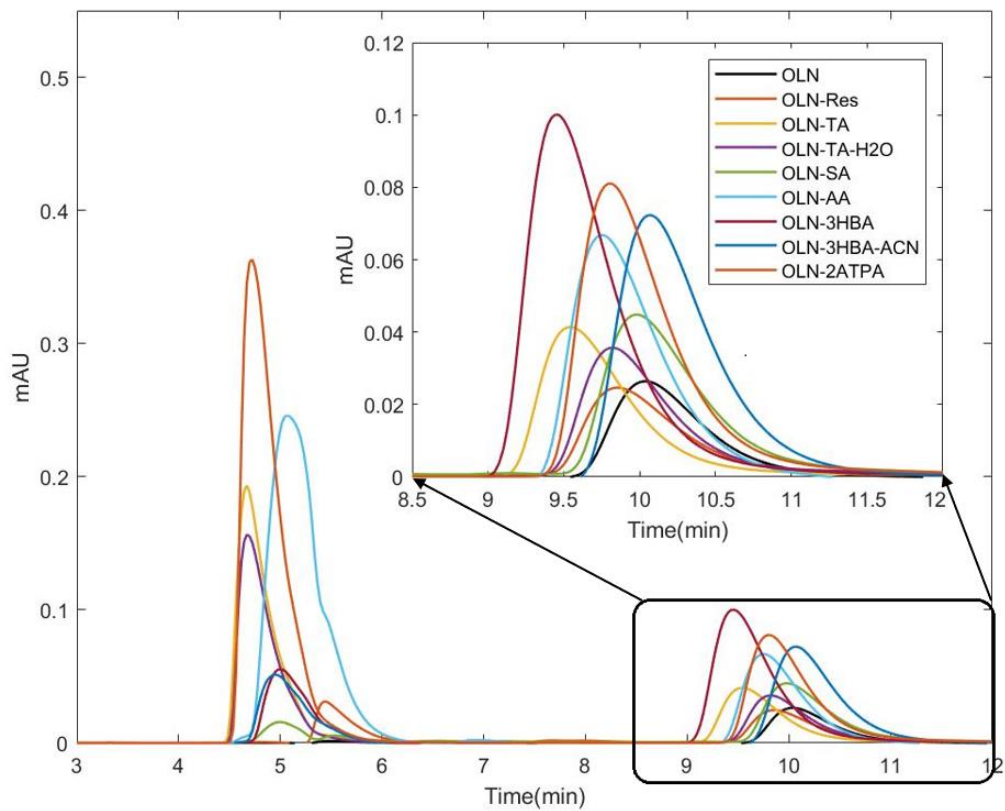


Figure B-6. HPLC diagram of OLN and its multicomponent solid phases

Appendix C: Chapter 5 appendix

C.1 In-situ Particle Size Distribution Monitoring:

C.1.1 Compare the result with Malvern standard samples

Standard samples (QAS4002) with known size distribution were purchased from Malvern Panalytical. Samples were put into a crystallizer and mixed with water, PCM was inserted to monitor the PSD, compare the DV10, DV50, DV90 obtained from PCM to the known distribution.

Result:

| | DV 10/um | DV 50/um | DV 90/um |
|---------------------------|----------|----------|----------|
| Variability and tolerance | 5.08% | 3.76% | 6.26% |
| Upper Specification limit | 40.194 | 74.883 | 112.124 |
| Target Value (QAS4002) | 38.252 | 72.171 | 105.52 |
| Lower limit | 36.31 | 69.459 | 98.916 |
| PCM obtained Data | 39 | 72 | 98 |
| Variance % | 1.96 | -0.24 | -7.13 |

It could be found that as an in-situ measurement instrument, the accuracy of PCM is good enough for standard samples (ball like).

Table C-1. Mass Fraction Solubility of Vanillin (g/g solution) and Liquid–Liquid Phase Separation Data (mass fraction, g/g solution) at Atmospheric Pressure ($P = 0.1 \text{ MPa}$)*

| 30°C Liquid-Liquid Equilibrium | | |
|---------------------------------------|--------|--------|
| W_1 | W_2 | W_3 |
| 0.4427 | 0.1774 | 0.3799 |
| 0.4704 | 0.1838 | 0.3458 |
| 0.4783 | 0.2081 | 0.3136 |
| 0.5047 | 0.2237 | 0.2717 |
| 0.5812 | 0.2094 | 0.2094 |
| 0.6709 | 0.1825 | 0.1467 |
| 0.7075 | 0.1533 | 0.1403 |
| 30°C Solid-Liquid Equilibrium | | |
| W_1 | W_2 | W_3 |
| 0.0000 | 0.6307 | 0.3693 |
| 0.0799 | 0.4202 | 0.4999 |
| 0.2233 | 0.2233 | 0.5535 |
| 0.3027 | 0.2018 | 0.4956 |
| 0.3767 | 0.1883 | 0.4350 |
| 0.9896 | 0.0000 | 0.0104 |

* W_1 , W_2 , and W_3 are the mass fractions of water, 1-Propanol, and Vanillin, respectively. The relative standard uncertainty of the solute weight measurement of solid–liquid equilibrium was estimated less than 0.05.

References

- (1) Abrams, D. S., & Prausnitz, J. M. (1975). Statistical thermodynamics of liquid mixtures: A new expression for the excess Gibbs energy of partly or completely miscible systems. *AICHE Journal*, 21(1), 116–128. <https://doi.org/10.1002/aic.690210115>
- (2) Chang, C.-W., Hsiung, T.-L., Lui, C.-P., & Tu, C.-H. (2015). Densities, surface tensions, and isobaric vapor–liquid equilibria for the mixtures of 2-propanol, water, and 1,2-propanediol. *Fluid Phase Equilibria*, 389, 28–40. <https://doi.org/10.1016/j.fluid.2014.12.040>
- (3) Cong, Y., Du, C., Xing, K., Bian, Y., Li, X., & Wang, M. (2022). Research on dissolution of actarit in aqueous mixtures: Solubility determination and correlation, preferential solvation, solvent effect and thermodynamics. *Journal of Molecular Liquids*, 358, 119141. <https://doi.org/10.1016/j.molliq.2022.119141>
- (4) Haghazarloo, H., Lotfollahi, M. N., Mahmoudi, J., & Asl, A. H. (2013). Liquid–liquid equilibria for ternary systems of (ethylene glycol+toluene+heptane) at temperatures (303.15, 308.15, and 313.15)K and atmospheric pressure: Experimental results and correlation with UNIQUAC and NRTL models. *The Journal of Chemical Thermodynamics*, 60, 126–131. <https://doi.org/10.1016/j.jct.2012.12.027>
- (5) Huang, W., Wang, H., Li, C., Wen, T., Xu, J., Ouyang, J., & Zhang, C. (2021). Measurement and correlation of solubility, Hansen solubility parameters and thermodynamic behavior of Clozapine in eleven mono-solvents. *Journal of Molecular Liquids*, 333, 115894. <https://doi.org/10.1016/j.molliq.2021.115894>
- (6) Li, X., He, Y., Xu, Y., Zhang, X., Zheng, M., & Zhao, H. (2020). 5-Nitrosalicylaldehyde in aqueous co-solvent mixtures of methanol, ethanol, isopropanol and acetonitrile: Solubility determination, solvent effect and preferential solvation analysis. *The Journal of Chemical Thermodynamics*, 142, 106014. <https://doi.org/10.1016/j.jct.2019.106014>
- (7) Liu, Q., Yan, Y., Wu, Y., Zhang, X., & Zhou, X. (2021). Systematic thermodynamic study of clorsulon dissolved in ten organic solvents: Mechanism evaluation by modeling and molecular dynamic simulation. *Journal of Molecular Liquids*, 341, 117217. <https://doi.org/10.1016/j.molliq.2021.117217>
- (8) Rabhi, F., Pietro, T. D., Mutelet, F., & Sifaoui, H. (2021). Extraction of butanol and acetonitrile from aqueous solution using carboxylic acid based deep eutectic solvents. *Journal of Molecular Liquids*, 325, 115231. <https://doi.org/10.1016/j.molliq.2020.115231>
- (9) Zheng, M., Farajtabar, A., & Zhao, H. (2018). Solute-solvent and solvent-solvent interactions and preferential solvation of hesperidin in aqueous cosolvent mixtures of ethanol, isopropanol, propylene glycol and n-propanol. *Journal of Molecular Liquids*, 264, 285–291. <https://doi.org/10.1016/j.molliq.2018.05.057>

Appendix D: Copyright permission

CCC RightsLink [Sign in/Register](#) ⓘ 🔍

Polymorphism control of L-Glutamic acid in a single-stage and a two-stage MSMR crystallizer by different seeding strategies
 Author: Weizhong Gong, Yuanyi Wu, Mengxing Lin, Sohrab Rohani
 Publication: Chemical Engineering Research and Design
 Publisher: Elsevier
 Date: June 2021
© 2021 Institution of Chemical Engineers. Published by Elsevier B.V. All rights reserved.

Journal Author Rights

Please note that, as the author of this Elsevier article, you retain the right to include it in a thesis or dissertation, provided it is not published commercially. Permission is not required, but please ensure that you reference the journal as the original source. For more information on this and on your other retained rights, please visit: <https://www.elsevier.com/about/our-business/policies/copyright#Author-rights>

BACK CLOSE WINDOW

© 2023 Copyright - All Rights Reserved | Copyright Clearance Center, Inc. | [Privacy statement](#) | [Data Security and Privacy](#) | [For California Residents](#) | [Terms and Conditions](#)
 Comments? We would like to hear from you. E-mail us at customercare@copyright.com

CCC RightsLink [Sign in/Register](#) ⓘ 🔍



Cocrystals, Salts, and Salt-Solvates of olanzapine; selection of cofomers and improved solubility
 Author: Weizhong Gong, Pradip Kumar Mondal, Soroush Ahmadi, Yuanyi Wu, Sohrab Rohani
 Publication: International Journal of Pharmaceutics
 Publisher: Elsevier
 Date: 25 October 2021
© 2021 Elsevier B.V. All rights reserved.


Journal Author Rights

Please note that, as the author of this Elsevier article, you retain the right to include it in a thesis or dissertation, provided it is not published commercially. Permission is not required, but please ensure that you reference the journal as the original source. For more information on this and on your other retained rights, please visit: <https://www.elsevier.com/about/our-business/policies/copyright#Author-rights>

BACK CLOSE WINDOW

© 2023 Copyright - All Rights Reserved | Copyright Clearance Center, Inc. | [Privacy statement](#) | [Data Security and Privacy](#) | [For California Residents](#) | [Terms and Conditions](#)
 Comments? We would like to hear from you. E-mail us at customercare@copyright.com

CCC RightsLink [Sign in/Register](#) ⓘ 🔍



Taurine in several aqueous binary solvents: Solubility prediction, measurement, modeling, solvent effect, and thermodynamics
 Author: Weizhong Gong, Pan Li, Sohrab Rohani
 Publication: Journal of Molecular Liquids
 Publisher: Elsevier
 Date: 1 December 2022
© 2022 Elsevier B.V. All rights reserved.

Journal Author Rights

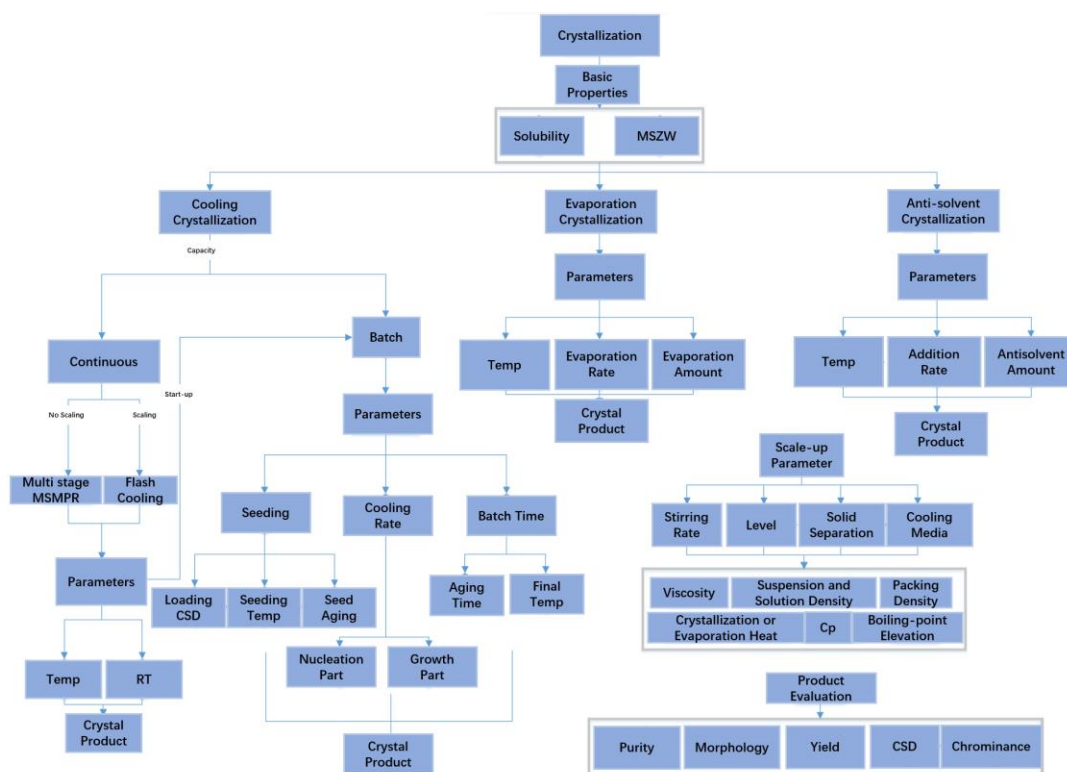
Please note that, as the author of this Elsevier article, you retain the right to include it in a thesis or dissertation, provided it is not published commercially. Permission is not required, but please ensure that you reference the journal as the original source. For more information on this and on your other retained rights, please visit: <https://www.elsevier.com/about/our-business/policies/copyright#Author-rights>

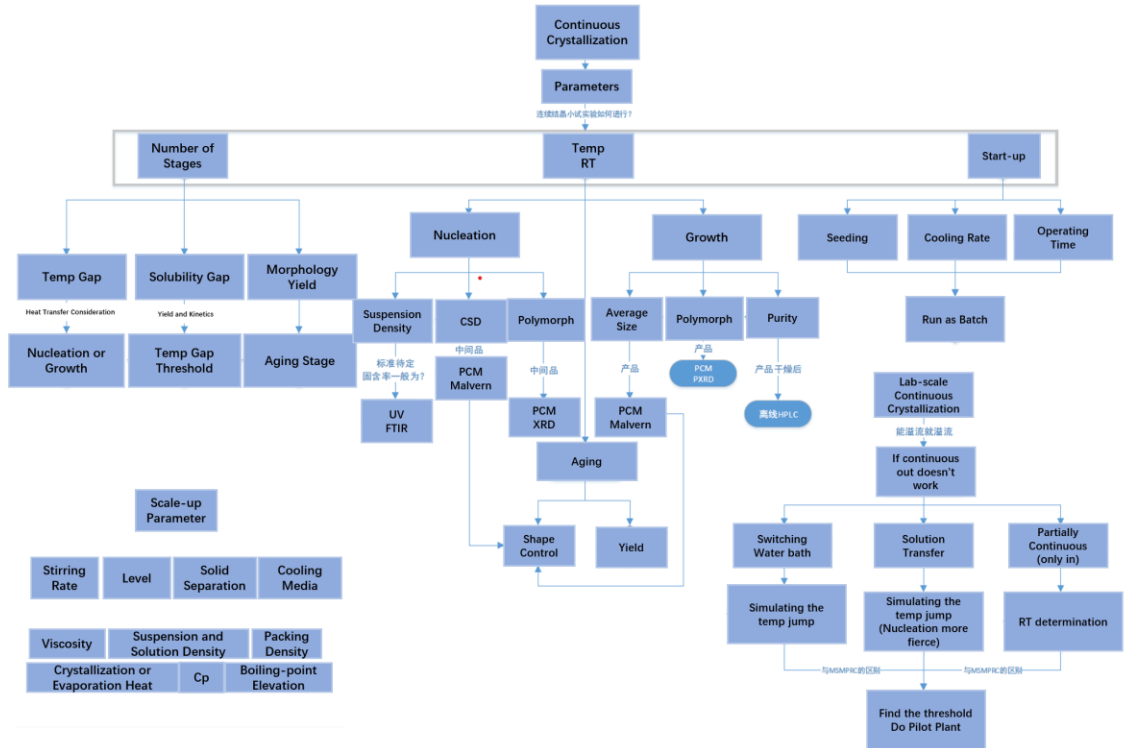
BACK CLOSE WINDOW

© 2023 Copyright - All Rights Reserved | Copyright Clearance Center, Inc. | [Privacy statement](#) | [Data Security and Privacy](#) | [For California Residents](#) | [Terms and Conditions](#)
 Comments? We would like to hear from you. E-mail us at customercare@copyright.com

Appendix E: Research in Wanhua Chemical Group Co. Ltd.

The research program given by Wanhua Chemical involves the numerical and the experimental studies of crystallization systems, to explore the operation conditions, design and operation of two pilot plant crystallizers to meet very stringent quality control requirements of the products (either purity or morphology). In-situ process analytical tools (PAT) such as PCM are offered, to monitor the real-time morphology. The collaborative research program addresses the difficulties associated with the operation of large-scale crystallization experiments which is generally lacking in the university environment. This research opportunity has provided me with ample experience working with expensive PAT hardware to monitor and control the process. The crystallization process development guideline is concluded in Scheme 0-1.





Scheme 0-1 Crystallization process development guideline

E.2 Vanillin Project:

Single-stage MSMPR with flash cooling

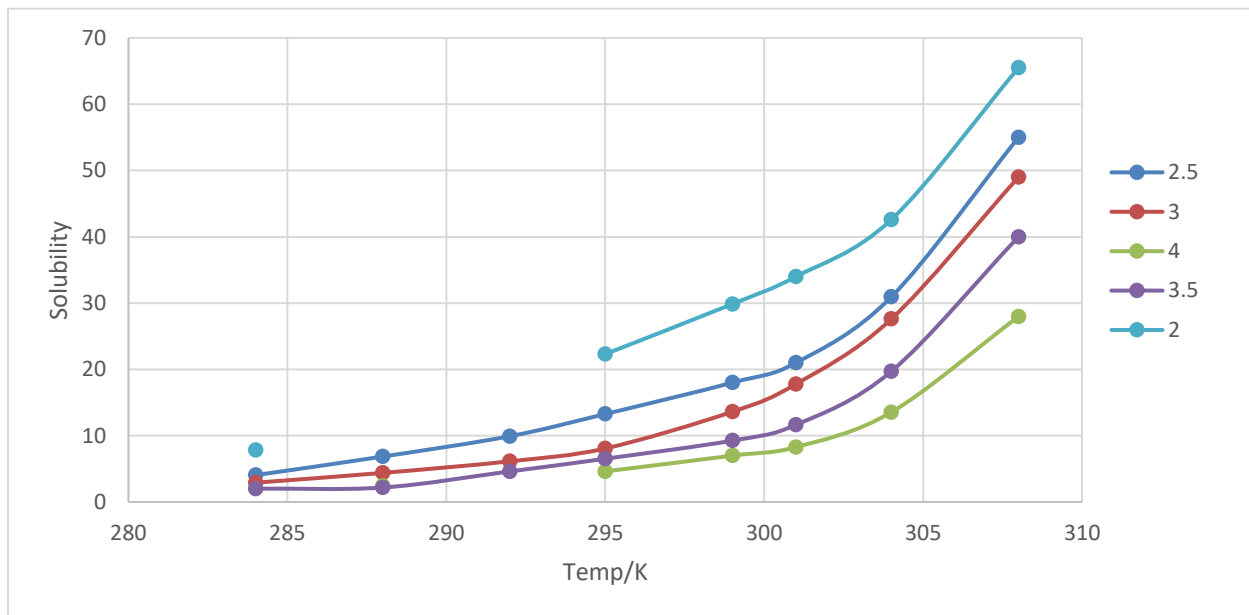
The goal was to achieve high block-like vanillin crystals as well as ensure a high product yield.

Problem Statement:

Two morphologies exist for vanillin crystals. When the supersaturation is high (fast cooling/evaporation), needle-like vanillin crystals are formed. How to steadily produce plate-like vanillin crystals with low aspect ratio is the key problem.

Solubility Test:

The selected solvent was water-ethanol binary solvent. The ratio had to be determined; thus a solubility test was conducted. It shall be noticed that when the temperature is above 60 °C, vanillin melts and produces a eutectic point.



Lab Experiments

Once the water-ethanol ratio was fixed, batch crystallization experiment was first performed to study the system. The initial temperature was 30°C, metastable zone was around 8°C. Seeding was first tried to see whether introducing plate-like seeds can tune the product morphology. The effects of seed timing, seed loading, cooling rate were all investigated.

It was found that when 5wt% plate-like vanillin crystals were suspended in the solution, the product would be plate like. A low cooling-rate crystallization with high mechanical stirring was then tested to see if the primary nucleation happens at low supersaturation levels, and what would be the resulting effect of the crystal morphology. Plate-like vanillin crystals were obtained as a result.

Appendix F: Matlab codes for crystallization process and solubility regression

E.1 Birth rate

```
% Birth of the stable polymorph
function B = Birth(kb,b,T,C,mu)
B =0;
C_star = solubility(T);
if C>C_star
    S = C./C_star;
    B = S.^(b).*(kb)*exp(-15/(log(S))^2)+6.0*10^4*(mu)^2*exp(-0.001/log(S));
    B(isnan(B))=0;
end
end
```

E.2 Dissolution rate

```
% Dissolution of the stable polymorph
function D = Dissolution(kd,T,C)
C_star = solubility(T);
D = kd.*(abs(C./C_star-1));
```

E.3 Growth

```
% Growth of the stable polymorph
function G = growth(kg1,kg2,T,C)
G=0;
C_star = solubility(T);
if C>C_star
    S = C./C_star;
    G = kg1.*abs(S-1).^(kg2)*exp(-0.16/(S-1));
    G(isnan(G))=0;
end
end
```

E.4 2-stage MSMPR

```
function df = multi_msmpr_fun_CSD(t,f,G,D,B,m,phi,residence_time,sn)
df = zeros(m*sn,1);
df(1) = G(1)./(phi).*(0-f(1)) + D(1)./(phi).*(f(2)-f(1)) + B(1)-
f(1)./residence_time(1);
df(2:m-1) = G(1)./(phi).*(f(1:m-2)-f(2:m-1)) + D(1)./(phi).*(f(3:m)-f(2:m-1))
- f(2:m-1)./residence_time(1);
df(m) = G(1)./(phi).*(f(m-1)-f(m)) + D(1)./(phi).*(0-f(m)) -
f(m)./residence_time(1);

if sn>1
for a=1:sn-1
```

```

    b=a+1; % 2:sn

df(a*m+1) = G(b)./(phi).*(0-f(a*m+1)) + D(b)./(phi).*(f(a*m+2)-f(a*m+1)) +
B(b) + (f((a-1)*m+1)-f(a*m+1))./residence_time(b);
df(a*m+2:b*m-1) = G(b)./(phi).*(f(a*m+1:b*m-2)-f(a*m+2:b*m-1)) +
D(b)./(phi).*(f(a*m+3:b*m)-f(a*m+2:b*m-1)) + (f((a-1)*m+2:a*m-1)-f(a*m+2:b*m-
1))./residence_time(b);
df(b*m) = G(b)./(phi).*(f(b*m-1)-f(b*m)) + D(b)./(phi).*(0-f(b*m)) +(f(a*m)-
f(b*m))./residence_time(b);

end
end

function dN
=multi_msmpr_fun_miu(~,N,T,rho_crystal,kv_stable,rho_crystal_1,kv_metastable,r
ho_solvent,...
    kb,b,kb_1,b_1, kg,g,kg_1,g_1, kd,kd_1,residence_time,Cinlet,sn,v_solvent)
dN = zeros(25.*sn,1);
g_d_1 = growth_1(kg_1,g_1,T(1),N(25))-
Dissolution_1(kd_1,T(1),N(25),(N(4)+N(16)));
g_d = growth(kg,g,T(1),N(25))-Dissolution(kd,T(1),N(25));
dN(1) = -N(1)./residence_time(1);
dN(2:6) = (1:5)'.*g_d_1.*N(1:5)-N(2:6)./residence_time(1);
dN(7) = -N(7)./residence_time(1);
dN(8:12) = (1:5)'.*g_d.*N(7:11)-N(8:12)./residence_time(1);
%-----
dN(13) = Birth_1(kb_1,b_1,T(1),N(25))-N(13)./residence_time(1);
dN(14:18) = (1:5)'.*g_d_1.*N(13:17)-N(14:18)./residence_time(1);
dN(19) = Birth(kb,b,T(1),N(25),(N(3)+N(15)))-N(19)./residence_time(1);
dN(20:24) = (1:5)'.*g_d.*N(19:23)-N(20:24)./residence_time(1);
dN(25)= -
3.*1000./rho_solvent.*rho_crystal_1.*kv_metastable.*g_d_1.*(N(3)+N(15))...
-3.*1000./rho_solvent.*rho_crystal.*kv_stable.*g_d.*(N(9)+N(21))...
+(Cinlet-N(25))./residence_time(1);

if sn>1
    g_d_1(2:sn) = (growth_1(kg_1,g_1,T((2:sn)),N((2:sn)*25))-
Dissolution_1(kd_1,T(1),N((2:sn)*25),(N((1:sn-1)*25+4)+N((1:sn-1)*25+16))));
    g_d(2:sn) = (growth(kg,g,T((2:sn)),N((2:sn)*25))-
Dissolution(kd,T(2:sn),N((2:sn)*25)));

dN((1:sn-1)*25+1) = (N((0:sn-2)*25+1)-N((1:sn-1)*25+1))./residence_time(2:sn);
%---- zeroth moment for metastable phase
dN((1:sn-1)*25+2) = 1.*g_d_1(2:sn)'.*N((1:sn-1)*25+1) + (N((0:sn-2)*25+2)-
N((1:sn-1)*25+2))./residence_time(2:sn); %---- First moment for metastable
phase
dN((1:sn-1)*25+3) = 2.*g_d_1(2:sn)'.*N((1:sn-1)*25+2) + (N((0:sn-2)*25+3)-
N((1:sn-1)*25+3))./residence_time(2:sn); %---- Second moment for metastable
phase
dN((1:sn-1)*25+4) = 3.*g_d_1(2:sn)'.*N((1:sn-1)*25+3) + (N((0:sn-2)*25+4)-
N((1:sn-1)*25+4))./residence_time(2:sn); %---- Third moment for metastable
phase
dN((1:sn-1)*25+5) = 4.*g_d_1(2:sn)'.*N((1:sn-1)*25+4) + (N((0:sn-2)*25+5)-
N((1:sn-1)*25+5))./residence_time(2:sn); %---- Fourth moment for metastable
phase

```

```

dN((1:sn-1)*25+6) = 5.*g_d_1(2:sn)'.*N((1:sn-1)*25+5) + (N((0:sn-2)*25+6)-
N((1:sn-1)*25+6))./residence_time(2:sn); %---- Fifth moment for metastable
phase

dN((1:sn-1)*25+7) = (N((0:sn-2)*25+7)-N((1:sn-
1)*25+7))./residence_time(2:sn); %---- zeroth moment
dN((1:sn-1)*25+8) = 1.* g_d(2:sn)'.*N((1:sn-1)*25+7) + (N((0:sn-2)*25+8) -
N((1:sn-1)*25+8)) ./residence_time(2:sn); %---- First moment for stable phase
dN((1:sn-1)*25+9) = 2.* g_d(2:sn)'.*N((1:sn-1)*25+8) + (N((0:sn-2)*25+9) -
N((1:sn-1)*25+9)) ./residence_time(2:sn); %---- Second moment for stable phase
dN((1:sn-1)*25+10) = 3.* g_d(2:sn)'.*N((1:sn-1)*25+9) + (N((0:sn-2)*25+10)-
N((1:sn-1)*25+10))./residence_time(2:sn); %---- Third moment for stable phase
dN((1:sn-1)*25+11) = 4.* g_d(2:sn)'.*N((1:sn-1)*25+10) + (N((0:sn-2)*25+11)-
N((1:sn-1)*25+11))./residence_time(2:sn); %---- Fourth moment for stable phase
dN((1:sn-1)*25+12) = 5.* g_d(2:sn)'.*N((1:sn-1)*25+11)+ (N((0:sn-2)*25+12)-
N((1:sn-1)*25+12))./residence_time(2:sn); %---- Fifth moment for stable phase
%-----
dN((1:sn-1)*25+13) = Birth_1(kb_1,b_1,T(2:sn),N((1:sn-1)*25+25))+N((0:sn-
2)*25+13)-N((1:sn-1)*25+13))./residence_time(2:sn); %---- zeroth moment for
metastable phase
dN((1:sn-1)*25+14) = 1.* g_d_1(2:sn)'.*N((1:sn-1)*25+13) + (N((0:sn-2)*25+14)-
N((1:sn-1)*25+14))./residence_time(2:sn); %---- First moment for metastable
phase
dN((1:sn-1)*25+15) = 2.* g_d_1(2:sn)'.*N((1:sn-1)*25+14) + (N((0:sn-2)*25+15)-
N((1:sn-1)*25+15))./residence_time(2:sn); %---- Second moment for metastable
phase
dN((1:sn-1)*25+16) = 3.* g_d_1(2:sn)'.*N((1:sn-1)*25+15) + (N((0:sn-2)*25+16)-
N((1:sn-1)*25+16))./residence_time(2:sn); %---- Third moment for metastable
phase
dN((1:sn-1)*25+17) = 4.* g_d_1(2:sn)'.*N((1:sn-1)*25+16) + (N((0:sn-2)*25+17)-
N((1:sn-1)*25+17))./residence_time(2:sn); %---- Fourth moment for metastable
phase
dN((1:sn-1)*25+18) = 5.* g_d_1(2:sn)'.*N((1:sn-1)*25+17) + (N((0:sn-2)*25+18)-
N((1:sn-1)*25+18))./residence_time(2:sn); %---- Fifth moment for metastable
phase

dN((1:sn-1)*25+19) = Birth(kb,b,T(2:sn),N((1:sn-1)*25+25),(N((1:sn-
1)*25+3)+N((1:sn-1)*25+15)))+(N((0:sn-2)*25+19)-N((1:sn-
1)*25+19))./residence_time(2:sn); %---- zeroth moment
dN((1:sn-1)*25+20) = 1.*g_d(2:sn)'.*N((1:sn-1)*25+19)+(N((0:sn-2)*25+20)-
N((1:sn-1)*25+20))./residence_time(2:sn); %---- First moment for stable phase
dN((1:sn-1)*25+21) = 2.*g_d(2:sn)'.*N((1:sn-1)*25+20)+(N((0:sn-2)*25+21)-
N((1:sn-1)*25+21))./residence_time(2:sn); %---- Second moment for stable phase
dN((1:sn-1)*25+22) = 3.*g_d(2:sn)'.*N((1:sn-1)*25+21)+(N((0:sn-2)*25+22)-
N((1:sn-1)*25+22))./residence_time(2:sn); %---- Third moment for stable phase
dN((1:sn-1)*25+23) = 4.*g_d(2:sn)'.*N((1:sn-1)*25+22)+(N((0:sn-2)*25+23)-
N((1:sn-1)*25+23))./residence_time(2:sn); %---- Fourth moment for stable phase
dN((1:sn-1)*25+24) = 5.*g_d(2:sn)'.*N((1:sn-1)*25+23)+(N((0:sn-2)*25+24)-
N((1:sn-1)*25+24))./residence_time(2:sn); %---- Fifth moment for stable phase

dN((1:sn-1)*25+25)= -
3.*1000./rho_solvent.*rho_crystal_1.*kv_metastable.*g_d_1(2:sn)'.*(N((1:sn-
1)*25+3)+N((1:sn-1)*25+15)) ...
-3.*1000./rho_solvent.*rho_crystal.* kv_stable.*
g_d(2:sn)'.*(N((1:sn-1)*25+9)+N((1:sn-1)*25+21))...

```

```

        +(N((0:sn-2)*25+25)-N((1:sn-
1)*25+25))./residence_time(2:sn); %----Concentration
end

```

E.4.1 2-stage MSMPR Main code:

```

%----- Kinetic parameters for metastable polymorph
Temperature=[50;25];kb_1 = 8*10^5; b_1 = 7/3; kg_1 = 2.5*10^-7; g_1 = 5/6;
kd_1 =3.5*10^(-5);
kb = 5.4*10^4; b = 7/3; kg = 6.5*10^(-8); g = 5/6; kd = 0;
kv_stable = 0.031; rho_stable = 1540;
kv_metastable =0.48; rho_metastable = 1540;
rho_solvent = 1000;v_solvent = 0.00015

%-----
stage_number=2;
residence_time=[60;60]*60; % unit-second
rtnumber=10;
Cinlet=0.04;
C_0=max(solubility_1(Temperature),solubility(Temperature));

%---- Seeding parameters for stable poylmorph
seed_mass_stable=[5e-7,0]; % 0*ones(1,stage_number); %[0,0,0]; %g/kg
stable_ave_size = 50*ones(1,stage_number)*10^-6; %seed_ave_siie
stable_sd = 5*ones(1,stage_number)*10^-6; %seed_standard
deviation

%---- Seeding parameters for metastable poylmorph
seed_mass_metastable=[0,0]; %g/kg
metastable_ave_size = 100*ones(1,stage_number)*10^-6;
metastable_sd = 10*ones(1,stage_number)*10^-6;
%-----
m=300; L0=0; LN =1000*10^-6; phi=(LN-L0)/m; L=(L0+phi/2):phi:(LN-phi/2);
a=360;delta_t=rtnumber*sum(residence_time)/a;time=(1:a)*delta_t./3600;

for sn=1:stage_number

CSD_stable_seed(sn,:) =normpdf(L,stable_ave_size(sn),stable_sd(sn));
CSD_metastable_seed(sn,:) =
normpdf(L,metastable_ave_size(sn),metastable_sd(sn));

stable_lamda(sn)=seed_mass_stable(sn)./(rho_stable*kv_stable*trapz(L,CSD_stabl
e_seed(sn,:) .*L.^3));
metastable_lamda(sn)=seed_mass_metastable(sn)./(rho_metastable*kv_metastable*t
rapz(L,CSD_metastable_seed(sn,:) .*L.^3));

CSD_metastable_seed(sn,:)=
metastable_lamda(sn).*CSD_metastable_seed(sn,)./v_solvent;
CSD_stable_seed(sn,:) =stable_lamda(sn).*CSD_stable_seed(sn,)./v_solvent;
%popolation density--unit-#/m.m3

f0_1(sn,:) = CSD_metastable_seed(sn,:); f0(sn,:) = CSD_stable_seed(sn,:);

```

```

%----- For the stable polymorph Initial conditions
miu_0(sn) = trapz(L,f0(sn,:)); miu_1(sn) = trapz(L,f0(sn,).*L);
miu_2(sn) = trapz(L,f0(sn,).*L.^2); miu_3(sn) = trapz(L,f0(sn,).*L.^3);
miu_4(sn) = trapz(L,f0(sn,).*L.^4); miu_5(sn) = trapz(L,f0(sn,).*L.^5);

%----- For the metastable polymorph Initial conditions
miu_0_1(sn) = trapz(L,f0_1(sn,:)); miu_1_1(sn) = trapz(L,f0_1(sn,).*L);
miu_2_1(sn) = trapz(L,f0_1(sn,).*L.^2); miu_3_1(sn) =
trapz(L,f0_1(sn,).*L.^3);
miu_4_1(sn) = trapz(L,f0_1(sn,).*L.^4); miu_5_1(sn) =
trapz(L,f0_1(sn,).*L.^5);

N(:,sn)=[miu_0_1(sn) miu_1_1(sn) miu_2_1(sn) miu_3_1(sn) miu_4_1(sn)
miu_5_1(sn) miu_0(sn) miu_1(sn) miu_2(sn) miu_3(sn) miu_4(sn) miu_5(sn)...
0 0 0 0 0 0 0 0 0 0 0 C_0(sn)];
NN(:)=N(:,sn);

result(1:13,sn) = [NN(1:12),NN(25)];
end
CSD_stable_seed = CSD_stable_seed(sn,:);
N0 = reshape(N,[],1);

for i=1:a
result(1,:) = N0((0:stage_number-1)*25+1) + N0((0:stage_number-1)*25+13);
%miu_0_1
result(2,:) = N0((0:stage_number-1)*25+2) + N0((0:stage_number-1)*25+14);
%miu_1_1
result(3,:) = N0((0:stage_number-1)*25+3) + N0((0:stage_number-1)*25+15);
%miu_2_1
result(4,:) = N0((0:stage_number-1)*25+4) + N0((0:stage_number-1)*25+16);
%miu_3_1
result(5,:) = N0((0:stage_number-1)*25+5) + N0((0:stage_number-1)*25+17);
%miu_4_1
result(6,:) = N0((0:stage_number-1)*25+6) + N0((0:stage_number-1)*25+18);
%miu_5_1
result(7,:) = N0((0:stage_number-1)*25+7) + N0((0:stage_number-1)*25+19);
%miu_0
result(8,:) = N0((0:stage_number-1)*25+8) + N0((0:stage_number-1)*25+20);
%miu_1
result(9,:) = N0((0:stage_number-1)*25+9) + N0((0:stage_number-1)*25+21);
%miu_2
result(10,:) = N0((0:stage_number-1)*25+10) + N0((0:stage_number-
1)*25+22);%miu_3
result(11,:) = N0((0:stage_number-1)*25+11) + N0((0:stage_number-
1)*25+23);%miu_4
result(12,:) = N0((0:stage_number-1)*25+12) + N0((0:stage_number-
1)*25+24);%miu_5
result(13,:) = N0((0:stage_number-1)*25+25); % concentration
%-----
for k=1:stage_number
B_stable(i,k) = Birth(kb,b,Temperature(k),result(13,k)',result(3,k)');
B_metastable(i,k) = Birth_1(kb_1,b_1,Temperature(k),result(13,k)');
Dissolution_stable(i,k) = Dissolution(kd,Temperature(k),result(13,k)');
Dissolution_metastable(i,k) =
Dissolution_1(kd_1,Temperature(k),result(13,k)',result(4,k)');

```

```

Growth_stable(i,k) = growth(kg,g,Temperature(k),result(13,k)');
Growth_metastable(i,k) = growth_1(kg_1,g_1,Temperature(k),result(13,k)');
end

Concentration(i,:)=result(13,:);
Supersaturation_stable(i,:) = result(13,:)'./solubility(Temperature);
Supersaturation_metastable(i,:) = result(13,:)'./solubility_1(Temperature);

Number_stable = reshape ((f0.*phi)',[],1);
Number_metastable = reshape ((f0_1.*phi)',[],1);

Mass_stable(i,:) = rho_stable/rho_solvent*kv_stable*1000*result(10,:);
Mass_metastable(i,:) =
rho_metastable/rho_solvent*kv_metastable*1000*result(4,:);

Number_ave_size_stable(i,:) = result(8,:)./result(7,)*10^6;
Number_ave_size_metastable(i,:) = result(2,:)./result(1,)*10^6;
Volume_ave_size_stable(i,:) = result(11,:)./result(10,)*10^6;
Volume_ave_size_metastable(i,:) = result(5,:)./result(4,)*10^6; %micrometer

[t1 F] =
ode45(@multi_msmpr_fun_CSD,[0,delta_t],Number_stable,[],Growth_stable(i,:),Dis
solution_stable(i,:),B_stable(i,:),m,phi,residence_time,stage_number);
[t2 F_1] =
ode45(@multi_msmpr_fun_CSD,[0,delta_t],Number_metastable,[],Growth_metastable(
i,:),Dissolution_metastable(i,:),B_metastable(i,:),m,phi,residence_time,stage_
number);

csd_stable = reshape(F(end,:)','m,stage_number);
csd_metastable = reshape(F_1(end,:)','m,stage_number);

for sn3=1:stage_number

    if (result(1,sn3)<=0 || result(2,sn3)<=0 || result(3,sn3)<=0 ||
result(4,sn3)<=0 || result(5,sn3)<=0)
        ff_1 = zeros(m,1);
        ff = csd_stable(:,sn3)./phi;           % no metastable crystals

    elseif (result(7,sn3)<=0 || result(8,sn3)<=0 || result(9,sn3)<=0 ||
result(10,sn3)<=0 || result(11,sn3)<=0)
        ff = zeros(m,1);
        ff_1 = csd_metastable(:,sn3)./phi;     % no stable crystals
    else
        ff = csd_stable(:,sn3)./phi;
        ff_1 = csd_metastable(:,sn3)./phi;     %population density
    end
    CSD_stable(sn3,:,i) = ff;
    CSD_metastable(sn3,:,i) = ff_1;

end

f0 = CSD_stable(:, :, i);
f0_1 = CSD_metastable(:, :, i);

```

```

[t N] =
ode45(@multi_msmpr_fun_miu,[0,delta_t],N0,[],Temperature,rho_stable,kv_stable,
rho_metastable,kv_metastable,rho_solvent,...
      kb,b,kb_1,b_1, kg,g,kg_1,g_1,
kd,kd_1,residence_time,Cinlet,stage_number,v_solvent);

N0 = real(N(end,:))';
miu_25_3(:, :, i) = reshape(N0,25,stage_number);

end

massblance(1)=Cinlet-Concentration(end,1)- Mass_stable(end,1)-
Mass_metastable(end,1)
massblance(2:stage_number)=Concentration(end,1:stage_number-1)-
Concentration(end,2:stage_number)...
    + (Mass_stable(end,1:stage_number-1)-Mass_stable(end,2:stage_number))...
    + (Mass_metastable(end,1:stage_number-1)-
Mass_metastable(end,2:stage_number))

yield = (Mass_stable(end,:)+Mass_metastable(end,:))./(Cinlet-
min(solubility(Temperature(stage_number)),solubility_1(Temperature(stage_numbe
r))))
Mass_stable_fraction =
Mass_stable(end,:)./(Mass_stable(end,:)+Mass_metastable(end,:))

number_of_rt = delta_t*(1:a)/sum(residence_time);
nuleation_rate_stable=B_stable./Growth_stable;
nuleation_rate_metastable=B_metastable./Growth_metastable;

figure(1)
for ii=1:stage_number
subplot(1,stage_number,ii)
yyaxis left
plot(number_of_rt,Mass_stable(:,ii),'--
',number_of_rt,Mass_metastable(:,ii),':', 'linewidth',2)
ylabel( 'solid mass (gsolute/kg solvent)')
ylim([0,Cinlet])
yyaxis right
plot(number_of_rt,solubility(Temperature(ii))*ones(length(number_of_rt),1),'--
',...
number_of_rt,solubility_1(Temperature(ii))*ones(length(number_of_rt),1),':',...
.
    number_of_rt,Concentration(:,ii),'-', 'linewidth',2)
ylim([0,Cinlet])
legend('solid mass of stable','solid mass of metastable','solubility of
stable','solubility of metastable','solution concentration' )
xlabel('# of residence time'), ylabel( 'Concentration (gsolute/kg solvent)')
title('MSMPR')
end

```


E.5 Single-stage MSMR with intermittent seeding

```

%----- Kinetic parameters for metastable polymorph
Eg_1=4.31*10^4; T_msmpr=25;kb_1 =3.05*10^7 ; b_1 = 1; kg_1 = 6.54; g_1 =
1.859; kd_1 =3.5*10^(-5);
Eg=1.76*10^5; kb1 = 7.28*10^6; kb2=4.85*10^8; b = 1; kg =3.84*10^22 ;
g = 1.047; kd = 0; fre = 1;%seed frequency
kv_stable = 0.031; rho_stable = 1540; % 25C
kv_metastable =0.48; rho_metastable = 1540;
rho_solvent = 1000; v_solvent=0.00015;
%-----
delta_t = 60;
residence_time =1*3600;rtnumber=20;
v = residence_time/(fre*60); %indicator of seed frequency
timegrid=residence_time*rtnumber/delta_t;

C_inlet=0.04; %solubility_1(T_inlet);
C_initial =solubility_1(T_msmpr);

T = ones(timegrid+1,1)*T_msmpr;
%-----
m=300; L0=0; LN =10^3*10^-6; phi=(LN-L0)/m; L=((L0+phi/2):phi:(LN-phi/2))';
%---- Seeding parameters for stable polymorph
seed_mass_stable=5e-7; %g/kg
stable_ave_size = 50*10^-6; %seed_average_size
stable_sd = 5*10^-6; %seed_standard deviation
CSD_stable(:,1) =normpdf(L,stable_ave_size,stable_sd); %pdf:density
stable_lambda=seed_mass_stable./(rho_stable*kv_stable*trapez(L,CSD_stable(:,1)
.*L.^3));
CSD_stable(:,1) = stable_lambda*CSD_stable(:,1)/v_solvent; % population
density--unit-#/m.m3
%---- Seeding parameters for metastable polymorph
seed_mass_metastable=5e-7;
metastable_ave_size = 100*10^-6;
metastable_sd = 10*10^-6;
CSD_metastable(:,1) =normpdf(L,metastable_ave_size,metastable_sd);
metastable_lambda=seed_mass_metastable./(rho_metastable*kv_metastable*trapez(L,C
SD_metastable(:,1) .*L.^3));
CSD_metastable(:,1)= metastable_lambda*CSD_metastable(:,1)/v_solvent;
%-----
f0 = CSD_stable(:,1); % the first column of CSD_stable is the CSD of
seeded crystal
f0_1 = CSD_metastable(:,1);
%----- For the stable polymorph Initial conditions
miu = trapz(L,f0.*L.^(0:5));
%----- For the metastable polymorph Initial conditions
miu_1 = trapz(L,f0_1.*L.^(0:5));

N0 = [ miu_1 miu zeros(1,12) C_initial]; %25 column
result(1,1:13) = [N0(1:12),N0(25)]; % 1 row, 13 column
miu_25(1,:) = N0;
%-----
B_stable = zeros(timegrid,1); B_metastable = zeros(timegrid,1); %#/s/kg

```

```

Dissolution_stable = zeros(timegrid,1); Dissolution_metastable =
zeros(timegrid,1); %m/s
Growth_stable = zeros(timegrid,1); Growth_metastable = zeros(timegrid,1);
%m/s

%---- Seeding parameters for operation
mseed = 5e-7;
Cseed=mseed/v_solvent;
CSD_seed(:,1) =normpdf(L,stable_ave_size,stable_sd); %pdf:density
seed_lamda=mseed./(rho_stable*kv_stable*trapz(L,CSD_seed(:,1) .*L.^3));
CSD_seed(:,1) = seed_lamda*CSD_seed(:,1)/v_solvent; % population density--
unit-#/m.m3
f0seed = CSD_seed(:,1); % the first column of CSD_stable is the CSD of
seeded crystal
%---- Seeding parameters for metastable polymorph
mseed_1=0;
CSD_seed_1(:,1) =normpdf(L,metastable_ave_size,metastable_sd);
seed_1_lamda=mseed_1./(rho_metastable*kv_metastable*trapz(L,CSD_seed_1(:,1)
.*L.^3));
CSD_seed_1(:,1)= seed_1_lamda*CSD_seed_1(:,1)/v_solvent;
f0seed_1 = CSD_seed_1(:,1);
fseed = f0seed.*phi;
fseed_1=f0seed_1*phi;
Nseed=[trapz(L,f0seed_1.*L.^(0:5)) trapz(L,f0seed.*L.^(0:5)) zeros(1,12)
Cseed]';
for i=1:timegrid

    result(i,1:12) = N0(1:12) + N0(13:24);
    result(i,13) = N0(25);

    Dissolution_stable(i) = Dissolution(kd,T(i),result(i,13));
    Dissolution_metastable(i) =
Dissolution_1(kd_1,T(i),result(i,13),result(end,4));
    Growth_stable(i) = growth(kg,g,T(i),result(i,13),Eg);
    Growth_metastable(i) = growth_1(kg_1,g_1,T(i),result(i,13),Eg_1);
    B_stable(i)=Birth(kb1,kb2,b,T(i),result(i,13),result(i,4),result(i,10));
    B_metastable(i)=Birth_1(kb_1,b_1,T(i),result(i,13),result(i,4));

    if i/v == fix(i/v)
        N0(1:24)=N0(1:24)+Nseed(1:24);
        Number_stable = f0.*phi;
        [~,F] =
ode45(@seed_msmpr_fun_CSD,[0,delta_t],Number_stable,[],Growth_stable(i),Dissol
ution_stable(i),B_stable(i),m,phi,residence_time,fseed);

        Number_metastable = f0_1.*phi;
        [~,F_1] =
ode45(@seed_msmpr_fun_CSD,[0,delta_t],Number_metastable,[],Growth_metastable(i
),Dissolution_metastable(i),B_metastable(i),m,phi,residence_time,fseed_1);

        ff = F(end,)./phi;
        ff_1 = F_1(end,)./phi; %population density

        CSD_stable(:,i+1) = ff;

```

```

CSD_metastable(:,i+1) = ff_1;
f0 = CSD_stable(:,i+1);
f0_1 = CSD_metastable(:,i+1);

[t1 N] =
ode45(@seed_msmpr_fun_miu,[0,delta_t],N0,[],T(i),rho_stable,kv_stable,rho_meta
stable,kv_metastable,...
      kb1,kb2,b,kb_1,b_1, kg,g,kg_1,g_1,
kd,kd_1,residence_time,C_inlet,Eg_1,Eg,Nseed);
N(N<0)=0;
N0 = real(N(end,:))';
miu_25(i+1,:)=N0;

else
Number_stable = f0.*phi;
[~,F] =
ode45(@single_msmpr_fun_CSD,[0,delta_t],Number_stable,[],Growth_stable(i),Diss
olution_stable(i),B_stable(i),m,phi,residence_time);

Number_metastable = f0_1.*phi;
[~,F_1] =
ode45(@single_msmpr_fun_CSD,[0,delta_t],Number_metastable,[],Growth_metastable
(i),Dissolution_metastable(i),B_metastable(i),m,phi,residence_time);

ff = F(end,:)./phi;
ff_1 = F_1(end,:)./phi;    %population density

CSD_stable(:,i+1) = ff;
CSD_metastable(:,i+1) = ff_1;
f0 = CSD_stable(:,i+1);
f0_1 = CSD_metastable(:,i+1);

[t1 N] =
ode45(@single_msmpr_fun_miu,[0,delta_t],N0,[],T(i),rho_stable,kv_stable,rho_me
tastable,kv_metastable,...
      kb1,kb2,b,kb_1,b_1, kg,g,kg_1,g_1,
kd,kd_1,residence_time,C_inlet,Eg_1,Eg);

N(N<0)=0;
N0 = real(N(end,:))';
miu_25(i+1,:)=N0;
end

end

Concentration= result(:,13);
Supersaturation_stable = result(:,13)./solubility(T(1:end-1));
Supersaturation_metastable = result(:,13)./solubility_1(T(1:end-1));

Number_ave_size_stable = result(:,8)./result(:,7)*10^6;
Number_ave_size_metastable = result(:,2)./result(:,1)*10^6;
Volume_ave_size_stable = result(:,11)./result(:,10)*10^6;
Volume_ave_size_metastable = result(:,5)./result(:,4)*10^6; %micrometer
Mass_stable_form = rho_stable/rho_solvent*kv_stable*1000*result(:,10);

```

```

Mass_metastable_form =
rho_metastable/rho_solvent*kv_metastable*1000*result(:,4);
mass_percent_stable =
Mass_stable_form./(Mass_stable_form+Mass_metastable_form);
yield = (C_inlet-N(end,25))./(C_inlet-
min(solubility(T_msmpr),solubility_1(T_msmpr)));

Mass_balance = C_inlet - (Mass_metastable_form(end) + Mass_stable_form(end) +
result(end,13))
yield_end = yield(end)
mass_percent_stable(end)
number_of_rt = delta_t*(1:timegrid)/residence_time;

function df = seed_msmpr_fun_CSD(t,f,G,D,B,m,phi,residence_time,fseed)
df = zeros(m,1);
df(1) = G./(phi).*(0-f(1)) + D./(phi).*(f(2)-f(1)) + B + (fseed(1)-
f(1))./residence_time;
df(2:m-1) = G./(phi).*(f(1:m-2)-f(2:m-1)) + D./(phi).*(f(3:m)-f(2:m-1)) +
(fseed(2:m-1)-f(2:m-1))./residence_time;
df(m) = G./(phi).*(f(m-1)-f(m)) + D./(phi).*(0-f(m)) +(fseed(m)-
f(m))./residence_time;
end

function dN
=seed_msmpr_fun_miu(~,N,T,rho_crystal,kv_stable,rho_crystal_1,kv_metastable,..
.
kb1,kb2,b,kb_1,b_1, kg,g,kg_1,g_1,
kd,kd_1,residence_time,Cinlet,Eg_1,Eg,Nseed)
dN = zeros(25,1);
g_d_1 = growth_1(kg_1,g_1,T(1),N(25),Eg_1)-
Dissolution_1(kd_1,T(1),N(25),(N(4)+N(16)));
g_d = growth(kg,g,T(1),N(25),Eg)-Dissolution(kd,T(1),N(25));
dN(1) = (Nseed(1)-N(1))./residence_time(1);
dN(2:6) = (1:5)'.*g_d_1.*N(1:5)+(Nseed(2:6)-N(2:6))./residence_time(1);
dN(7) = (Nseed(7)-N(7))./residence_time(1);
dN(8:12) = (1:5)'.*g_d.*N(7:11)+(Nseed(8:12)-N(8:12))./residence_time(1);
%-----
dN(13) = Birth_1(kb_1,b_1,T(1),N(25),(N(4)+N(16)))+(Nseed(13)-
N(13))./residence_time(1);
dN(14:18) = (1:5)'.*g_d_1.*N(13:17)+(Nseed(14:18)-
N(14:18))./residence_time(1);
dN(19) = Birth(kb1,kb2,b,T(1),N(25),(N(4)+N(16)),(N(10)+N(22)))+(Nseed(19)-
N(19))./residence_time(1);
dN(20:24) = (1:5)'.*g_d.*N(19:23)+(Nseed(20:24)-N(20:24))./residence_time(1);
dN(25)= -3*rho_crystal_1.*kv_metastable.*g_d_1.*(N(3)+N(15))...
-3*rho_crystal.*kv_stable.*g_d.*(N(9)+N(21))...
+(Cinlet+Nseed(25)-N(25))./residence_time(1);
end

function df = single_msmpr_fun_CSD(t,f,G,D,B,m,phi,residence_time)
df = zeros(m,1);
df(1) = G./(phi).*(0-f(1)) + D./(phi).*(f(2)-f(1)) + B-f(1)./residence_time;
df(2:m-1) = G./(phi).*(f(1:m-2)-f(2:m-1)) + D./(phi).*(f(3:m)-f(2:m-1)) -
f(2:m-1)./residence_time;
df(m) = G./(phi).*(f(m-1)-f(m)) + D./(phi).*(0-f(m)) - f(m)./residence_time;

```

```

function dN
=single_msmpr_fun_miu(~,N,T,rho_crystal,kv_stable,rho_crystal_1,kv_metastable,
...
    kb1,kb2,b,kb_1,b_1, kg,g,kg_1,g_1, kd,kd_1,residence_time,Cinlet,Eg_1,Eg)
dN = zeros(25,1);
g_d_1 = growth_1(kg_1,g_1,T(1),N(25),Eg_1)-
Dissolution_1(kd_1,T(1),N(25),(N(4)+N(16)));
g_d = growth(kg,g,T(1),N(25),Eg)-Dissolution(kd,T(1),N(25));
dN(1) = -N(1)./residence_time(1);
dN(2:6) = (1:5)'.*g_d_1.*N(1:5)-N(2:6)./residence_time(1);
dN(7) = -N(7)./residence_time(1);
dN(8:12) = (1:5)'.*g_d.*N(7:11)-N(8:12)./residence_time(1);
%-----
dN(13) = Birth_1(kb_1,b_1,T(1),N(25),(N(4)+N(16)))-N(13)./residence_time(1);
dN(14:18) = (1:5)'.*g_d_1.*N(13:17)-N(14:18)./residence_time(1);
dN(19) = Birth(kb1,kb2,b,T(1),N(25),(N(4)+N(16)),(N(10)+N(22)))-
N(19)./residence_time(1);
dN(20:24) = (1:5)'.*g_d.*N(19:23)-N(20:24)./residence_time(1);
dN(25)= -3*rho_crystal_1.*kv_metastable.*g_d_1.*(N(3)+N(15))...
        -3*rho_crystal.*kv_stable.*g_d.*(N(9)+N(21))...
        +(Cinlet-N(25))./residence_time(1);

```

E.6 Solubility regression

E.6.1 Apelblat Model

```

function f = apelblat(K,T)
A = K(1);
B = K(2);
C = K(3);
f = A + B./T + C.*log(T);

%lamdah different solvent fraction different parameters
w2=[0;0.1;0.2;0.3;0.4;0.5]; %solvent fraction here 1 is water
w1=ones(6,1)-w2;
T=[298.15;303.15;308.15;313.15;318.15]; %second solvent fraction
R=w2./w1;
r=[R;R;R;R;R;R];
x1=[142.6;98.16;63.01;36.89;21.49;10.61]./10000; %Solubility under 1 temp for
different solvent fraction
x2=[167.9;117.37;71.57;43.61;24.08;11.31]./10000;
x3=[198.6;139.03;82.42;47.16;25.82;12.02]./10000;
x4=[231.3;164.84;102.64;53.07;29.06;12.96]./10000;
x5=[269.4;196.28;123.65;65.86;32.95;17.43]./10000;
X1=[x1,x2,x3,x4,x5];
A = X1(1,:);
S0=[1,1,1]; %initial values
S1=lsqcurvefit(@apelblat,S0,T,X1(1,:));
f1=apelblat(S1,T);
Temp=[1./T,log(T)];
LM1=fitlm(Temp,X1(2,:));
LM2=fitlm(Temp,X1(3,:));

```

```

LM3=fitlm(Temp,X1(4,:));
LM4=fitlm(Temp,X1(5,:));
LM5=fitlm(Temp,X1(6,:));
s1=0;
t1=0;
for i=1:5
    AAD(i)=(f1(i)-A(i))/A(i);
    RMS(i) = (f1(i)-A(i))^2;
    s1=s1+abs(AAD(i));
    t1=t1+abs(RMS(i));
end
RAD1=s1/5;
RMD=sqrt(t1/5);
sp=f1';

```

E.6.2 λ h Model

```

function f=lamdah(S,T1)
%T1=data(:,1);x1=data(:,2);
%X(:,1):T X(:,2):Tm
lambda = S(1);
h = S(2);
f = 1./((exp(lambda*h*(1./T1-1./(330+273.13)))-1)/lambda+1);

%lamdah different solvent fraction different parameters
w2=[0;0.1;0.2;0.3;0.4;0.5]; %solvent fraction here 1 is water
w1=ones(6,1)-w2;
T=[298.15;303.15;308.15;313.15;318.15]; %second solvent fraction
R=w2./w1;
r=[R;R;R;R;R;R];
x1=[142.6;98.16;63.01;36.89;21.49;10.61]./10000; %Solubility under 1 temp for
different solvent fraction
x2=[167.9;117.37;71.57;43.61;24.08;11.31]./10000;
x3=[198.6;139.03;82.42;47.16;25.82;12.02]./10000;
x4=[231.3;164.84;102.64;53.07;29.06;12.96]./10000;
x5=[269.4;196.28;123.65;65.86;32.95;17.43]./10000;
X1=[x1,x2,x3,x4,x5];
A = X1(5,:);
S0=[1,1]; %initial values
[S1,RESNORM,RESIDUAL,EXITFLAG,OUTPUT,LAMBDA,J]=lsqcurvefit(@lamdah,S0,T,X1(5,:
)');
f1=lamdah(S1,T);
J=full(J);
[Q,R] = qr(J,0);
h = min(.9999, sum(Q.*Q,2));
adjfactor = 1 ./ sqrt(1-h);
fullr = X1(5,:) - f1;
rr = fullr(:);
radj = rr .* adjfactor;
rankJ = size(J,2);
Rinv = R \ eye(size(R));
pinvJTJ = Rinv*Rinv';
VQ = Q;
    %mse = sig.^2;

```

```

        %Sigma = mse*pinvJTJ;
        p = numel(S1);
        %n = length(radj);
        n = length(radj);
rs = sort(abs(r));
s = median(rs(max(1,min(n,p)):end)) / 0.6745;
MSE = (RESIDUAL'*RESIDUAL)/(n-p);
CovB = inv(J'*J)*MSE;
D=diag(CovB);
SE=sqrt(D);
s1=0;
t1=0;
for i=1:5
    AAD(i)=(f1(i)-A(i))/A(i);
    RMS(i) = (f1(i)-A(i))^2;
    s1=s1+abs(AAD(i));
    t1=t1+abs(RMS(i));
end
RAD1=s1/5;
RMD=sqrt(t1/5);
sp=f1';

```

E.6.3 NRTL model

`function y=NRTL(K,X)` %K is the fitting parameter,X is the sum of input

```

x1 = X(:,1); %mole fraction of solute
x2 = X(:,2); %mole fraction of solvent1
x3 = X(:,3);
T = X(:,4); % corresponding Temp
H_fus=22197; %J/mol
T_fus=330+273.13; %K
T_fus=T_fus*ones((size(x1)));
R=8.314;
% only x1 is independent variable
tau_12 = K(1)/(R*T); %K1 = d_g12 T/K
tau_13 = K(2)/(R*T);
tau_23 = K(3)/(R*T);
tau_21 = K(4)/(R*T);
tau_31 = K(5)/(R*T);
tau_32 = K(6)/(R*T);
alpha_12 = 0.1;alpha_21 = 0.1;
alpha_13 = 0.1;alpha_31 = 0.1;
alpha_23 = 0.1;alpha_32 = 0.1;
G12 = exp(-alpha_12*tau_12);G21 = exp(-alpha_21*tau_21);
G13 = exp(-alpha_13*tau_13);G31 = exp(-alpha_31*tau_31);
G23 = exp(-alpha_23*tau_23);G32 = exp(-alpha_32*tau_32);
ln_gamma1 =
((x2.*G21+x3.*G31).*(x2.*G21.*tau_21+x3.*G31.*tau_31))./(x1+x2.*G21+x3.*G31)./(
(x1+x2.*G21+x3.*G31) +((x2.*G12).*(x2.*tau_12+x3.*G32.*tau_12-
x3.*G32.*tau_32))./(x1.*G12+x2+x3.*G32))./(x1.*G12+x2+x3.*G32)+((x3.*G13).*(x2.
*G23.*tau_13+x3.*tau_13-
x2.*tau_23.*G23))./(x1.*G13+x2.*G23+x3))./(x1.*G13+x2.*G23+x3);

```

```

y = log(x1)+ln_gamma1+(H_fus/R).*(1./T-1./T_fus);

%NRTL
w2=[0;0.1;0.2;0.3;0.4;0.5]; %solvent fraction here 1 is water
w1=ones(6,1)-w2;
T=[298.15;303.15;308.15;313.15;318.15]; %second solvent fraction
R=w2./w1;
r=[R;R;R;R;R;R];
T=[298.15*ones(6,1);303.15*ones(6,1);308.15*ones(6,1);313.15*ones(6,1);318.15*
ones(6,1)];
X4=T;
xm1=[142.6;98.16;63.01;36.89;21.49;10.61]./10000; %Solubility under 1 temp for
different solvent fraction
xm2=[167.9;117.37;71.57;43.61;24.08;11.31]./10000;
xm3=[198.6;139.03;82.42;47.16;25.82;12.02]./10000;
xm4=[231.3;164.84;102.64;53.07;29.06;12.96]./10000;
xm5=[269.4;196.28;123.65;65.86;32.95;17.43]./10000;
X1=[xm1;xm2;xm3;xm4;xm5];
X2=(1./(1+r)).*(ones(size(X1))-X1);%water
X3=ones(size(X1))-X1-X2;%second
H_fus=22197; %J/mol
T_fus=330+273.13; %K
T_fus=T_fus*ones((size(X1)));
K0=[415.174633428731,39511.5392176358,31658.0873074477,-
1285.84121754338,36837.4264172079,27967.8262397137]; %initial values
K1=[-364.031122513534,-12096.2926098047,-23301.5709032888,-
553.877281141047,46187.4475469827,6425.59889156923];
K2=[171.359231721184,39691.0768371614,-
1054.98522073185,31661.0370332973,36580.2822883902,28186.9157869135];
X=[X1,X2,X3,X4];
y0=zeros((size(X1)));
S1=lsqcurvefit(@NRTL,K1,X,y0);
S2=lsqnonlin(@NRTLC4EG,K2);
[S3,RESNORM,RESIDUAL,EXITFLAG,OUTPUT,LAMBDA,J]=lsqnonlin(@NRTLSEEG,K0);
f1=exp(NRTL(S1,X)+log(X1));%calculated solubility
f3=(NRTLSEEG(S3)+1).*X1;
J=full(J);
[Q,R] = qr(J,0);
h = min(.9999, sum(Q.*Q,2));
adjfactor = 1 ./ sqrt(1-h);
fullr = y0- f3;
rr = fullr(:);
radj = rr .* adjfactor;
rankJ = size(J,2);
Rinv = R \ eye(size(R));
pinvJTJ = Rinv*Rinv';
VQ = Q;
%mse = sig.^2;
%Sigma = mse*pinvJTJ;
p = numel(S3);
%n = length(radj);
n = length(radj);
rs = sort(abs(r));
s = median(rs(max(1,min(n,p)):end)) / 0.6745;
MSE = (RESIDUAL'*RESIDUAL)/(n-p);

```



```

CovB = pinv(J'*J)*MSE;
D=diag(CovB);
SE=sqrt(D);
s1=0;
t1=0;
s3=0;
t3=0;
for i=1:30
    AAD(i)=(f1(i)-X1(i))/X1(i);
    RMS(i) = (f1(i)-X1(i))^2;
    AAD3(i)=(f3(i)-X1(i))/X1(i);
    RMS3(i) = (f3(i)-X1(i))^2;
    s1=s1+abs(AAD(i));
    t1=t1+abs(RMS(i));
    s3=s3+abs(AAD3(i));
    t3=t3+abs(RMS3(i));
end
RAD1=s1/30;
RAD3=s3/30;
RMD=sqrt(t1/30);
RMD3=sqrt(t3/30);
[x,y] = meshgrid([298.15,303.15,308.15,313.15,318.15],1:-0.1:0.5);
z=[xm1,xm2,xm3,xm4,xm5];
figure(1)
surf(x,y,z)
shading interp
colorbar
xlabel('Temp/K')
ylabel('w1')
zlabel('Taurine fraction')

z2=zeros(6,5);
for i=1:5
    for k=1:6
        z2(k,i)=f3((i-1)*6+k,1);
    end
end
figure(2)
surf(x,y,z2)
shading interp
colorbar
xlabel('Temp/K')
ylabel('w1')
zlabel('Taurine fraction')

```

E.6.4 UNIQUAC model

```

function y=Uniquac(K,X) %K is the fitting parameter,X is the sum of input

x1 = X(:,1); %mole fraction of solute
x2 = X(:,2); %mole fraction of solvent1
x3 = X(:,3);
T = X(:,4); % corresponding Temp
H_fus=22197; %J/mol

```

```

T_fus=330+273.13; %K
T_fus=T_fus*ones((size(x1)));
R=8.314;
% only x1 is independent variable
tau_12 = exp(K(1)./(T)); %K1 = d_g12 T/K
tau_13 = exp(K(2)./(T));
tau_23 = exp(K(3)./(T));
tau_21 = exp(K(4)./(T));
tau_31 = exp(K(5)./(T));
tau_32 = exp(K(6)./(T));

q1 = 4.921; r1 = 3.995;
q2 = 1.4; r2 = 0.92;%water
q3 = 2.2488; r3 = 2.4088; %second
z = 10;
l1 = 0.5*z*(r1-q1)-(r1-1);
l2 = 0.5*z*(r2-q2)-(r2-1);
l3 = 0.5*z*(r3-q3)-(r3-1);
theta1 = q1*x1./(q1*x1+q2*x2+q3*x3); theta2 = q2*x2./(q1*x1+q2*x2+q3*x3);
theta3 = q3*x3./(q1*x1+q2*x2+q3*x3);
psy1 = r1*x1./(r1*x1+r2*x2+r3*x3); psy2 = r2*x2./(r1*x1+r2*x2+r3*x3); psy3 =
r3*x3./(r1*x1+r2*x2+r3*x3);
ln_gamma1 = (0.5*z)*q1.*log(theta1./psy1)+log(psy1./x1)+psy2.*(l1-
r1/r2*l2)+psy3.*(l1-r1/r3*l3)-
q1*log(theta1+theta2.*tau_21+theta3.*tau_31)+((q1*theta2.*tau_21+q1*theta3.*ta
u_31)./(theta1+theta2.*tau_21+theta3.*tau_31)-
q1*theta2.*tau_12./(theta1.*tau_12+theta2.*tau_32)-
q1*theta2.*tau_13./(theta1.*tau_13+theta2.*tau_23+theta3));
y = log(x1)+ln_gamma1+(H_fus/R).*(1./T-1./T_fus);

%Uniquac
w2=[0;0.1;0.2;0.3;0.4;0.5;]; %solvent fraction here 1 is water
w1=ones(6,1)-w2;
T=[298.15;303.15;308.15;313.15;318.15]; %second solvent fraction
R=w2./w1;
r=[R;R;R;R;R;];
T=[298.15*ones(6,1);303.15*ones(6,1);308.15*ones(6,1);313.15*ones(6,1);318.15*
ones(6,1)];
X4=T;
xm1=[142.6;98.16;63.01;36.89;21.49;10.61]./10000; %Solubility under 1 temp for
different solvent fraction
xm2=[167.9;117.37;71.57;43.61;24.08;11.31]./10000;
xm3=[198.6;139.03;82.42;47.16;25.82;12.02]./10000;
xm4=[231.3;164.84;102.64;53.07;29.06;12.96]./10000;
xm5=[269.4;196.28;123.65;65.86;32.95;17.43]./10000;
X1=[xm1;xm2;xm3;xm4;xm5;];
X2=(1./(1+r)).*(ones(size(X1))-X1);%water
X3=ones(size(X1))-X1-X2;%second
H_fus=22197; %J/mol
T_fus=330+273.13; %K
T_fus=T_fus*ones((size(X1)));
K0=[166.850442341300,3118.17967952437,4358.89937236733,-303.915681289514,-
253.041153687467,-491.924486555558]; %initial values
K1=[166.850442341300,3118.17967952437,4358.89937236733,-303.915681289514,-
253.041153687467,-491.924486555558];

```

```

X=[X1,X2,X3,X4];
y0=zeros((size(X1)));
S1=lsqcurvefit(@Uniquac,K0,X,y0);
[S2,RESNORM,RESIDUAL,EXITFLAG,OUTPUT,LAMBDA,J]=lsqnonlin(@UniquacRSE,K1);
f1=exp(Uniquac(S1,X)+log(X1));%calculated solubility
f3=(UniquacRSE(S2)+1).*X1;
J=full(J);
[Q,R] = qr(J,0);
h = min(.9999, sum(Q.*Q,2));
adjfactor = 1 ./ sqrt(1-h);
fullr = y0- f3;
rr = fullr(:);
radj = rr .* adjfactor;
rankJ = size(J,2);
    Rinv = R \ eye(size(R));
    pinvJTJ = Rinv*Rinv';
    VQ = Q;
    %mse = sig.^2;
    %Sigma = mse*pinvJTJ;
    p = numel(S2);
    %n = length(radj);
    n = length(radj);
rs = sort(abs(r));
s = median(rs(max(1,min(n,p)):end)) / 0.6745;
MSE = (RESIDUAL'*RESIDUAL)/(n-p);
CovB = pinv(J'*J)*MSE;
D=diag(CovB);
SE=sqrt(D);
t=S2/SE';
s1=0;
t1=0;
s3=0;
t3=0;
for i=1:30
    AAD(i)=(f1(i)-X1(i))/X1(i);
    RMS(i) = (f1(i)-X1(i))^2;
    AAD3(i)=(f3(i)-X1(i))/X1(i);
    RMS3(i) = (f3(i)-X1(i))^2;
    s1=s1+abs(AAD(i));
    t1=t1+abs(RMS(i));
    s3=s3+abs(AAD3(i));
    t3=t3+abs(RMS3(i));
end
RAD1=s1/30;
RAD3=s3/30;
RMD=sqrt(t1/30);
RMD3=sqrt(t3/30);
[x,y] = meshgrid([298.15,303.15,308.15,313.15,318.15],1:-0.1:0.5);
z=[xm1,xm2,xm3,xm4,xm5];
figure(1)
surf(x,y,z)
shading interp
colorbar
xlabel('Temp/K')
ylabel('w1')

```

```

xlabel('Taurine fraction')

z2=zeros(6,5);
for i=1:5
    for k=1:6
        z2(k,i)=f3((i-1)*6+k,1);
    end
end
figure(2)
surf(x,y,z2)
shading interp
colorbar
xlabel('Temp/K')
ylabel('w1')
xlabel('Taurine fraction')

```

E.6.5 Wilson model

```

function y=Wilson(K,X) %K is the fitting parameter,X is the sum of input

x1 = X(:,1); %mole fraction of solute
x2 = X(:,2); %mole fraction of solvent1
x3 = X(:,3);
T = X(:,4); % corresponding Temp
H_fus=22197; %J/mol
T_fus=330+273.13; %K
T_fus=T_fus*ones((size(x1)));
V=ones(3,1);
V(3)=55.8;
V(2)=18;
V(1)=110.7; %initial values
R=8.314;
% only x1 is independent variable
lamda_12 = (V(2)/V(1)).*exp(-K(1)./(R*T)); %K1 = d_lamda12 T/K
lamda_13 = (V(3)/V(1)).*exp(-K(2)./(R*T));
lamda_23 = (V(3)/V(2)).*exp(-K(3)./(R*T));
lamda_21 = (V(1)/V(2)).*exp(-K(4)./(R*T));
lamda_31 = (V(1)/V(3)).*exp(-K(5)./(R*T));
lamda_32 = (V(2)/V(3)).*exp(-K(6)./(R*T));
ln_gamma1 = (1-log(x1+lamda_12.*x2+lamda_13.*x3)-
((x1./(x1+lamda_12.*x2+lamda_13.*x3))+((lamda_21.*x2)./(lamda_21.*x1+x2+lamda_
23.*x3))+((lamda_31.*x3)./(lamda_31.*x1+lamda_32.*x2+x3)))); % activity
equation from wilson
y = log(x1)+ln_gamma1+(H_fus/R).*(1./T-1./T_fus);

%Wilson
w2=[0;0.1;0.2;0.3;0.4;0.5;]; %solvent fraction here 1 is water
w1=ones(6,1)-w2;
T=[298.15;303.15;308.15;313.15;318.15]; %second solvent fraction
R=w2./w1;
r=[R;R;R;R;R;];
T=[298.15*ones(6,1);303.15*ones(6,1);308.15*ones(6,1);313.15*ones(6,1);318.15*
ones(6,1)];
X4=T;

```

```

xm1=[142.6;98.16;63.01;36.89;21.49;10.61]./10000; %Solubility under 1 temp for
different solvent fraction
xm2=[167.9;117.37;71.57;43.61;24.08;11.31]./10000;
xm3=[198.6;139.03;82.42;47.16;25.82;12.02]./10000;
xm4=[231.3;164.84;102.64;53.07;29.06;12.96]./10000;
xm5=[269.4;196.28;123.65;65.86;32.95;17.43]./10000;
X1=[xm1;xm2;xm3;xm4;xm5;];
X2=(1./(1+r)).*(ones(size(X1))-X1);%water
X3=ones(size(X1))-X1-X2;%second
V=ones(3,1);
V(3)=55.8;
V(2)=18;
V(1)=110.7; %initial values
X=[X1,X2,X3,X4];V=ones(3,1);
H_fus=22197; %J/mol
T_fus=330+273.13; %K
T_fus=T_fus*ones((size(X1)));
R=8.314;
K0=[-
7783.01606398076,5278.85424132866,1485.14097378667,1011.08716151173,4259.55745
062212,2689.78377537925]; %initial values
K1=[2742.66032852498,46142.2887942580,2917.12312457321,1114.98824649138,6401.8
0339090203,6082.41493628328];
X=[X1,X2,X3,X4];
y0=zeros((size(X1)));
S1=lsqcurvefit(@Wilson,K0,X,y0);
[S2,RESNORM,RESIDUAL,EXITFLAG,OUTPUT,LAMBDA,J]=lsqnonlin(@WilsonRSE,K1);
f1=exp(Wilson(S1,X)+log(X1));%calculated solubility
f3=(WilsonRSE(S2)+1).*X1;
J=full(J);
[Q,R] = qr(J,0);
h = min(.9999, sum(Q.*Q,2));
adjfactor = 1 ./ sqrt(1-h);
fullr = y0- f3;
rr = fullr(:);
radj = rr .* adjfactor;
rankJ = size(J,2);
Rinv = R \ eye(size(R));
pinvJTJ = Rinv*Rinv';
VQ = Q;
    %mse = sig.^2;
    %Sigma = mse*pinvJTJ;
    p = numel(S1);
    %n = length(radj);
    n = length(radj);
rs = sort(abs(r));
s = median(rs(max(1,min(n,p)):end)) / 0.6745;
MSE = (RESIDUAL'*RESIDUAL)/(n-p);
CovB = inv(J'*J)*MSE;
D=diag(CovB);
SE=sqrt(D);
s1=0;
t1=0;
s3=0;
t3=0;

```

```

for i=1:30
    AAD(i)=(f1(i)-X1(i))/X1(i);
    RMS(i) = (f1(i)-X1(i))^2;
    AAD3(i)=(f3(i)-X1(i))/X1(i);
    RMS3(i) = (f3(i)-X1(i))^2;
    s1=s1+abs(AAD(i));
    t1=t1+abs(RMS(i));
    s3=s3+abs(AAD3(i));
    t3=t3+abs(RMS3(i));
end
RAD1=s1/30;
RAD3=s3/30;
RMD=sqrt(t1/30);
RMD3=sqrt(t3/30);
[x,y] = meshgrid([298.15,303.15,308.15,313.15,318.15],1:-0.1:0.5);
z=[xm1,xm2,xm3,xm4,xm5];
figure(1)
surf(x,y,z)
shading interp
colorbar
xlabel('Temp/K')
ylabel('w1')
zlabel('Taurine fraction')

z2=zeros(6,5);
for i=1:5
    for k=1:6
        z2(k,i)=f1((i-1)*6+k,1);
    end
end
figure(2)
surf(x,y,z2)
shading interp
colorbar
xlabel('Temp/K')
ylabel('w1')
zlabel('Taurine fraction')

```

Curriculum Vitae

Name: Weizhong Gong

Post-secondary Education and Degrees: East China University of Science and Technology (ECUST)
Shanghai, China
Sep. 2015 - June.2019 B.Eng

The University of Western Ontario
London, Ontario, Canada
Sep. 2017 - June.2019 B.Eng

The University of Western Ontario
London, Ontario, Canada
Sep. 2019 - Apr.2024 Ph.D

Honours and Awards: Secondary Scholarship of the school Year I in ECUST, 2016
UWO In-Course Scholarships Year IV, 2018
Outstanding Volunteers in ECUST, 2015
Dean's Honor List, 2018 & 2019

Related Work Experience Teaching Assistant
The University of Western Ontario
Process Dynamics and Control -- Winter. 2020/2021/2022
Engineering Thermodynamics. -- Fall. 2021/2022
Staged Operations -- Fall. 2019

Publications:

- (1) Gong, W., Wu, Y., Lin, M., & Rohani, S. (2021). Polymorphism control of l-Glutamic acid in a single-stage and a two-stage MSMR crystallizer by different seeding strategies. *Chemical Engineering Research and Design*, 170, 23-33.
- (2) Gong, W., Mondal, P. K., Ahmadi, S., Wu, Y., & Rohani, S. (2021). Cocrystals, salts, and salt-solvates of olanzapine; selection of cofomers and improved solubility. *International Journal of Pharmaceutics*, 608, 121063.
- (3) Gong, W., Li, P., & Rohani, S. (2022). Taurine in several aqueous binary solvents: Solubility prediction, measurement, modeling, solvent effect, and thermodynamics. *Journal of Molecular Liquids*, 367, 120522.
- (4) Ahmadi, S., Mondal, P. K., Wu, Y., Gong, W., Mirmehrabi, M., & Rohani, S. (2021). Virtual multicomponent crystal screening: Hydrogen bonding revisited. *Crystal Growth & Design*, 21(10), 5862-5872.